Investigation of Universal Behavior in Symmetric Diblock Copolymer Melts

A THESIS
SUBMITTED TO THE FACULTY OF THE GRADUATE SCHOOL
OF THE UNIVERSITY OF MINNESOTA
BY

Pavani Medapuram

IN PARTIAL FULFILLMENT OF THE REQUIREMENTS
FOR THE DEGREE OF
DOCTOR OF PHILOSOPHY

Advisor: David Morse

December 2015

Acknowledgments

I would like to thank Prof. David C. Morse for being a great advisor - brilliant, insightful, and a truly wonderful teacher. Dave was always available for discussing research and answering questions; I inevitably left every meeting with him inspired to achieve his level of clarity and thoroughness in both thinking and communication. To work with him has been a great learning experience for me - one that will constantly drive me to achieve perfection in what I do.

I am grateful to my collaborators from whom I have learned so very much - all the way from setting up a simulation to writing a paper: Jens Glaser, Prof. Frank S. Bates, Timothy Gillard, and Prof. Mark Matsen. A special note of thanks to Jens Glaser for guiding me through several programming challenges, teaching me numerous shortcuts and tricks, and for introducing me to GPUs, without which I simply could not have produced the large body of simulation results presented in this thesis. I would also like to thank my group members Raghuram Thiagarajan, Andrew Gustafson, Taher Ghasimakbari, and Joshua Myson for being wonderful coworkers.

I would like to thank all my Minneapolis friends: Jikku Thomas, Aditya Kedlaya, Anand Kartha, Rahul Saladi, Haritha Bellam, Divyanshu, Aruna Ramakrishnan, Thaseem Thajudeen, Palak Ambwani, Suma Karnam, and Bala. They made the last six years fun and fulfilling and I will forever cherish their friendships. I would also like to thank some of my fellow PhD students: Ravali Raju, Sarit Dutta, Karen Haman, Lucas Mcintosh, Abhiram Muralidhar, and Akash Arora. They were the reason for countless coffee breaks and conversations.

My parents and brother have always been a limitless source of love and inspiration for me. My heartfelt gratitude to them for constantly supporting me and for never making me feel far from home despite the distance (Thank you internet). I have counted on their wisdom and advice time and time again, and words cannot even begin to express my love and respect for them.

Lastly, to Raghu, for being an unconditional source of love and support and for being there through all the pleasures and tribulations of a PhD. I am indeed fortunate to have had his calm intellect and cheerful attitude by my side for the last six years. I look forward to our journey ahead, together.

To,
Amma and Nanna

Abstract

Coarse-grained theories of dense polymer liquids such as block copolymer melts predict a universal dependence of equilibrium properties on a few dimensionless parameters. For symmetric diblock copolymer melts, such theories predict a universal dependence on only $\chi_e N$ and $\overline{N}$, where χ_e is an effective interaction parameter, N is the degree of polymerization, and $\overline{N}$ is a measure of overlap. This thesis focuses on testing the universal behavior hypothesis by comparing results for various properties obtained from different coarse-grained simulation models to each other. Specifically, results from pairs of simulations of different models that have been designed to have matched values of $\overline{N}$ are compared over a range of values of χN. The use of vastly different simulation models allows us to cover a vast range of $\overline{N} \simeq 200$ - 8000 that includes most of the experimentally relevant range.

Properties studied here include collective and single-chain correlations in the disordered phase, block and chain radii of gyration in the disordered phase, the value of $\chi_e N$ at the order-disorder transition (ODT), the free energy per chain, the latent heat of transition, the layer spacing, the composition profile, and compression modulus in the ordered phase. All results strongly support the universal scaling hypothesis, even for rather short chains, confirming that it is indeed possible to give an accurate universal description of simulation models that differ in many details. The underlying universality becomes apparent, however, only if data are analyzed using an adequate estimate of χ_e, which we obtained by fitting the structure factor $S(q)$ in the disordered state to predictions of the recently developed renormalized one-loop (ROL) theory. The ROL theory is shown to provide an excellent description of the dependence of $S(q)$ on chain length and thermodynamic conditions for all models, even for very short chains, if we allow for the existence of a nonlinear dependence of the effective interaction parameter χ_e upon the strength of the AB repulsion.

The results show that behavior near the ODT exhibits a different character at moderate and high values of $\overline{N}$, with a crossover near $\overline{N} \simeq 10^4$. Within the range $\overline{N} \lesssim 10^4$ studied in this work, the ordered and disordered phases near the ODT both contain strongly segregated domains of nearly pure A and B, in contrast to the assumption of weak segregation underlying the FredricksonHelfand (FH) theory. In this regime, the FH theory is inaccurate and substantially underestimates the value of $\chi_e N$ at the ODT. Results for the highest values of $\overline{N}$ studied here agree reasonably well with FH predictions, suggesting that the theory may be accurate for $\overline{N} \gtrsim 10^4$. Self-consistent field theory (SCFT) grossly underestimates $(\chi_e N)_{\mathrm{ODT}}$ for modest $\overline{N}$ because it cannot describe strong correlations in the disordered phase. SCFT is found, however, to yield accurate predictions for several properties of the ordered lamellar phase.

A detailed quantitative comparison of experimental results to theoretical predictions and obtained simulations results is also presented. Experimental results for structure factor obtained from small-angle neutron and X-ray scattering (SANS and SAXS) measurements are analyzed using methods closely analogous to those used to analyze simulation results. Peak scattering intensity results of different chain lengths of a AB pair are fitted to the ROL theory predictions in order to estimate the effective interaction parameter $\chi_e(T)$ of the chemical system. The resulting $\chi_e(T)$ estimates are used to obtain ODT values $(\chi_e N)_{\mathrm{ODT}}$ of different experimental systems, which we compare to the scaling law obtained from simulation results and to theoretical predictions. The results are largely consistent with the expected systematic decrease with increasing $\overline{N}$ and lie closer to the simulations scaling law than to any theoretical prediction. These results confirm the overwhelming importance of fluctuation effects in systems with modest values of $\overline{N} = 10^2 - 10^3$, and the usefulness of coarse-grained simulations as a starting point for quantitative modeling.

Contents

List of Tables

List of Figures

Chapter 1

Introduction

Polymers are chain molecules, composed of long sequences of repeating chemical units (i.e., monomers). Diblock copolymers (for example, *A*-*A*-*A*-*B*-*B*-*B*) are polymers that consist of two linear blocks containing different types of monomer. In a liquid of diblock copolymer molecules, unfavorable interactions between unlike monomers results in a tendency for the two different monomer types to separate into different regions of space. If the two blocks of each chain were not chemically linked, this would lead to macroscopic phase separation, such as that seen in a mixture of oil and vinegar. Diblock copolymers instead tend to form ordered structures in which different blocks segregate into micro-domains that form a periodic pattern; the exact pattern varies depending on the composition fraction f of the two blocks as shown in Fig.1.1. This occurs only when the repulsion between unlike monomers is sufficiently strong at temperatures below a certain critical temperature. When the repulsion is weaker, diblock copolymers form a disordered melt like phase in which there is no permanent pattern. A transition from the disordered phase to an ordered phase is known as an order-disorder transition (ODT).[2] In this work, we exclusively study symmetric diblock copolymers ($f_A = 0.5$), which form lamellae in the ordered phase.

Numerous experimental and computational studies have been conducted to investigate the behavior of diblock copolymers and, in particular, the order-disorder transition. Block copolymers synthesized from a wide variety of different types of chemical building blocks have been experimentally studied. These studies have shown a remarkable degree of similarity among results obtained

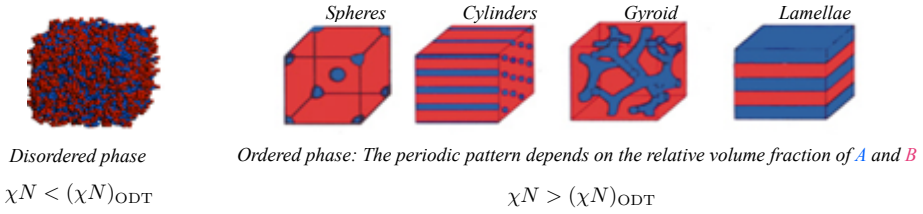

Figure 1.1: Disordered and ordered phases of diblock copolymers.

from different molecules.

Theoretical understanding of diblock copolymers is largely based on the self-consistent field theory theory (SCFT) of phase behavior[3] and the closely related random phase approximation (RPA) theory of composition fluctuations.[4] SCFT is a highly simplified theory in which all of the required information about chemical structure is summarized by the values of a few parameters. For idealized diblock copolymers with structurally similar A and B monomers, SCFT predicts a phase diagram that depends upon only two parameters: (1) the fraction f_A of A monomers within each chain, and (2) the product χN of an interaction parameter χ and the degree of polymerization N. Interaction parameter χ is a measure of the thermodynamic incompatibility between A and B monomers, and is related to the excess free energy cost of solvating a block of A monomers in a matrix of pure B. While SCFT has proved very successful in rationalizing a large body of experimental data, it is far from perfect.

Understanding of the limitations of the SCFT and RPA for block copolymers has long relied primarily on the work of Fredrickson and Helfand.[5] These authors adapted earlier work by Brazovskiĭ[6] on weakly first order crystallization transitions to describe the order-disorder transition of nearly-symmetric diblock copolymers. The Fredrickson-Helfand (FH) theory predicts corrections to the SCFT and RPA whose magnitudes are controlled by a dimensionless number $\overline{N} = N(cb^3)^2$, sometimes referred to as the invariant degree of polymerization. Here, N is the degree of polymerization, c is the monomer concentration, and b is the statistical segment length. Predicted corrections decrease with increasing $\overline{N}$, thus recovering SCFT and RPA predictions in the limit $\overline{N} \to \infty$. The parameter $\overline{N}$ is a measure of overlap among polymers in a dense liquid: $\overline{N}^{1/2}$ is proportional to the number $\overline{N}^{1/2} \sim R^3 c/N$ of polymers of steric volume N/c

that can be packed into the volume R^3 pervaded by a random walk coil of size $R \sim \sqrt{N}b$.

The Fredrickson-Helfand theory was designed to describe only the dominant effects of strong composition fluctuations very near the order disorder transition of very long, nearly symmetric diblock copolymers. Several authors[7,8] attempted to construct a more complete theory of corrections to the SCFT/RPA of FH theory, but encountered similar conceptual difficulties that delayed progress for many years. The most serious conceptual problem arose from the fact that predictions obtained from highly coarse-grained models were found to be very sensitive to the treatment of short wavelength correlations, at length scales that the underlying models were never designed to describe. A more recent generation of "renormalized one-loop" theories[9–17] overcame this and other problems and allowed the development of much more rigorous theories of corrections to the random walk and random phase approximations in homopolymer melts,[10–12] polymer blends,[9,14,15] and diblock copolymer melts.[14,17] The analytical treatment of composition fluctuations in disordered phase by the "renormalized one-loop" (ROL) theory developed by Morse and coworkers makes an important qualitative prediction: It predicts that equivalent behavior should be obtained in "corresponding states of systems that may differ in many details, but that are characterized by equal values for SCFT dimensionless parameters *and* the invariant degree of polymerization or overlap parameter $\overline{N}$. The hypothesis is a generalization of predictions of previous theories and appears to have a broader physical significance than the theories that inspired it.

In this work, we present a detailed investigation of this "corresponding states" or universal behavior using mainly computer simulations of symmetric diblock copolymers ($f_A = 0.5$). To this end, we focus on obtaining results from different coarse-grained simulation models for several properties in the disordered and ordered phases, including the ordered-disorder transition location, and subsequently, comparing these results to examine if corresponding thermodynamic states of different simulation models yield equivalent results. Corresponding thermodynamic states of symmetric diblock copolymers are states with equal values of the parameters $\chi_e N$ and $\overline{N}$, where χ_e is an effective Flory-Huggins interaction parameter and N is the degree of polymerization. In addi-

tion, wherever available, we compare simulations results to existing theoretical predictions to test the accuracy and validity of different theoretical predictions. The main conceptual problem in making comparisons amongst any combination of experiments, simulation, and theory is the absence of a clear method for defining the phenomenological interaction parameter χ in terms of the interaction parameter of a simulation model or temperature T in experiments.

1.1 Objectives and Outline

This thesis aims to investigate the universal behavior in symmetric diblock copolymer melts by extensively comparing results of different simulation models to each other and to theoretical predictions. In addition, it presents results from a few popular experimental studies in this same contextual framework.

Chapter 2 provides the relevant background required for this work. It discusses predictions for diblock copolymer properties by the popular SCF/RPA and FH theories and also, the more recently developed renormalized one-loop (ROL) theory for correlations in the disordered phase. The corresponding states or universality hypothesis for the behavior of symmetric diblock copolymer melts is formally postulated using the same notation as these theoretical predictions. Recent simulations studies by our group that test the accuracy of ROL theory predictions and provide preliminary evidence for the corresponding states behavior in disordered phase are reviewed. A brief overview of related experimental studies in the field is also presented.

The main strategy employed in this work for obtaining the corresponding states behavior is to compare results from corresponding thermodynamic states of different simulation models. To this end, we use four different coarse-grained simulation models, models H, S1, S2, and S3, throughout this work. Chapter 3 presents the design and calibration of these four models. It also presents a key concept used recurrently in this work, which is the method for accurately defining an effective Flory-Huggins interaction parameter χ_e.

In chapter 4, we present a detailed comparison of results for collective and single-chain correlations in the disordered phase from simulations of different models to predictions of the ROL theory and to each other. Both ROL theory

predictions and the corresponding state hypothesis are tested for a wide range of $\overline{N}$ values by virtue of obtaining results from different simulation models with vastly different interaction potentials and microscopic parameters.

Chapter 5 presents our method for obtaining accurate ODT locations in simulations. In chapter 6, we present an extensive study on the dependence of various properties of symmetric diblock copolymers on the invariant degree of polymerization $\overline{N}$ and the interaction parameter $\chi_e N$, focusing particularly on the vicinity of the ODT. Properties studied include the free energy per chain, the free energy derivative, the order-disorder transition, the latent heat of transition, the layer spacing, the composition profile and compression modulus in the ordered phase. Use of four different coarse-grained simulation models, models H, S1, S2, and S3, allows us to span a wide range of $\overline{N} \simeq 200 - 8000$ that includes most of the typical experimental range.

Chapters 7 and 8 present a detailed quantitative comparison of experimental results to simulations results of chapter 6 and to theoretical predictions. Scattering results from small-angle neutron and X-ray scattering (SANS and SAXS) experiments are analyzed in the same manner as simulations results to obtain estimates for effective interaction parameter $\chi_e(T)$ of experimental systems. Experimental ODT values obtained from resulting $\chi_e(T)$ estimates are then compared to simulations results and theoretical predictions for ODT.

Chapter 2

Background

In this chapter, we provide the required background for understanding the behavior of symmetric diblock copolymer melts in disordered and ordered phases and the order-disorder transition. Section 2.1 discusses the relevant theories in the field. Section 2.2 presents the standard methods used for estimating the phenomenological AB interaction parameter χ_e that is required as an input parameter for all theories. Section 2.3 provides a brief review of previous simulations studies in the field, including recently completed ones by our group. Section 2.4 discusses existing studies on comparison of experimental results to theoretical predictions.

2.1 Theory

We consider a dense, nearly incompressible melt of AB diblock copolymers, with N monomers per chain. We assume equal volumes per monomer for A and B monomers. Let $c = NM/V$ denote total monomer concentration, or inverse monomer volume, where M is the total number of chains in a total volume V. Let f_A denote the volume fraction of A monomers in each chain, while b_A and b_B denote statistical segment lengths for A and B monomers. We focus on the case of symmetric block copolymers, with $f_A = 1/2$ and $b_A = b_B = b$. Let $R_{e0} = \sqrt{N}b$ denote the random-walk end-to-end length and $R_{g0} = \sqrt{N/6}b$ the corresponding radius of gyration.

The extent of overlap in a dense polymer liquid can be characterized by a

dimensionless concentration

$$\overline{C} \equiv cR_{e0}^3/N = \sqrt{N}cb^3. \tag{2.1}$$

The so-called invariant degree of polymerization $\overline{N}$ is given by the square

$$\overline{N} \equiv \overline{C}^2 = N(cb^3)^2 \tag{2.2}$$

and is thus also a dimensionless measure of overlap.

Let G denote the excess free energy of the system, defined relative to an appropriate reference state. Let

$$g = G/(Mk_BT) \tag{2.3}$$

denote the dimensionless free energy per chain, normalized by the thermal energy k_BT, where k_B is Boltzmann's constant and T is absolute temperature.

Since a diblock melt contains two types of monomer, A and B, indexed by type indices i and j, we can define a 2×2 correlation function matrix with elements

$$S_{ij}(\mathbf{q}) \equiv \int \mathrm{d}\mathbf{r}\, e^{i\mathbf{q}\mathbf{r}} \langle \delta c_i(\mathbf{r}) \delta c_j(\mathbf{0}) \rangle \quad . \tag{2.4}$$

where $\delta c_i(\mathbf{r})$ is deviation of the concentration $c_i(\mathbf{r})$ of i monomers from its spatial average.

In a dense liquid, long-wavelength fluctuations in the total monomer density $c(\mathbf{r}) \equiv c_A(\mathbf{r}) + c_B(\mathbf{r})$ are much smaller than corresponding fluctuations in the composition field

$$\psi(\mathbf{r}) \equiv \frac{1}{2} \left[\, \delta c_A(\mathbf{r}) - \delta c_B(\mathbf{r}) \, \right], \tag{2.5}$$

It is thus convenient to define a scalar structure function

$$S(\mathbf{q}) \equiv \int \mathrm{d}\mathbf{r}\, e^{i\mathbf{q}\cdot\mathbf{r}} \langle \psi(\mathbf{r}) \psi(\mathbf{0}) \rangle \quad . \tag{2.6}$$

to characterize pure composition fluctuations. Rotational symmetry in the disordered phase guarantees that $S(\mathbf{q})$ depends only on the magnitude of the wavevector $\mathbf{q}$. The scalar structure factor $S(q)$ for a disordered diblock copolymer exhibits a maximum value $S(q^*)$ at a peak wavenumber q^* of order the

inverse polymer coil size. Measurements for $S(q)$ are obtained from small-angle neutron and X-ray scattering (SANS and SAXS) experiments, and therefore, the structure factor $S(q)$ is often called as the scattering intensity.

No liquid is completely incompressible. In a slightly compressible liquid, we expect the matrix $S_{ij}(q)$ at q of order the inverse coil size to have one large eigenvalue, with an eigenvector $\epsilon^- = (1, -1)$ that corresponds to fluctuations of $\psi(\mathbf{r}) \equiv c_A(\mathbf{r}) - c_B(\mathbf{r})$ at fixed concentration, and a second much smaller eigenvalue with an orthogonal eigenvector $\epsilon^+ = (1, 1)$ that corresponds to concentrations in total concentration $c(\mathbf{r})$. The function $S(q)$ gives the variance of the composition mode.

The vectors ϵ^+ and ϵ^- defined above are also exact eigenvectors of $S_{ij}(q)$ in the special case considered in this work, as a result of symmetry. The simulations presented here all use symmetric models of diblock copolymers, with equal number of A and B beads of identical structure. In this case, the system is symmetric under exchange of the labels of A and B beads. As a result, eigenvectors of $S_{ij}(q)$ must be either even or odd under this symmetry, and so must be given exactly by ϵ^+ and ϵ^- for all q, even in a compressible liquid.

Let $\Omega_{ij}(\mathbf{q})$ denote the intramolecular contribution to $S_{ij}(q)$, *i. e.,* , the contribution to $S_{ij}(q)$ for $q \neq 0$ that arises from correlations between pairs of monomers of types i and j within the same chain. This can also be written as a single-chain average

$$\Omega_{ij}(\mathbf{q}) = \frac{c}{N} \sum_{s \in i} \sum_{s' \in j} \langle e^{\mathbf{q} \cdot [\mathbf{R}(s) - \mathbf{R}(s')]} \rangle_{1-\text{chain}} \quad , \tag{2.7}$$

in which c/N is the number concentration of polymers, s and s' are monomer indices that are restricted to lie within the i and j blocks of the copolymer, respectively, $\mathbf{R}(s)$ is the position of monomer s, and $\langle \cdots \rangle_{1-\text{chain}}$ denotes an average over conformations of a single chain.

2.1.1 Standard Theories: SCFT and RPA

For many years, theoretical study of block copolymers has been dominated by the self-consistent field theory (SCFT) of phase behavior,[3,18] and by the random phase approximation (RPA) theory of composition fluctuations and scattering.[4]

Both these theories are intimately related: The RPA prediction for the structure factor $S(q)$ in disordered phase is derived using a SCFT approximation to estimate the free energy cost of infinitesimal composition fluctuations.

SCFT[3,19–21] is as a form of density functional theory for inhomogeneous polymer liquids such as block copolymer melts and homopolymer blends.[14] It is based on an expression for the free energy functional $G\left[\langle c\rangle\right]$ as a sum $G\left[\langle c\rangle\right] = G_{\text{chain}}\left[\langle c\rangle\right] + G_{\text{int}}\left[\langle c\rangle\right]$, where $\langle c\rangle$ represents the average concentration fields $\langle c_A(\mathbf{r})\rangle$ and $\langle c_B(\mathbf{r})\rangle$. $G_{\text{chain}}\left[\langle c\rangle\right]$ denotes the free energy of an ideal system of non-interacting chains and $G_{\text{int}}\left[\langle c\rangle\right]$ is the contribution from interactions between chains. The underlying assumptions of the theory are that polymer chains are random walks and that $G_{\text{int}}\left[\langle c\rangle\right]$ is a local functional of $\langle c\rangle$, independent of chain length and architecture. The simplest and most common form of SCFT, which we compare to in this work, obtains an expression for the local free energy by characterizing the free energy cost of contact between A and B monomers using a phenomenological parameter, the effective Flory-Huggins interaction parameter χ_e.

Because SCFT is based on an idealized model of polymers as continuous random walks, its predictions are invariant under a mathematical transformation that changes the nominal degree of polymerization N by redefining a "monomer", by grouping an arbitrary number of chemical repeat units into a single coarse-grained monomer. The thermodynamic state of a system is specified in SCFT by the values of a few dimensionless parameters that are invariant under this transformation. We refer to these as SCFT state variables. The SCFT state variables for an incompressible AB diblock copolymer are the product $\chi_e N$, the volume fraction f_A and the ratio b_A/b_B.

SCFT yields predictions for the dimensionless free energy g per chain in each phase as a function $g(\chi_e N, f_A, b_A/b_B)$ of these state variables. For the special case of symmetric diblock copolymer considered here, the only SCFT state variable is $\chi_e N$, and so SCFT predicts a free energy $g = g(\chi_e N)$ that depends on $\chi_e N$ alone. Because the only characteristic length scale in the standard model is the random-walk coil size R_{e0} or R_{g0}, SCFT yields predictions for quantities that involve a length scale in which all lengths appear non-dimensionalized by the coil size R_{e0} or R_{g0}. For example, SCFT yields a prediction for the ratio d/R_{e0}

of the layer spacing d in the lamellar phase of a symmetric diblock copolymer to R_{e0} as a universal function of $\chi_e N$. Predictions for structure factor $S(q)$ are given as predictions for a normalized inverse structure factor

$$H(q) \equiv cNS^{-1}(q) \quad , \tag{2.8}$$

which is invariant under a rescaling of N and c. Corresponding predictions for $\Omega_{ij}(q)$ may be given as predictions for $\Omega_{ij}(q)/cN$.

Leibler developed the random phase approximation (RPA) theory[4] for the behavior of composition fluctuations in the disordered phase, starting with the SCFT free energy expression. According to Leibler's RPA treatment, the exact expression for $S(q)$ is given by

$$H_0(q) \equiv cNS^{-1}(q) = F_0(q) - 2\chi_e N \tag{2.9}$$

where $F_0(q) = cN\Sigma_{ij}\Omega_{ij}(q)/\det|\Omega_{ij}(q)|$ is the single-chain form factor and is a function of the intramolecular correlation function $\Omega_{ij}(q)$, and χ_e is an effective interaction parameter. The RPA derives analytical expressions for $\Omega_{ij}(q)$ by assuming random-walk statistics for single polymer chains. In its most general form, the RPA allows χ_e to exhibit an arbitrary dependence on the temperature, concentration, and parameters of the Hamiltonian, but requires that χ_e be independent of q, N, and architecture. Here and hereafter, we use a subscript 0 to denote quantities such as $H_0(q) \equiv cNS_0^{-1}(q)$, $S_0(q)$, and $F_0(q)$ that are calculated using the RPA or random-walk approximations.

The analytic expression for $F_0(q)$ can be expressed as a dimensionless function $F_0(x)$ of a quantity $x \equiv (qR_{g0})^2$, where $R_{g0} = \sqrt{Nb^2/6}$ is the radius of gyration of a Gaussian chain with statistical segment length b. This function exhibits a minimum value of $F_0(x^*)$ at x^*, leading to a peak value of $S(q^*)$ in the function $S_0(q)$ at $q_0^* = \sqrt{x^*}/R_{g0}$. For symmetric copolymers, the minimum value is $F_0(x^*) = 20.99$ at $x^* = 3.785$.[5] This implies a peak in $S_0(q)$ at $q_0^* = 1.946/R_{g0}$ with $cNS_0^{-1}(q^*) = H_0(q_0^*) = 2[(\chi_e N)_s - \chi_e^* N]$, where $(\chi_e N)_s = F_0(x^*)/2 = 10.495$ is the predicted spinodal value of $\chi_e N$. SCFT predicts a second-order transition between the disordered and lamellar phases at this critical value.[4]

Experimental measurements of scattering intensity are often analyzed based on Eq. A.[1,22–32] While the agreement is satisfactory for scattering intensity measurements at temperatures much greater than the order-disorder transition (weak segregation region),[23,24,33] discrepancies observed in the vicinity of transition clearly indicate the inadequacies of RPA and the underlying SCFT model for studying phase transitions.[22,25–32] The limitations of SCF (and RPA) theory are largely due to its assumption that polymer melts consist of long, strongly interpenetrating polymer chains that can be well approximated as ideal random walks interacting with an average field representing only the local interactions between chains. This picture, as one might imagine, definitely does not hold true in real experimental systems.

2.1.2 Fredrickson-Helfand (FH) Theory

It was understood from the outset[4] that the second-order transition predicted by Leibler's RPA must actually be first order, on the basis of work by Brazovskiĭ[6] on the effects of strong order-parameter fluctuations on weakly first order crystallization transitions. Fredrickson and Helfand[34] attempted to correct this deficiency of SCFT and RPA by applying Brazovskiĭ's theory of weak-crystallization to symmetric and nearly symmetric diblock copolymers. The Fredrickson-Helfand (FH) theory yields predictions in which all quantities depend on the invariant degree of polymerization $\overline{N}$ in addition to the SCFT state variables. All predictions of the theory are found, moreover, to reduce to SCFT predictions in the limit $\overline{N} \to \infty$. For symmetric diblock copolymers, the FH theory predicts a first-order transition from a homogeneous phase to a weakly ordered lamellar phase at a transition value

$$\chi_e N = 10.5 + 41.0\overline{N}^{-1/3} \quad . \tag{2.10}$$

The theory assumes that the average volume fraction $\phi_A(\mathbf{r})$ of A monomers within the ordered phase near the transition exhibits a sinusoidal composition profile,

$$\phi_A(z) = \frac{1}{2} + A\cos(2\pi z/d) \quad , \tag{2.11}$$

where z is a distance measured normal to the layers and d is the preferred layer

spacing. It predicts an amplitude

$$A = 1.63\overline{N}^{-1/6} \tag{2.12}$$

in the ordered phase at the ODT.

The FH theory is based on a variety of approximations that are known to limit its validity to large values of $\overline{N}$, and to the vicinity of the transition. Its exact range of validity has, however, remained unclear. Fredrickson and Helfand concluded that the theory could be rigorously justified only for astronomically large values of $\overline{N} > 10^{10}$, which are far above those obtainable in any real polymer. They also noted, however, that the theory is free of obvious internal contradictions for values as low as $\overline{N} \sim 10^4$, and conjectured that it could remain accurate down to approximately this value. An even lower bound on the possible range of validity of the theory can be obtained by noting that Eq. 2.12 yields $A > 1/2$, and thus gives values of $\phi_A(\mathbf{r})$ outside the physical bounds $0 < \phi_A(\mathbf{r}) < 1$, for $\overline{N} < 1245$. This implies that the theory cannot possibly remain valid for $\overline{N} < 10^3$. Our simulations results in chapter 6 suggest that the FH theory becomes accurate for $\overline{N} > 10^4$, in agreement with the more optimistic of the two estimates originally offered by Fredrickson and Helfand.

The FH theory suffers from a severe conceptual problem known as ultraviolet (UV) divergence because of which predictions of the theory for many quantities are sensitive to the value of an arbitrary cutoff length. A host of related coarse-grained theories were developed to extend and refine the FH theory.[7,12,14,16,17,34–37] The first generation of these theories were based on approximations similar to those of the original theory, and shared most of its limitations.[35–37]

2.1.3 Renormalized One-Loop (ROL) Theory

Recently, Grzywacz, Qin, and Morse,[14,16,17] developed the renormalized one-loop (ROL) theory of correlations in the disordered phase of diblock copolymers to get rid of the UV divergence problem. They used a procedure known as "renormalization" that is standardly used to eliminate UV divergences in statistical field theories[38] by absorbing the divergent terms into definitions of

phenomenological parameters of theory. As a result, the ROL theory yields predictions for the structure factor $S(q)$ that are based on less restrictive approximations than the FH theory. Unfortunately, the ROL theory does not provide predictions for the free energy or structure of the ordered phase, or for the value of $\chi_e N$ at the ODT.

To analyze deviations from the RPA prediction for $S(q)$, the ROL theory starts with an Ornstein-Zernike (OZ) equation similar to that used in the polymer reference interaction site (PRISM) theory,[39,40]

$$S_{ij}^{-1}(q) = \Omega_{ij}^{-1}(q) - C_{ij}(q), \quad . \tag{2.13}$$

Here, $\Omega_{ij}^{-1}(q)$ is the matrix inverse of the 2×2 matrix of intramolecular correlation functions $\Omega_{ij}(q)$, and $C_{ij}(q)$ is the so called direct correlation function. The direct correlation function C_{ij} can be interpreted, somewhat heuristically, as an effective interaction between monomers of type i and j.

In an incompressible system, or an AB system that is symmetric under relabeling of A and B monomers, the OZ equation for $S_{ij}(q)$ may be reduced to an equation for the inverse scalar correlation function $S^{-1}(q)$. In these cases, $S^{-1}(q) = \sum_{ij} \epsilon_i^- \epsilon_j^- S_{ij}^{-1}(q)$, where $\epsilon^- = (1, -1)$. Applying this to Eq. 2.13, and multiplying by cN, we obtain an expression

$$H(q) \equiv cNS^{-1}(q) = F(q) - 2\chi_a(q)N \quad . \tag{2.14}$$

closely analogous to the RPA, in which

$$\begin{aligned} F(q) &\equiv cN \sum_{ij} \epsilon_i^- \epsilon_j^- \Omega_{ij}^{-1}(q) \\ &= cN \frac{\Omega_{11}(q) + \Omega_{12}(q) + \Omega_{21}(q) + \Omega_{22}(q)}{\Omega_{11}(q)\Omega_{22}(q) - \Omega_{12}^2(q)} \end{aligned} \tag{2.15}$$

and

$$\chi_a(q) \equiv \frac{c}{2} \sum_{ij} \epsilon_i^- \epsilon_j^- C_{ij}(q) \quad , \tag{2.16}$$

We will refer to Eq. 2.14 as the incompressible Ornstein-Zernike (OZ) equation.

The function $F(q)$ defined in Eq. 2.15 is a generalization of the function that was calculated for Gaussian diblock copolymers by Leibler,[4] generalized to allow for non-Gaussian single-chain statistics. The function $\chi_a(q)$, which we refer to as an "apparent" interaction parameter, is generalization of the RPA interaction parameter χ_e. The RPA can be recovered from Eq. 2.14 by assuming random-walk statistics, which yields an explicit expression for $F(q)$ as a function of q and N, and assuming that $\chi_a(q)$ is independent of q and N.

The ROL theory predicts corrections to both the random walk model of single-chain statistics and to the RPA prediction for $S(q)$. Predictions for $S(q)$ are most conveniently expressed as expressions for the invariant quantities $H(q) \equiv cNS^{-1}(q)$, $F(q)$ and

$$X(q) \equiv \chi_a(q)N \quad , \tag{2.17}$$

with $H(q) = F(q) - 2X(q)$. ROL predictions are of the form

$$\begin{aligned} F(q) &= F_0(q) + \overline{N}^{-1/2} F_1(qR_{g0}, \chi_e N) \\ X(q) &= \chi_e N + \overline{N}^{-1/2} X_1(qR_{g0}, \chi_e N) \\ H(q) &= H_0(q) + \overline{N}^{-1/2} H_1(qR_{g0}, \chi_e N) \quad . \end{aligned} \tag{2.18}$$

Here, F_1, X_1 and H_1 are dimensionless functions of qR_{g0} and $\chi_a^* N$ that are defined by Fourier integrals, which must be evaluated by numerical integration, which satisfy $H_1 = F_1 - 2X_1$. Because the ROL theory predicts corrections to the RPA that decrease as $\overline{N}^{-1/2}$, the RPA is recovered in the limit $\overline{N} \to \infty$.

ROL predictions for $F(q)$ are obtained from corresponding predictions for $\Omega_{ij}(q)/cN$. ROL predictions for the radii of gyration of polymers and individual blocks, which are discussed in sec. 3.2.1, have been inferred from the low q behavior of the elements of $\Omega_{ij}(q)/cN$.

The notation used in Eq. 2.18 is intentionally incomplete, because it indicates that the one-loop corrections depend on an invariant interaction parameter "$\chi_e N$", but does not specify which of several possible definitions of χ should be used for this purpose. This ambiguity reflects the fact that there are actually two versions of the theory, which we will refer to as the "perturbative" and "self-consistent" variants, that are distinguished by different choices for this pa-

rameter. In the "perturbative" version of the theory, which was discussed in the original derivation,[14] the input parameter to the Fourier integrals that define the one-loop corrections was taken to be the RPA interaction parameter χ_e, which is rigorously independent of N. In the "self-consistent" version of the theory, which was introduced in subsequent work on blends[41] and diblock copolymers,[42] this parameter was taken to be the "apparent" interaction χ_a^*, which is related to the maximum peak intensity by

$$cNS^{-1}(q^*) \equiv 2[(\chi_e N)_s - \chi_a^* N], \tag{2.19}$$

in which $(\chi_e N)_s = 10.495$ is the RPA prediction for the spinodal value of $\chi_e N$. Therefore, χ_a^* is defined to be the value of the RPA interaction parameter χ_e that would be inferred by fitting the actual peak intensity to the RPA prediction. In the self-consistent ROL theory, $H(q)$ is thus given by an equation of the form

$$H(q) = H_0(q) + \overline{N}^{-1/2} H_1(qR_{g0}, \chi_a^* N) \quad , \tag{2.20}$$

in which χ_a^* is related to the maximum value $H(q^*) = \max_q[H(q)]$ by Eq. 2.19, yielding an implicit equation for $H(q^*)$.

The self-consistent version of the ROL theory is designed to mimic the behavior of the Brazovskiĭ-Leibler-Fredrickson-Helfand (BLFH) theory near ODT. The use of a self-consistently determined value of $\chi_a^* N$ is neither required nor prohibited by the logic of the original ROL theory.[14] It is a physically motivated modification that was introduced, in the application to block copolymers,[42] in an attempt to combine the virtues of the ROL theory, which provides a systematic expansion that is expected to be accurate where corrections to the RPA are small, with those of Brazovskiĭ-Leibler-Fredrickson-Helfand (BLFH) theory, which was designed to capture the dominant behavior near the ODT, where corrections to the RPA become very large.

2.1.4 Correlations in Real Space

For some purposes, it is useful to have an approximate expression for the real-space correlation function $S(\mathbf{r}) = \langle \psi(\mathbf{r})\psi(\mathbf{0}) \rangle$, as well as for its Fourier trans-

form $S(\mathbf{q})$. Near the ODT, the function $S(\mathbf{r})$ exhibits exponentially decaying oscillations with an oscillation period $d^* \equiv 2\pi/q^*$.[43] In this limit, we may approximate the RPA prediction for $S(r)$ (where $r \equiv |\mathbf{r}|$) by expanding the RPA prediction for $H(q) = cNS^{-1}(q)$ to harmonic order in $q - q^*$, giving $H(q) \simeq H(q^*)[1 + (q - q^*)^2\xi^2]$. By using this approximation for $H(q)$ to evaluate the inverse Fourier transform of $S(q)$, and retaining only the dominant contribution for $\xi \gg d^*$, we obtain

$$S(r) \simeq \frac{Ac^2}{(\overline{N}\tau)^{1/2}} \frac{\sin(q^* r)}{q^* r} e^{-r/\xi} \quad , \tag{2.21}$$

in which the ratio of the decay length ξ to the layer spacing $d^* = 2\pi/q^*$ is given for symmetric copolymers by

$$\frac{\xi}{d^*} = \left(\frac{2F"(x^*)(x^*)^2}{(2\pi)^2 H(q^*)} \right)^{1/2} = \left(\frac{0.70}{H(q^*)} \right)^{1/2} \quad , \tag{2.22}$$

where $F"(x^*) = d^2F(x)/dx^2|_{x_*} = 0.9624$[5] and $A = [27x^*/(\pi^2 F"(x^*)]^{1/2} = 3.28$.

A similar analysis can be applied to the true correlation function, simply by using the actual minimum value of $H(q)$ and the second derivative of this function with respect to q rather than RPA predictions for these quantities in the Taylor expansion of $H(q)$. Corrections to the RPA are known to have a large effect on the minimum value of $H(q)$ near the ODT, but smaller effects on the curvature of this function and on the value of q^*. (The Fredrickson-Helfand theory predicted no change in either of these two quantities). We thus expect Eqs. 2.21 and 2.22 to provide useful approximations for ξ and $S(r)$ even near the ODT, as long as we define $H(q^*)$ using the measured peak intensity, rather than the RPA prediction for this quantity. When used in this way, Eq.2.22 provides a useful starting point for understanding finite size effects in simulations.

2.1.5 Corresponding States Hypothesis

Authors of the ROL theory have argued elsewhere[44] that the above one-loop correction to $S(q)$ is simply the first term in a renormalized loop expansion of corrections to RPA and SCF predictions and that if analyzed further would yield a Taylor expansion of $H\left(qR_{g0}, \chi_e N, \overline{N}\right)$ in powers of $\overline{N}^{-1/2}$, in which

the ROL theory for $S(q)$ retains only the first two terms. They believe that this generalized scaling relation has a wider range of validity than the one-loop approximation. Moreover, all post-SCF coarse-grained theories of corrections to the SCFT/RPA phenomenology, including the FH and ROL theories, yield predictions for properties of diblock copolymer melts as functions of the invariant degree of polymerization $\overline{N}$ and of the SCFT state parameters. These elements thus collectively seem to suggest an underlying universality (model- and chemistry-independence) in the coarse-grained behavior of disordered and ordered phases, in which all properties over length scales similar to R_g can be expressed as functions of $\overline{N}$ and of the dimensionless parameters of SCFT.[41,45]

The main objective of the current work is to verify (and obtain) this universality or corresponding states hypothesis for symmetric diblock copolymers. In the specific case of symmetric diblock copoylmers, the universality hypothesis implies that the dimensionless equilibrium free energy per chain g in each phase is given by a universal function of $\chi_e N$ and $\overline{N}$ alone,

$$g = g(\chi_e N, \overline{N}) \quad . \tag{2.23}$$

If so, the value of $\chi_e N$ at the ODT (where the free energies of the two phases are equal) should depend on $\overline{N}$ alone. It has long been believed that the SCF and RPA theories become exact in the limit of infinitely long, strongly interpenetrating polymers.[34,46] Consequently, we expect scaling relationships of various properties to reduce to SCFT predictions in the limit $\overline{N} \to \infty$.

Simulations provides a great strategy for testing the universality hypothesis because it is relatively inexpensive to vary $\chi_e N$ and $\overline{N}$ *independently* over wide ranges in simulations. Accordingly, in this work, we compare results from simulations of diverse models to verify if corresponding thermodynamic states of different simulation models yield equivalent results for various properties in the two phases and for the order-disorder transition $(\chi_e N)_{\mathrm{ODT}}$. As mentioned above, corresponding states of symmetric diblock copolymers are states with equal values of the two parameters $\chi_e N$ and $\overline{N}$. Our main strategy, therefore, is to examine if results from systems of different simulation models at matched values of $\overline{N}$ collapse when plotted *vs.* $\chi_e N$, as they must do so if the hypothesis were true.

2.2 Estimating the Interaction Parameter χ_e

There have been many simulations studies on diblock copolymer behavior over the last 25 years.[44,47–78] Very few of these studies have, however, been analyzed in a way that allows quantitative comparison of the results of different coarse-grained simulation models to each other, or to theoretical predictions. The most important reason being the lack of an adequate method for estimating the Flory-Huggins interaction parameter χ_e in terms of the microscopic interaction parameters of a simulation model.

The simulations presented here, like most previous coarse-grained simulations, use structurally symmetric models in which the A and B blocks are identical, but in which the non-bonded pair interaction between A and B monomers is slightly more repulsive than the interaction between similar (AA or BB) pairs. Specifically, we study several models in which the non-bonded interaction between i and j monomers is a function of the form

$$V_{ij}(r) = \epsilon_{ij} u(r), \tag{2.24}$$

in which ϵ_{ij} is an energy prefactor, with $\epsilon_{AA} = \epsilon_{BB}$, and $u(r)$ is a dimensionless function that vanishes beyond some cutoff distance r_c. See section 3.1 for the different functional forms for $u(r)$ used in the different simulation models in this work. The degree of repulsion between A and B monomers is controlled by varying the control parameter

$$\alpha \equiv \epsilon_{AB} - \epsilon_{AA}, \tag{2.25}$$

while keeping ϵ_{AA}, T and other parameters constant. In such simulations, the effective interaction parameter is expected be a model-dependent function $\chi_e(\alpha)$ of α.

Previous comparisons of simulations results to theoretical predictions have generally assumed that χ_e is a linear function of α, of the form

$$\chi_e(\alpha) = z\alpha/k_B T \tag{2.26}$$

where z is a model-dependent dimensionless prefactor. Methods of estimating

the coefficient z have generally relied[79] on either (1) some form of random-mixing approximation, thus ignoring monomer scale correlations, or (2) a perturbation theory that allows a value for z to be obtained by analyzing intermolecular pair correlations in a reference homopolymer liquid.[79–81]

The original Flory-Huggins mean-field lattice model combines the random-mixing approximation and the mean-field assumption that interaction free energy density is a local functional of composition, independent of chain length and architecture, for obtaining the free energy of mixing in polymer mixtures. Accordingly, the Flory-Huggins theory uses the lattice coordination number for z in Eq.2.26, thus ignoring all composition correlations for neighboring lattice sites. Below, we briefly discuss the second method based on a perturbation theory.

A more accurate linear approximation for χ_e can be obtained from statistical-mechanical perturbation theory, by considering an expansion of the free energy[81] or the exchange chemical potential[79,80] of a binary mixture of chains of equal length N to first order in powers of α, using a homopolymer ($\alpha = 0$) liquid as a reference state. When applied to a lattice model, this yields a linear approximation for χ in which z is simply given by the average number of neighboring lattice sites occupied by intermolecular neighbors (i.e., by monomers belonging to other chains) in a simulation of a reference homopolymer liquid. When applied to off-lattice bead spring models like those studied here, this line of reasoning yields an effective coordination number

$$z(N) = c \int d^3\mathbf{r}\; u(\mathbf{r}) g_{\text{inter}}(\mathbf{r}), \tag{2.27}$$

in which c is the monomer concentration and $g_{\text{inter}}(\mathbf{r})$ is the intermolecular radial distribution function in a reference homopolymer ($\alpha = 0$) liquid containing chains of length N.

Several authors have previously interpreted results of simulations of both block copolymers and polymer blends using a linear approximation for χ_e in which the coefficient z in Eq.2.26 is approximated by a value of $z(N)$ defined as in Eq.2.27, and in which the value of $z(N)$ is extracted from simulations of chains of length equal or similar to that of the chains of interest. One ambiguity

that arises immediately in this scheme is the fact that the value of $z(N)$ obtained from simulations of homopolymer melts depends somewhat upon chain length N,[80,81] while χ_e is (by definition) independent of N. Morse and Chung[81] developed an analytic theory for the N-dependence of $z(N)$, which was found to vary as $z(N) \simeq z_\infty[1 + D\overline{N}^{-1/2}]$ with $D = (6/\pi)^{3/2} = 2.64$. These authors also showed that an exact expression for the coefficient of the first term in a Taylor expansion of $\chi_e(\alpha)$ is obtained by simply replacing z in Eq.2.26 by the limiting value z_∞. The required value can be obtained by extrapolation of values of $z(N)$ obtained from simulations of finite chains. We hereafter refer to the resulting approximation for $\chi_e(\alpha)$, with $z = z_\infty$, as the perturbative linear approximation, and denote it by $\chi_e^{(1)}(\alpha)$. The difference between $z(N)$ and $z(\infty)$ is approximately 30 % for $\overline{N} \simeq 10^2$, 8% for $\overline{N} \simeq 10^3$ and 3 % for $\overline{N} \simeq 10^4$, and thus cannot be ignored in precise comparisons of simulations with modest values of $\overline{N}$.

2.3 Simulations

Over the past 30 years, several simulations studies[47–76] have been conducted on the behavior diblock copolymers. See appendix F in Ref.[41] for a comprehensive review of all relevant simulations studies. These studies mainly focused on measurements of the disordered phase structure factor, deviations from Gaussian statistics, individual block dimensions, and fluctuations induced shift in the ODT location. Results from these works agree qualitatively with those from corresponding experimental studies.

Studies on ODT obtained estimates of ODT based on observations of spontaneous melting transitions, emergence of the Bragg peak in structure factor, and measurements of discontinuity in properties such as specific heat capacity and AB pair energy.[48–50,53,54,59–62,69,82] Most of these studies used the naive estimate $\chi_e = z\alpha/k_{\mathrm{B}}T$ for interaction parameter χ_e, where z is the lattice coordination number for lattice models and the average number of non-bonded interacting neighbors for off-lattice models. Some studies used a reduced coordination number $z - 2$ to account for bonded neighbors. Matsen's group simulated diblock copolymers of different chain lengths and compositions on a FCC lattice model

to map out a fluctuations influenced phase diagram.[69] They obtained an ODT estimate of $(\chi_e N)_{\mathrm{ODT}} = 40 \pm 1$ for a symmetric copolymer with $N = 39$ and $\overline{N} = 138$[41] based on the lattice coordination number definition for χ_e. A later work[75] by the same authors, however, reported a significantly lower estimate of $\chi N_{\mathrm{ODT}} \simeq 18$ for the same system, which was a direct consequence of switching to the perturbative linear approximation for χ_e (see section 2.2). This work thus illustrates the overwhelming importance of using an accurate definition for χ_e, particularly when trying to quantitatively estimate the $\overline{N}$-dependence of fluctuation effects on phase boundaries. Another important lesson from previous simulations studies on ODT is to exercise caution against hysteresis and finite-size effects in obtaining ODT locations.

2.3.1 Recent Simulations

Recently conducted simulations studies[41,44] in our group tested the accuracy of the ROL theory of correlations, the adequacy of the perturbative linear approximation for χ_e, and the validity of the scaling hypothesis for structure factor $S(q)$ in terms of dimensionless parameters qR_{g0}, $\chi_e N$, and $\overline{N}$. To do this, results were obtained for structure factor $S(q)$ in the disordered phase from three substantially different coarse-grained simulation models. The three models simulated were: (1) a lattice Monte Carlo model, the bond-fluctuation model (model "L"),[80,83] (2) a beadspring model with harsh repulsive interactions (model "H"), similar to that of Kremer and Grest,[57,64] and (3) a beadspring model with very soft repulsion between beads, and strongly overlapping beads (model "S").[63,84]

The first of these studies[41] tested the accuracy of ROL theory predictions using simulations of different chain lengths ($N = 16, 32, 64$, and 128) of model H. For each chain length, two cases were examined: (1) $\alpha = 0$ (ideal diblock copolymer melts) and (2) Non-zero values of α spanning the entire disordered phase ($0 < \alpha < \alpha_{\mathrm{ODT}}$). In the first case, simulations results for the q dependence of the structure factor $S(q)$ were compared to ROL theory predictions, which were found to agree perfectly for all four chain lengths. In the second case, the author obtained dependence of peak intensities $S(q^*)$ and peak positions q^* as functions of α for all values of α in the disordered phase. The perturbative linear approximation $\chi_e(\alpha) \simeq z_\infty \alpha / k_{\mathrm{B}}T$ was then used to relate α and χ_e in

order to compare simulations results to ROL theoretical predictions that are given as functions of $\chi_e N$. The comparison of $S(q^*)$ *vs.* $\chi_e N$ concluded that although the agreement between simulations and the ROL theory is reasonably good for all values of $\chi_e N$ for the two longer chain lengths (N =64, 128), the agreement becomes increasingly worse in the large $\chi_e N$ regime for the shorter chain lengths (N =16, 32). It was unclear, however, if this discrepancy was due to the inadequacy of the first order perturbation approximation for $\chi_e(\alpha)$ or the failure of ROL theory predictions for lower $\overline{N} \propto N$ values, particularly in the vicinity of the transition. This ambivalence was resolved by the author by plotting results of q^* as a function of the apparent interaction parameter $\chi_a^* N$ rather than the effective interaction parameter for a comparison of simulations results to ROL theoretical predictions without having to deal with the problem of $\chi_e(\alpha)$ definition. Note that the apparent interaction parameter, as defined in Eq.chiaStarDef, is related to the measured peak intensity $cNS^{-1}(q^*)$. Plots of q^* comparison proved the accuracy of ROL theory predictions for the entire disordered phase range of α and for all values of chain length (or equivalently, $\overline{N}$), thereby exposing the inadequacy of the first order perturbation approximation for $\chi_e(\alpha)$.

In the subsequent study,[44] the authors focused exclusively on testing the scaling hypothesis for structure factor. For this purpose, they devised two tests, both of which did not require knowledge of $\chi_e(\alpha)$. The first test, similar to the one just described, involved a comparison of the relationship between the two observable quantities, q^* and $\chi_a^* N$. The second involved a test of whether the data for normalized peak intensity $cNS^{-1}(q^*)$ from different models could be collapsed by searching for an N-independent mapping between corresponding values of the AB repulsion parameter in different models. they obtained results for structure factor from the three models (models L, H, and S) and compared results of pairs of systems of different models, but with the same value of $\overline{N}$. Results from both tests were consistent with a universal scaling relationship for $S(q)$, even for rather short chains, confirming that it is indeed possible to give an accurate universal description of simulation models that differ in many details. Notably, the level of agreement between different models, at matched values of $\overline{N}$, for the relationship between q^* and $\chi_a^* N$ was substantially better than the

already rather good agreement obtained between the results of model H and the ROL theory in the earlier study discussed above. This suggests that the universal scaling hypothesis, which is the main focus of this thesis and formally postulated in section above, must indeed have a wider range of validity than the ROL or any other existing theory.

2.4 Experiments

Experiments on nearly symmetric copolymers have included systems with values of $\overline{N}$ spanning a range of approximately $\overline{N}$ =200 - 20,000. We cite only a few particularly important or well-known examples: The most symmetric copolymer in a heavily cited study of the phase diagram of poly(styrene-*b*-isoprene) copolymers had $\overline{N} \simeq 1100$.[85,86] A recent study of poly(isoprene-*b*-L lactic acid)[87] used polymers with $\overline{N} \simeq 230$. The study of poly(ethylene-propylene-*b*-ethylene) (PEP-PE) copolymers that was used to test the FH theory[25–27,41] used a system with $\overline{N} \simeq 5000$ for scattering experiments.

Most experiments on block copolymer melts are interpreted within the context of either the SCF theory of phase transitions and the random phase approximation (RPA) theory of scattering in the disordered phase, or (less frequently) the FH theory. Typically, experiments are analyzed by assuming a simple form for the temperature dependence of χ_e, usually $\chi_e(T) = A/T + B$, and adjusting the parameters A and B to fit a limited set of data to theoretical predictions. When applied to scattering data from a single system, this procedure presumes the accuracy of whichever theory is used to fit the data, and so does not provide a test of that theory's accuracy.

To test a theory in which $\chi_e(T)$ appears as a parameter, one must generally use data from one set of measurements to estimate $\chi_e(T)$ and then use this estimate to predict the outcome of a different set of measurements. Among possible strategies for doing this are: (1) using scattering results from one sample over a range of temperatures to calibrate $\chi_e(T)$ and using this to test a theoretical prediction for the order-disorder transition temperature, (2) comparing results for scattering and order-disorder transitions from block copolymers of the same chemistry (i.e., the same monomer pair) but varied chain lengths within the

same temperature range, or (3) comparing experiments on chains of the same chemistry but different architecture, such as diblock copolymers and blends. In light of the size of the literature, surprisingly few experiments have been designed to precisely test theoretical predictions about block copolymers using any of these strategies.

The most important evidence for the approximate validity of FH theory for experimentally relevant values of $\overline{N}$ is still the seminal study of symmetric poly(ethylene-propylene-*b*-ethyl-ethylene) (PEP-PEE) diblock copolymers by Bates and coworkers.[25,26] In this work, the authors estimated $\chi_e(T)$ by fitting ODT temperatures of several nearly symmetric PEP-PEE copolymers of different molecular weights to FH predictions for ODTs. They then used the resulting function $\chi_e(T)$ as an input to the FH theory to predict the peak intensity $S(q^*)$ in the disordered phase for a single system ($\overline{N} \simeq 5000$), thereby obtaining rather good agreement with results of small angle neutron scattering (SANS) measurements on that system near its ODT. Subsequent work has not provided equally rigorous tests of the theory with other systems with significantly different values of $\overline{N}$. We are not aware of any study that has demonstrated the ability of the FH theory or any competing theory to predict scattering behavior of diblock copolymers of different lengths, nor of any attempt to compile results from different systems with significantly different values of $\overline{N}$ in order to test the prediction of a systematic dependence of various properties on $\overline{N}$.

A more extensive body of experimental evidence, primarily by Balsara and coworkers,[88–93] has demonstrated the ability of the RPA to describe homopolymer blends and some mixtures of homopolymers and copolymers. In these experiments, an estimate of $\chi_e(T)$ that was obtained by fitting results from binary homopolymer blends was used as an input to the RPA to predict results of scattering experiments involving mixtures containing homopolymers of varying lengths or mixtures of homopolymers and copolymers. Agreement between RPA and experiment was obtained for a variety of mixtures that undergo macroscopic phase separation, for which $S(q)$ is maximum at $q = 0$, including mixtures containing copolymer as a minority component. The success of these comparisons suggested that corrections to the RPA and Flory-Huggins theories are comparatively small for systems that undergo macroscopic phase separation. This, in

turn, suggested that measurements on blends might provide useful estimates for $\chi_e(T)$ as a starting point for analyzing experiments on diblock copolymers.

Results of studies that have compared measurements on diblock copolymers and polymer blends are more perplexing. Anecdotal comparisons of systems for which literature data is available for both blends and diblock copolymers suggest that, when $\chi_e(T)$ is estimated by fitting results of experiments on blends, the resulting estimate $(\chi_e N)_{\rm ODT}$ for the value of $\chi_e N$ at the ODT of corresponding diblock copolymers usually significantly exceeds the value of $(\chi_e N)_{\rm ODT} = 10.5$ predicted by SCFT, by factors of up to 2. Examples include experimentally observed ODT values of poly(isoprene-styrene (PI-PS)[86] and poly(ethylene-oxide-*b*-isoprene) (PEO-PI)[94] diblock copolymers. In a comparison of SANS results from diblock copolymers and binary blends of polyethylene (PE) and polypropylene (PP) by Jeon, Balsara and coworkers,[93] the authors concluded that reasonably accurate predictions for the peak intensity $S(q^*)$ in diblock copolymers could be obtained by fitting blend data to the RPA theory to estimate $\chi_e(T)$ and using this as an input to the Fredrickson-Helfand theory. This conclusion is not, however, consistent with the conclusions of a particularly extensive comparison of results of symmetric diblock copolymers and blends of polyethylene (PE) and polyethylenepropylene (PEP) by Maurer, Bates, Lodge and coworkers.[1] These authors instead concluded that no combination of the available theories gave a consistent account of scattering and phase boundary results from homopolymer blends and diblock copolymers of this chemistry. Because this qualitative disagreement between the results of Maurer *et al.*[1] and most other experiments remains unexplained, comparisons of measurements on diblock copolymers and blends have thus far not helped clarify our understanding of diblock copolymers.

Despite the size of the experimental literature on diblock copolymer melts, quantitative understanding of the accuracy of theoretical predictions for structure factor $S(q)$ and the order-disorder transition has thus remained surprisingly limited and contradictory.

Chapter 3

Simulation Models

In this chapter, we discuss the different simulations models that we used for verifying and obtaining the corresponding states behavior of symmetric diblock copolymer melts. All simulations reported in this work were conducted using one of four coarse-grained bead-spring models, which we refer to as models H, S1, S2, and S3. This chapter focuses on the design and calibration of these four models. As discussed in section 2.3.1, the main reason for our use of different simulation models is so that we can compare results from pairs of systems of different simulation models with matched values of $\overline{N}$. In order to examine the validity of corresponding states behavior in terms of $\overline{N}$ range, the four simulation models have been designed to have distinctly different values for the ratio $\overline{N}/N \equiv (cb^3)^2$, thus allowing us to span a wide range of $\overline{N}$ values using a much narrower range for chain length N values. This is extremely useful because it helps us avoid simulations of long chain length systems that are computationally expensive, and particularly so, in the vicinity of the order-disorder transition.

This chapter is organized as follows: Section 3.1 introduces the simulation models (H, S1, S2, and S3). Section 3.2 discusses the calibration of model parameters. Section 3.3 presents our simulation methods.

3.1 Models

The simulations presented here, like most previous simulations, use coarse-grained simulation models that do not use an all-atom description of polymer

chains and aim to capture only the essential, universal aspects of macroscopic behavior of polymer melts using a few phenomenological parameters for representing the important microscopic interactions. All coarse-grained simulations in this work were conducted using one of the four continuum bead-spring models, models H, S1, S2, and S3. All four models are structurally symmetric models in which the A and B blocks are identical, but in which the interaction between a non-bonded pair of A and B monomers is slightly more repulsive than that between similar or like (AA or BB) pairs. As mentioned in section 2.2, the non-bonded pair interaction between i and j monomers in our models is of the form $V_{ij}(r) = \epsilon_{ij} u(r)$, where ϵ_{ij} is an energy pre-factor, with $\epsilon_{AA} = \epsilon_{BB}$, and $u(r)$ is a dimensionless function that vanishes beyond some cutoff distance r_c. Different models implement different functional forms for $u(r)$, as discussed below. The strength of repulsion between A and B monomers is controlled by varying the control parameter

$$\alpha \equiv \epsilon_{AB} - \epsilon_{AA}, \tag{3.1}$$

while keeping ϵ_{AA}, T and other parameters constant. Therefore, the effective Flory-Huggins interaction parameter is expected be a model-dependent function $\chi_e(\alpha)$ of the excess AB repulsion strength α. All four models have a harmonic bond potential, of the form

$$V_{\mathrm{bond}}(r) = \kappa(r - l_0)^2/2 \tag{3.2}$$

The behavior of each model is studied as a function of chain length N and of the AB repulsion strength $\alpha \equiv \epsilon_{AB} - \epsilon_{AA}$, at fixed values of temperature T, pressure P, ϵ_{AA} and all other potential energy parameters. What we call a "model" is thus defined by a choice of a functional form for $u(r)$ of the non-bonded pair potential, and of values for all parameters except N and α. Values for all simulation model parameters are given in Table 3.1. All quantities are expressed in terms of base units, which we have fixed as the units of mass (m), length (σ), and energy ($k_{\mathrm{B}}T$). For the sake of convenience, the magnitude of all three basic units is taken as unity throughout this work.

Model H (H denotes "hard") is very similar to the heavily studied model of Kremer, Grest and coworkers.[57,64] It uses a harshly repulsive Weeks-Chandler-

Model	ϵ_{AA}	r_c	κ	l_0	c
H	1.0	$2^{1/6}$	400.0	1.0	0.7
S1	25.0	1.0	3.406	0.0	3.0
S2	25.0	1.0	1.135	0.0	1.5
S3	25.0	1.0	0.867	0.0	1.5

Table 3.1: Model parameters expressed in units of $k_BT = 1$ and $\sigma = 1$. Here, c denotes the extrapolated monomer concentration for infinite homopolymers at the specified pressure.

Anderson (WCA) non-bonded pair potential, for which

$$u(r) = 4\left[(\sigma/r)^{-12} - (\sigma/r)^{-6}\right] + 1 \quad \text{(H)}, \tag{3.3}$$

for $r < r_c$, with $r_c = 2^{1/6}\sigma$. Other potential parameters of model H are rest length $l_0 = 1.0\sigma$ for bonded pair potential and prefactor $\epsilon_{AA} = \epsilon_{BB} = 1.0k_{\mathrm{B}}T$ for non-bonded interactions between like monomer pairs.

Models S1, S2, and S3 are "soft" models similar to those originally introduced for use in dissipative particle dynamics (DPD) simulations.[63,84] They use a pair potential of the form

$$u(r) = \frac{1}{2}\left(1 - \frac{r}{\sigma}\right)^2 \quad \text{(S1, S2, S3)} \tag{3.4}$$

with a cutoff $r_c = 1.0\sigma$. With the use of this relatively soft potential, we are able to simulate systems with higher monomer concentrations than is possible with the harsh WCA potential of model H systems. Increase of the monomer concentration c is known to be a better strategy for accessing experimentally relevant, i.e., relatively high values of $\overline{N}$ than simulating systems of very long chain lengths as the latter requires a significantly large number of CPU hours for equilibration.[95] For all three soft models, rest length for bonded pair potential is $l_0 = 0$ and prefactor for non-bonded pair potential is $\epsilon_{AA} = 25k_{\mathrm{B}}T$. The primary differences between models S1, S2 and S3 are differences in values of the spring constant κ and pressure P (or corresponding monomer concentration), which have been adjusted to give a specific sequence of values for the dimensionless parameter cb^3, as described below.

The monomer concentrations of models H and S1 are fixed at $c = 0.7\sigma^{-3}$

and $c = 3.0\sigma^{-3}$, respectively. The monomer concentrations of models S2 and S3 are taken to be half that of model S1, *i. e.,* $c = 1.5\sigma^{-3}$. In other words, a model S1 system has twice as many chain segments per unit volume than a model S2 (or S3) system. This design choice allows us to compare results of simulation models (S1, S2 and S3) that have precisely the same potential functions but are coarse-grained to vastly different degrees. Since the spring constant κ value controls the statistical segment length b of a model, κ values of models H, S1, S2, and S3 were chosen such that they result in statistical segment lengths, and consequently, values of $\overline{N}/N = (cb^3)^2$ with ratios of nearly 1:4:16:32 for models H, S1, S2, and S3, respectively. Because all simulations in this work were conducted for chain lengths N = 16, 32, 64, and 128 that differ by multiples of 2, these ratios imply that some pairs of simulations of different models have nearly equal values of $\overline{N}$. Specifically, simulations of H-64 (model H with N=64) and S1-16 (model S1 with N=16) both have $\overline{N} \simeq 240$, while S1-64 and S2-16 both have $\overline{N} \simeq 960$, S1-128, S2-32, and S3-16 all have $\overline{N} \simeq 1920$, and S2-64 and S3-32 both have $\overline{N} \simeq 3840$. In addition, use of several models with widely varying values of $\overline{N}/N$ allows us to explore a wide range of $\overline{N} \simeq 100 - 7600$ values that more or less overlaps with the $\overline{N}$ range explored in experiments, using a very narrow range of low and moderate chain lengths. For examples of experimental $\overline{N}$ values: $\overline{N} \simeq 1100$ in a classic study of poly(styrene-*b*-isoprene),[85,86] $\overline{N} \simeq 220$ in a recent study of poly(isoprene-*b*-L lactic acid),[87] and $\overline{N} \simeq 5000$ in the study of poly(ethylene-propylene-*b*-ethylethylene) used to test the BLFH theory.[25–27,41]

3.2 Calibration

Here, we present the analysis used to estimate model parameters b, P, and $\chi_e(\alpha)$ required for designing simulations systems and subsequently, for comparing results of different models. Values of parameters b and P are determined by extrapolating results from simulations of homopolymer melts ($\alpha = 0$) of finite chain lengths to a hypothetical system of infinitely long chains. We present two methods for defining $\chi_e(\alpha)$: The first one is the linear approximation for $\chi_e(\alpha)$ based on the perturbation theory[81] discussed in section 2.2 and the sec-

ond is a nonlinear function for $\chi_e(\alpha)$ extracted by fitting peak structure factor data to ROL theory predictions. Resulting estimates of parameters b, P, and perturbation coefficient z_∞ are given in Table 3.2.

3.2.1 Statistical Segment Length

Values of the statistical segment length b for each model were obtained by evaluating the radius of gyration $R_g(N)$ for homopolymers of several chain lengths and extrapolating to obtain the limit $b^2 = \lim_{N\to\infty} 6R_g^2(N)/N$. The ROL theory[15,78] predicts corrections to the random walk statistics and states that $R_g^2(N)$ should vary with N in a homopolymer melt as

$$R_g(N)^2 = \frac{Nb^2}{6}\left[1 - \frac{1.42}{\overline{N}^{1/2}} + \frac{\gamma}{N} + \cdots\right] \quad . \tag{3.5}$$

The dominant $\mathcal{O}(\overline{N}^{-1/2})$ correction is a universal correction that arises from the incompressibility of the liquid, as first discussed by Wittmer, Semenov, Beckrich and coworkers.[10–12] The predicted prefactor of 1.42 for monodisperse chains was calculated by Qin and Morse.[41] The subdominant $\mathcal{O}(1/N)$ contribution is non-universal, however, because it includes corrections that arise from the discrete structure of the chain, and thus has a coefficient γ that must be treated as a model-dependent fitting parameter.

Because Eq. 3.5 defines b for continuum models as a property of a hypothetical system of infinite homopolymers with a specified concentration c and a corresponding pressure P, it can be evaluated by extrapolating results of either NVT or NPT simulations. Values of b for models H, S1, S2, and S3 were obtained by measuring radius of gyration $R_g(N)$ from NVT homopolymer simulations with the target monomer concentrations $c = MN/V$ for several values of N. The target monomer concentration, as mentioned earlier, is $c = 0.7, 3.0, 1.5, 1.5\sigma^{-3}$ for models H, S1, S2, and S3 respectively. Data for $R_g(N)$ of each model was subsequently fit to Eq. 3.5 by treating b and γ as fitting parameters. For model H, we used the same spring constant value, $\kappa = 400k_BT$ as was used in our group's previous simulations studies.[15] This value yields statistical segment length $b = 1.404\sigma$ of model H. Subsequently, we chose κ values of models S1, S2, and S3 such that the resulting estimates of statistical segment length b from

fit to Eq. 3.5 satisfy our design requirement of $\overline{N}/N = (cb^3)^2$ values with ratios of 1:4:16:32 for models H, S1, S2, and S3, respectively. In order to determine the specific, desired values of κ, we ran a series of simulations at several different trial κ values and obtained statistical segment length b as a function of spring constant κ at both the target monomer concentrations ($c(\sigma^{-3})$ =3.0 and 1.5). For example, see Fig. 3.1 for plots of variation of statistical segment length b with spring constant κ used to determine κ values of models S2 and S3. Figs. 3.2 and 3.3 shows fits to Eq. 3.5 for all four models after κ values have been fixed. Estimates of b obtained from these fits are given in Table 3.2.

3.2.2 Pressure

Most simulations in this work were carried out in a constant pressure, constant temperature (NPT) ensemble, using a fixed pressure for each model. The pressure P of each model was chosen so as to give a monomer concentration value $c = MN/V$ equal to the target value in the limit $\alpha = 0$, $N \to \infty$ of infinitely long homopolymers. Similar to our method for estimating the statistical segment length b, pressure P for each model was obtained by extrapolating $P(N)$ data measured from homopolymer ($\alpha = 0$) NVT simulations of several chain lengths at the target monomer concentration c to the hypothetical limit $N \to \infty$. The extrapolation was easy because results for pressure $P\,(N)$ show a nearly perfect linear dependence on $1/N$, giving $P\,(N) = P_\infty + \delta/N$. Fig. 3.4 shows the resulting linear fits for all four models. The extrapolated value $P = P_\infty$ is used for all NPT simulations of the model.

3.2.3 Effective Coordination Number

As discussed in section 2.2, the Flory-Huggins interaction parameter χ_e for structurally symmetric models is given to first order in α by $\chi_e(\alpha) \simeq z_\infty \alpha / k_B T$, where the coefficient z_∞ is an "effective coordination number" that can be extracted from homopolymer simulations. This coefficient is given by the $N \to \infty$ limit of a quantity $z(N) = \langle U_{inter} \rangle / (MN\epsilon)$, where U_{inter} is the intermolecular pair interaction energy in a homopolymer melt of M chains of length N with a pair potential $V(r) = \epsilon u(r)$ for bead-spring models, or a nearest-neighbor interaction

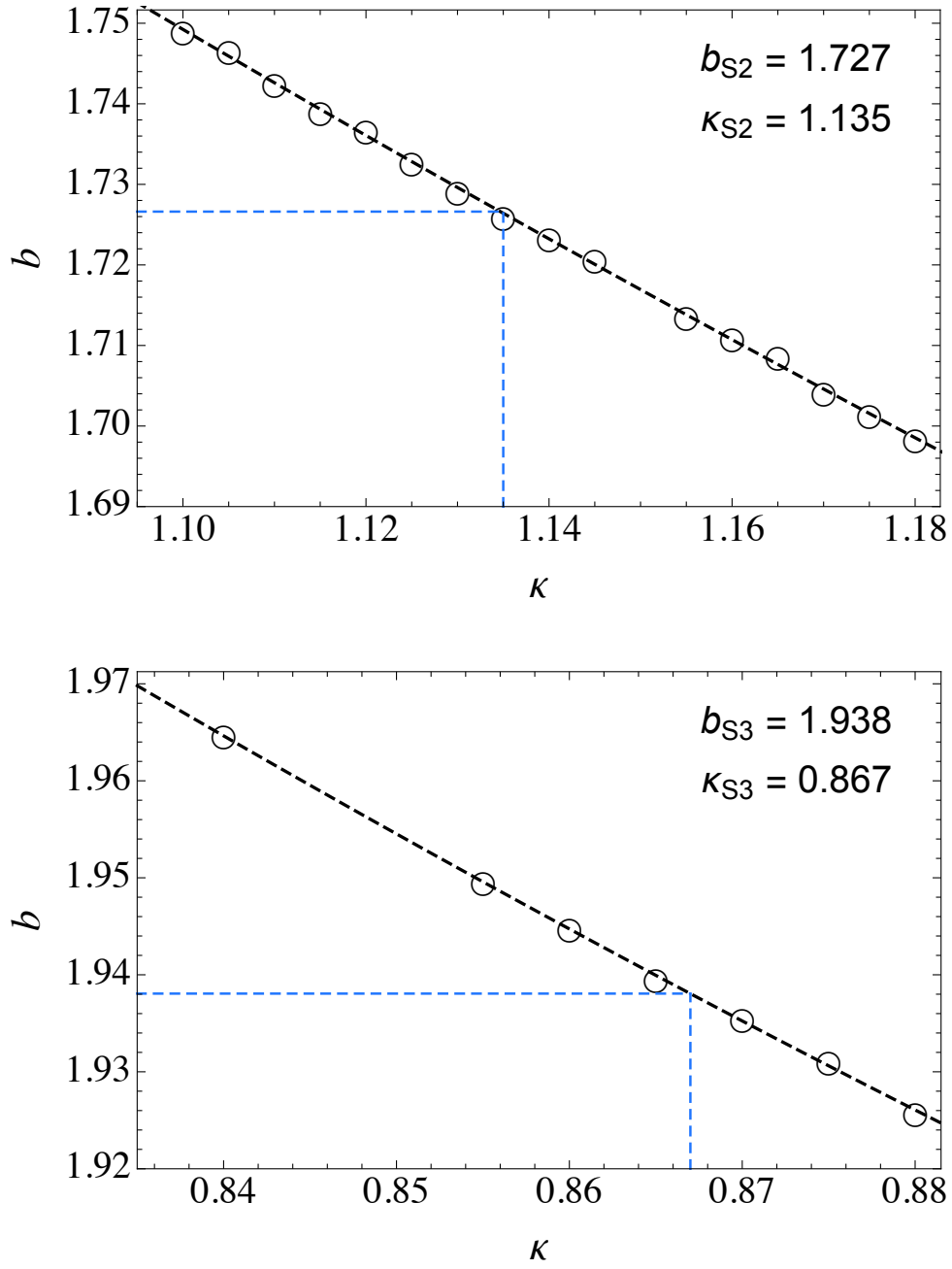

Figure 3.1: Statistical segment length b obtained from fit of $R_g(N)$ data to Eq. 3.5 *vs.* bonded potential parameter κ. These plots are used to select κ values of models (upper) S2 and (lower) S3 given our requirement for specific values of the ratio $\overline{N}/N = (cb^3)^2$.

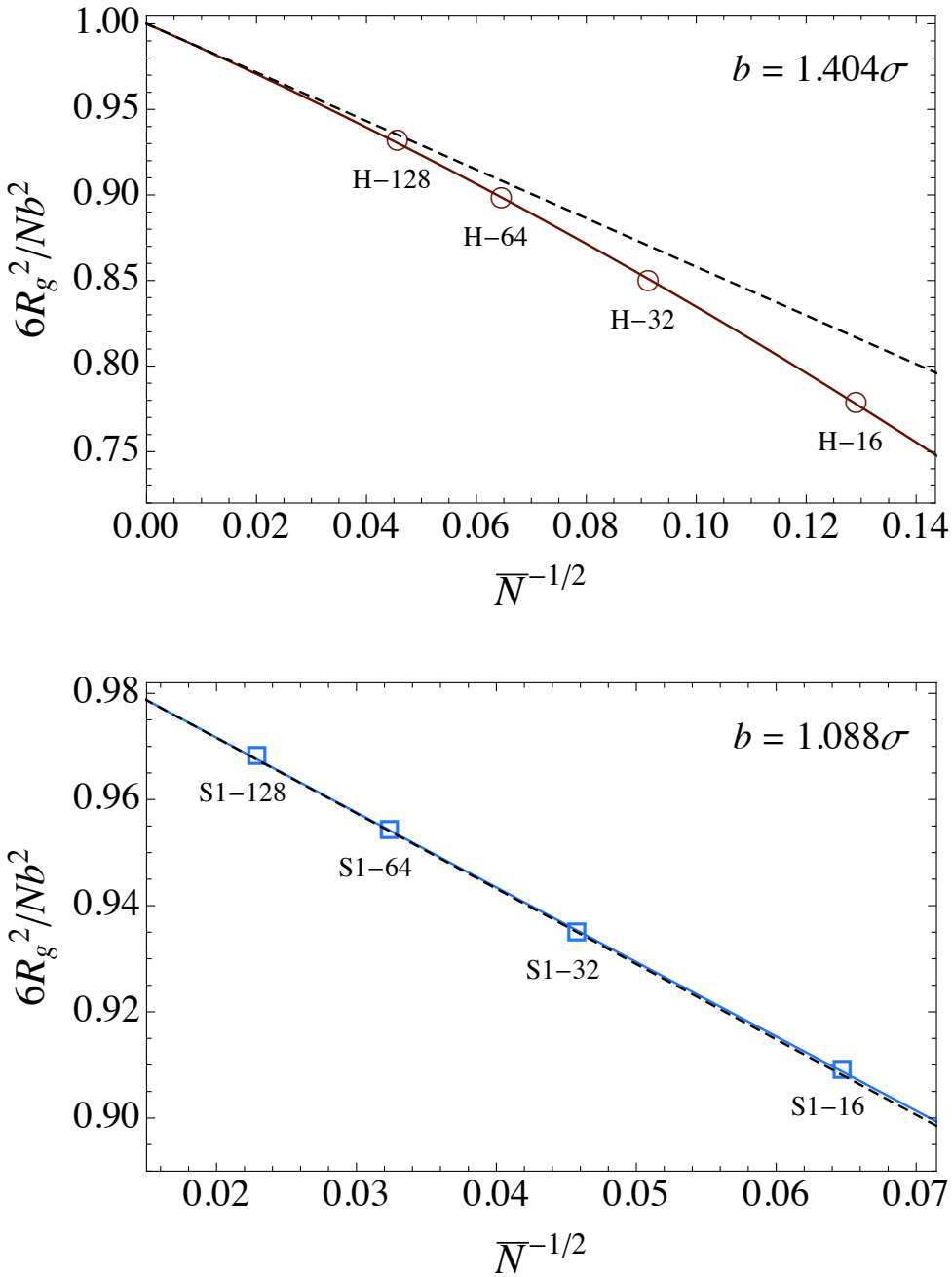

Figure 3.2: Results for radius of gyration $\frac{6R_g^2}{Nb^2}$ at $\alpha = 0$ *vs.* $\overline{N}^{-1/2}$ are fitted to the ROL prediction $R_g(N)^2 = \frac{Nb^2}{6}\left[1 - \frac{1.42}{\overline{N}^{1/2}} + \frac{\gamma}{N} + \cdots\right]$ for models H (upper) and S1 (lower). In fitting the data, statistical segment length b and the coefficient of the unknown term of order N^{-1} were treated as model-dependent free parameters. A best fit to the data (symbols) is shown by the solid line. The dashed line is the asymptotic line $\frac{R_g^2}{N} = \frac{b^2}{6}(1 - \frac{1.42}{\overline{N}^{1/2}})$. Results from fit: $b = 1.404\sigma$ and 1.088σ for models H and S1, respectively.

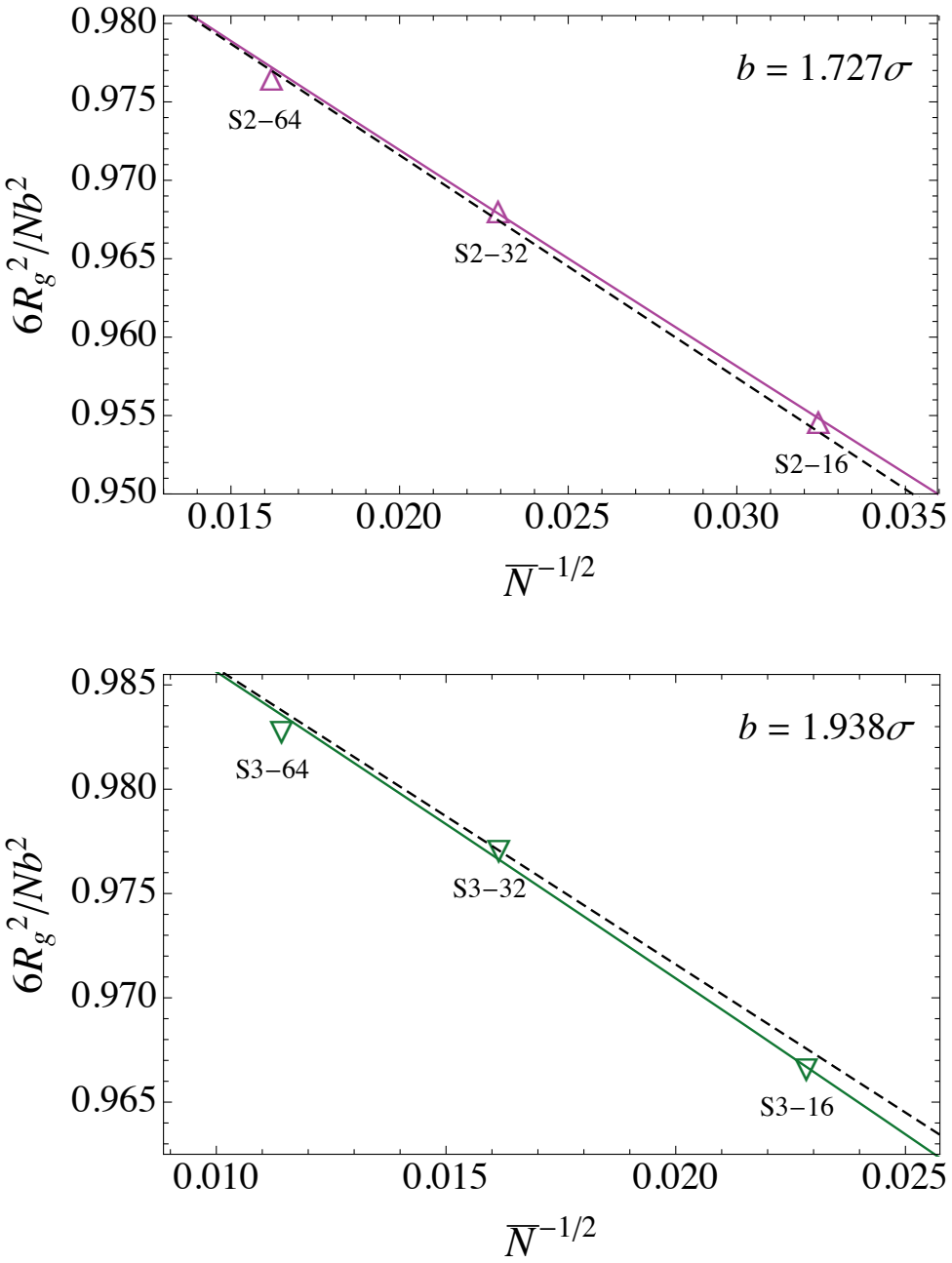

Figure 3.3: Results for radius of gyration $\frac{6R_g^2}{Nb^2}$ at $\alpha = 0$ *vs.* $N^{-1/2}$ are fitted to the ROL prediction $R_g(N)^2 = \frac{Nb^2}{6}\left[1 - \frac{1.42}{N^{1/2}} + \frac{\gamma}{N} + \cdots\right]$ for models S2 (upper) and S3 (lower). In fitting the data, statistical segment length b and the coefficient of the unknown term of order N^{-1} were treated as model-dependent free parameters. A best fit to the data (symbols) is shown by the solid line. The dashed line is the asymptotic line $\frac{R_g^2}{N} = \frac{b^2}{6}(1 - \frac{1.42}{N^{1/2}})$. Results from fit: $b = 1.727\sigma$ and 1.938σ for models S2 and S3, respectively.

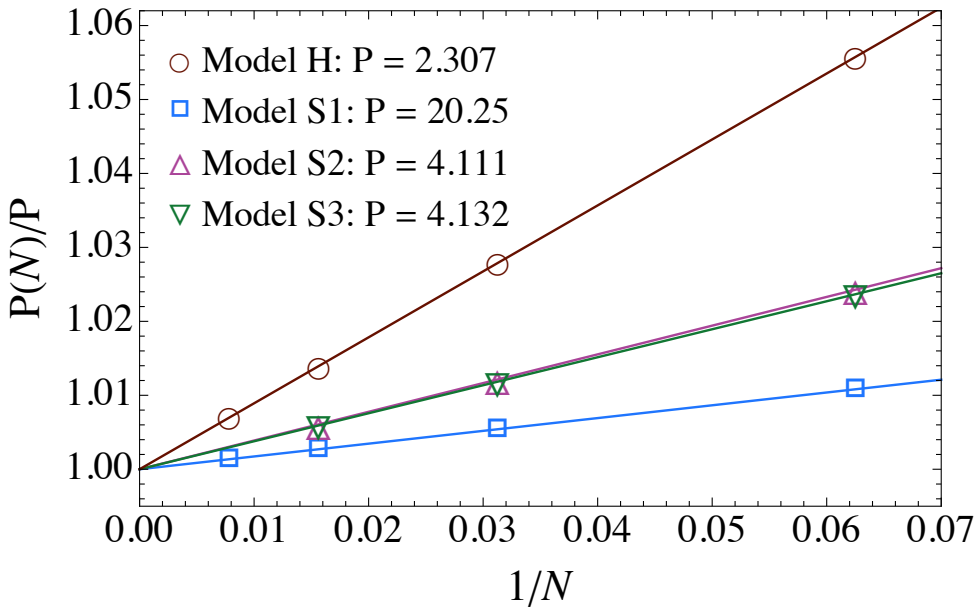

Figure 3.4: Results for $P(N)/P$ (symbols) *vs.* $1/N$ of all four models. Solid lines are fits to $P(N) = P_\infty + \delta/N$.

of strength ϵ in a lattice model. It was also predicted by Morse and Chung[81] that $z(N)$ should vary with N as

$$z(N) \simeq z_\infty \left[1 + \frac{(6/\pi)^{3/2}}{N^{1/2}} + \frac{\delta}{N}\right] \quad , \tag{3.6}$$

where z_∞ and δ are model-dependent parameters. Values of z_∞ were determined for models H, S1, S2, and S3 by running NVT homopolymer simulations at the target concentration c for several chain lengths, and fitting the results for each model to Eq. 3.6, using z_∞ and δ as fitting parameters. Fig. 3.5 shows the resulting fits. Values are given in table 3.2.

3.2.4 Effective Interaction Parameter $\chi_e(\alpha)$ from Fit to ROL Theory

In section 2.3.1, we discussed recent simulation studies[41,44,77] by our group that tested both the adequacy of the perturbative linear approximation for χ_e,[41,44] and the accuracy of the ROL theory of correlations.[77,78] These studies showed that the perturbative linear approximation does indeed yield excellent results

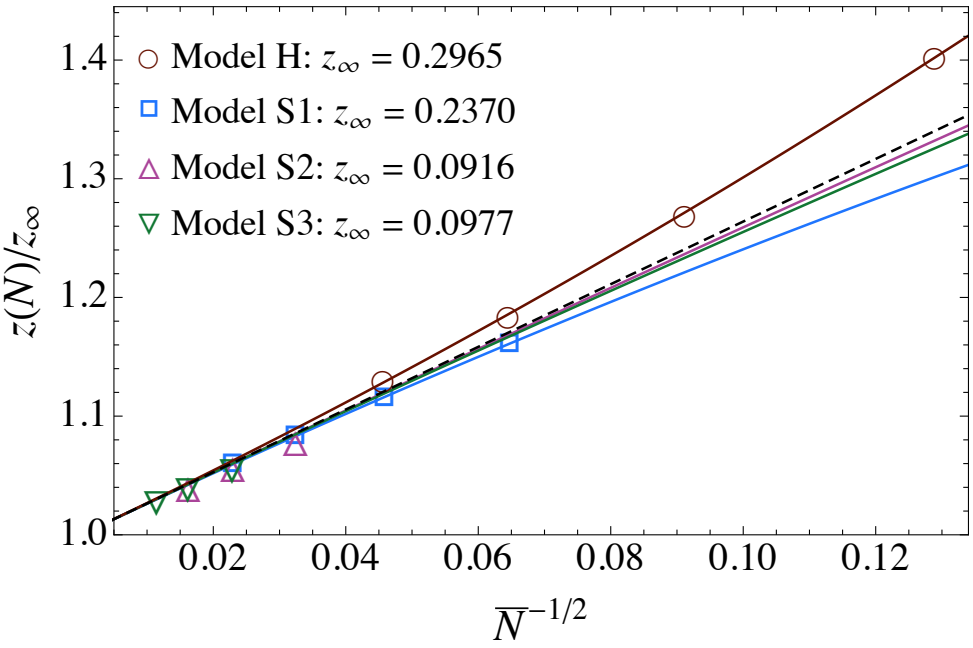

Figure 3.5: Results for $z(N)/z_\infty$ (symbols) *vs.* $\overline{N}^{-1/2}$ of all four models. Solid lines are fits to Eq. 3.6. The dashed line is the predicted asymptote $1 + (6/\pi)^{3/2}\bar{N}^{-1/2}$.

for small α, but suggested the necessity of allowing for a nonlinear dependence of $\chi_e(\alpha)$ on α in order to make sense of results obtained near the ODT for the relatively short chains used in most simulations. Section 4.2.2 discusses our method for obtaining nonlinear functions $\chi_e(\alpha)$ for each model by simultaneously fitting results for normalized peak structure factor $cNS^{-1}(q^\star)/2$ *vs.* α of different chain lengths of a model to ROL theory predictions of $cNS^{-1}(q^\star)/2$ *vs.* χN. To enforce consistency with the rigorous results provided by perturbation theory, this fit is constrained to yield a derivative $d\chi_e/d\alpha$ that reduces in the limit $\alpha = 0$ to the value given by the perturbative linear approximation.

Refer to Table 4.1 in section 4.2.2 for estimates of coefficients of $\chi_e(\alpha)$ functions of models H, S1, S2, and S3.

3.3 Simulation Methods

All simulations presented here are either NVT or NPT molecular dynamics (MD) simulations that were implemented using the integrator of Martyna, Tobias, and

Model	b	$(cb^3)^2$	P	z_∞
H	1.404	3.753	2.307	0.2965
S1	1.088	14.93	20.249	0.237
S2	1.727	59.70	4.111	0.0916
S3	1.938	119.21	4.132	0.0977

Table 3.2: Estimates of parameters b, P, and perturbation coefficient z_∞ for all four models.

Klein.[96] All simulations used a time step $\Delta t = 0.005$ in natural units ($k_BT = 1$, $\sigma = 1$, bead mass =1). All simulations were conducted using either the GPU-accelerated HOOMD-Blue code[97] or the multi-CPU C++ package named Simpatico.[98]

Three different types of simulation were performed for each system: (1) First, conventional NPT simulations with a cubic cell L^3 were used to measure properties of the disordered phase and to obtain initial estimates of the ODT α_{ODT} location from observations of spontaneous phase transitions, as discussed below. (2) Second, simulations of the ordered phase were performed using initial conditions in which the system was artificially ordered with layers perpendicular to the z axis, using a deformable tetragonal $L_x \times L_x \times L_z$ simulation cell, in which L_x and L_z are allowed to fluctuate independently so as to allow the layer spacing to adjust to create a state of isotropic pressure. All measurements of the ordered phase were performed using this deformable unit cell. (3) Finally, well-tempered metadynamics simulations were performed for each system to precisely locate the ODT.

All simulations were carried out on systems large enough to contain approximately three layers of the ordered phase. The total number of particles (monomers) per system varied from NM = 32,000 to 480,000. The number of molecules M used for each system in conventional MD simulations was chosen so that a simulation in an $L \times L \times L$ cubic box with monomer concentration MN/L^3 equal to the target value c would have a box dimension L as close as possible (given that M must be an integer) to 3 times the RPA prediction for the layer spacing d at the ODT, for which $d = 2\pi/q_0^*$ and $q_0^* = 1.95/R_{g0}$. Resulting values for M and L are given in Table 3.3 for all systems studied here.

Initial estimates of α values at ODT α_{ODT} were obtained from observations

Model	M	L	α_{ODT}	$(\chi_e N)_{\mathrm{ODT}}$	$\overline{N}$
H-64	2026	57.004	1.587	22.863	240.20
S1-16	2007	22.038	4.920	22.756	238.86
S1-32	2555	30.094	2.220	19.571	477.71
S1-64	3269	41.162	1.031	17.241	955.42
S1-128	4162	56.208	0.478	15.328	1910.85
S2-16	3137	32.224	14.678	17.438	955.45
S2-32	4145	44.551	5.771	15.610	1910.90
S2-64	5573	61.953	2.534	14.345	3821.80
S3-16	3967	34.847	12.430	15.703	1907.33
S3-32	5391	48.631	4.990	14.392	3814.65
S3-64	7227	67.559	2.213	13.361	7629.31

Table 3.3: Characteristics of all simulations systems studied in this work. M and L are the number of molecules and approximate cell size (in units with $\sigma = 1$) used in conventional MD simulations of the disordered phase. Values of α_{ODT} are determined using the well-tempered metadynamics method discussed in chapter 5. Corresponding values of $(\chi_e N)_{\mathrm{ODT}}$ are calculated using the non-linear approximation for $\chi_e(\alpha)$ of each model.

of spontaneous ordering of initially disordered configurations and spontaneous melting of initially ordered configurations. For this purpose, separate sets of simulations were performed starting from disordered and artificially ordered initial configurations, at closely spaced values of α near the expected value of α_{ODT}. Simulations that were designed to study spontaneous ordering transitions all used a cubic unit cell, because attempts to simulate the disordered phase using a deformable tetragonal cell can lead to uncontrolled variations in the unit cell shape. Spontaneous transitions between ordered and disordered phases were identified by monitoring the behavior of structure factor $S(q)$. The magnitude of peak structure factor $S(q^*)$ increases with increasing value of control parameter α and exhibits a steep jump when the system orders at ODT α_{ODT}, thus providing a clear signature of a phase transition.

Fig. 3.6 shows a comparison of the behavior of the structure factor $S(q)$ in the disordered phase (upper panel) over a range of values of $\alpha < \alpha_{\mathrm{ODT}}$ and in the ordered phase at $\alpha = \alpha_{\mathrm{ODT}}$ (lower panel). The ordered phase is easily distinguishable from the disordered phase by the appearance of a primary Bragg peak at $q^* R_{g0} \simeq 1.5$ with an intensity that is more than an order of magnitude

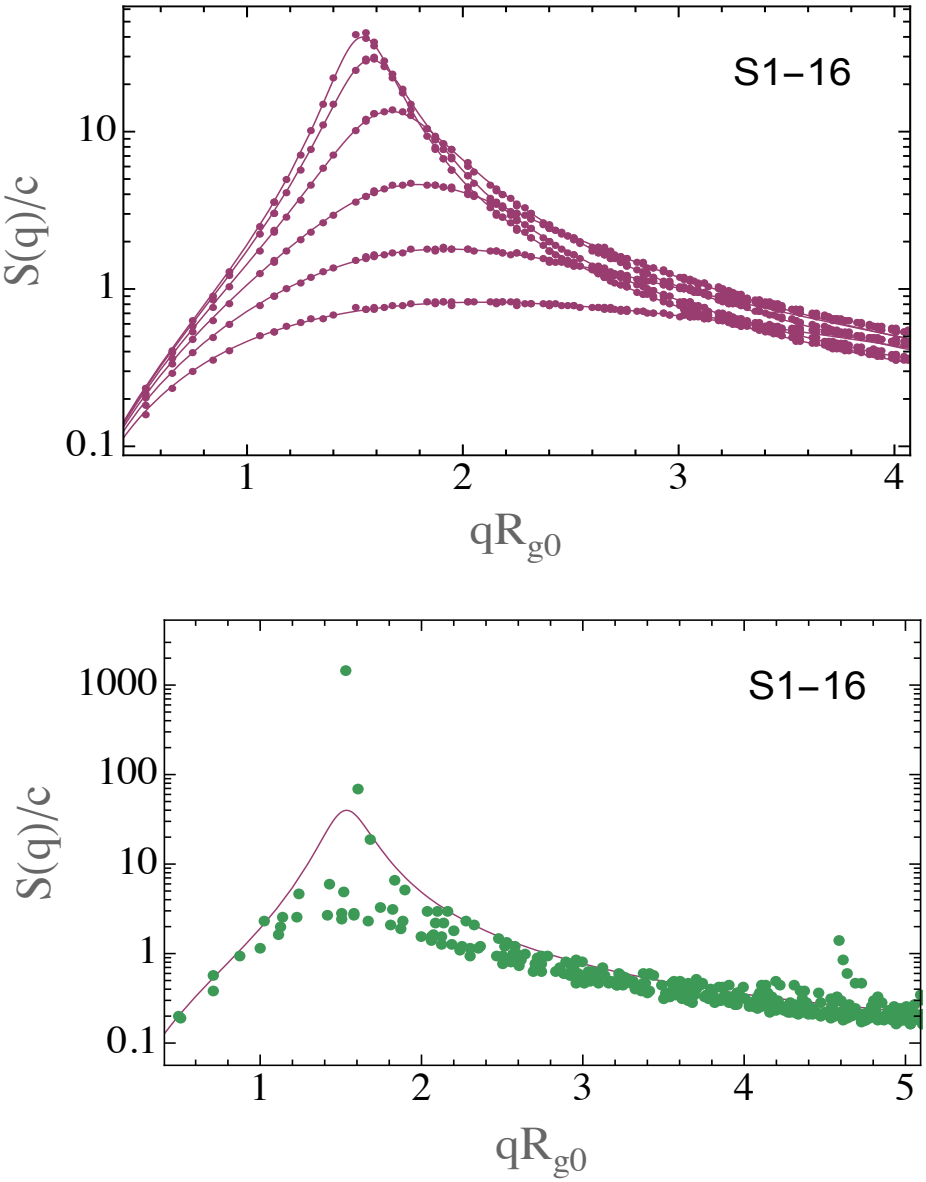

Figure 3.6: Structure factor $S(q)$ of model S1-16 as measured in the disordered phase over a range of values of $0 \leq \alpha \leq 4.90$ (upper) and in the ordered phase at the ODT, at $\alpha_{\rm ODT} = 4.92$ (lower). (upper) Results for $S(q)$ in the disordered phase for $\alpha = 0.0$ 1.5, 2.7, 3.725, 4.50, and 4.90, corresponding to $\chi_e N = 0.0$, 6.43, 12.07, 17.01, 20.79 and 22.76. These simulations of the disordered phase used a system of 4933 chains. (lower) Symbols show values of $S(q)$ at discrete allowed values of q in the ordered phase at $\alpha = \alpha_{\rm ODT} = 4.92$, or $(\chi_e N)_{ODT} = 22.85$. The solid line shows the fit to results for $S(q)$ in the disordered phase very near the ODT ($\alpha = 4.90$) for comparison. This simulation of the ordered phase was performed in a flexible tetragonal unit cell containing 3 layers and 2004 chains.

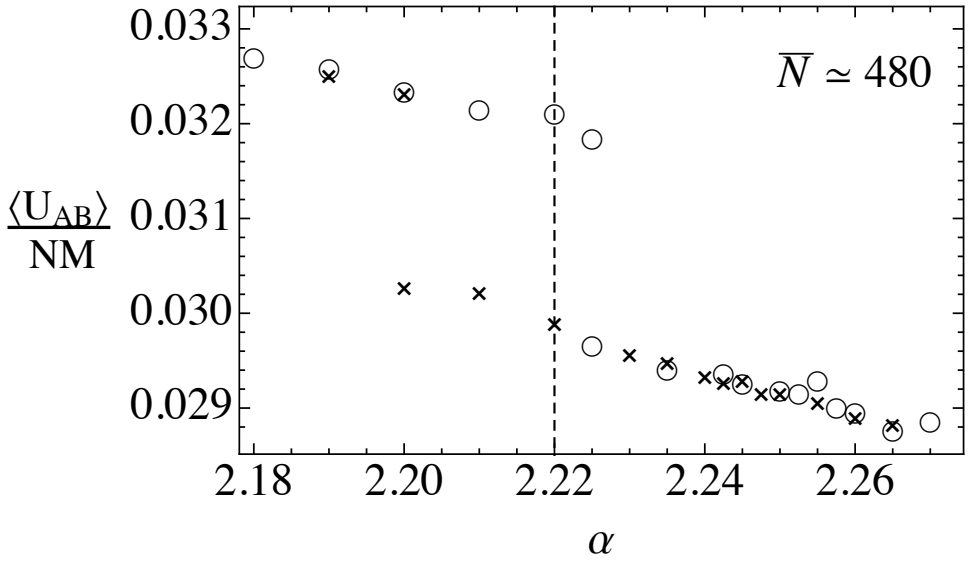

Figure 3.7: A plot showing hysteresis in AB pair energy per particle $\langle U_{AB}\rangle/NM$ obtained from simulations of model S1-32, at several values of the AB repulsion parameter α (or ϵ_{AB}) near the ODT value. Circles and crosses represent results from simulations initialized with disordered and artificially ordered configurations, respectively. The dashed line indicates the value of α at the equilibrium ODT as obtained from well-tempered metadynamics simulations.

greater than the maximum value of $S(q)$ in the disordered phase just below the ODT. Note the appearance of a much smaller Bragg peak at $q = 3q^*$, and the suppression of diffuse scattering at other wavevectors in the ordered phase. There is no Bragg peak at $2q^*$ because of the symmetry between A and B monomers, which allows Bragg scattering only at odd multiples of q^*. The ordered phase simulations were conducted in flexible tetragonal unit cells with three layers aligned perpendicular to the x axis, giving a primary peak at wavevector (300). Simulations of the disordered phase used a cubic unit cell. In both phases, the displayed value $S(q)$ at a wavenumber q is obtained by averaging over all wavevectors $\mathbf{q}$ that are related by the point group of the simulation unit cell, and thus average over results for up to 48 wavevectors in the disordered phase and up to 8 in ordered phase. The results for the disordered phase fall on a universal curve because the rotational symmetry of the disordered phase guarantees that $S(\mathbf{q})$ depends only on the magnitude of wavevector $\mathbf{q}$. Conversely, results from the ordered phase do not fall onto a single curve when plotted in this way because wavevectors with similar magnitudes, but with different components in directions parallel and perpendicular to the ordering direction, are structurally distinct in a phase with broken rotational symmetry.

The strongest diffuse scattering in the ordered phase, excluding the Bragg peaks, occurs at "satellite" peaks at values of q slightly greater than the Bragg peak wavenumbers, i.e., at $q > q^*$ and $q > 3q^*$. These satellite peaks arise from wavevectors with the same component parallel to the ordering direction as the corresponding Bragg peak and different components in the perpendicular directions. For example, the strongest satellite peaks near the main (300) peak have wavevectors (310) and (311). We assume that these peaks arise from coherent undulations of the layers, i.e., from pure undulation modes in which a point at position (y, z) within an interface between A and B rich regions in the nth layer is displaced along the x direction by an amount $h_n(y, z) \propto e^{i\mathbf{q}\cdot\mathbf{r}}$, where $\mathbf{q}$ is a wavevector parallel to the layers, with the same displacement for all layers.

Almost all of the systems studied here exhibit a range of values of α near the ODT in which both ordered and disordered configurations can remain sta-

ble throughout a long MD run (tens to hundreds of million MD steps). This hysteresis is visible in Fig. 3.7, where we show results for the AB pair energy per monomer $\langle U_{AB} \rangle / NM$ obtained from simulations that were initialized with ordered and disordered configurations, for model S1-32. This metastable region becomes wider for longer chains, and made it impossible for us to estimate ODTs of some of the systems with sufficient accuracy for the purposes of this work. We, therefore, implemented a method known as well-tempered metadynamics to precisely identify ODT locations in our simulations systems.

Chapter 4

Correlations in the Disordered Phase

We present a detailed comparison of simulations results for correlations in the disordered phase of symmetric AB diblock copolymer melts to predictions of the renormalized one-loop (ROL) theory. The behavior of structure factor $S(q)$ and single-chain correlations are studied over a range of chain lengths ($N = 16, \ldots, 128$) for models H and S1 with harshly repulsive and very soft pair interactions, respectively. Similar disordered phase simulations were not conducted for models S2 and S3 because results from models H and S1 (called as model S in this chapter) proved adequate for understanding the behavior of correlations in disordered phase. Results for all disordered phase properties of models H and S are consistent with the existence of a universal scaling hypothesis. According to this hypothesis, equivalent results are obtained for all properties from states with equal values of the parameters $\chi_e N$ and $\overline{N}$, where χ_e is an effective Flory-Huggins interaction parameter and N is a degree of polymerization. The underlying universality becomes apparent, however, only if data is analyzed using a nonlinear function for the dependence of the effective interaction parameter χ_e upon the AB repulsion strength α. Our approach for estimating the nonlinear function $\chi_e(\alpha)$ of a simulation model, as discussed in section 3.2.4, is to simultaneously fit results of structure factor $S(q)$ in the disordered phase of different chain lengths of the model to the ROL theory predictions. The ROL theory is found to provide an excellent fit to results for $S(q)$

from all simulation models over a wide range of chain lengths and values of $\chi_e(\alpha)N$. The decrease in peak wavenumber q^* with increasing χ_e is shown to be unrelated to changes in single-chain correlations (*i. e.,* coil dimensions), and to instead be a result of intermolecular correlations. Results for all quantities are consistent with the hypothesis that the ROL theory gives an exact description of the dominant $\mathcal{O}(N^{-1/2})$ corrections to RPA and random-walk predictions in the limit of infinite chain length N.

The work presented in this chapter was done in collaboration with Dr. Jens Glaser, and has been published previously.[78] The chapter is organized as follows: Section 4.1 focuses on the behavior of $S(q)$ in the limit of thermodynamically ideal copolymers, with $\chi = 0$. Section 4.2 presents an analysis of results for the parameter dependence of the peak intensity $S(q^\star)$ in systems with nonzero χ. The analysis differs from that given for model H in section 2.3 in that we use a nonlinear function for χ_e in terms of the AB repulsion strength α. This difference is found to dramatically improve the level of agreement between ROL theory and simulations of short chains. Section 4.3 tests ROL predictions for the peak wavenumber q^*. Section 4.4 presents a more detailed analysis of results for $S(q)$ based on the use of the OrnsteinZernike equation to explicitly separate $S^1(q)$ into intra- and intermolecular contributions. Section 4.5 presents results for radii of gyration of the chain and of individual blocks. Conclusions are summarized in section 4.6.

All simulations were carried out in NVT ensemble in periodic cubic simulation cells of volume $V = L^3$. The number of molecules M was chosen so as to yield a cell length $L \simeq 3d_0^*$ approximately 3 times the RPA layer spacing of $d_0^* \equiv 2\pi/q_0^*$, or $L \simeq 9.67R_{g0}$, in systems that have exactly the chosen monomer concentration for each model. (The length L and the monomer concentration $c = MN/L^3$ cannot both be set to exactly specified values simply because M must be an integer). A list of system sizes used for different chain lengths is given in Table 3.3 in chapter 3.

4.1 Ideal Diblocks ($\chi_e = 0$)

In this section, we first compare simulations results and ROL predictions for $S(q)$ in the case of thermodynamically "ideal" diblocks, with $\alpha = 0$. In this limit, A and B monomers are physically indistinguishable, but are labeled for the purpose of defining $S(q)$. This is an idealization of a small-angle neutron scattering (SANS) experiment that measures the correlation hole in a melt of diblock copolymer containing blocks of hydrogenated and deuterated versions of the same monomer, idealized by ignoring the small but nonzero χ between hydrogenated and deuterated monomers. Moreover, no estimate of χ_e is required to test ROL theory predictions for symmetric copolymers with $\alpha = 0$, because χ_e is known[17] to be exactly zero in this limit.

It has been shown analytically, in appendix B of Ref.,[17] that in the special case of perfectly symmetric diblock copolymers with $\alpha = 0$, $\chi_a(q)$ of Eq. eq:OZinc is exactly zero for all q. This implies that, in this case,

$$cNS^{-1}(q) = F(q) \quad , \tag{4.1}$$

where $F(q)$ is defined using the exact single-chain correlation functions in a dense homopolymer liquid. Eq. 4.1 is an exact result that is a consequence of the symmetry of the system under interchange of the labels of A and B monomers, and thus applies only to this special case. In this case, however, it implies that $S(q)$ is completely determined by single-chain statistics, and that deviations from RPA predictions are a result of non-Gaussian chain statistics.

Each panel in Fig. 4.1 shows a comparison of simulations results to ROL and RPA predictions for pairs of simulations of models H and S with matched values of $\overline{N}$. The upper panel shows results for simulations H-64 (H64) and S-16 (S16), which both have $\overline{N} = 240$. The lower panel shows a comparison for model H-128 and model S-32, for which $\overline{N} = 480$. For both values of $\overline{N}$, the results obtained with the two models agree very well with one another and with ROL predictions at wavenumbers near the peak in $S(q)$.

From the upper panel of Fig. 4.1, it is also clear, however, that results from model S-16 show a systematic deviation from results of model H-64 and from ROL predictions at higher values of q. These high-q deviations are results of the

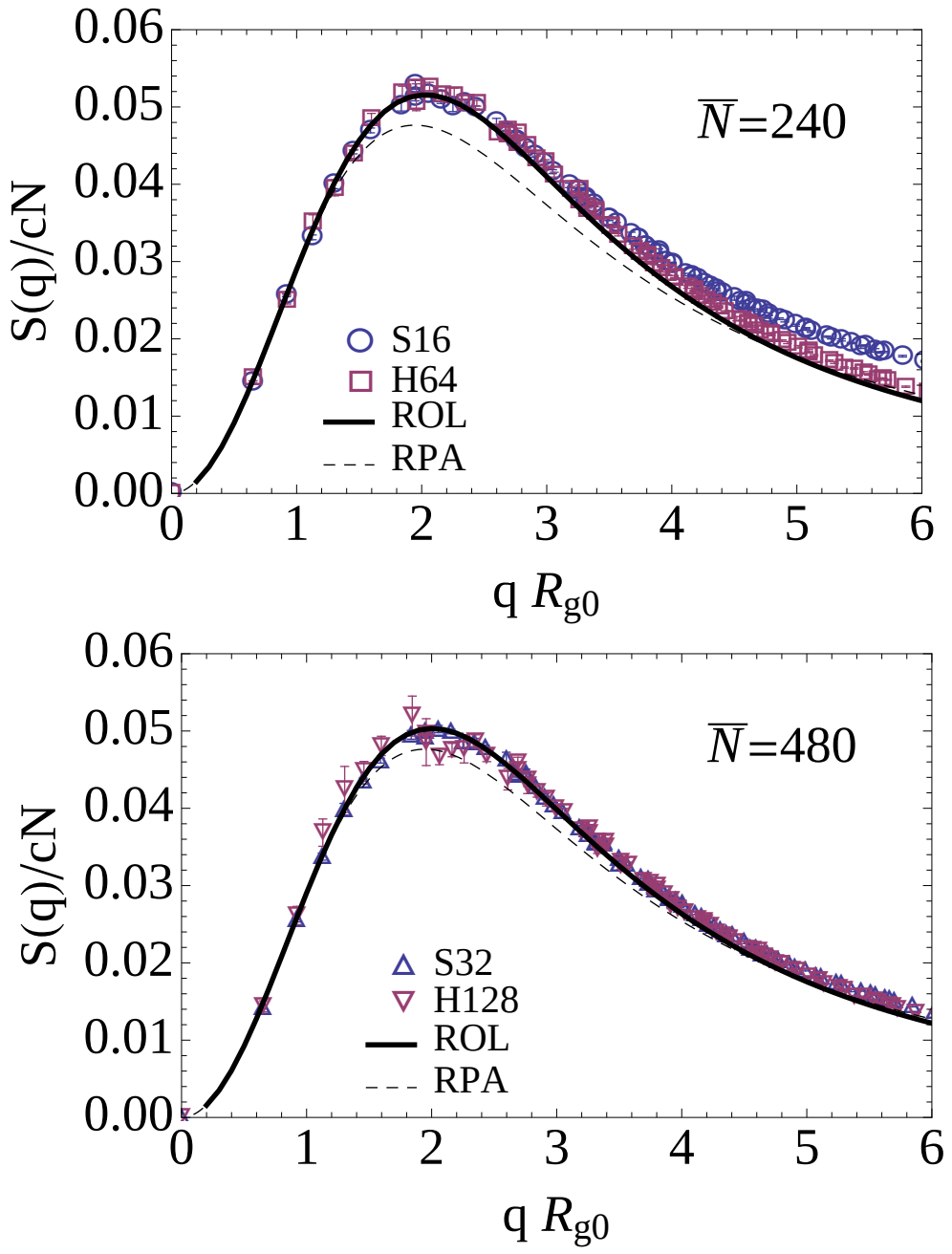

Figure 4.1: Comparison of the simulated $S(q)$ to one-loop theory (solid curve) and RPA (dashed curve), at $\alpha = 0$, for simulations of models H and S with matched values of $\overline{N} \simeq 240$ (uooer panel, H-64 and S-16) and $\overline{N} \simeq 480$ (lower panel, H-128 and S-32).

discrete chain structure, which become noticeable as q approaches the inverse monomer size $1/\sigma$. This deviation from the ROL prediction is more pronounced for model S-16 than for model H-64 simply because H-64 has four times as many monomers per chain.

Corrections to random-walk behavior that arise from discrete chain structure can be distinguished from the universal corrections predicted by the one-loop theory because they are expected to exhibit a different dependence on q and N. Universal corrections should exhibit a universal (*i. e.,* model-independent) dependence on qR_{g0} and on $\overline{N}$. Corrections that arise from discrete chain structure should instead depend on the absolute wavenumber q, independent of R_{g0} or N. If the universal and non-universal correction to $S^{-1}(q)$ are approximately additive, and if universal contributions are adequately approximated by the ROL theory, then $S^{-1}(q)$ should be well approximated as sum

$$S^{-1}(q) \simeq S^{-1}_{\rm ROL}(q) + S^{-1}_{\rm local}(q) \tag{4.2}$$

in which $S^{-1}_{\rm ROL}(q) = F_{\rm ROL}(qR_{g0}, \overline{N})/cN$ is the ROL prediction, which exhibits a universal dependence on qR_{g0} and $\overline{N}$, and $S_{\rm local}(q)$ is a "local" contribution arising from discrete chain structure. The local contribution may be entirely different for different models, but should be independent of N.

In Fig. 4.2, we test Eq. 4.2 by plotting the difference $c[S^{-1}(q) - S^{-1}_{\rm ROL}(q)]/c$ *vs.* $q\sigma$ for multiple chain lengths of each model, in an attempt to isolate $S^{-1}_{\rm local}(q)$. As proposed, results for this difference from different chain lengths collapse onto a common curve for each model when plotted *vs.* $q\sigma$ (rather than *vs.* qR_{g0}), but yield different curves for models H and S. Consistent with our interpretation, these deviations are large only for $q\sigma \gtrsim 1$. The solid lines through the data for each model are purely empirical fits of the function $S^{-1}_{\rm local}(q)$ for each model, as discussed in the figure caption.

This identification of a non-universal "local" contribution to $S^{-1}(q)$ can be used to refine our comparison of simulations data for $S(q)$ to the ROL theory. The local contribution is expected to have a negligible effect for $q \sim q^\star$ for long chains, because $q^* \propto N^{-1/2}$, but can be important for very short chains. Fig. 4.3 shows an analysis of our results for $S(q)$ for model H-16, for which the effects of discrete chain structure are strongest. The open squares represent

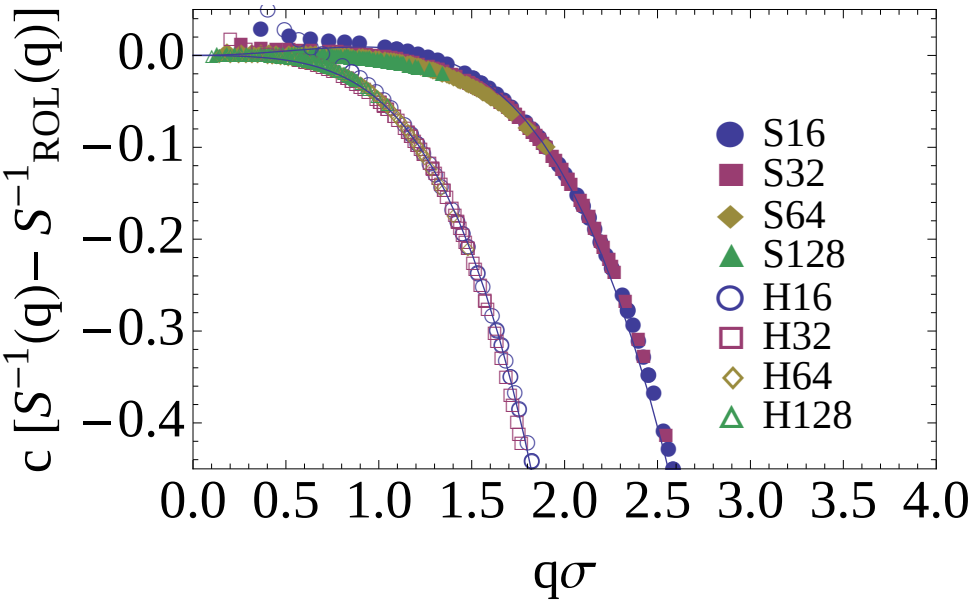

Figure 4.2: Difference between measured values of $S^{-1}(q)/c$ in homopolymer melts and ROL predictions for this quantity, *vs.* $q\sigma$. Data is shown for four different chain lengths $N = 16, 32, 64, 128$ for model H (open symbols) and model S (filled symbols). Solid curves are fits to an empirical function $cS^{-1}_{\rm local}(q\sigma) = a(q\sigma)^2 + b(q\sigma)^4$. The fit parameters are $a = -0.0111$, $b = -0.0376$ (model H), and $a = 0.0227$, $b = -0.0140$ (model S).

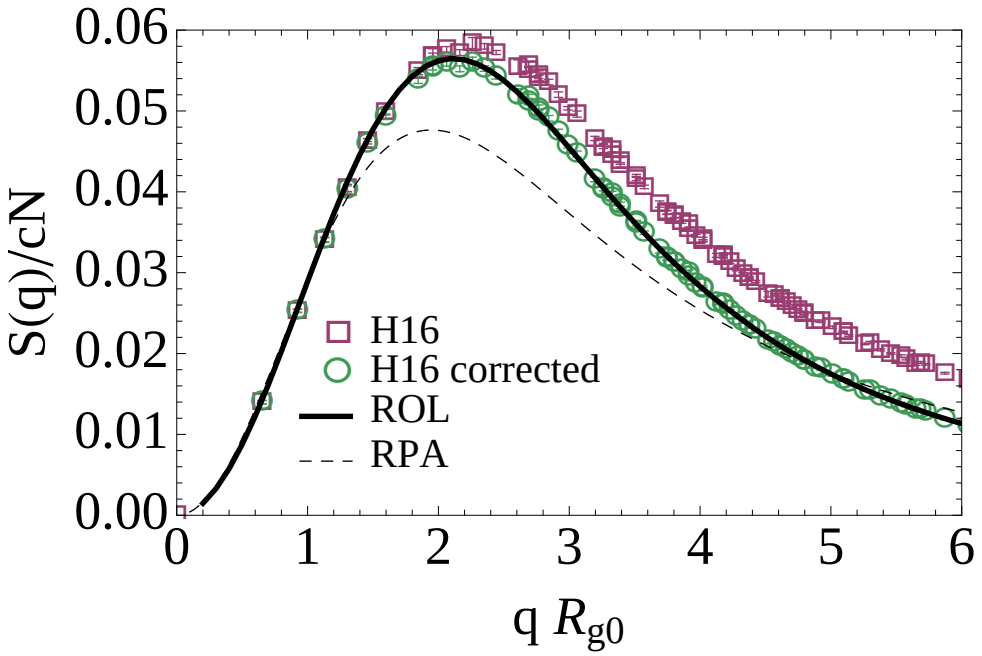

Figure 4.3: Comparison of the simulations results for $S(q)$ (open squares), simulations results that have been corrected by subtracting $S_{\rm local}(q)$ (open circles) to the RPA (dashed curve) and ROL (solid line), for model H-16 at $\alpha = 0$. The corrected results were obtained by subtracting N-independent function that was obtained by fitting the data shown in Fig. 4.1 from the raw data.

the raw simulations results for $S(q)/cN$. The open circles represent the results for a function $S'(q)$ obtained by subtracting our estimate of $S^{-1}_{\rm local}(q)$ from each measured value of $S^{-1}(q)$. The ROL theory, indicated by the solid line, shows a somewhat astonishing level of agreement with the corrected data. Agreement is equally good for all remaining data sets for both models. Explicitly correcting for the effects of discrete chain structure thus brings the ROL into nearly perfect agreement with our simulations results in the limit $\alpha = 0$, even for very short chains.

4.2 Peak Scattering Intensity

This section shows comparisons of simulations results to ROL predictions for the dependence of peak scattering intensity $S(q^*)$ on interaction parameter $\chi_e N$ using the two estimates of $\chi_e(\alpha)$ discussed in chapters 2 and 3. First, in subsection 4.2.1, we use the linear approximation $\chi_e^{(1)}(\alpha)$ provided by first order

perturbation theory. The virtue of this approach is that it involves no free parameters, since the required coefficient of proportionality z_∞ was obtained from independent simulations of homopolymer melts. This approach is found to yield reasonable agreement between theory and simulations for small values of α, and thus for long chains, but to fail at the larger values of α accessed in simulations of shorter chains.

Then, in subsection 4.2.2, we use the nonlinear function for $\chi_e(\alpha)$ obtained from a simultaneous fit of simulations results for $cNS^{-1}(q^*)$ of several different chain lengths of a model to ROL theory predictions.

4.2.1 Linear $\chi_e(\alpha)$

Fig. 4.4 shows results for the normalized inverse scattering intensity $cNS^{-1}(q^*)/2$ *vs.* $\chi_e^{(1)}(\alpha)N$. In this figure, the abscissa for each of the simulations data points has been plotted using Eq. 2.26 for $\chi_e^{(1)}(\alpha)$. Results for models H and S are presented in the upper and lower panels, respectively. The RPA prediction $cNS^{-1}(q^*)/2 = 10.5 - \chi_e N$ is shown by the dashed line in each plot. The horizontal dashed line in each plot shows the value of $cNS^{-1}(q^*)/2 = 0.35$ at which Eq. 2.22 yields $\xi \simeq d^*$. Data from simulations very near the ODT, for which $cNS^{-1}(q^*)/2$ falls below this bound, have been excluded from both the plots and the fit in the next section to avoid data that may be corrupted by finite size effects. In the upper panel, data from older simulations of model H[77] (open symbols) using two different box sizes for each chain length are plotted along with the results of our new MD simulations (closed symbols), to show that the results are independent of L within this range of values of the ordinate $cNS^{-1}(q^*)/2$.

When assessing the successes and failures of this approach, it is important to remember that the value of χ_e at a given value of $\chi_e^{(1)}N$ is inversely proportional to N, and that α is roughly proportional to χ_e. The range of values of α accessed in simulations of different chain lengths thus decreases by approximately a factor of 2 when N is doubled.

Upon inspection of these plots, a few trends become apparent. Agreement between theory and simulations results is reasonably good for the longest chain lengths, particularly for model H. Agreement is also very good for all chain

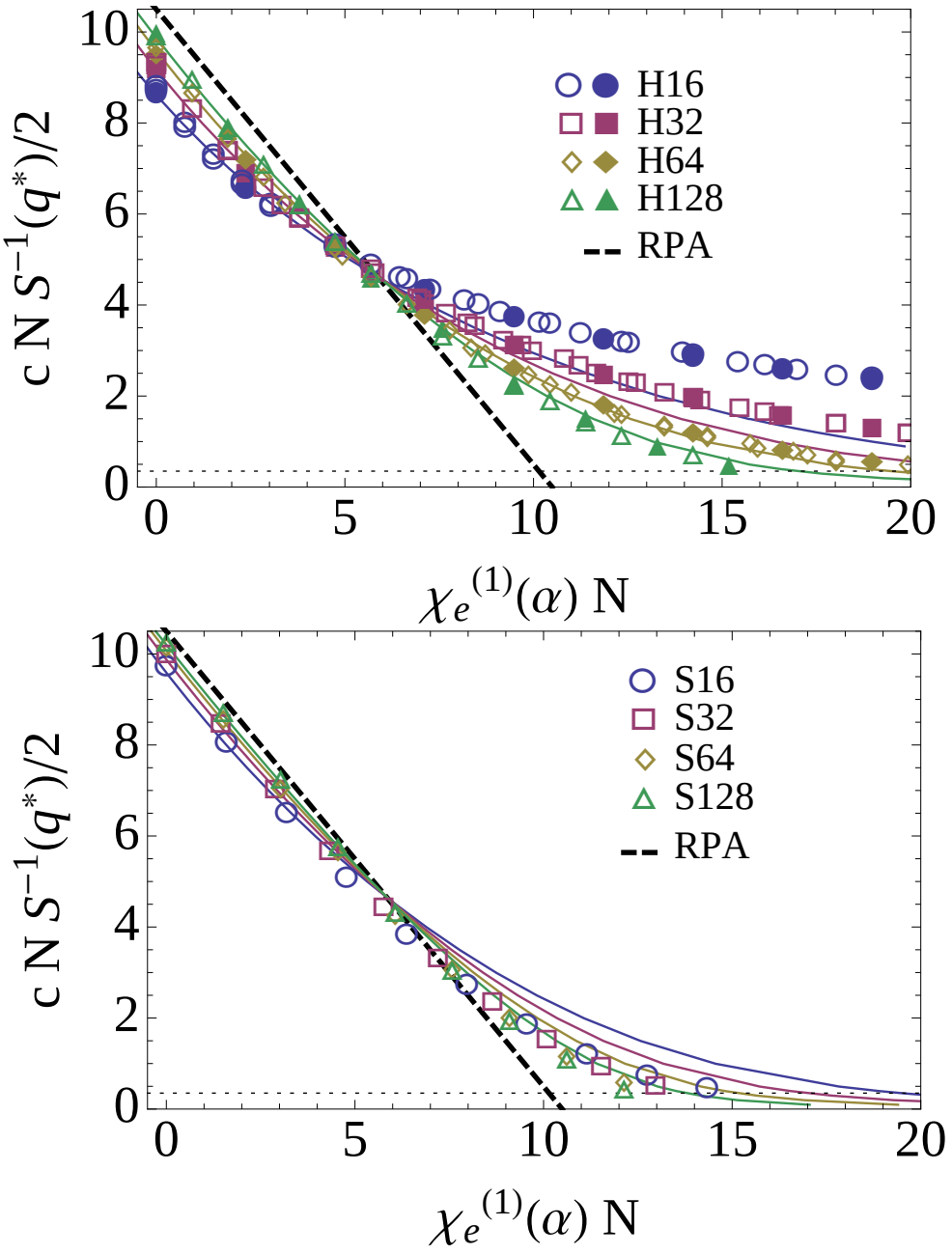

Figure 4.4: Normalized inverse peak structure factor $cNS^{-1}(q^\star)/2$ *vs.* $\chi_e^1 N = z_\infty \alpha N$. Data is shown for model H (upper panel) and model S (lower panel). Solid curves are predictions by ROL theory. Data for model H corresponds to two different system sizes: Those given in Table 3.3 are shown as filled symbols and those corresponding to previously published data[77] are shown as open symbols.

lengths, in both models, at small values of $\chi_e^{(1)}N$, corresponding to small values of α. Agreement thus appears to be best wherever α is small. Conversely, agreement is worst where α is largest, at large values of $\chi_e N$ and small values of N.

Interestingly, the discrepancies between simulations results and theory are qualitatively different for the two models. In model H (upper panel), simulations of H-16 and H-32 yield values of $cNS^{-1}(q^*)/2$ that are significantly greater than theoretical predictions. In model S (lower plot), simulations results for $cNS^{-1}(q^*)/2$ are instead all less than corresponding predictions.

The fact that the largest errors are consistently found where α is largest, independent of $\chi_e^{(1)}N$, suggests that these discrepancies may be primarily the result of the breakdown of our linear approximation for $\chi_e(\alpha)$ at large values of α, rather than primarily a failure of the ROL theory. This hypothesis is also suggested by the fact that the errors are very different for these two models, since the nature of nonlinearities in $\chi_e(\alpha)$ may be completely different for different models.

4.2.2 Nonlinear $\chi_e(\alpha)$

In order to allow for possibility of a nonlinear dependence of $\chi_e(\alpha)$ upon α, we have expressed the function $\chi_e(\alpha)$ for each model as a nonlinear function with 2-3 free parameters and adjusted the values of these parameters to fit the data for four chain lengths. Despite the introduction of several adjustable parameters, this procedure provides a nontrivial test of the accuracy of the ROL theory because we attempt to simultaneously fit data from simulations of several different chain lengths using a single function $\chi_e(\alpha)$, without allowing $\chi_e(\alpha)$ to depend on N. This is conceptually very similar to a hypothetical procedure of fitting the function $\chi_e(\alpha)$ for each model so as to fit the peak intensity data for one chain length, using as many parameters as required to fit that data, and then using the resulting function $\chi_e(\alpha)$ within the ROL theory to predict scattering intensities for the other three chain lengths.

Our choice of what functional form to use to fit $\chi_e(\alpha)$ for each model is somewhat arbitrary. The only rigorous constraints are that, for symmetric diblocks, $\chi_e(\alpha)$ must vanish for $\alpha = 0$ for reasons of symmetry, and that $d\chi_e(\alpha)/d\alpha$ must

approach the known value of z_∞/k_BT at $\alpha = 0$.

This method is analogous to that used to estimate $\chi_e(T)$ in many experimental studies, by fitting disordered phase SANS data to theoretical predictions. The quality of the fit is, however, considerably improved by our use of the ROL theory for $S(q)$ to fit the data, rather than the less accurate RPA or BLFH theories, and is strongly constrained by our use of perturbation theory to predict the behavior of $\chi_e(\alpha)$ for small α. The resulting estimates of $\chi_e(\alpha)$ are subjected to a very stringent test in this work because they are used here to analyze measurements of a variety of thermodynamic properties that are not used to estimate $\chi_e(\alpha)$.

Bead-spring simulations used for this purpose were cubic NPT simulations carried out at the same pressure as obtained above and used in all simulations. In order to obtain a $\chi_e(\alpha)$ estimate for each model that is reliable over the entire range of α values large enough to reach the ODT for the shortest chains of interest (*i. e.,* for $N = 16$ for models S1, S2, and S3 and $N = 64$ for model H), we included $S(q)$ data for models S1, S2, and S3 from additional simulations of chains of length $N = 12$ in the data set used for fitting to estimate $\chi_e(\alpha)$. These additional simulations of short chains are not used to measure other properties, and are therefore not reported in subsequent chapters of this work.

Fig. 4.5 shows examples of the q dependence of $S(q)$ in the disordered phase, obtained from simulations of S1-32, S1-128, S2-16, and S2-64. Each discrete point in a $S(q)$ plot (circles) corresponds to data from a family of symmetry related wavevectors that are commensurate with the simulation unit cell. The lines through the points in these plots are fits to an empirical model of the form

$$cNS^{-1}(q) \simeq F_0(qR_{g0}) + a + bq^2 + cq^4 \tag{4.3}$$

in which $F_0(qR_{g0})$ is the RPA prediction for $F(q)$, and in which a, b, and c are adjustable parameters. This empirical function is used to estimate values of peak wavenumber q^* and peak structure factor $S(q^*)$ as functions of α for each simulation system (see Fig. 4.6). The fit parameters a, b, and c have no physical relevance. As shown in plots of Fig. 4.5, the quality of the fit is extremely good for all chain lengths and α values except in the vicinity of the order-disorder transition, particularly in systems with longer chains.

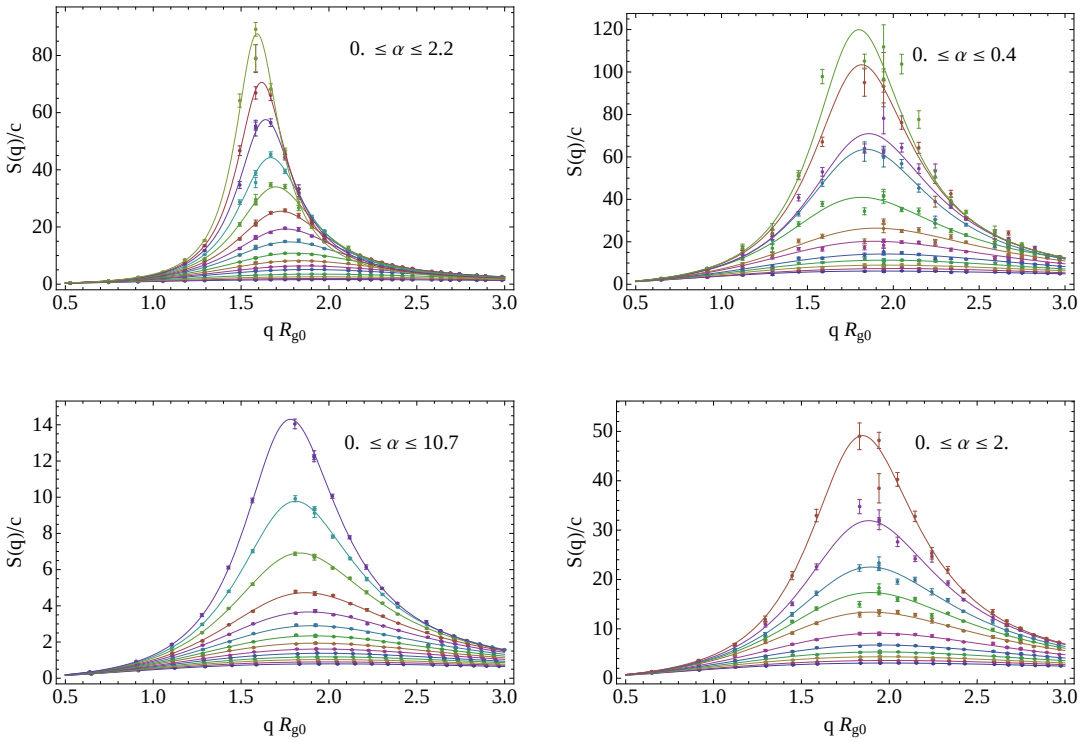

Figure 4.5: Reduced structure factor $S(q)/c$ as a function of the dimensionless wavenumber qR_{g0} of S1-32 (upper left), S1-128 (upper right), S2-16 (lower left), and S2-64 (lower right) systems, each for a range of $\alpha < \alpha_{\mathrm{ODT}}$ values. The lines through the data are fits to Eq. 4.3 obtained using data upto $qR_{g0} = 3.0$.

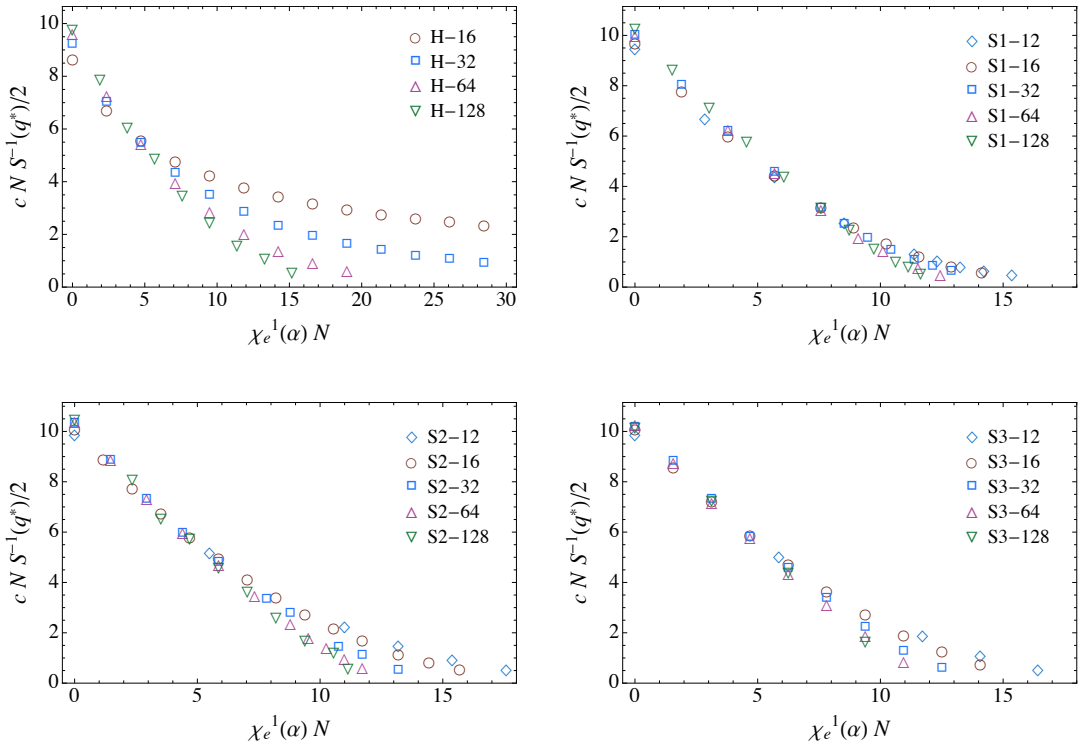

Figure 4.6: Dependence of normalized inverse peak structure factor $cNS^{-1}(q^*)/2$ on the linear approximation $\chi_e^1(\alpha)N = z_\infty\hat{\alpha}N$ of different chain lengths for models H (upper left), S1 (upper right), S2 (lower left), and S3 (lower right).

An estimate for $\chi_e(\alpha)$ for each model was obtained by a simultaneous fit of ROL theory predictions to simulation results for $cNS^{-1}(q^*)$ from several different chain lengths, using the same function for $\chi_e(\alpha)$ for all chain lengths. The fit assumed the functional form

$$\chi_e(\alpha) = \frac{z_\infty \hat{\alpha} + a_2 \hat{\alpha}^2}{1 + d_1 \hat{\alpha} + d_2 \hat{\alpha}^2} \tag{4.4}$$

for each model, where $\hat{\alpha} = \alpha / k_B T$, with $d_2 = 0$ in all models except model H. The coefficients a_2, d_1 and (for model H) d_2 are treated as fitting parameters. The use of z_∞ as the leading term in the numerator constrains the fit to agree with the results of perturbation theory.[81] The functional form for model H, for which $d_2 \neq 0$, was chosen to make $\chi_e(\alpha)$ approach a finite limit as $\alpha \to \infty$, for physical reasons that are discussed below. The form used for all other models (with $d_2 = 0$) yields a linear increase for large α. Results of the fits for models H, S1, S2, and S3 are shown in Fig. 4.7. In each plot, values of the abscissa $\chi_e(\alpha)N$ for each simulation data point have been calculated using a function $\chi_e(\alpha)$ obtained from a simultaneous least squares fit to data from all four/five chain lengths. The RPA predicts a linear function $cNS^{-1}(q^*)/2 = 10.5 - \chi_e N$, which is shown by the dashed line in each plot. Data from simulations very near the ODT, for which $cNS^{-1}(q^*)/2$ falls below a bound of 0.35 at which Eq. 2.22 yields $\xi \simeq d^*$, have been excluded from the fit to avoid data that may be corrupted by finite size effects. In any case, note that the fitting procedure is not particularly sensitive to the behavior of $S(q)$ very near the ODT, or the accuracy of the ROL theory in this regime, because the vast majority of the data used in the fit was obtained far from the ODT, where the ROL theory is most accurate and where the fit is most strongly constrained by our use of perturbation theory. Resulting values for the coefficients a_2, d_1 and (for model H) d_2 are given in Table 4.1. Plots of the resulting estimates of $\chi_e(\alpha)$ are shown in Fig. 4.8. It is clear from the figure that the linear approximation $\chi_e(\alpha) = z_\infty \hat{\alpha}$ nearly suffices for model H of chain length $N = 64$, which was the only chain length for which ODT and other properties were evaluated for this model.

Our choice of a functional form for $\chi_e(\alpha)$ in model H was motivated by the realization that, for this model, $\chi_e(\alpha)$ must approach a finite limit as $\alpha \to \infty$.

Model	z_∞	a_2	d_1	d_2
H	0.2965	2.56	8.20	2.123
S1	0.237	0.138	0.438	0
S2	0.0916	-0.00087	0.00420	0
S3	0.0977	-0.00144	0.00086	0

Table 4.1: Estimates of coefficients in Eq. 4.4 for $\chi_e(\alpha)$ for all four models, as determined by fitting simulation results.

The WCA pair potential used in this model is a truncated and shifted Lennard-Jones potential for which $V_{ij}(r) = 0$ for inter-particle distances greater than or equal to $r_c = 2^{1/6}\sigma$. In the limit $\epsilon_{ij} \to \infty$, $V_{ij}(r)$ approaches a hard sphere interaction with a hard sphere diameter r_c. In the limit $\alpha \to \infty$, pairs of A and B monomers thus experience a hard-core interaction with a hard-core diameter $r_c \simeq 1.12\sigma$, while pairs of like (AA or BB) monomers experience a WCA potential with $\epsilon = k_BT$, corresponding to an effective hard sphere diameter of approximately σ. In this limit, the model is thus expected to yield behavior similar to a model of slightly unequal hard core-diameters, for which we expect a finite, modest value χ_e. Some of our simulations of model H-16 for obtaining $S(q)$ used ϵ_{AB} up to $7k_{\rm B}T$, compared to $\epsilon_{AA} = k_{\rm B}T$, and thus may approach this limiting behavior. To allow for the resulting saturation, we chose to have a non-zero value for d_2 of model H so as to yield a finite value $\chi_e \to a_2/d_2$ as $\hat{\alpha} \to \infty$, while giving $\chi_e \simeq \chi_e^{(1)}$ for small α.

On the other hand, simulations of models S1, S2, and S3 use a much softer potential and access a range of values ($\alpha < 5$ for S1-16) in which $\alpha = \epsilon_{AB} - \epsilon_{AA}$ remains significantly smaller than $\epsilon_{AA} = 25k_{\rm B}T$ used in these models. The function $\chi_e(\alpha)$ for these models is thus expected to exhibit a nearly linear dependence on α over the relevant range of values. We thus chose to fit $\chi_e(\alpha)$ for these models to a modified form of Eq. 4.4 in which we set $d_2 = 0$ and treat a_2 and d_1 as adjustable parameters, giving a function that increases linearly for large α.

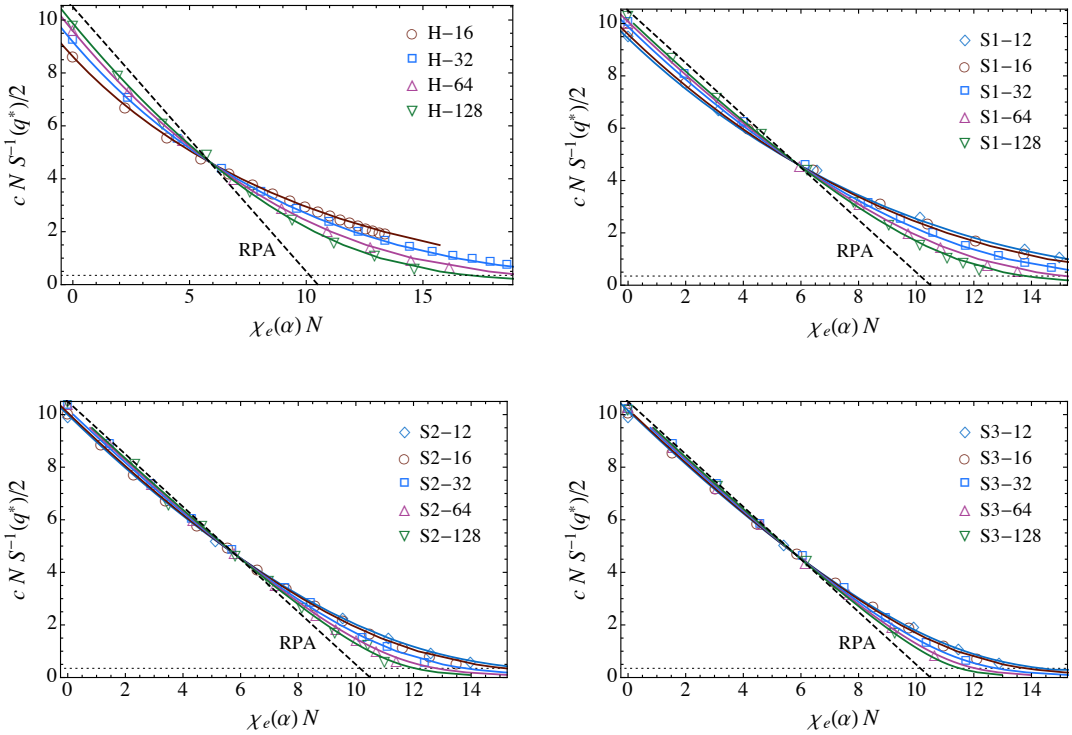

Figure 4.7: Fit of the normalized inverse peak structure factor $cNS^{-1}\left(q^*\right)/2$ to ROL theory predictions, using a single function $\chi_e(\alpha)$ for different chain lengths $N = 12, 16, 32, 64, 128$ of models H (upper left), S1 (upper right), S2 (lower left), and S3 (lower right). The horizontal dashed line at $cNS^{-1}\left(q^*\right)/2 = 0.35$ indicates the estimated onset of finite-size effects for $S^{-1}(q^*)$ and below which data points have been excluded from the fit.

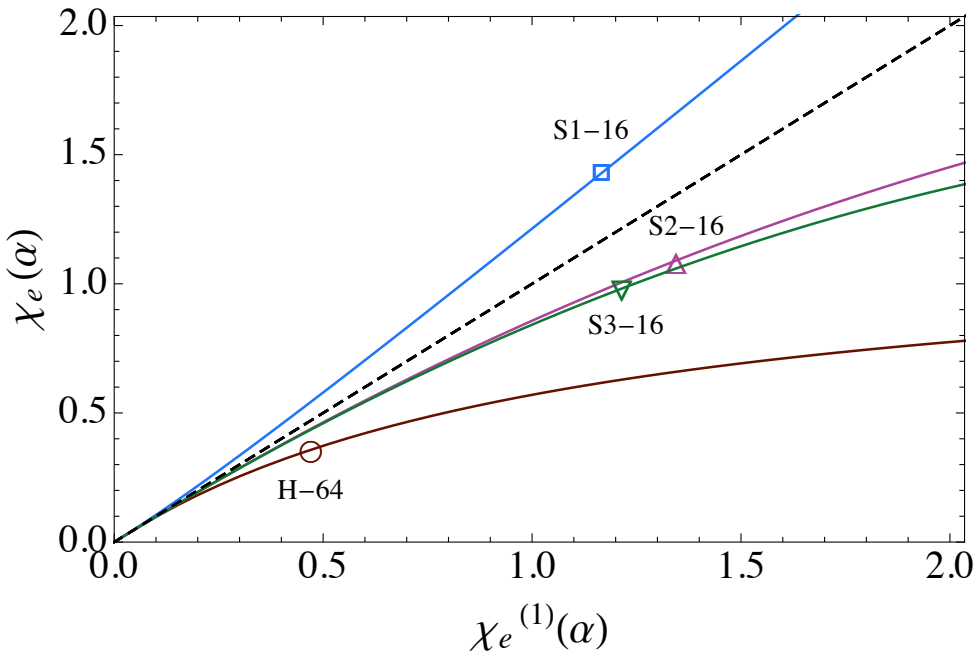

Figure 4.8: Estimates of $\chi_e(\alpha)$ obtained for the four models by fitting scattering results to the ROL theory. The symbols indicate values of χ_e at the ODT for the shortest chain length for which we have located the ODT for each model. The dashed line shows the linear approximation $\chi_e(\alpha) = \chi_e^{(1)}(\alpha)$.

4.3 Peak Wavenumber

Previous experiments[25,26,99] and simulations[48,49,67] have shown that the peak wavenumber $q^\star$ in symmetric diblock copolymer melts decreases monotonically with increasing $\chi_e N$, with a particularly fast drop near the ODT. The RPA instead predicts a constant peak wavenumber $q_0^\star$.

Fig. 4.9 shows a comparison of simulations results and ROL predictions for the fractional deviation $(q^* - q_0^*)/q_0^*$ from the RPA prediction plotted *vs.* $\chi_a^* N$ for both model H (upper panel) and model S (lower panel). In this and several subsequent plots, we plot a quantity of interest *vs.* the apparent interaction $\chi_a^* N$, rather than *vs.* an estimate of $\chi_e N$. Because $\chi_a^* N$ is a measurable quantity, which is related to the inverse peak intensity by Eq. 2.19, this approach allows us to test many theoretical predictions in a manner that does not rely on any estimate of $\chi_e(\alpha)$. Predicted values of q^* have been calculated by numerically identifying the maximum of $S(q)$ predicted by the self-consistent ROL theory at each value of $\chi_a^* N$, which is also the input parameter to the one-loop correction

$H_1(qR_g, \chi_a^* N)$ in this theory. Agreement between theoretical predictions and simulations is excellent for all four chain lengths for model S, though some statistically significant discrepancies are visible near the ODT, particularly for the shortest chain, S-16. Agreement is also good for models H-64 and H-128, which correspond to the same values of $\overline{N}$ as for S-16 and S-32, but deteriorates noticeably for H-32 and (particularly) H-16.

In the limit of very long chains, the ROL theory predicts a fractional shift in q^* that decreases asymptotically as $\overline{N}^{-1/2}$ with increasing $\overline{N}$. To show this, and as an introduction to the analysis of this shift given in section 4.4, it is useful to analyze this asymptotic behavior. The ROL prediction for q^* is given by the minimum of Eq. 2.18 for $H(q)$ with respect to normalized wavenumber $Q \equiv qR_{g0}$. If we treat H_0 and H_1 at fixed $\chi_a^* N$ as functions of Q alone, the peak wavenumber $Q^* \equiv q^* R_{g0}$ is determined by the condition

$$0 = H_0'(Q^*) + \overline{N}^{-1/2} H_1'(Q^*) \tag{4.5}$$

where prime denotes differentiation with respect to Q. Taylor expanding both functions about $Q_0^* = q_0^* R_{g0}$ to linear order in $\delta Q^* \equiv Q^* - Q_0^*$, using the fact that $H_0'(Q_0^*) = 0$, and retaining only terms of order $\overline{N}^{-1/2}$ yields a dominant correction

$$\delta Q^* \simeq -\frac{1}{\overline{N}^{1/2}} \frac{H_1'(Q_0^*)}{H_0''(Q_0^*)} \tag{4.6}$$

plus corrections of order N^{-1} and smaller. Here, H_0"(Q) denotes the second derivative of $H_0(Q)$ with respect to Q. The sign of δQ^* is determined by the sign of the derivative $H_1'(Q)$ of the deviation from the RPA.

Fig. 4.10 compares simulations results for the normalized deviation $\overline{N}^{1/2}(q^* - q_0^*)/q_0^*$, for all models except H-32 and H-16. The fact that the data from widely disparate chain lengths almost collapse in this representation shows that simulations results for $q^* - q_0^*$ do indeed scale as $\overline{N}^{-1/2}$ for sufficiently large enough $\overline{N}$. The solid line in this figure shows the ROL theory for this quantity in the limit $\overline{N} \to \infty$, which is given Eq. 4.6. For purposes of clarity, we show only the $\overline{N} \to \infty$ asymptote in this figure, because the ROL predictions for this quantity do show a weak dependence on $\overline{N}$, and would crowd the figure if included. The simulations results do not agree as well with this $\overline{N} \to \infty$ asymptote as with

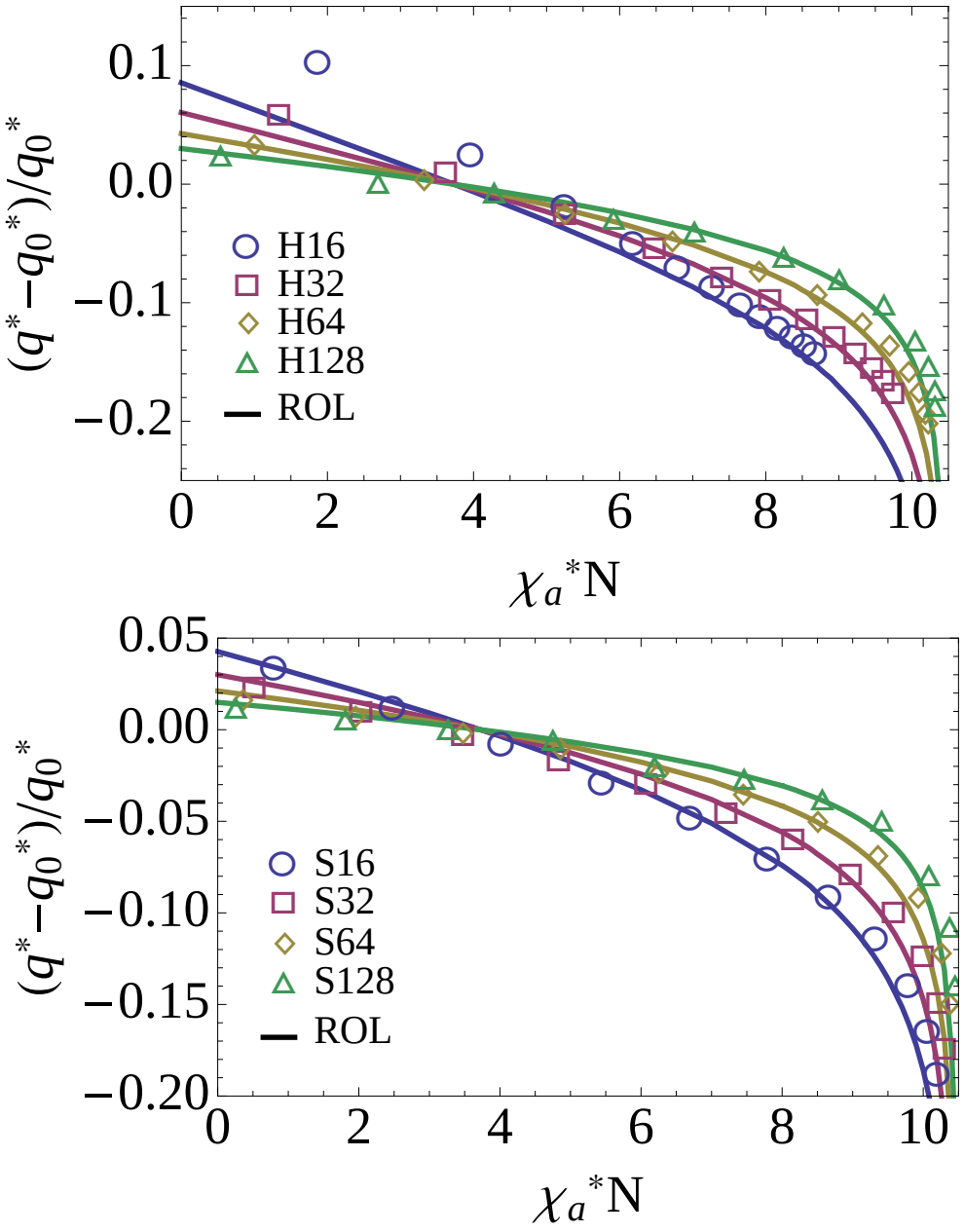

Figure 4.9: Fractional shift $(q^\star - q_0^\star)/q_0^\star$ of the peak wave number $q^\star$ *vs.* $\chi_a^\star N$, for several chain lengths in models H (upper panel) and S (lower panel). The solid curves are predictions of ROL theory.

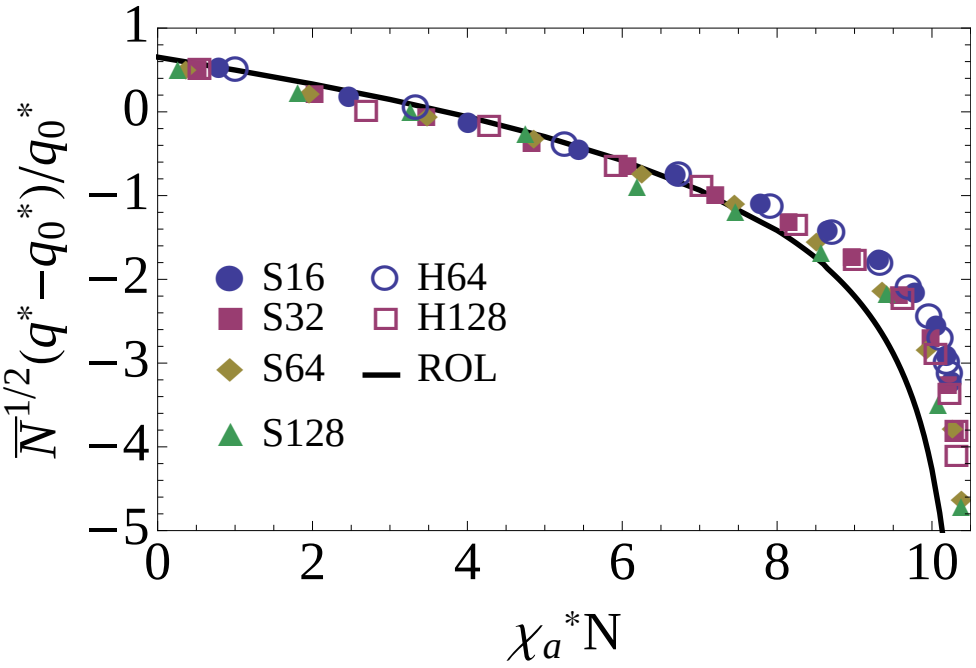

Figure 4.10: Normalized shift $\overline{N}^{1/2}(q^\star - q_0^\star)/q_0^\star$ in the scattering peak wave number *vs.* $\chi_a^\star N$, scaled by $\overline{N}^{1/2}$, for several chain lengths in model H and S. The solid curve is the asymptotic prediction of ROL theory, for infinitely long chains.

predictions of the full ROL theory, which are shown in Fig. 4.9, particularly at large values of $\chi_a^* N$. A close look at the data also reveals, however, that data from the longest chains lie closest to the predicted asymptote, consistent with the existence of slow but systematic convergence to the predicted asymptote.

4.4 Intra- and Intermolecular Contributions to $S^{-1}(q)$

The incompressible OZ equation provides a natural way of separating corrections to the RPA prediction for $S^{-1}(q^*)$ that arise directly from deviations from random walk statistics, which can be quantified by measuring $F(q)$, from more complicated collective effects, which enter via the function $\chi_a(q)$. As already noted, both $F(q)$ and $\chi_a(q)$ can be extracted directly from simulations data. By measuring $F(q)$ and $\chi_a(q)$, we gain additional insight into the physical origin

of corrections to RPA predictions for $S(q)$, and can test ROL predictions more rigorously than is possible by measuring $S(q)$ alone.

Simulations data for the quantity $H(q) = cNS^{-1}(q)$ may be expressed as a sum of three contributions

$$H(q) = H_0(q) + \delta F(q) - 2N\delta\chi_a(q) \tag{4.7}$$

in which $H_0(q) \equiv cNS_0^{-1}(q) = F_0(q) - 2\chi_e N$ is the RPA predictions, and in which

$$\begin{aligned} \delta F(q) &\equiv F(q) - F_0(q) \\ \delta\chi_a(q) &\equiv \chi_a(q) - \chi_e \quad . \end{aligned} \tag{4.8}$$

Fig. 4.11 shows the results of applying this decomposition to simulations of models H-64 and S-16, which have matched values of $\overline{N} \simeq 240$. Simulations for systems with $\alpha = \chi_e N = 0$ are shown in the upper panel and simulations of systems with nearly matched values of $\chi_e N \simeq 9.7$ are shown in the lower panel. The quantities $cNS^{-1}(q)$, $F(q)$ and $\chi_a(q)$ have been obtained directly from measurements of $S(q)$ and $\Omega_{ij}(q)$, while $cNS_0^{-1}(q)$, $F_0(q)$, and $\delta\chi_a(q)$ have been calculated using the estimates of b and $\chi_e(\alpha)$ obtained in subsection 2.2.2. Throughout this analysis, we use the nonlinear expression for $\chi_e(\alpha)$ obtained by fitting peak intensity data. In the lower panel, in which $\chi_e N \simeq 9.7$, we show the total $cNS^{-1}(q)$ (triangles), the RPA contribution $cNS_0^{-1}(q)$ (dashed line), and the corrections $\delta F(q)$ (squares) and $-2\delta\chi_a(q)N$ (circles). In the upper panel, in which $\chi_e N = 0$, we do not show $-2\delta\chi_a(q)N$ because it is known[17] that $\chi_a(q)$ and $\delta\chi_a(q)$ must vanish in this limit. (We have confirmed that simulations results for $\chi_a(q)$ are equal to zero within statistical errors). In each plot, we have also marked both the RPA peak wavenumber q_0^*, which is the minimum of $cNS_0^{-1}(q)$, and the actual peak wavenumber q^*, which is the minimum of $cNS^{-1}(q)$.

Plotting data from two different models (H-64 and S-16) with matched values $\overline{N}$ and $\chi_e N$ allows us to confirm the universality of the results. We observe very good agreement between the two models at wave numbers near q^* for all three functions $\delta F(q)$, $N\delta\chi(q)$ and $cNS^{-1}(q)$. Discrepancies between the models become noticeable at higher q, particularly in $\delta F(q)$.

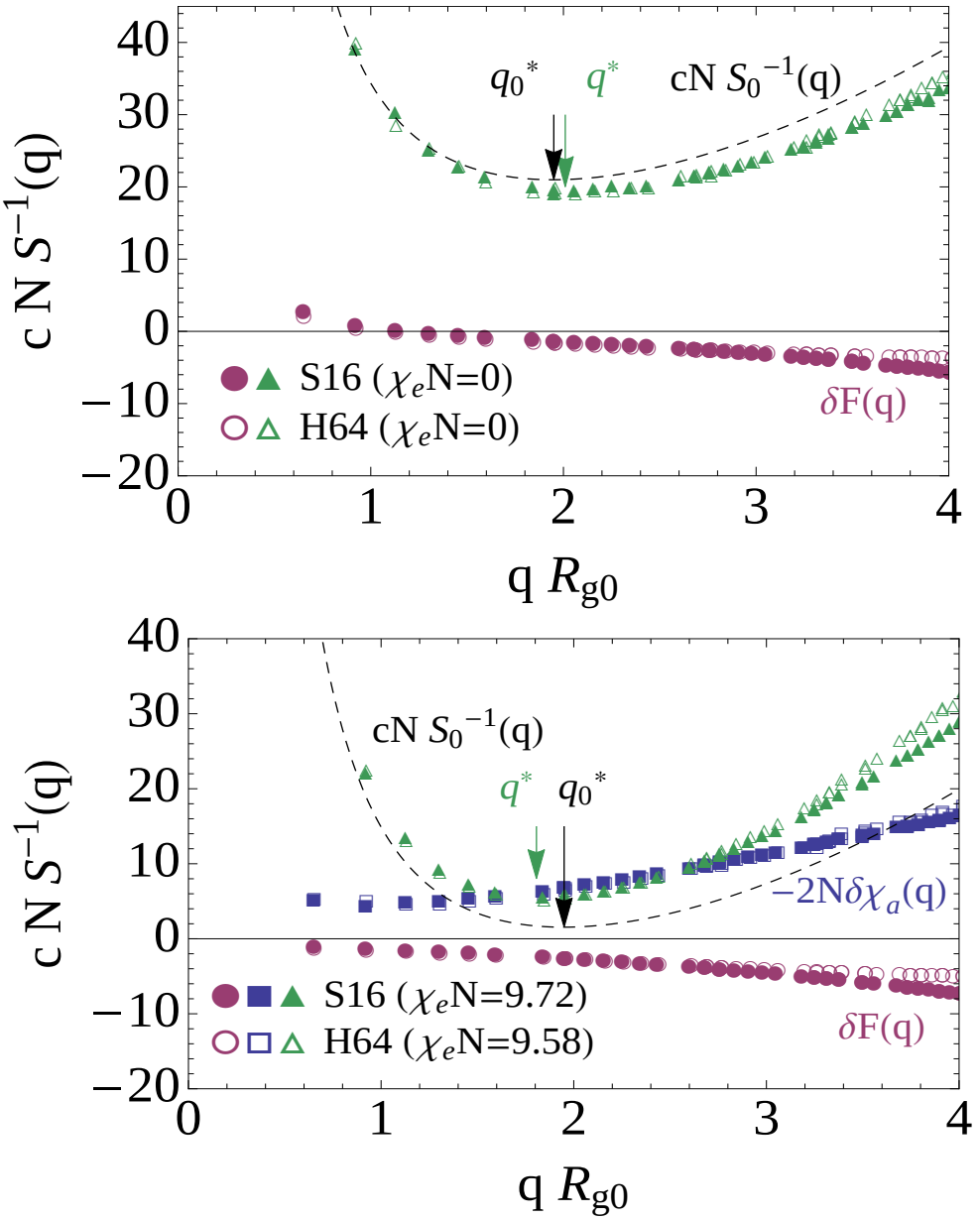

Figure 4.11: Individual contributions to the inverse structure factor $cNS^{-1}(q)$ from intra- and intermolecular correlations *vs.* qR_{g0}, at $\chi_e N = 0$ (upper) and $\chi_e N \simeq 10$ (lower). Circles represent data for the correction $\delta F(qR_g)$ to Leibler's intramolecular correlation function $F(qR_g)$, squares represent data for the correction $\delta\chi(qR_g)$ to the apparent χ-parameter χ_a. The intermolecular corrections have been obtained as described in the main text, using a value for $\chi_e(\alpha)N$ from Fig. 4.8. The dashed curve is the RPA prediction for $cNS^{-1}(qR_g)$, and its minimum $q_0^\star$ is indicated by an arrow. The peak location q^* of the actual structure factor is also indicated by an arrow. Data is shown for chains of matched value $\overline{N} \simeq 240$ in models S ($N = 16$, filled symbols) and H ($N = 64$, open symbols). The intermolecular part $\delta\chi_a(q)$ is identically zero at $\chi_e N = 0$ (not shown).

4.4.1 Physical Origin of Shift in q^*

The experimental observation of a decrease in q^* near the ODT was originally interpreted by Almdal, Rosedale and Bates[99] as being a result of change in the chain conformations from Gaussian to "stretched". The analysis of ROL predictions in Ref.[17] suggested instead that the shift in q^* is unrelated to changes in overall coil dimensions or intramolecular correlations. The physical origin of deviations from RPA predictions for both q^* and $S(q^*)$ can be clarified, without relying on a specific theory, by examining how $\delta F(q)$ and $-2N\delta\chi_a(q)$ effect the location and magnitude of the minimum in $cNS^{-1}(q)$. Contributions to $H(q)$ that increase with increasing wavenumber q near q_0^* tend to shift q^* to lower values, while contributions that decrease with increasing q tend to increase q^*, as indicated in Eq. 4.6. The relevant features are visible in the two panels of Fig. 4.11, which show typical examples of the behavior at small and large values of $\chi_e N$, respectively. In both cases, $\delta F(q)$ is negative and decreases with increasing q for $q \sim q^*$. The effect of $\delta F(q)$ alone, in the absence of $\delta\chi_a(q)$, would thus be to decrease the minimum value of $S^{-1}(q^*)$, or increase $S(q^*)$, and to increase q^*. This is the behavior that is observed for $\chi_e N = 0$, where both simulations and the ROL theory yield enhanced peak intensity $S(q^*)$ and a peak wavenumber $q^* > q_0^*$. For $\chi_e N > 0$, the contribution $-2N\delta\chi_a(q)$ is instead always a positive function that increases with increasing q for $q \sim q^*$. The effect of this contribution, by itself, would thus be to always decrease $S(q^*)$ and decrease q^*. The observed behavior of q^* and $S(q^*)$ is the result of a competition between these two contributions, which yields $q^* > q_0^*$ and enhanced values of $S(q^*)$ at low values of $\chi_e N$, where $\delta F(q)$ dominates, but $q^* < q_0^*$ and suppressed scattering (relative to the RPA) close to the ODT, where $-2N\delta\chi_a(q)$ dominates. The monotonic decrease of q^* with increasing $\chi_e N$ is a direct result of the increasing importance of the contribution $-2N\delta\chi_a(q)$ with increasing $\chi_e N$.

The physical significance of this mathematical decomposition can be made clearer by considering a hypothetical theory that attempts to modify the RPA by taking into account the fact that the chains are not random walks, but that retains the use of a local self-consistent field approximation for the intermolecular interactions. This approach naturally suggests an approximation in which the function $F(q)$ is calculated using the observed ensemble of chain conformations,

rather than a random walk approximation, but in which $\chi_a(q)$ is approximated by a q-independent parameter χ_e, as in the RPA. This approximation would predict a peak wavenumber q^* that is always greater than q_0^* and that increases with increasing $\chi_e N$ because of the increase in the absolute magnitude of $\delta F(q)$. The fact that this simple modification of the RPA gives the wrong *sign* for the dependence of q^* upon $\chi_e N$ makes it clear, we think, that attribution of the decrease in q^* to changes in single chain statistics is simply incorrect.

Previous simulations studies have compared the fractional shift in q^* to corresponding changes in the polymer radius of gyration R_g, the root-mean-squared distance R_{AB} between the A and B blocks, and the radii of gyration of individual blocks. Fried and Binder[49] were the first to show that R_g and R_{AB} increased with increasing $\chi_e N$, in qualitative agreement with the idea that the shift in q^* was the result of chain stretching. They also pointed out, however, that that fractional shift in q^* is larger than the change in R_g or R_{AB}, indicating that the association between the shift in q^* and the changes in overall chain dimensions was not quantitatively consistent. This comparison of q^* to R_g is, however, arguably not very relevant. The polymer radius of gyration is related to the behavior of $\Omega_{ij}(q)$ at very low q, in the Guinier regime. The free energy cost of a composition modulation at a nonzero wavenumber q^* of order the inverse coil size is controlled by the value of $F(q)$ at q^*. There is thus no inconsistency in our conclusion that R_g and R_{AB} increase with increasing $\chi_e N$, but that $\delta F(q)$ varies with q near q^* in a manner that (in isolation) would actually tend to increase q^*.

4.4.2 Comparison to ROL Theory Predictions

Fig. 4.12 shows a comparison of simulations results and ROL predictions for $\delta F(q)$ and $-2N\delta\chi(q)$ for models H64 and S-16 at $\chi_e N \simeq 9.7$. For both models, $q^* R_{g0} \simeq 1.8$. Agreement with the ROL theory is good, but not perfect, in the range of q in which the two simulation models give similar results.

Figs. 4.13 and 4.14 show how the values of $\delta F(q_0^*)$ and $\delta\chi_a(q_0^*)N$ at the RPA peak wavenumber q_0^* depend on $\chi_a^* N$. In both plots, these deviations are multiplied by $\overline{N}^{1/2}$ in order to approximately collapse results from different chain lengths. The ROL prediction is shown by a solid line in each of these

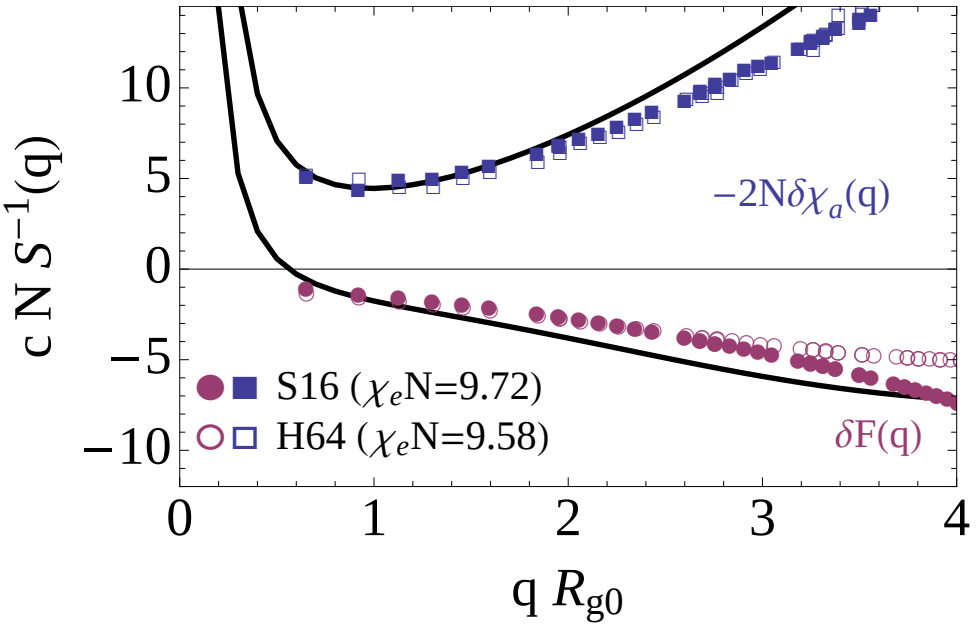

Figure 4.12: Intra- and intermolecular corrections to the RPA for $cNS^{-1}(qR_g)$ *vs.* qR_{g0}, for models H-64 and S-16 at $\chi_e N \simeq 10$ at $\overline{N} \simeq 240$. The intramolecular correction $\delta F(q)$ is indicated by circles, the intermolecular corrections $-2N\delta\chi(qR_g)$ by squares. Solid curves are ROL theory predictions for both quantities.

plots. If the self-consistent ROL theory were exact, this representation would exactly collapse the data from all chain lengths onto each other, and onto this theoretical prediction. We have chosen to plot values of both quantities at q_0^*, rather than at the true peak position q^* in order to simplify comparison with theory, but have confirmed that almost identical plots are obtained if we plot simulations results evaluated at the true peak position q^*.

Fig. 4.13 shows $\overline{N}^{1/2}\delta F(q_0^*)$ *vs.* $\chi_a^* N$ for all four chain lengths of model S and for models H-64 and H-128. The collapse of data from different chain lengths and models is quite good, confirming that the corrections are universal and that they do indeed scale as $\overline{N}^{-1/2}$. The agreement between simulations results and ROL predictions is excellent for $\chi_e N \simeq 0$, but deteriorates significantly near the ODT. Here, as in Fig. 4.10, data from the longest chains lies closest to the ROL prediction, consistent with slow convergence towards to the ROL prediction. Because both axes in this graph are measurable quantities, it provides a test of the ROL theory that does not rely on the choice of values for any adjustable parameters.

Fig. 4.14 shows corresponding plots of $-\overline{N}^{1/2}2N\delta\chi_a(q_0^*)$ *vs.* $\chi_a^* N$. The upper plot shows results for model H and the lower plot for model S, showing all four chain lengths in each case. Here, $\delta\chi_e(q^*)$ has been calculated using the estimate for $\chi_e(\alpha)$ obtained in subsection 4.2.2 by fitting peak intensity data. The collapse of the results for different chain length is excellent. Agreement between ROL predictions and simulations results is (again) good, but not perfect. Because $\delta\chi_a(q_0^*)$ is calculated by subtracting an estimate for $\chi_e(\alpha)$ from the measured $\chi_a(q_0^*)$, the comparison shown in this plot is sensitive to our estimate of $\chi_e(\alpha)$.

The agreement between ROL predictions and simulations results for $H(q^*)$ in Fig. 4.7 is noticeably better than the agreement shown in Figs. 4.13 and 4.14 for δF and $-2N\delta\chi_a$. This is possible because of a cancellation of errors: The simulations data for $-2N\delta\chi_a(q_0^*)$ lie systematically below the ROL prediction in Fig. 4.14 by an amount that is similar to the amount that data for $\delta F(q_0^*)$ lie above the ROL prediction in Fig. 4.13, yielding a smaller error for the sum of these two terms. (Note the difference in scales for different plots). This is a natural consequence of the fact that the free parameters in our model for $\chi_e(\alpha)$ were chosen so as to optimize agreement between ROL predictions and simula-

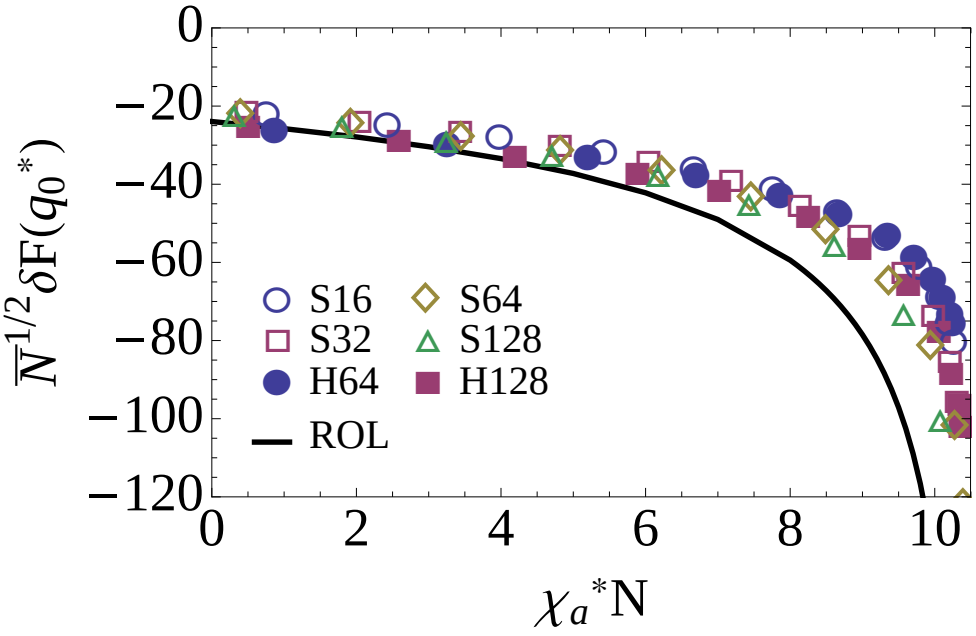

Figure 4.13: Normalized intramolecular part $cN\overline{N}^{1/2}\delta F(q_0)$ of the corrections to the RPA inverse peak scattering intensity $S^{-1}(q_0^*)$ *vs.* $\chi_a^\star N$. Shown is data for chains of length chains of length $N = 64, 128$ in model H (open symbols), and $N = 16, 32$ in model S (filled symbols), representing values of $\overline{N} \simeq 240$ (circles) and $\overline{N} \simeq 480$ (squares). The solid curve is the prediction of ROL theory.

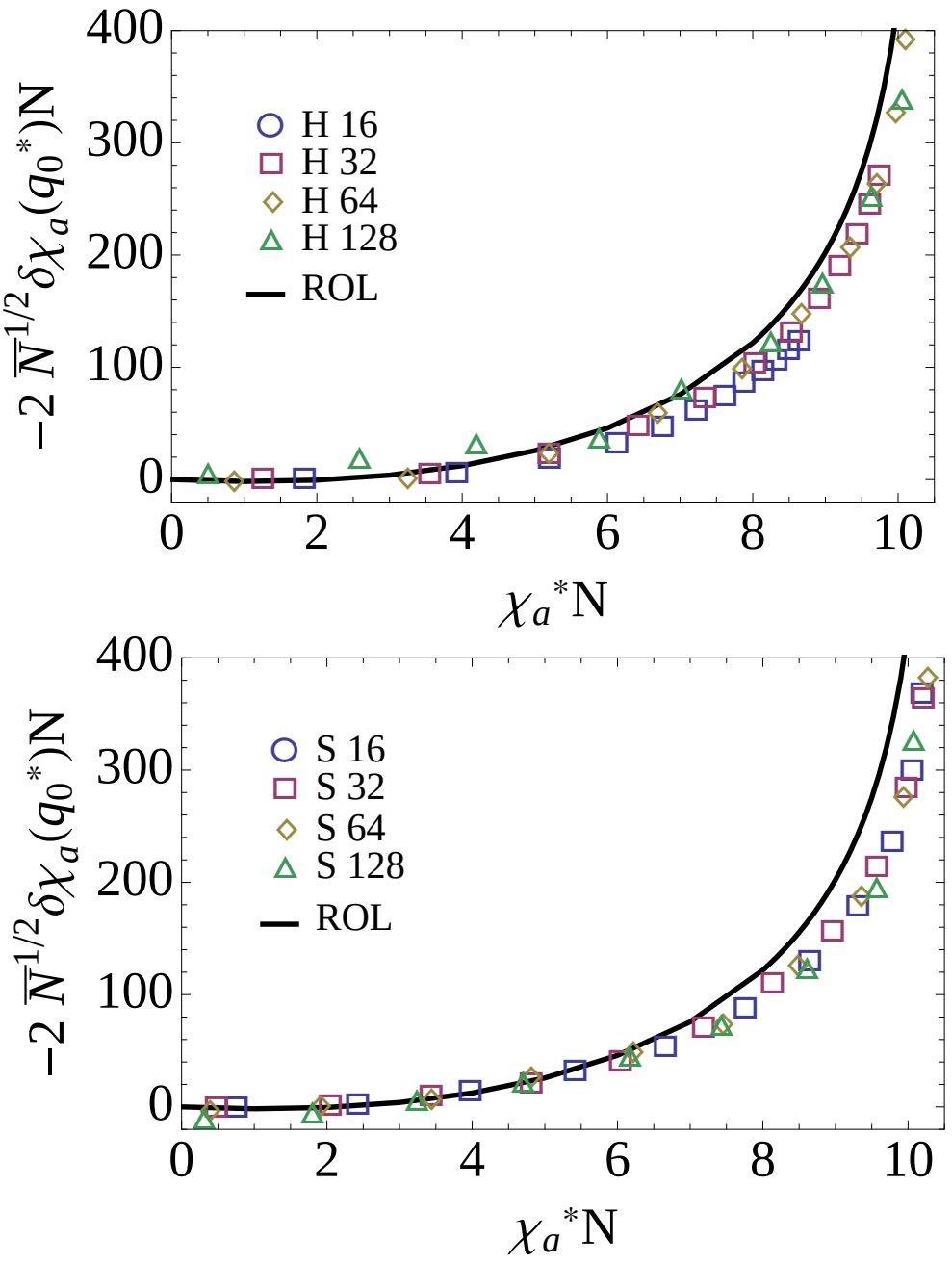

Figure 4.14: Normalized inter-molecular contribution $\overline{N}^{1/2}\delta\chi N(q_0)$ to the corrections to the RPA inverse peak scattering intensity $S^{-1}(q_0^*)$ *vs.* $\chi_a^\star N$, for model H (upper) and four different chain lengths $N = 16, 32, 64, 128$ in model S (lower). To determine $\delta\chi(q_0)N$ from $\chi_a(q_0)N$, the function $\chi_e(\alpha)$ has been used, which is plotted in Fig. 4.8.

tions data for $H(q^*)$. Because there are substantial errors in ROL predictions for $\delta F(q)$, which are unaffected by any changes in our estimate $\chi_e(\alpha)$, our procedure for fitting $\chi_e(\alpha)$ introduces compensating errors in $-2N\delta\chi_a(\alpha)$ in order optimize the fit for $H(q^*)$.

4.5 Chain and Block Radii of Gyration

Previous simulations studies[41] measured changes in the overall polymer radius of gyration R_g, the radii of gyration $R_{g,AA}$ and $R_{g,BB}$ of the A and B blocks, and the root-mean-square distance R_{AB}^2 between the centers of mass of the two blocks. For symmetric diblock copolymers, for which $R_{g,AA} = R_{g,BB}$, these quantities are related by (see Eqs. 36-38 in Ref.[17])

$$R_g^2 = R_{g,AA}^2 + R_{AB}^2/4 \tag{4.9}$$

It is known that R_g and R_{AB} increase with increasing $\chi_e N$ but that $R_{g,AA}$ shrinks. Here, we show results for R_g^2 and $R_{g,AA}^2$ in order to test the universality of the results from different models, the scaling with $\overline{N}$, and the level of agreement with ROL predictions.

Results for the chain length dependence of R_g^2 for homopolymers (or copolymers with $\alpha = 0$) have already been shown in Figs. 3.2 and 3.3, where we used this data to determine b. We found that the ROL theory accurately described the dominant $\mathcal{O}(\overline{N}^{-1/2})$ corrections to random walk behavior, but that we needed a non-universal $1/N$ correction to accurately fit the data for $R_g^2(N)$ *vs.* N for short chains, particularly for model H. This $1/N$ correction is model dependent because it arises, in part, from the effects of discrete chain structure. For example, the difference between using N (the number of beads) and $N-1$ (the number of bonds) in expressions for the mean-squared end-to-end length or squared radii of gyration would show up as a non-universal correction of $\mathcal{O}(1/N)$, with a prefactor that depends on details of discrete chain structure. We expect the most important effects of discrete chain structure to be the same in systems with zero or small but nonzero values of α. To focus attention on

more universal phenomena, we have thus chosen to plot the difference

$$\Delta R_g^2(N,\alpha) = R_g^2(N,\alpha) - R_g^2(N,0) \tag{4.10}$$

between squared radii of gyration at nonzero and zero values of α.

Fig. 4.15 shows results for the fractional change $\Delta R_g^2/R_{g0}^2$ *vs.* $\chi_a^* N$ for two pairs of simulations with matched values of $\overline{N} = 240$ (upper panel, H-64 and S-16) and $\overline{N} = 480$ (lower panel, H-128 and S-32). The collapse of the results from the two models in each pair confirms the universality of the results.

Next, we compare the data for $\Delta R_g^2(N;\alpha)$ to the ROL prediction. Because results from models H and S appear to be equivalent, we focus for this purpose on data from model S. Fig. 4.16 shows results for the normalized deviation $\overline{N}^{1/2}\Delta R_g^2/R_{g0}^2$ *vs.* $\chi_a^* N$ for all four chain lengths, N =16, 32, 64, 128, as well as the ROL prediction (solid line). If the ROL theory were exact, the data would collapse in this representation. Differences between theory and simulations data are larger for this quantity than for most others. The results for the shortest chains show qualitative differences from ROL predictions: The ROL theory predicts an essentially linear decrease with increasing $\chi_a^* N$ for $\chi_a^* N < 7$ and a rapid increase near the ODT. Simulations results from the two shortest chain lengths (N =16 and 32) show the predicted increase near the ODT, but are essentially independent of $\chi_a N$ at lower values of $\chi_a^* N$. The two longest chain lengths exhibit develop a linear decrease with $\chi_a N$ with a slope that increases with increasing N, but that remains significantly smaller than predicted.

Results for ΔR_g^2 thus do not closely approach ROL predictions over this range of chain lengths, but exhibit behavior that appears consistent with slow convergence to ROL predictions with increasing $\overline{N}$. The ROL theory is believed to yield the first correction to random walk model within an expansion in powers of $\overline{N}^{-1/2}$. In the representation used in Fig. 4.16, we thus expect the data to approach the ROL prediction as $\overline{N} \to \infty$, with differences between the one-loop theory and data for finite N that decrease as $\overline{N}^{-1/2}$ for sufficiently long chains. That is, we expect that

$$\frac{\overline{N}^{1/2}\Delta R_g^2(\alpha)}{R_{g0}^2} \simeq K_1(\chi_a^\star N) + \overline{N}^{-1/2} K_2(\chi_a^\star N) + \cdots \tag{4.11}$$

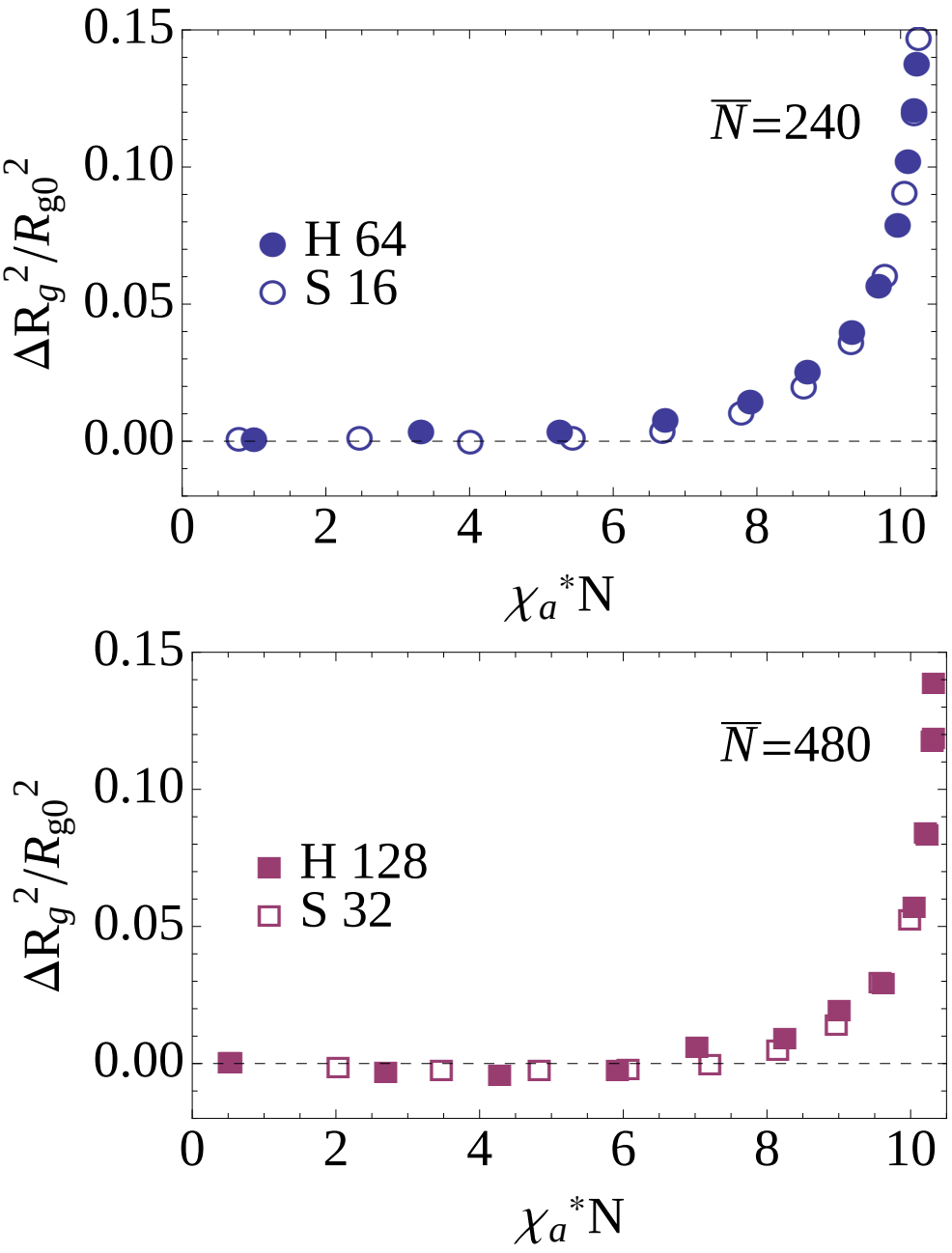

Figure 4.15: Deviation ΔR_g^2 of the squared radius of gyration at finite interaction parameter α from the value at $\alpha = 0$, normalized by the ideal radius of gyration, as a function of the $\chi_a^\star N$. Shown is data for model H (N=64, 128) and model S (N=16, 32) at two different matched values of $\overline{N} \simeq 240$ (upper) and $\overline{N} \simeq 480$ (lower).

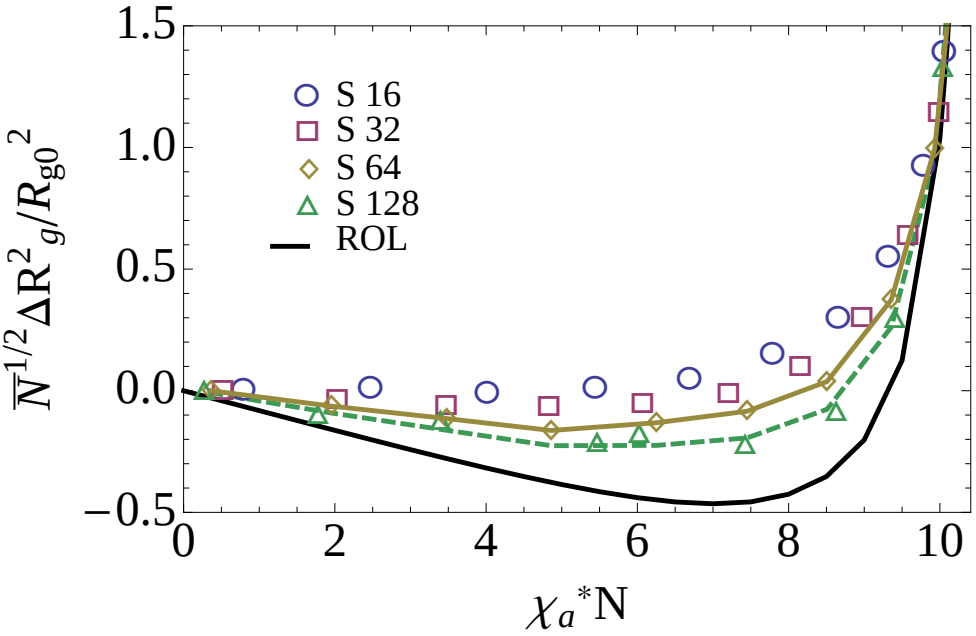

Figure 4.16: Normalized deviation $\overline{N}^{1/2}\Delta R_g^2/R_{g0}^2$ of the squared radius of gyration from its value at $\alpha = 0$, as function of $\chi_a^\star N$, for chain lengths $N = 16, 32, 64, 128$ of Model S. The top solid curve is a piecewise linear interpolation of the data for $N = 64$. The dashed curve represents the extrapolation of that curve to $N = 128$. The extrapolation is calculated from the difference between the top solid curve and the bottom solid curve representing ROL theory, assuming the asymptotic $\overline{N}^{-1/2}$-approach discussed in the main text.

where $K_1(\chi_a^\star N)$ is the ROL prediction and K_2 is a correction arising from two-loop corrections.[13,16] This pattern of convergence is clearly not valid for all of the chain lengths shown in Fig. 4.16, since it implies that the differences between subsequent values of N should decrease by factors of $1/\sqrt{2}$ when N is doubled, which is clearly not the case for the shorter chains. It does appear, however, that the data for the two longest chains lengths, S-64 and S-128, is consistent with this pattern of convergence. We have tested this as follows: We fitted a line through the data for S-64 (shown in the figure) and took the difference between this interpolation and the ROL prediction to estimate the function K_2. By multiplying this difference by $1/\sqrt{2}$ and adding it back to the ROL prediction, we obtained a prediction for the expected location of data for S-128. The resulting prediction, shown as a dashed line, is in reasonable agreement with our data. This confirms that data for these longest two chains is consistent with the hypothesized pattern of convergence to the ROL theory in the limit $\overline{N} \to \infty$.

4.5.1 R_g of Individual Blocks

Figs. 4.17 and 4.18 show results for the change in the radius of gyration $R_{g,AA}$ of the A (or B) blocks of symmetric diblock copolymer, in a form analogous to that given in Figs. 4.15 and 4.16 for the overall radius of gyration. As found in previous work, we find that the radius of gyration shrinks with increasing $\chi_e N$.

Fig. 4.17 shows a test of the universality of this quantity, in which we show results for $\Delta R^2_{g,AA}/R^2_{g0,AA}$ from simulations of models H and S with matched values of $\overline{N} = 240$ (upper panel) and $\overline{N} = 480$ (lower panel). In contrast to the nearly perfect universality found in a similar comparison for the overall radii of gyration, we find a noticeable difference between results from models H and S with matched $\overline{N}$. The difference is most obvious for the shortest chains ($\overline{N} \simeq 240$, upper panel), for which the discrepancy is about 1% at $\chi_a^* N \simeq 8$. This difference is much less for the longer chains with $\overline{N} \simeq 480$. We believe that this difference may be the result of a slight α-dependence of the statistical segment length b, which (if present) would be different for different models, but which we have ignored thus far. Because the difference is quite small, it appears to us that a discrepancy of this magnitude would have been difficult to detect

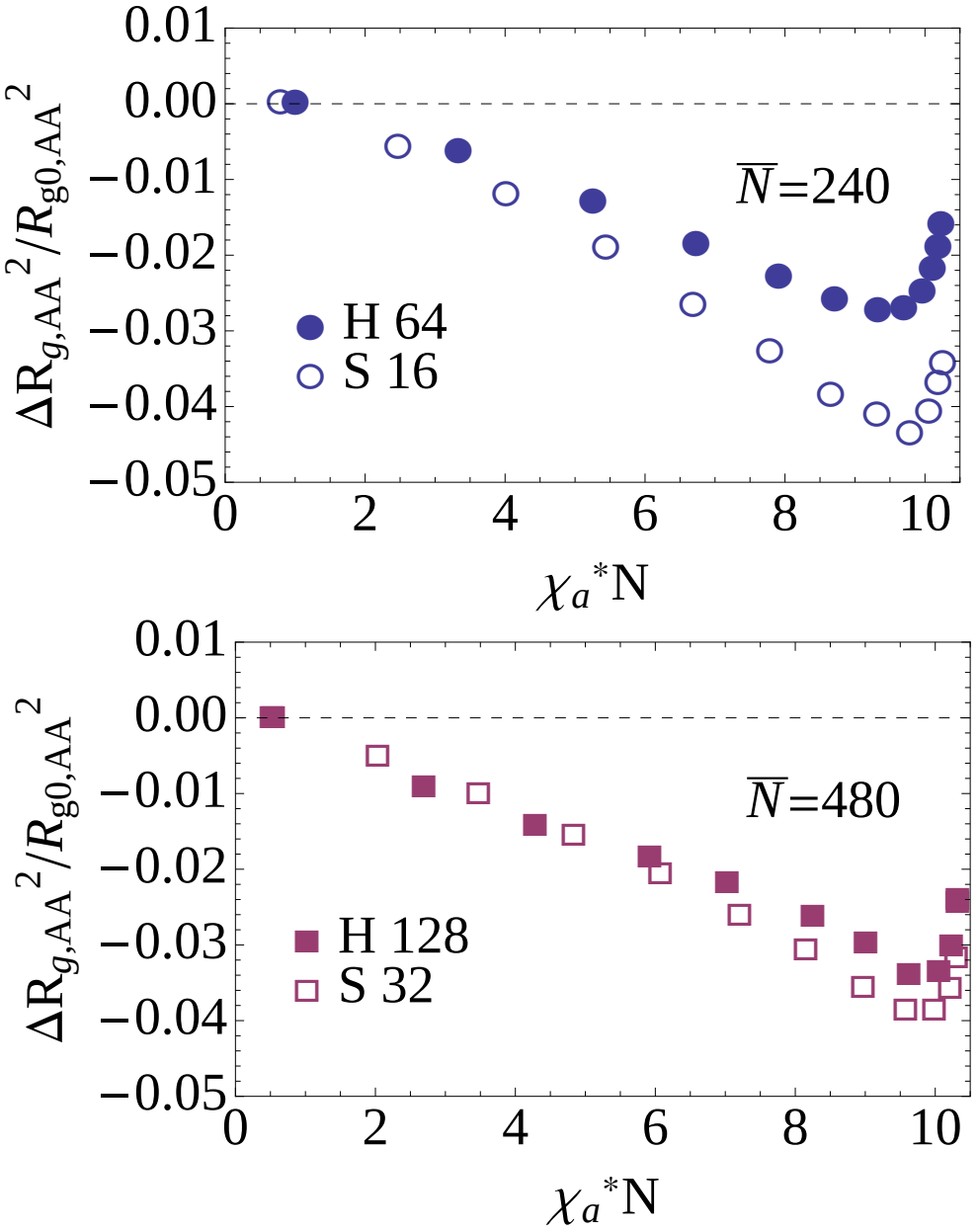

Figure 4.17: Deviation $\Delta R^2_{g,AA}$ of the squared block radius of gyration for finite α from its value at $\alpha = 0$, as a function of $\chi^\star_a N$, normalized by the ideal block radius of gyration $R_{g0,AA}$, for models H and S. Shown are data for two different matched values $\overline{N} \simeq 240$ (upper) and $\overline{N} \simeq 480$ (lower).

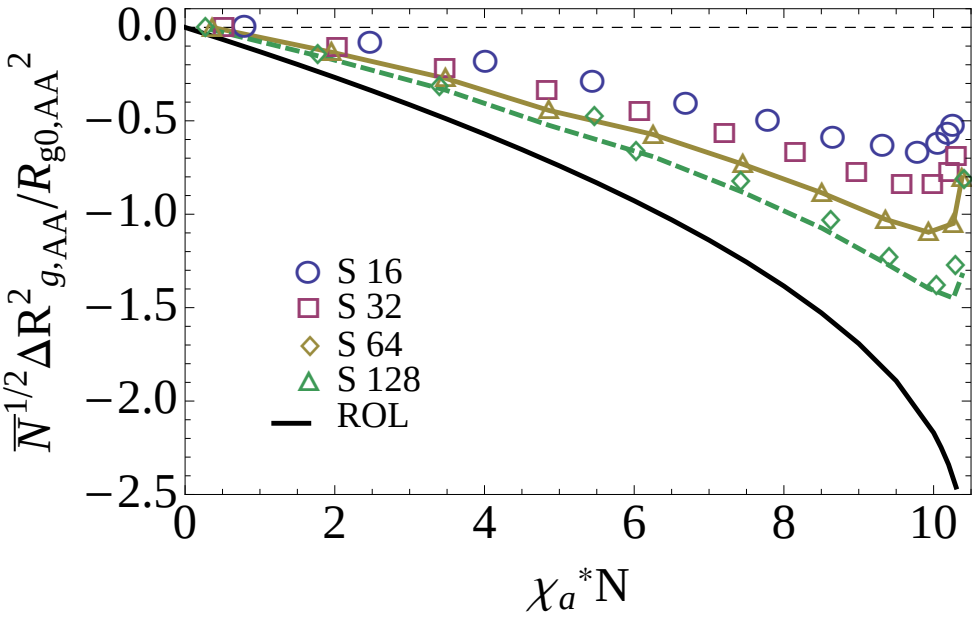

Figure 4.18: Normalized deviation $\overline{N}^{1/2}\Delta R^2_{g,AA}/R^2_{g0,AA}$ of the squared block radius of gyration $R_{g,AA}$ at finite α from its value at $\alpha = 0$, *vs.* $\chi^\star_a N$ for four different chain lengths $N = 16, 32, 64$ and 128 in model S. The top solid and the dashed curve represent a piecewise linear interpolation for $N = 64$, and an extrapolation for $N = 128$, respectively, as discussed in the main text. The bottom solid curve is the asymptotic prediction of ROL theory.

in our earlier tests of universality of data for q^* and R_g. As an example, we note that in the upper panel of Fig. 4.15, values of R_g^2 for model S (open circles) actually are slightly below those for model H (filled circles), and that a 1% increase in the value of R_g^2 for model S and $\chi_a^* N \simeq 8$ would not substantially change the apparent level of agreement in that figure. Despite this evidence of a slight non-universality, for the sake of simplicity, we have chosen not to refine the analysis given here so as to allow for an α-dependent statistical segment length for each model.

Fig. 4.18 compares simulations results for the normalized deviation $\overline{N}^{1/2}\Delta R^2_{g,AA}/R_{g0,AA}$ for all four chain lengths of model S to ROL predictions for this quantity. The relationship between the simulations results and the ROL predictions is very similar to that obtained with the overall radius of gyration: There are substantial quantitative discrepancies over the range of chain lengths studied here, but the behavior is consistent with convergence to ROL predictions in the limit $\overline{N} \to \infty$. To show this, we applied the same analysis of the relationship between

data from S-64 and S-128 as that applied to the overall radius of gyration. The solid line through the data from model S-64 is an interpolation, and the dashed line is a prediction for where we expect results for S-128 to lie based on the results for S-64. The relationship of the data from these two longest chain lengths again seems to be consistent with our hypothesis of slow convergence towards to the ROL prediction.

Simulations results for the block radii of gyration also, however, show one qualitative feature that is not described correctly by the ROL theory: All of the results for $\Delta R^2_{g,AA}$ show an upturn at large values of $\chi^*_a N$, very near the ODT, while the ROL theory predicts a monotonic decrease. The position of the resulting minimum in $\Delta R^2_{g,AA}$ *vs.* $\chi^*_a N$ moves to closer values of $\chi^*_a N$ with increasing $\overline{N}$. Much, but not all, of the data that shows this feature is in the region $10.5 - \chi^*_a N \lesssim 0.35$ where finite size effects are a potential problem. Despite this, we think that this is a real physical effect, rather than a finite size artifact, since it is an obvious, very reproducible feature that appears in systems of very short chains (*e. g.,* S-16) at somewhat lower values of $\chi^*_a N$ for which we have seen no evidence of finite size effects. The stretching of individual blocks, as well as the distance between blocks, is a generic feature of strongly segregated ordered phases in which comparatively sharp interfaces separate regions of nearly pure A or B. In this limit, individual blocks must stretch as the unit cell size increases in order to allow polymers that are tethered to interfaces at one end to uniformly fill domains of nearly pure A or B, as required by the incompressibility constraint. This is very different from the behavior found in the disordered phase farther from the ODT, which is predicted by the ROL theory, in which sufficiently long individual blocks respond very much like polymers in a poor solvent, and shrink in order to increase their self-concentration and decrease contact with monomers of the other species. We thus conjecture that this upturn reflects a crossover to a structure of more strongly segregated disordered domains in which the relationship between the block size and domain spacing begins to more closely mimic that expected in any strongly segregated structure. Whatever the origin of this phenomena, it is missed entirely by the ROL theory.

Erukhimovich and Dobrynin[100] and Barrat and Fredrickson[35] have previously

presented predictions for changes in the dimensions of polymers and individual blocks within a block copolymer melt. The calculation of Barrat and Fredrickson predicts an expansion of the radius of gyration of the chain as a whole and shrinkage of individual blocks, in qualitative agreement with those obtained from the ROL theory. This calculation is, however, based on an expression for the screened interaction that vanishes in the limit $\chi = 0$ (their eq 7 for Φ), which we believe to be incorrect. The expression used in the ROL theory (eq 77 of Ref.[14]) is the same as that obtained by Vilgis and Borsali,[101] which reduces in the limit $\chi = 0$ to the appropriate nonzero screened interaction for an incompressible homopolymer melt. It appears to us that Barrat and Fredrickson may have made an error between their eqs 6 and 7 when taking the incompressible limit of a product of matrices that become singular or divergent in this limit. The calculation of Erukhimovich and Dobrynin for both symmetric and asymmetric diblock copolymers is based on a starting point closely analogous to that of the ROL theory for single-chain properties, including the use of the expression of Vilgis and Borsali for the screened interaction (eqs 6 and 7 of Ref.[100]). The ErukhimovichDobrynin calculation, like other calculations of that era, relies, however, on several mathematical approximations that limit its intended region of validity to the immediate vicinity of the ODT. The most obvious of these is the use of a Lorentzian approximation for the integrand in all Fourier integrals that become sharply peaked around q^* near the ODT. Quantitative comparison of our predictions to those of Ref.[100] is complicated by the fact that these authors calculated corrections to the mean-squared end-to-end length of polymer and individual blocks, whereas we have calculated corresponding radii of gyration, and by the fact that these authors did not explain some aspects of the fully self-consistent version of their theory. We note, however, that the results plotted for the more straightforward perturbative version of their theory, in which the screened interaction is calculated using the RPA χ parameter (Figure 1, plot b, dashed line 1), show an increase in the size of individual blocks upon increasing χN near the RPA spinodal, in contrast to the monotonic shrinkage predicted by the analogous ROL calculation. We do not see any obvious reason for this unexpected qualitative difference but have not examined this earlier calculation in detail.

4.6 Conclusions

We have compared the results of extensive simulations of disordered symmetric diblock copolymers to predictions of the renormalized one-loop (ROL) theory. Comparison of results from two rather different models, which were designed to yield pairs of systems with matched values of $\overline{N}$, allowed us to test the universality of all results. The use of two different models and chains of up to N =128 beads also allowed us to explore a range of values of $\overline{N}$ =60-1920 that overlaps with the lower end of the experimentally relevant range.

The ROL theory is found to yield accurate predictions for all quantities that we studied above for sufficiently long chains, and remarkably accurate predictions for some of them. All of our simulations results appear to be consistent with the hypothesis that the ROL correctly predicts the dominant $\mathcal{O}(\overline{N}^{-1/2})$ corrections to the RPA in the limit $\overline{N} \to \infty$, but the rate of convergence is different for different quantities.

The ROL theory gives particularly accurate predictions for the structure factor $S(q)$ of symmetric copolymers in the limit $\alpha = 0$. In this limit, the theory is found to remain accurate even for very short chains (*e. g.,* , model H-16), if we explicitly correct for contributions that arise from local chain structure. Because $S(q)$ is entirely determined by intramolecular correlations in this limit, this success of the theory is a testimony to the accuracy of the theory of single chain correlations in dense one-component liquids, which was pioneered by Beckrich, Semenov and collaborators.[10–12]

The theory also provides very accurate predictions for the peak wavenumber $q^\star$ for all but the shortest chains. Because we use the measured "apparent" peak intensity $\chi_a^* N$ as a correlating variable for this purpose, our analysis of the behavior of $q^\star$ does not involve any fitting parameters.

To test ROL predictions for the dependence of the peak intensity $S(q^\star)$ upon the RPA interaction parameter $\chi_e(\alpha)$, however, we needed to estimate or fit the function $\chi_e(\alpha)$. The linear approximation $\chi_e^{(1)}(\alpha)$ was found to be adequate for the longest chains studied here, but inadequate for the range of α used in simulations of short chains. It has been shown here, however, that the ROL theory can be brought into excellent agreement with data from both models, even for short chains, by using the nonlinear function $\chi_e(\alpha)$ obtained in section

3.2.4. As described in chapter 2, Model H yields a strongly nonlinear function $\chi_e(\alpha)$ that exhibits saturation at large values of α, for reasons that are well-understood.

The physical origins of corrections to RPA predictions for $q^\star$ and $S(q^\star)$ have been clarified by separating intra- and intermolecular contributions to $cNS^{-1}(q)$. We discussed a simple modification of the RPA in which changes in single-chain correlations are taken into account by using the measured single-chain correlation functions to calculate Leibler's function $F(q)$, rather than random-walk statistics, but in which we retain the RPA treatment of χ as a wavenumber independent parameter. It was shown that the resulting approximation would actually predict an increase in q^*. The observed decrease in q^* with increasing $\chi_e N$ is instead a result of the wavenumber dependence of the apparent interaction parameter $\chi_a(q)$ predicted by the ROL theory. We thus conclude the observed shift in q^* is not a direct result of changes in single-chain statistics or overall coil size.

Predictions for a variety of single-chain properties, including radii of gyration of chains and blocks and $F(q_0^*)$, show behavior that appears to be consistent with convergence towards ROL predictions as $\overline{N} \to \infty$, but with slower convergence than seen for other quantities. As reported in earlier simulations, the radii of gyration of individual blocks shrink with increasing $\chi_e N$ over most of the range of parameters that we studied. Interestingly, however, we also see evidence of an increase of the block radii of gyration with increasing $\chi_e N$ very close to the ODT. Because this behavior occurs in a region where finite size effects are a potential problem, further study using larger systems would be useful, but we suspect that this qualitative observation is robust. We conjecture that this represents a crossover to a strongly-segregated disordered regime in which the relationship between the block radii and the domain size becomes similar to that found in ordered phases. This is the only phenomena observed in our simulations that was not reasonably well described by the ROL theory, and suggests a possible breakdown of the theory very near the transition in systems of relatively short chains.

Chapter 5

Identification of Order-Disorder Transition

This chapter presents the well-tempered metadynamics method method we implemented for obtaining accurate ODT estimates α_{ODT} in our simulations. Briefly, the method involves obtaining the system's free energy G as a function of an appropriate collective bias potential Ψ, and subsequently, identifying ODT as the state at which free energy of disordered and ordered phases are equal. This method was developed by Dr. Jens Glaser, a post-doc in Prof. Morse's group. A more elaborate discussion of the method will be presented in a separate publication authored by him.

5.1 Introduction

Metadynamics (MetaD) is an adaptive biasing technique that is used to obtain the free energy surface of a system in particle-based simulations. Since the MetaD algorithm is well documented in literature,[102,103] we only summarize the main ideas and the implementation details for use in diblock copolymer systems here. Like other adaptive techniques, MetaD uses a bias potential $V(\Psi)$ that evolves during the simulation in a manner that is designed to discourage the system from revisiting the states it has already visited during the course of a simulation, and therefore, to increase the rate of otherwise rare transitions between different macroscopic states, or different regions of configuration space in

Ψ. It does so by filling the unknown free energy landscape $G(\Psi)$ with 'computational sand', *i. e.,* by constructing a bias potential $V(\Psi)$ from deposition of small Gaussian hills centered in all the points in configuration space the system visits during the course of a simulation. Accordingly, if a new Gaussian hill is deposited at every time interval t', the bias potential $V(\Psi, t)$ at time t is given by

$$V(\Psi, t) = \sum_{\substack{t' < t \\ t'=0, \tau_G, 2\tau_G, ..., }} w e^{-\frac{(\Psi - \Psi(t'))^2}{2\sigma^2}} \tag{5.1}$$

Here, parameters w and σ denote the height and width of the deposited Gaussian hills, and have dimensions of energy and parameter Ψ, respectively. The parameters, bias deposition rate w/τ_G and σ must be optimized because they determine the accuracy and efficiency of the resulting free energy surface (FES). The free energy surface (FES) is reconstructed up to a constant by taking the negative of the bias potential $G(\Psi) = -V(\Psi) + C$ accumulated up to a certain time t_{total} of the simulation. For diblock copolymer systems studied here, simulations of about 10^8 time steps were typically required to obtain a reliable estimate of the complete free energy surface.

The bias potential $V(\Psi)$ in MetaD is chosen to depend on an arbitrary, but physically meaningful parameter(s) Ψ known as collective variable(s). A collective variable can be any explicit function of the bead positions $\mathbf{r}_i$. Since forces on the particles resulting from the bias potential $V(\Psi)$ need to be calculated in a MetaD simulation, an appropriate collective variable Ψ for order-disorder transition would be any differentiable function of the bead positions that yields easily distinguishable values in ordered and disordered states. Therefore, in what follows, we simply refer to the collective variable as order parameter. In section 5.2, we present our choice for order parameter definition. MetaD, in contrast to the popularly used Umbrella sampling method, allows for an adaptive bias potential instead of a fixed umbrella sampling window, and thus does not require a manual choice of window parameters and subsequent 'stitching together' of histograms. The power of the method comes at the cost of having to optimize several parameters, such as the height and width of the Gaussians used to fill the free energy landscape, as well as the filling speed, in order to improve the speed of convergence towards the equilibrium free energy surface.

For instance, by choosing a too high deposition rate, the method becomes less sensitive to small features in the free energy landscape, and the system is not allowed to equilibrate between subsequent updates of the bias potential. Conversely, by choosing a too low rate, an equilibrated free energy surface may not be achieved during the course of a simulation.

WTMetaD[103] is a flavor of metadynamics that largely solves these convergence issues by decreasing the bias deposition rate $\propto 1/t$ with simulation time. This is achieved by exponentially scaling the height of added Gaussians as a function of the accumulated bias at a given point of the free energy surface. It is given by $we^{-\frac{V(\Psi,t)}{\Delta T}}$), where ΔT is a parameter of dimension temperature ($k_{\mathrm{B}} = 1$). Generally speaking, $\Delta T = 0$ corresponds to an unbiased simulation, whereas $\Delta T \to \infty$ corresponds to standard MetaD, which does not guarantee the asymptotic convergence of deposited bias $V(\Psi)$ with the FES $-G(\Psi)$. In contrast, WTMetaD uses intermediate values of ΔT, which guarantee the existence of a unique free energy surface to which the simulation converges asymptotically in finite time, up to a constant logarithmically divergent in time. Moreover, because the height is continuously rescaled, the final FES in WTMetaD depends to a lesser extent on the bias deposition rate than in standard MetaD, thus reducing the impact of an improper choice of this parameter. The method can be further improved by allowing the Gaussian width to adapt to the local free energy surface, which would help speed up the sampling and improve the degree of smoothing of the final FES.[104] Accordingly, in our implementation of the WTMetaD algorithm, the Gaussian width is adaptively selected according to the variance of order parameter fluctuations at a given point of the free energy surface, *i. e.,* $\sigma^2 \equiv \delta\Psi^2$. Lastly, we applied multiple-walker[105] simulations for the larger systems of chains of length 64 and 128 (typically using 12 walkers), in which weakly-coupled replicas of the system were run simultaneously to construct a common bias potential, that was accumulated by summing up the Gaussian contributions from the participating walkers.

5.2 Multi-mode Order Parameter

The key in the design of the metadynamics algorithm is to choose an appropriate collective variable Ψ. An appropriate collective variable Ψ for the order-disorder transition can be any differentiable function of the bead positions that yields easily distinguishable values in ordered and disordered states. To address the problem of multiple modes, *i. e.,* wave-vectors $\mathbf{q}$ that are commensurable with the simulation box (even in NPT simulations), we chose to implement a continuously differentiable multi-mode order parameter that computes the sum of higher powers ($n = 4$) of the composition mode amplitudes over all reciprocal-lattice vectors up to the highest wave number implied by the spatial discretization. The procedure to compute the order parameter and the resulting forces on the particles in every time step of the simulation is as follows. First, particle positions are assigned to the real-space grid of the composition field, and are weighted with a mode amplitude a_j specific to the particle species ($a_A = -a_B = 1$). We use a particle-mesh technique similar to those used in electrostatics calculations for Molecular Dynamics simulations [e.g. in particle-particle particle-mesh (PPPM) implementations]. Subsequently, the real-space grid is transformed into a reciprocal space grid using a fast Fourier transform (FFT) and multiplied with a local low-pass filter. After that, the filtered grid is back-transformed into real-space using the inverse FFT, and from this the forces on the particles are computed, which involves the derivative of the particle-assignment functions. The entire scheme is exact in the sense that the calculated forces are exactly those that correspond to the bias potential, *i. e.,* the algorithm is energy-conserving in NVE simulations (at fixed bias potential).

5.2.1 Definition

Although the order parameter allows for any physically meaningful definition that distinguishes between the states of interest, we chose to minimize discretization artifacts, *i. e.,* aliasing and loss of translational invariance, by employing a higher-order accurate particle-mesh interpolation scheme. Particles of species j are interpolated onto the density grid $\rho(\mathbf{r})$ using the triangular-shaped cloud (TSC) assignment function with a continuous second derivative,[106] according to

the prescription

$$\rho_j(\mathbf{r}) \equiv \sum_{\substack{i=1 \\ \mathrm{t_i}=j}}^{N} \tilde{W}(\mathbf{r}-\mathbf{r}_i), \tag{5.2}$$

where $\mathbf{r} = (iH_x, jH_y, kH_z)$ is a grid position with $H_i = L_i/n_x$ being the cell dimensions for a grid of n_i cells across every edge of length L_i in an orthorhombic simulation box, $\mathbf{r}_i$ are the (off-lattice) particle coordinates. The particle types in Eq. (5.2) are $t_i \in A, B$ and determine the mode amplitudes a_j, which in turn multiply the particle densities $\rho_j(\mathbf{r})$ to give the composition field

$$\psi(\mathbf{r}) \equiv \rho_{\mathrm{A}}(\mathbf{r}) - \rho_{\mathrm{B}}(\mathbf{r}). \tag{5.3}$$

In an analogous electrostatics calculation, the mode amplitudes a_j would represent the particle charges. The particle-mesh assignment function

$$\tilde{W}(\mathbf{r}-\mathbf{r}_i) \equiv W\left(\frac{x-x_i}{H_x}\right) W\left(\frac{y-y_i}{H_y}\right) W\left(\frac{z-z_i}{H_z}\right) \tag{5.4}$$

is a product of independent interpolation functions for every spatial direction $i = x, y, z$,

$$W_i(\tilde{x}) = \begin{cases} \frac{3}{4} - \tilde{x}^2 & |x| \leq 1/2 \\ \frac{1}{2}\left(\frac{3}{2} - |\tilde{x}|\right)^2 & \frac{1}{2} \leq |\tilde{x}| \leq \frac{3}{2} \\ 0 & \text{otherwise} \end{cases}. \tag{5.5}$$

The numerical interpolation of the particle positions onto the three-dimensional composition grid $\psi(\mathbf{r})$ requires a neighborhood (stencil) computation for every grid cell, taking into account particles up to $3/2H_i$ away from the cell center in every direction H_i. The reciprocal space $\Psi(\mathbf{q})$ is calculated numerically using a fast Fourier transform (FFT), according to

$$\psi(\mathbf{q}) \equiv \sum_{\substack{\mathbf{r}= \\ (iH_x, jH_y, kH_z)}} \psi(\mathbf{r}) e^{i\mathbf{q}\cdot\mathbf{r}}. \tag{5.6}$$

The composition mode amplitudes $\psi(\mathbf{q})$ on the reciprocal lattice are then used to define the order parameter as the sum of absolute magnitudes of those amplitudes, raised to the power n and weighted with a kernel function $f(q)$ that is

used to cut off wave numbers larger than a critical wave number q_{cut}.

$$\Psi^n \equiv \frac{1}{2N^n} \sum_{\substack{\mathbf{q}= \\ 2\pi\left(\frac{l}{L_x},\frac{m}{L_y},\frac{n}{L_z}\right)}} \left|\psi(\mathbf{q})\right|^n f\left(\frac{q}{q_{\mathrm{cut}}}\right) \tag{5.7}$$

The order parameter Ψ^n is normalized such that it is of order unity in an ordered (lamellar) phase, whereas it approaches zero with increasing system size in a disordered configuration. The rationale for the high wavenumber cut-off q_{cut} is to suppress short-wavelength fluctuations on scales shorter than the length scale of interest, *i. e.,* the domain spacing $d^\star$, or conversely, of modes with $q \gtrsim q^\star$. The precise form of the cut-off function $f(q)$ was chosen as an analytic function to avoid artifacts, but nevertheless one with a well-defined shoulder. We chose a modified Fermi function

$$f(x) = \left\{1 + \exp\left[12\,(x-1)\right]\right\}^{-1}, \tag{5.8}$$

that is implemented numerically as a multiplication of the reciprocal grid with a local function. The choice of the power n is dictated by the desire for a continuously differentiable order parameter with moderate sensitivity on the microscopic configuration, to be able to integrate the equations of motion with a sufficiently large time step, while still providing good signal to noise ratio between ordered and disordered configurations. The first requirement implies small values of n (e.g. $n = 2$). The latter requirement would be optimally fulfilled in the limit $n = \infty$ of a discontinuous order parameter, which in this limit would become the maximum norm over all mode amplitudes. Such an order parameter is often used for non-biased simulations. It was found empirically that choosing $n = 4$ provides a better order parameter than $n = 2$. Finally, the order parameter in Fig. 5.2 in which we show the constrained free energy is the n-th root $(\Psi^n)^{1/n}$. The reason for not using Ψ directly in a metadynamics simulation is to avoid a possibly divergent force on the particles for order parameter values close to zero.

5.2.2 Derivative with Respect to Particle Coordinates

In a metadynamics simulation, forces are computed from the order parameter to bias the simulation according to

$$\mathbf{f}_i = -\frac{\mathrm{d}V}{\mathrm{d}\Psi^4}\frac{\partial \Psi^4}{\partial \mathbf{r}_i} \tag{5.9}$$

Below, an expression is obtained for the order parameter derivative with respect to particle positions, and its numerical implementation is outlined. First, we calculate the derivative of the implicitly $\mathbf{r}_i$-dependent quantity $\psi(\mathbf{q})$ appearing in a single term of the reciprocal-space sum in Eq. (5.7),

$$\begin{aligned}
\frac{\partial}{\partial \mathbf{r}_i}\left|\psi\right|^4 &= 2\left[\left(\frac{\partial}{\partial \mathbf{r}_i}\psi^\star\right)\psi + \left(\frac{\partial}{\partial \mathbf{r}_i}\psi\right)\psi^\star\right]\left|\psi\right|^2 && (5.10)\\
&= 4\left(\mathrm{Re}\,\psi\frac{\partial}{\partial \mathbf{r}_i}\psi^\star\right)\left|\psi\right|^2 && (5.11)\\
&= 4\mathrm{Re}\left|\psi\right|^2\psi\frac{\partial}{\partial \mathbf{r}_i}\psi^\star(\mathbf{q}) && (5.12)\\
&= 4\mathrm{Re}\left|\psi\right|^2\psi\sum_{\mathbf{r}} e^{-i\mathbf{q}\cdot\mathbf{r}}\sum_j a_{t_i}\frac{\partial}{\partial \mathbf{r}_i}\tilde{W}(\mathbf{r}-\mathbf{r}_j) && (5.13)\\
&= 4\mathrm{Re}\left|\psi\right|^2\psi\sum_{\mathbf{r}} e^{-i\mathbf{q}\cdot\mathbf{r}} a_{t_i}\frac{\partial}{\partial \mathbf{r}_i}\tilde{W}(\mathbf{r}-\mathbf{r}_i). && (5.14)
\end{aligned}$$

By combining Eqs. 5.7 and 5.14 and changing the order of summation, it follows

$$\begin{aligned}
\frac{\partial \Psi^4}{\partial \mathbf{r}_i} &= \frac{2a_{t_i}}{N}\mathrm{Re}\sum_{\substack{\mathbf{r}\\ |r_j - r_{i,j}| \\ \leq \frac{3}{2}H_j}}\frac{\partial}{\partial \mathbf{r}_i}\tilde{W}(\mathbf{r}-\mathbf{r}_i)\\
&\qquad \sum_{\mathbf{q}}\left|\psi\right|^2\psi e^{-i\mathbf{q}\cdot\mathbf{r}} f\left(\frac{q}{q_{\mathrm{cut}}}\right). && (5.15)
\end{aligned}$$

The inner summation in Eq. 5.15 is computed numerically as an inverse FFT of the smoothed composition field on the reciprocal lattice [computed in Eq. (5.6)], and the outer sum is implemented as a stencil computation taking into neighbors inside a radius of one cell around the cell holding particle i. The expression involves partial derivatives of the product $\tilde{W}$ of grid interpolation functions with respect to the normalized particle coordinates $\tilde{r}_i = r_i/H_i$.

5.2.3 Virial

In constant-pressure (NPT) simulations, the bias potential contribution to the pressure tensor has to be calculated as well. For an additional potential $V(\Psi)$ applied to a system with a box shape matrix $h_{\alpha\beta}$, this contribution can be computed analogously to the particle forces, by using the chain rule. We start from the general expression for the virial contribution $\Pi_{\alpha\gamma}$ given in Ref. (Nosé Klein) [Eq.(A7)],

$$-\frac{\partial V}{\partial h_{\alpha\beta}} = \sum_{\gamma} \Pi_{\alpha\gamma} (\det h) h^{-1}_{\beta\gamma}, \tag{5.16}$$

where $\det \mathbf{h}$ is the system volume, and h^{-1} the inverse of the box shape matrix. According to the chain rule, the derivative on the LHS of Eq. 5.16 can be expressed as

$$\frac{\partial V}{\partial h_{\alpha\beta}} = \frac{\mathrm{d}V}{\mathrm{d}\Psi^4} \frac{\partial \Psi^4}{\partial h_{\alpha\beta}} \tag{5.17}$$

By expressing coordinates occurring in the order parameter Ψ^4 as scaled coordinates $s_\alpha = h^{-1}_{\alpha\beta} r_\beta$, and by expressing reciprocal lattice vectors in terms of the inverse of the box shape matrix, $q_\alpha = 2\pi \sum_\gamma m_\gamma h^{-1}_{\gamma\alpha}$ ($m_\gamma \in \mathbb{Z}$), it can be shown that terms of the form $\mathbf{q} \cdot \mathbf{r}$ and scaled arguments $\tilde{\mathbf{r}}_i - \tilde{\mathbf{r}}$ to the interpolation function $\tilde{W}$ do not contribute to the derivative $\partial\Psi^4/\partial h_{\alpha\beta}$. On the other hand, we note that [according to Eq. 5.8]

$$\frac{\partial f}{\partial h_{\alpha\beta}}\Big|_{x=\frac{q}{q_{\mathrm{cut}}}} = \frac{-1}{2 q_{\mathrm{cut}} q} f^2 \left(\frac{q}{q_{\mathrm{cut}}}\right) \left(\frac{1}{f}\right)' \Big|_{x=\frac{q}{q_{\mathrm{cut}}}} \frac{\partial q^2}{\partial h_{\alpha\beta}}, \tag{5.18}$$

the only virial contribution arises from the low-pass filter $f(x)$. Furthermore,

$$\begin{aligned} \frac{\partial q^2}{\partial h_{\alpha\beta}} &= 2 \sum_{\delta} \frac{\partial q_\delta}{\partial h_{\alpha\beta}} q_\delta & (5.19)\\ &= -8\pi^2 \sum_{\gamma\delta\eta} m_\gamma m_\eta h^{-1}_{\gamma\alpha} h^{-1}_{\beta\delta} h_{\eta\delta} & (5.20)\\ &= -2 \sum_{\delta} q_\alpha q_\delta h^{-1}_{\beta\delta}, & (5.21) \end{aligned}$$

where in Eq. 5.20 we used

$$\frac{\partial h^{-1}_{\mu\nu}}{\partial h_{\alpha\beta}} = -h^{-1}_{\mu\alpha} h^{-1}_{\beta\nu}, \tag{5.22}$$

and, taking Eqs. 5.16,5.17, 5.18 & 5.21 together, one finds

$$(\det \mathbf{h})\Pi_{\alpha\beta} = -\sum_{\gamma} h_{\beta\gamma} \frac{\partial V}{\partial h_{\alpha\gamma}} \tag{5.23}$$

$$= -\frac{\partial V}{\partial \psi^4} \frac{1}{N^4} \sum_{\mathbf{q}} \left|\psi\right|^4 f^2 \frac{q_\alpha q_\beta}{q q_{\mathrm{cut}}} \left(\frac{1}{f}\right)', \tag{5.24}$$

an expression that can be computed numerically using the smoothed reciprocal-space grid as an input.

5.3 Choice of Metadynamics Parameters

For the cut-off function $f(q)$ in Eq. 5.7, we chose a system-dependent value for q_{cut} that is approximately $1-5\%$ larger than our best estimate for the true equilibrium wavenumber $q^\star$ in the ordered phase at the approximate ODT location α_{ODT} obtained from a tetragonal NPT simulation. Moreover, the grid discretization was chosen to maximize the spatial resolution, while keeping the simulation efficiency within reasonable bounds. We found that a value of $n_x = n_y = n_z = 16$ was sufficient to resolve lamellar phases of three domains across, which corresponds to the system size for which ODTs were determined for all our systems, and occasionally used values of 32 or 64 to verify the absence of dominant finite sizes effects. It was confirmed that with these parameter choices we could distinguish between disordered and spontaneously ordered configurations, as well as artificially induce ordered configurations using Umbrella sampling with a fixed harmonic bias potential.

The improvement in convergence in WTMetaD relative to standard MetaD comes at a cost, in that the way the free energy surface is reconstructed is changed from standard MetaD, and several different estimators have been proposed to extract an optimally converged free energy surface. We used three different estimators, including the original one from Ref.,[103] and the improved

estimators proposed in Refs.[104] and,[107] and accepted simulation results only when the free-energy difference between all three estimators was within or below $k_{\mathrm{B}}T$. Ref.[103] showed that the error in the reconstructed free energy surface depends on the value chosen for the effective temperature ΔT ($k_{\mathrm{B}} = 1$). We chose ΔT by first running preliminary simulations to obtain approximately converged FES, and then set ΔT to be approximately the depth of the free energy wells (typical values are $5 - 20 k_{\mathrm{B}}T$). We found that over- or undershooting this value by about 50% doesn't affect the converged FES results by more than one $k_{\mathrm{B}}T$. During the simulation, the bias potential is accumulated on a linear grid, but sufficiently fine grids with $10^4 - 10^5$ points along the order parameter coordinate proved sufficient for resolving all free energy features resulting from a nonlinear Ψ^4-parameter.

In the multiple-walkers simulations, typically, half of the walkers were initialized with an artificially induced ordered phase configuration by running an initial, short ($10^5 - 10^6$ time steps) simulation before the actual WTMetaD run using Umbrella sampling with a fixed harmonic bias potential designed to drive the system into the ordered phase.

The initial Gaussian height of our WTMetaD simulation was chosen as $w = k_{\mathrm{B}}T/n_w$ where n_w is the number of walkers, and Gaussians were deposited every 1000 time steps to ensure sufficient time for the system to relax between Gaussian updates.

5.4 Implementation

The WTMetaD algorithm was implemented as a publicly accessible Integrator plug-in[108] to the HOOMD-blue simulation framework.[97] The particle-mesh scheme used to compute the order parameter and the forces derived from it have been fully implemented on the GPU using the CUFFT library, as part of the same plug-in. The implementation also runs on multiple GPUs, using a distributed FFT algorithm,[109,110] which was needed for some larger systems.

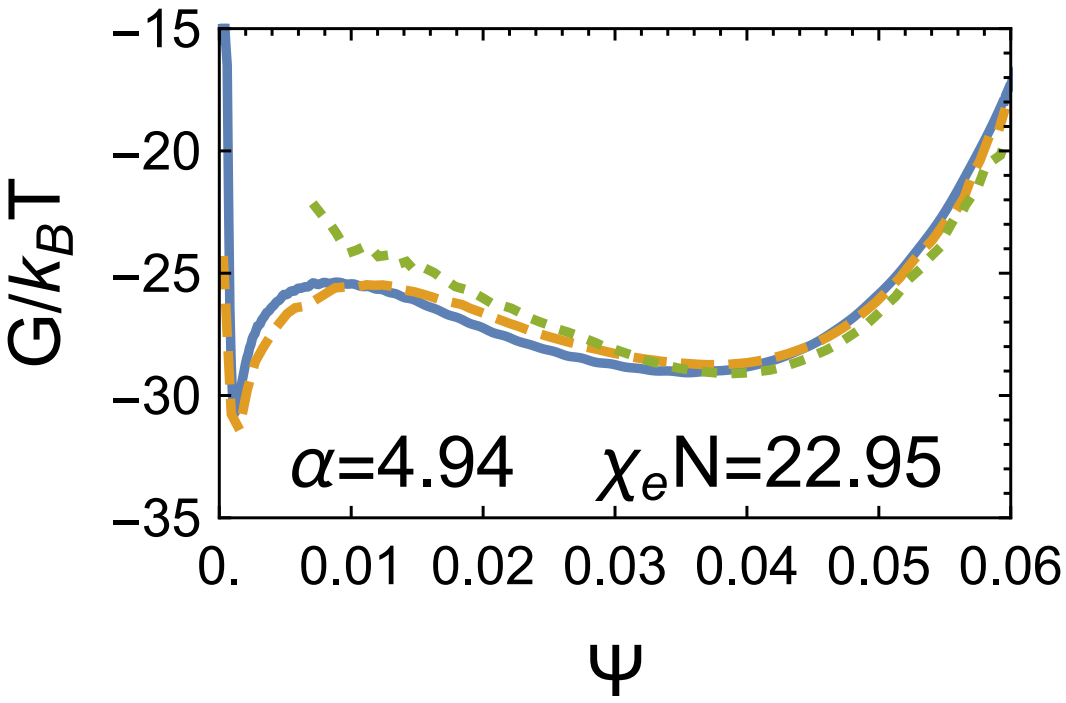

Figure 5.1: Validation of a WTMetaD-biased NPT simulation against an unbiased simulation for a system of three ordered layers in model S1-16 ($M = 2007$ chains) at $\alpha = 4.940$ slightly above the critical ODT value ($\alpha = 4.92$). The blue solid curve is the result of well-tempered metadynamics. The broken curves (green and yellow) are obtained by directly integrating the system without bias potential and recording a histogram $P(\Psi)$ of order parameter values, $G(\Psi) = -k_{\mathrm{B}}T \ln P(\Psi)$. Statistics were obtained by averaging over 10 independent runs of 10^8 time steps each. The yellow dashed curve was obtained from a system initialized in the disordered state and the green dotted curve was obtained from a system initialized with an ordered configuration.

5.4.1 Validation

In order to validate our implementation of the WTMetaD algorithm, free energy surface reconstructed from a biased WTMetaD simulation was compared to that from an unbiased simulation for a system of sufficiently small size that it should be ergodic and hence, should produce equivalent results for biased and unbiased simulations. Fig. 5.1 shows results form this validation for model S1-16 of $M = 2007$ chains, in a tetragonal NPT simulation with initial box dimensions chosen so as to accommodate three lamellar domains across one axis.

5.4.2 Choice of a Commensurate Simulation Box

WTMetaD simulations were carried out using cubic $L \times L \times L$ unit cells since they sample both ordered and disordered configurations. The box length L and the number of molecules M were chosen so as to accommodate a stress-free lamellar phase ordered in the $\{300\}$ orientation at the value of α at which the simulation was run. In preparation for every WTMetaD simulation, a preliminary sweep over α-values in tetragonal NPT simulations was performed, in which an ordered phase was induced artificially by means of an external periodic potential, to determine the equilibrium layer spacing $q^\star$ and monomer concentration as functions of α. For system sizes and cell dimensions chosen in this manner, ordered configurations oriented with primary wave-vectors in the $\{300\}$ or $\{211\}$ families all yield a layer spacing $d = L/3$ nearly equal to the preferred spacing. In our WTMetaD simulations, ordered configurations were found to spontaneously orient along both of these families of Miller planes, with no obvious preference for either family of orientations.

5.4.3 Free Energy Extrapolation

WTMetaD yields an estimate of the system's free energy $G(\Psi)$ for the α value at which the simulation was run. To reduce the number of simulations necessary to iteratively find the interaction parameter α_{ODT} at the ODT for a given model using WTMetaD, we implemented an extrapolation scheme that allows one to identify the ODT using a converged FES obtained at any value of α in the neighborhood of α_{ODT}. To estimate the FES for a value of α close to a value of $\alpha = \alpha_0$ for which the FES was actually measured, we use the following linear perturbation result for the Gibbs free energy $G(\Psi, \alpha)$

$$G(\Psi, \alpha) = G(\Psi, \alpha_0) + \frac{\partial G}{\partial \alpha}\Big|_{\Psi, \alpha=\alpha_0} (\alpha - \alpha_0) + \mathcal{O}(\Delta\alpha^2), \tag{5.25}$$

where the derivative of the Gibbs free energy was measured at a value of $\alpha = \alpha_0$ by averaging values of the quantity

$$\frac{\partial G}{\partial \alpha}\Big|_{\Psi, \alpha=\alpha_0} = \frac{\langle U_{AB} \rangle\big|_{\Psi, \alpha_0}}{\epsilon + \alpha} \tag{5.26}$$

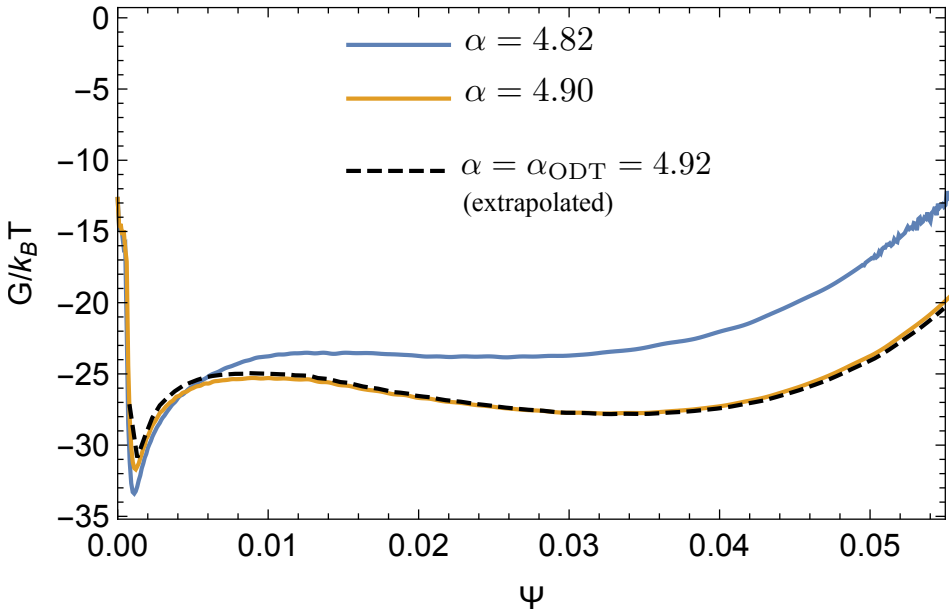

Figure 5.2: Extrapolation of the Gibbs free energy via linear perturbation. The blue and yellow curves are free energy surfaces for $\alpha = 4.82$ and 4.9, respectively. The black dashed curve is the result of extrapolating the FES at $\alpha = 4.82$ to the ODT value $\alpha_{\mathrm{ODT}} = 4.92$ of the interaction parameter.

for all values Ψ of the order parameter over the course of a biased simulation. This scheme made it possible for us to identify the ODT for most systems from the results of a single WTMetaD simulation at a well chosen value of α near the true ODT. The true ODT value α_{ODT} is subsequently identified using an equal area construction, by requiring that regions near the ordered and disordered minima in $G(\psi)$ yield equal contributions to the integral $\int d\Psi \; e^{-G(\Psi,\alpha)/k_{\mathrm{B}}T}$, corresponding to equal probabilities in an unbiased simulation. Fig. 5.2 shows an example of an extrapolation of free energy surface used to refine a very good initial guess for α_{ODT} for S1-16.

Chapter 6

Order-Disorder Transition and Lamellar Phase

We present a comprehensive study of how properties of symmetric diblock copolymers depend on the invariant degree of polymerization $\overline{N}$, focusing on the vicinity of the order-disorder transition (ODT). All results presented in this chapter have been published in Ref.[111] Use of four different coarse-grained simulation models, models H, S1, S2, and S3, allow us to span a wide range of $\overline{N} \simeq 200 - 8000$ that includes most of the typical experimental range. Properties discussed here include the free energy per chain, the free energy derivative, the order-disorder transition, the latent heat of transition, the layer spacing, the composition profile and compression modulus in the ordered phase. Equivalent results for all properties are obtained from corresponding thermodynamic states of different simulation models, *i. e.,* states with equal values of the parameters $\chi_e N$ and $\overline{N}$. Once again, we find that the key element in obtaining universal (*i. e.,* model-independent) results from different simulation models is to use nonlinear estimates for $\chi_e(\alpha)$ obtained by fitting results for the normalized inverse peak structure factor $cNS^{-1}(q^*)$ in the disordered phase to the ROL theory predictions.

Presentation of results in this chapter is organized as follows: Section 6.1 presents results for the derivative of the free energy per chain with respect to $\chi_e N$, which is proportional to the AB pair energy. Section 6.2 presents results for the corresponding free energy g. Section 6.4 presents results for an

invariant form of the latent heat of transition. Section 6.5 presents results for the composition profile in the ordered phase. We show there that the profile is strongly segregated but nearly sinusoidal at the ODT, and discuss the role of interfacial fluctuations in suppressing higher harmonics by "smearing" the average profile. Section 6.6 presents an analysis of local monomer environments in the ordered and disordered phases, which shows the structural similarity of the ordered and disordered phases near the ODT. Section 6.7 presents results for the dependence of peak wavenumber q^* in the disordered phase and domain spacing d in the ordered phase on $\chi_e N$ and $\overline{N}$, and shows a comparison of the ordered phase results to SCFT predictions. Section 6.8 presents results for the dependence of the smectic compression modulus on $\chi_e N$ and $\overline{N}$. Section 6.9 is an analysis of the expected magnitude of errors in values of $(\chi_e N)_{\rm ODT}$ in systems in which the simulation cell is not commensurate with the preferred layer spacing. Section 6.10 summarizes our conclusions.

6.1 Free Energy Derivative

The scaling hypothesis, $g = g(\chi_e N, \overline{N})$ of Eq. 2.23 was tested by comparing results from different simulation models for the free energy g and its derivatives. This section focuses on the derivative of g with respect to $\chi_e N$, which we denote by

$$g' \equiv \frac{\partial g(\chi_e N, \overline{N})}{\partial(\chi_e N)} \quad . \tag{6.1}$$

The free energy g or its derivative g' cannot be directly measured in a simulation. We can, however, measure the partial derivative of g with respect to control parameter α (or ϵ_{AB}) at fixed values of ϵ_{AA} and all other parameters. This quantity is related to the non-bonded AB pair energy per chain $\langle U_{AB}\rangle/M$ by the identity

$$\frac{\partial g}{\partial \alpha} = \frac{1}{k_{\rm B}T}\frac{\langle U_{AB}\rangle}{M\epsilon_{AB}} \quad . \tag{6.2}$$

The derivative $\partial g/\partial\alpha$ is not expected to be universal (*i. e.,* , model-independent), because χ_e is a model-dependent function of α, but it can be used to calculate the universal quantity g': Given an independent estimate of the function $\chi_e(\alpha)$ for each model of interest, the chain rule $\partial g/\partial(\chi_e N) = (\partial g/\partial\alpha)/\partial(\chi_e N)/\partial\alpha$

can be applied to obtain the relationship

$$g' = \frac{1}{k_B T} \frac{\langle U_{AB}(\alpha) \rangle}{MN\epsilon_{AB}(\alpha)} \left[\frac{d\chi_e(\alpha)}{d\alpha} \right]^{-1} . \tag{6.3}$$

This identity was used to evaluate g' from simulations data. Physically, g' is a measure of the number of AB contacts per monomer, expressed in a universal form appropriate for comparison of different models.

Similar reasoning can be used to derive a relationship between g' and the excess enthalpy H, which we use for analysis of experimental data in chapters 7 and 8. Consider a system in which we vary the temperature T for a system with a fixed Hamiltonian and fixed pressure P, as normally done in experiments. In this situation, the interaction parameter is a function $\chi_e(T)$ of T alone. By using the Gibbs-Helmholtz identity $\partial(G/T)/\partial(1/T) = H$ and applying the chain rule, we find that

$$g' = \frac{\langle H \rangle}{NM} \left[k_{\mathrm{B}} \frac{d\chi_e(T)}{d(1/T)} \right]^{-1} \quad . \tag{6.4}$$

If we approximate $\chi_e(T) = A/T + B$, as often done in the analysis of experimental data, then $d\chi_e/d(1/T) = A$.

Scaling hypothesis (2.23) implies that, if g is a universal function of $\chi_e N$ and $\overline{N}$, so is the derivative $g'(\chi_e N, \bar{N})$. If so, results for g' from simulations of different models for chains with matched values of $\overline{N}$ should collapse when plotted *vs.* $\chi_e N$. In practice, such a plot can be constructed from simulations data only if one has an accurate independent estimate of $\chi_e(\alpha)$ for each model, since this function is required both to evaluate the abscissa $\chi_e N$ and to evaluate Eq. 6.3 for the ordinate g'. The quality of the collapse is thus expected to reflect the accuracy of one's estimate of $\chi_e(\alpha)$, as well as the accuracy of the physical scaling hypothesis.

Fig. 6.1 shows an attempt to collapse data for models H-64 and S1-16, both of which have $\overline{N} \simeq 240$, by using the perturbative linear estimate $\chi_e^{(1)}(\alpha) = z_\infty \alpha / k_{\mathrm{B}} T$ to plot g' *vs.* $\chi_e N$. With this approximation, agreement between the two models is poor. As would be expected from previously shown results on ODT, there is a noticeable difference in estimated values of $\chi_e N$ at the ODT, which are indicated here by arrows. Results for g' itself agree only for $\chi_e N \simeq 0$, where the linear approximation for $\chi_e^{(1)}$ becomes exact. This comparison along

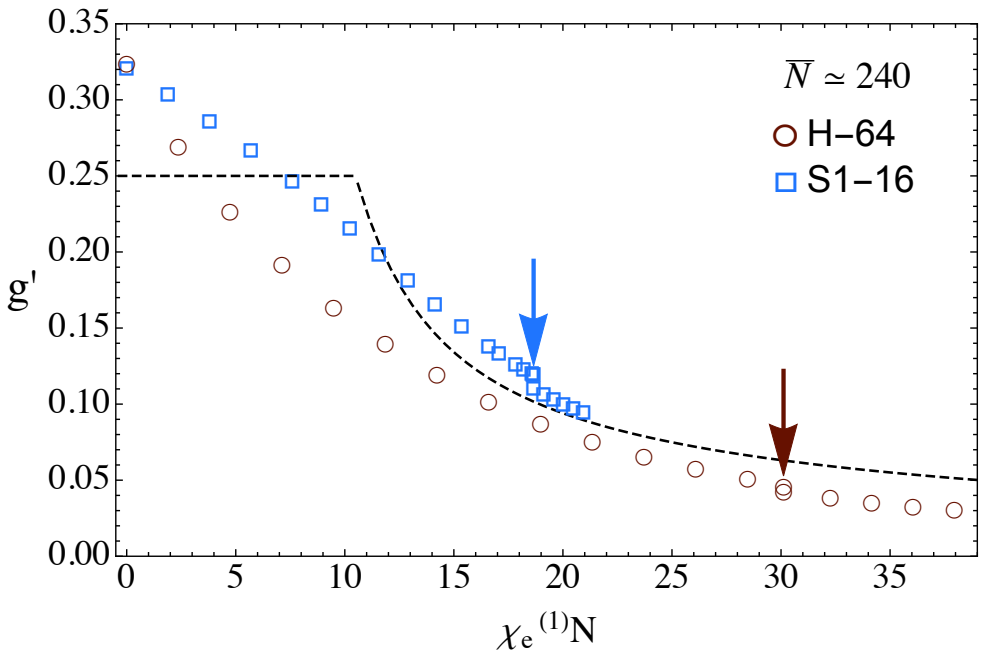

Figure 6.1: Plot of $g' \equiv \partial g/\partial(\chi_e^{(1)}N)$ *vs.* $\chi_e^{(1)}N$ for models H-64 and S1-16, both of which have $\overline{N} \simeq 240$. The dashed curves represent SCFT predictions for $g'(\chi_e N)$ in the disordered and ordered phases. The arrows mark values of ODT for the two models.

with others like it, some of which were discussed in previous chapters, suggest that a linear approximation for $\chi_e(\alpha)$ is generally not adequate for analyzing simulations data near the ODT, except for systems of very long chains.

Fig. 6.2 shows corresponding plots of g' *vs.* $\chi_e N$ constructed using the non-linear estimate of $\chi_e(\alpha)$ obtained for each model by fitting $S(q)$ in the disordered phase. The first three panels show results for pairs of simulations of different models with nearly matched values of $\overline{N} \simeq$240, 960, 3840, respectively. The last panel shows results for system S3-64, for which $\overline{N} \simeq 7680$. In the first three plots, agreement between simulations with matched values of $\overline{N}$ is excellent. The successful collapse of data in the first three plots verifies both the hypothesized universality of $g(\chi_e N, \overline{N})$ and the accuracy of our estimate of $\chi_e(\alpha)$.

In these plots, the SCFT prediction of the value $(\chi_e N)_{\rm ODT} = 10.5$ is marked by a vertical dotted line. The actual ODT, as identified by metadynamics from the previous chapter, is identified by a small discontinuity in the value of g', and is marked in each plot by a vertical dashed line. In plots a-c, excellent

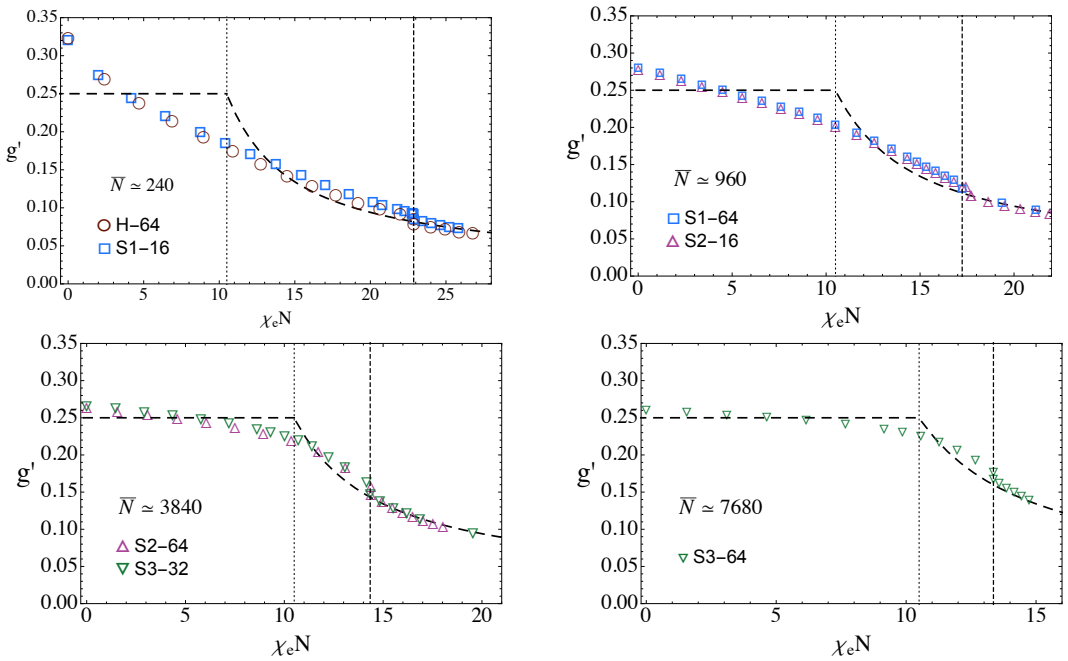

Figure 6.2: Plots of $g' \equiv \partial g/\partial(\chi_e N)$ *vs.* $\chi_e N$ for different $\overline{N}$ values. The dashed curves represent SCFT predictions for $g'(\chi_e N)$ in the disordered and ordered phases. In each plot, the dashed and dotted vertical lines indicate the measured ODT and the SCFT prediction respectively. In plots a-c, which display results for two systems, the ODT is shown for the system with larger N.

agreement is obtained for values of $(\chi_e N)_{\mathrm{ODT}}$ for pairs of systems with matched values of $\overline{N}$. In these plots, the vertical line shows the value of $(\chi_e N)_{\mathrm{ODT}}$ for the member of the pair with larger value for N.

The SCFT prediction for $g'(\chi_e N)$ is shown in each plot by a dashed line, which has a constant value $g' = 0.25$ for $\chi_e N < 10.5$ and decreases with increasing $\chi_e N$ at higher $\chi_e N$. This prediction for g' is a measure of the degree of AB contact, which is given by the spatial average $g' \equiv \overline{\phi_A \phi_B}$ of the product $\phi_A(\mathbf{r})\phi_B(\mathbf{r})$ of the predicted local volume fractions of A and B monomers. In the disordered phase of a symmetric diblock copolymer, where $\phi_A(\mathbf{r}) = \phi_B(\mathbf{r}) = 1/2$ everywhere, this yields $g' = \phi_A \phi_B = 0.25$. In the ordered phase, g' decreases with increasing $\chi_e N$ as the degree of AB contact decreases due to an increase in the ratio of the domain spacing to the width of an individual interface. The SCFT prediction for g' is continuous at the predicted ODT because SCFT predicts a continuous (second-order) phase transition.

Agreement between simulation results and SCFT predictions for g' is mediocre in the disordered phase, particularly near the ODT and for small values of $\overline{N}$. The fact that $g' < 0.25$ near the ODT is a consequence of composition fluctuations that decrease the extent of AB contact near the ODT. The fact that $g' > 0.25$ at $\chi_e N = 0$ is a more subtle packing effect, which is a result of the fact that the probability of intermolecular AB contact increases with decreasing chain length even when $\alpha = 0$, as discussed for polymer blends in Ref.[81]

Somewhat surprisingly, however, simulations results and SCFT predictions for g' are in excellent agreement in the ordered phase near the ODT. Agreement appears to be particularly good in the ordered phase at low and intermediate values of $\overline{N}$ (plots a-c). A slightly larger discrepancy appears at the highest value of $\overline{N} = 7680$. The results suggest that SCFT, when combined with an adequate method of estimating χ_e, provides a surprisingly good quantitative description of the structure of the ordered phase in the intermediate segregation regime studied here. We assume that the accuracy near the ODT is actually better for lower values of $\overline{N}$ because SCFT is most appropriate for comparatively strongly segregated ordered states, or values of $\chi_e N$ that are not too close to the SCFT critical value of 10.5, while the value of $\chi_e N$ at the ODT increases with decreasing $\overline{N}$.

The value of g' is discontinuous at the ODT, as discussed in greater length in section 6.4. The fact that the magnitude of this discontinuity is rather small, suggests that the disordered phase near the ODT exhibits a structure of A- and B-rich domains rather similar to that of the ordered phase, lacking only long range order. This physical picture is supported by results presented in subsequent sections, and has been suggested previously by Lee, Bates *et al*[87] on the basis of experimental evidence from short diblock copolymers.

The Brazovskii and Fredrickson-Helfand theories suggest that, for sufficiently large values of $\overline{N}$, deviations from SCFT predictions for the properties of the disordered phase should become negligible outside of a Ginzburg region that corresponds roughly to the range of values of $\chi_e N$ between the SCFT ODT at $(\chi_e N)_{\mathrm{ODT}} = 10.5$ and the true ODT. Our results for the dependence of g' upon $\chi_e N$ suggest that this picture is accurate only for $\overline{N} \gtrsim 10^4$. For the smallest values $\overline{N} \simeq 240$ and 960, g' exhibits a completely featureless decrease with increasing $\chi_e N$ over the entire range from $\chi_e N = 0$ to $(\chi_e N)_{\mathrm{ODT}}$, with no identifiable Ginzburg regime. For the largest value of $\overline{N} \simeq 7680$, however, the dependence of g' *vs.* $\chi_e N$ does begin to resemble the behavior expected for very large values of $\overline{N}$, in which g' remains close to the SCFT value of $g' = 0.25$ for $\chi_e N < 10.5$ and then drops more rapidly within a narrower range of values between the SCFT and actual ODT.

6.2 Free Energy per Chain

The normalized free energy per chain g in the disordered phase can be obtained by numerically integrating data for $\partial g/\partial \alpha$ from $\alpha = 0$. The value of g in the disordered phase can be obtained by setting $g(\alpha = 0) = 0$ by convention for homopolymers and integrating up from $\alpha = 0$. The free energy in the ordered phase can then be obtained by equating values of g in the ordered and disordered phases at the ODT value $(\chi_e N)_{\mathrm{ODT}}$ that is obtained from well-tempered metadynamics, and then integrating with respect to α within the ordered phase. Data of $\partial g/\partial \alpha$ (i.e., $\langle U_{AB} \rangle$) in the ordered phase is obtained from simulations with an adjustable unit cell, to avoid commensurability effects. Fig. 6.3 shows plots of g *vs.* $\chi_e N$ that were obtained by this method, for the same

set of systems and values of $\overline{N}$ as those shown in Fig. 6.2. SCFT predictions for $g(\chi_e N)$ are shown by a solid line. This yields a straight line with $g(\chi_e N) = \chi_e N/4$ for $\chi_e N < 10.5$, where SCFT predicts a stable disordered phase. SCFT predictions for the unstable homogeneous phase at $\chi_e N > 10.5$ are shown by a dashed continuation of this straight line.

Simulation results for g within the ordered phase are found to agree well with SCFT predictions. Agreement is particularly good at intermediate values of $\overline{N}$ (960 and 3840), with somewhat larger discrepancies of opposite sign at the lowest ($\overline{N} = 240$) and highest ($\overline{N} = 7680$) values shown. Results for g agree reasonably well with SCFT predictions for $\chi_e N < 10.5$. In the regime $10.5 < \chi_e N < (\chi_e N)_{\mathrm{ODT}}$ between the SCFT and actual ODTs, where the disordered phase develops stronger composition fluctuations, results for g in the disordered phase lie much closer to SCFT predictions for the ordered phase (the solid curve) than to predictions for a hypothetical homogeneous phase (the straight dashed line). This suggests that, in this parameter regime, the disordered phase develops a fluctuating structure of A and B domains similar to that predicted by SCFT for the ordered phase, but without long range order.

The level of agreement between simulation results and SCFT predictions for g does not follow trivially from the agreement between simulation results and SCFT predictions for g' in the ordered phase, which only requires that results for g agree with SCFT to within a constant offset. Note that the value of g at the ODT is actually calculated by integrating through the disordered phase, where the agreement between results and SCFT for g' is comparatively poor.

In SCFT, the total free energy per chain can be expressed as the sum of AB interaction free energy, which is proportional to g', and an entropic contribution that arises from chain stretching and localization of chains. An analogous decomposition is useful at a heuristic level for interpreting simulation data. Because g' is directly proportional to the average AB pair energy, we may also use g' as a measure of the extent of AB contact in simulations. The extent of agreement between simulations and SCFT for both g and g' in the ordered phase suggests that SCFT provides a reasonably accurate prediction for the cost of chain stretching within the ordered phase, as well as the extent of AB contact. The differences between simulation results and SCFT predictions for

g are largest for very low values of $\overline{N}$ (*e. g.,* , $\overline{N} \simeq 240$). Agreement between SCFT and simulation results for g' in the ordered phase near the ODT are, however, particularly good at low values of $\overline{N}$. This suggests that the errors in SCFT predictions for the free energy at modest values of $\overline{N}$ are not primarily the result of errors in predictions for the extent of AB contact, as quantified by g', and are thus presumably dominated by errors in SCFT predictions for the conformational entropy of relatively short chains.

6.3 Order-Disorder Transition

Fig. 6.4 shows a summary of our results for $(\chi_e N)_{\mathrm{ODT}}$ for all of the systems discussed here, including different chain lengths (N =16, 32, 64, and 128) and different models (H, S1, S2, and S3). Results for specific systems are marked by labels such as S1-32, etc. All values shown here were obtained using well-tempered metadynamics simulations to locate α_{ODT} with an unprecedented level of accuracy.

The fact that results for $(\chi_e N)_{\mathrm{ODT}}$ from a variety of models collapse onto a common curve when plotted *vs.* $\overline{N}$ shows that $(\chi_e N)_{\mathrm{ODT}}$ is indeed a universal function of $\overline{N}$, independent of microscopic differences between simulation models. This conclusion is demonstrated even more directly by the near perfect agreement between results obtained from simulations of different models using matched values of $\overline{N}$, such as S1-16 and H-64, which appear as overlapping symbols in this plot.

The SCFT and BLFH predictions are shown in Fig.6.4 as a horizontal long-dashed line and solid curve, respectively. BLFH theory significantly underestimates $(\chi_e N)_{\mathrm{ODT}}$ at small values of $\overline{N} \lesssim 10^3$, but seems to approach the simulation results near the upper end of the range studied here. Because we believe that the BLFH theory should become accurate for sufficiently large $\overline{N}$, we expect the BLFH prediction to become more accurate at values of $\overline{N} \gtrsim 10^4$. The short dashed curve through the simulations data is an empirical fit to our results for systems with $\overline{N} \lesssim 10^4$. It is given by a sum

$$(\chi_e N)_{\mathrm{ODT}} = 10.5 + 41.0\overline{N}^{-1/3} + 127.0\overline{N}^{-0.56} \tag{6.5}$$

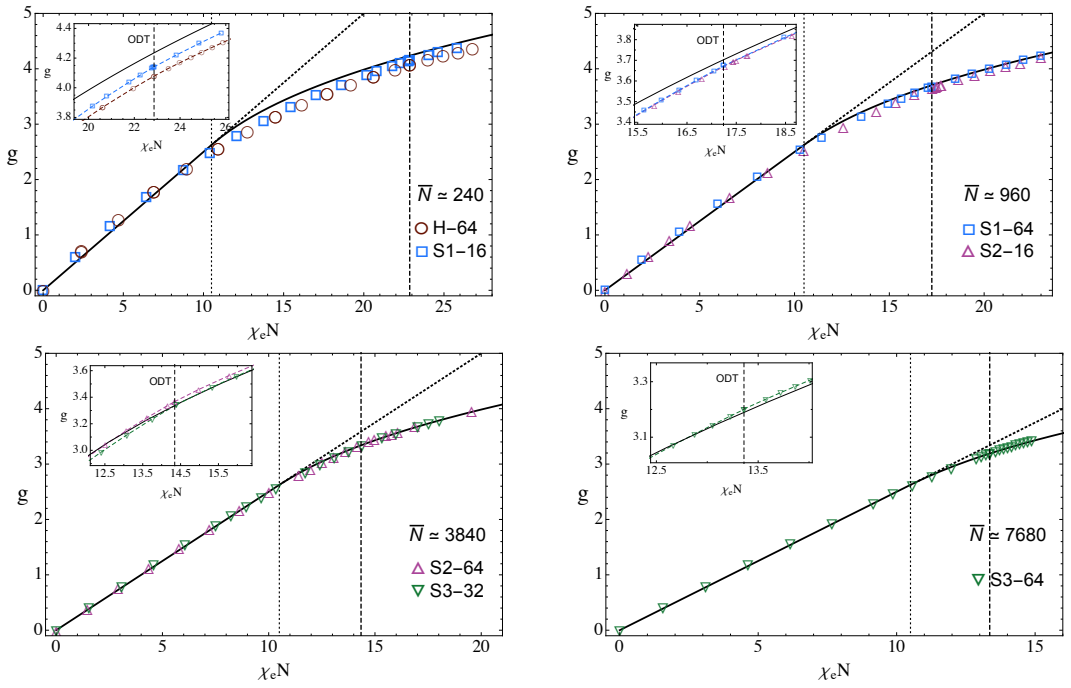

Figure 6.3: Plots of free energy per chain g *vs.* $\chi_e N$ for different values of $\overline{N}$, defined relative to that of a homopolymer ($\alpha = 0$) reference state. Solid curves show the SCFT prediction for $g(\chi_e N)$. For a homogeneous liquid, SCFT yields $g(\chi_e N) = (\chi_e N)/4$. In each plot, the dashed and dotted vertical lines indicate the measured ODT and the SCFT prediction respectively. In plots that display results for two systems, the ODT is shown for the system with larger N. In each plot, the inset shows free energy in disordered and ordered phases in the immediate vicinity of ODT. The solid curves are SCFT predictions, and the dashed curves are guidelines connecting the simulation data, which are marked in symbols.

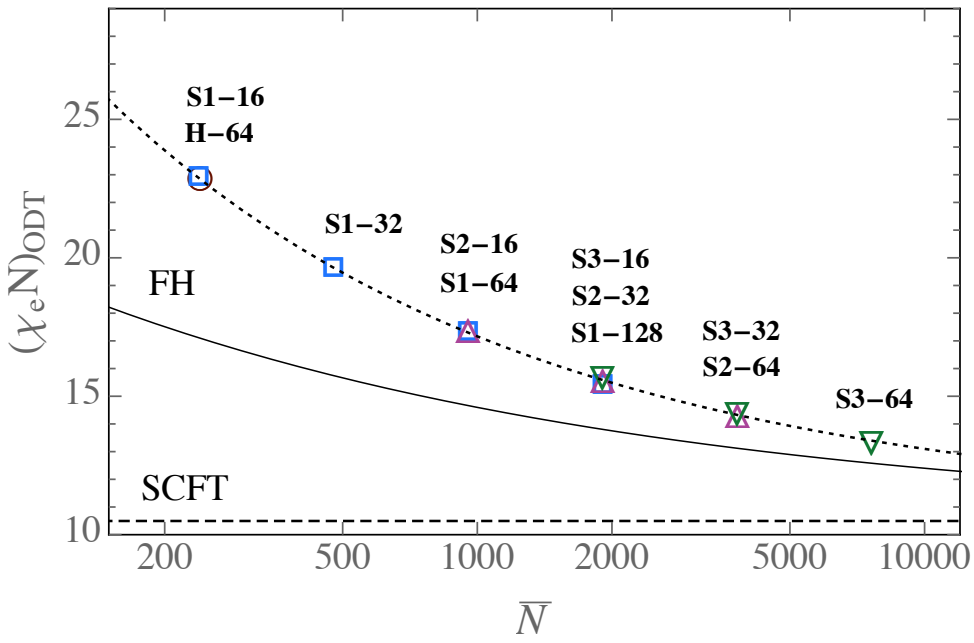

Figure 6.4: Values of $\chi_e N$ at the ODT *vs.* $\overline{N}$ obtained from simulations of models, H, S1, S2, and S3 with labels for specific systems. The long-dashed and solid lines represent the SCFT and BLFH theory predictions respectively. The short-dashed curve is an empirical fit to the simulation results, given by Eq. (6.5)

of the BLFH prediction (the first two terms) plus an additional power law that was chosen to fit this data.

Our publication in Ref.[112] included a similar plot that included data from lattice Monte Carlo simulations conducted by coauthors T. Beardsley and M. Matsen. The lattice Monte-Carlo results for $(\chi_e N)_{\rm ODT}$ were found to fall on the same master curve. Data from these lattice simulations is not included here simply because many of the quantities for which we report results below have not been measured for this lattice model.

6.4 Latent Heat

Because the ODT is a first-order transition, the value of the first derivative g' is discontinuous across the transition. We use $\Delta g'$ to denote the magnitude of the discontinuity in g' at the ODT, given by the difference between values of g'

in the disordered and ordered phases at the ODT. This quantity is a measure of the latent heat of transition, expressed in universal form: Using Eq. 6.4 for g', we find that

$$\Delta g' = \frac{\Delta H}{NM}\left[k_{\mathrm{B}}\frac{d\chi_e(T)}{d(1/T)}\right]^{-1} \quad , \tag{6.6}$$

where ΔH is the total latent heat of transition for a system of M chains.

Fig. 6.5 shows a summary of values of $\Delta g'$ plotted *vs.* $\overline{N}$ for all systems. Fig. 6.6 shows values for the corresponding fractional change $\Delta g'/g'_{\mathrm{ord}}$, where g'_{ord} denotes the value of g' in the ordered phase at the ODT. Despite the presence of some scatter in the data, results for all simulations seem to fall on a master curve when plotted *vs.* $\overline{N}$, consistent with the scaling hypothesis.

Fig. 6.6 shows that the fractional change in g' is almost independent of $\overline{N}$ over the range studied here, but decreases very slightly with increasing $\overline{N}$. The fractional change in g' is equal to the fractional change in the average AB pair energy. In a model of both ordered and disordered phases as strongly segregated structures in which AB contact occurs primarily across interfaces, this fractional change is expected to also be equal to the fractional change in the amount of AB interfacial area per unit volume. In this model, a nearly constant value for this fractional change would arise naturally if the geometry of the lamellar and disordered phases is almost independent of $\overline{N}$.

Fig. 6.5 shows that $\Delta g'$ actually increases slightly with increasing $\overline{N}$ over the range studied here. The absolute discontinuity $\Delta g'$ increases despite the slight decrease in the fractional discontinuity because g'_{ord} increases with increasing $\overline{N}$. This increase in g'_{ord} occurs because the value of $\chi_e N$ at the ODT decreases with increasing $\overline{N}$, yielding wider interfaces and more AB contact in the ordered phase at the ODT with increasing $\overline{N}$. Though the observed behavior is thus understandable within a picture of strongly segregated structures, it seems to contradict the prediction of BLFH theory that the transition should become second order in the limit $\overline{N} \to \infty$, which requires that $\Delta g' \to 0$ in this limit. The only way to resolve these two pictures is if $\Delta g'$ reaches a maximum at some crossover and decreases monotonically at higher values of $\overline{N}$, outside the range studied here. Further simulations at higher values of $\overline{N}$ were run to determine if this conjecture is correct.

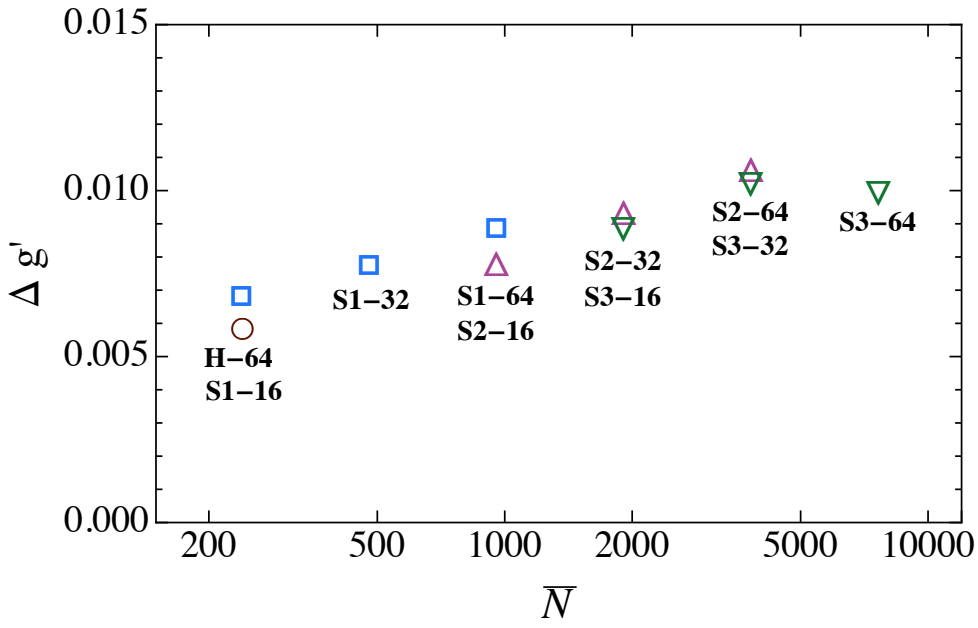

Figure 6.5: Discontinuity $\Delta g'$ in g' across the ODT plotted *vs.* $\overline{N}$. In this and other figures that compare results obtained using different models, we use circles for data from model H, squares for model S1, triangles for model S2, and inverted triangles for model S3.

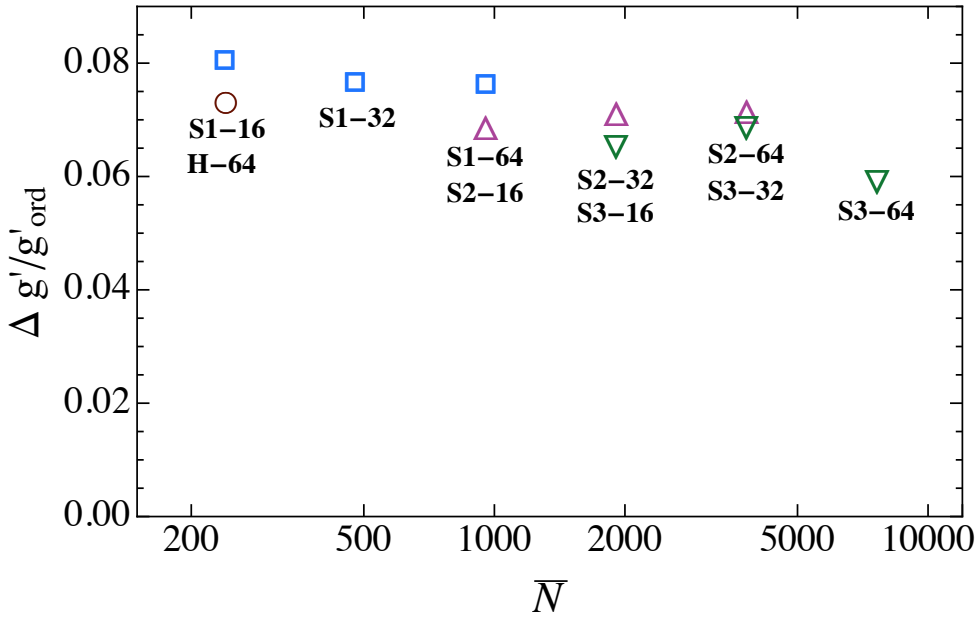

Figure 6.6: Fractional change in g' across the ODT, given by the ratio $\Delta g'/g'_{\rm ord}$, *vs.* $\overline{N}$ value. Here, $g'_{\rm ord}$ is the value of g' in the ordered phase at the ODT.

6.5 Composition Profile

To characterize the composition profile in an ordered phase with layers normal to the z axis, we measured the average number fraction $\phi_A(z)$ of A monomers as a function of a scaled normal coordinate z/L, where L is the unit cell length in the z direction. In a simulation cell with m layers, the obtained profile is expected to have a Fourier expansion of the form

$$\phi_A(z/L) = 1/2 + \sum_{n=1}^{\infty} A_n \cos(\pi n z/d) \quad , \tag{6.7}$$

with $d \equiv L/m$, in which the even terms should vanish for a symmetric copolymer as a result of the symmetry of the system under relabeling of A and B monomers.

Some care is required when computing $\phi_A(z/L)$ to avoid "smearing" of the profile by random displacements of the entire structure in the z direction over the course of a long MD simulation. To calculate the composition, instantaneous histograms of values of z/L for A and B monomers are periodically accumulated, from which an instantaneous profile $\phi_A(z/L)$ is calculated, and coefficients of the complex Fourier expansion of each such instantaneous profile are computed, as a sum

$$\phi_A(z/L) = 1/2 + \sum_{n=1}^{\infty} \mathrm{Re}\left(C_n e^{i2\pi n z/L}\right) \quad . \tag{6.8}$$

The origin of the z coordinate is then shifted for each such instantaneous profile such that the complex coefficient C_m, the fundamental mode of a profile containing m layers, with a period $d = L/m$, becomes a real number. Each instantaneous profile is added to an accumulated average profile only after applying this coordinate shift. This yields an average profile $\phi_A(z/L)$ with a Fourier expansion in which the only non-negligible coefficients are found to be those consistent with an expansion of the form given in Eq. 6.7, with only odd values of n and inversion symmetry about $z = 0$.

Fig. 6.7 shows an example of the resulting composition profiles $\phi_A(z/L)$ in the ordered phase at the ODT in a system with three layers, for a pair of systems with matched values of $\overline{N} \simeq 960$ (S1-64 and S2-16). The fact that the two resulting plots of $\phi_A(z/L)$ overlap is consistent with our scaling hypothesis, which predicts that the structure at the ODT should be the same for systems

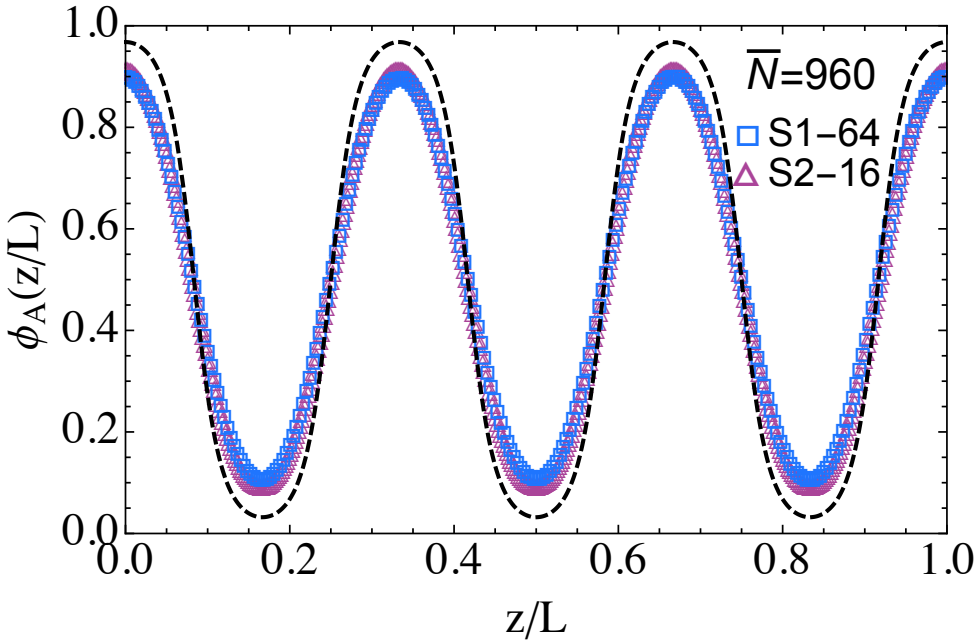

Figure 6.7: Composition profile in the ordered phase at the ODT for systems with $\overline{N} \simeq 960$. Here $\phi_A(z/L)$ is the average volume fraction of A monomers, calculated as discussed in the text. Symbols are simulation results for systems S1-64 and S2-16. The dashed line is the SCFT prediction for $\phi_A(z)$ in an ordered phase with $\chi_e N = 17.24$, the measured value of $(\chi_e N)_{\rm ODT}$ for system S1-64.

with matched values of $\overline{N}$. For this value of $\overline{N}$, the average composition profile at the ODT is strongly modulated, reaching approximately 90 % volume fraction of the majority component in the middle of each domain. It is also almost perfectly sinusoidal, in a sense that we quantify below.

For comparison, Fig. 6.7 also shows the SCFT prediction for the composition profile in an ordered phase with $\chi_e N = 17.24$ equal to the measured value of $(\chi_e N)_{\rm ODT}$ for system S1-64 (the dashed line). The SCFT prediction is more strongly segregated than the simulation results, reaching 96 % volume fraction for the majority component, and less sinusoidal, exhibiting somewhat flatter maxima and minima in the middle of each domain.

Fig. 6.8 shows a summary of results for the maximum value of $\phi_A(z/L)$ within the middle of the A domain in the ordered phase at the ODT, plotted *vs.* $\overline{N}$. Because the profile is nearly sinusoidal at the ODT, $\max \phi_A\,(z/L) \simeq 1/2 + A_1$. The fact that the results fall on a common curve again confirm that the structure of the ordered phase at the ODT exhibits a universal dependence on $\overline{N}$. It is clear

from these results that the ordered phase remains rather strongly segregated over the entire range of values of $\overline{N}$ that is studied, but that $\max \phi_A(z/L)$ does decrease very slowly with increasing $\overline{N}$, consistent with the expected approach to a second order transition in the limit $\overline{N} \to \infty$.

The dashed line in Fig. 6.8 shows the SCFT prediction for $\max[\phi_A(z/L)]$ in the ordered phase at the value of $(\chi_e N)_{\rm ODT}$ obtained for each $\overline{N}$ in our simulations. This is calculated using Eq. 6.5 to estimate the dependence of $(\chi_e N)_{\rm ODT}$ on $\overline{N}$. The average profile obtained at the ODT in simulations is always somewhat less strongly segregated than the profile predicted by SCFT at the corresponding value of $\chi_e N$.

The solid line shows the prediction of the BLFH theory for this quantity, which is given by $A = 1.63\overline{N}^{-1/6}$. This equation yields $A > 1/2$, and thus gives values of $\phi_A(z/L)$ outside the physical bounds $0 < \phi_A(z/L) < 1$, for $\overline{N} < 1245$. This simple observation shows that the BLFH theory cannot possibly remain valid for $\overline{N} < 10^3$, and suggests that it must begin to fail somewhat above this value. The results given here show that the BLFH theory gives a reasonably accurate prediction for the largest value of $\overline{N}$ studied here, and suggest that the simulation results and BLFH predictions converge for $\overline{N} \gtrsim 10^4$.

Fig. 6.9 shows values for the ratio $\rm A_3/A_1$ of the third and first Fourier amplitudes of the composition profile in the orderd phase *vs.* $\chi_e N$ for different $\overline{N}$ values. Values obtained in the ordered phase at the ODT are shown by solid symbols. The long dashed line shows SCFT predictions for this ratio. The horizontal dashed line represents the ratio of $A_3/A_1 = 1/3$ characteristic of a square wave, which is the asymptote of the SCFT prediction in the limit $\chi_e N \to \infty$. Very small values of $A_3/A_1 \simeq 0.01$ - 0.02 are obtained at the ODT, quantifying the claim that the composition profile is nearly sinusoidal at the ODT. For each value of $\overline{N}$, this ratio increases as $\chi_e N$ is increased, indicating the slow evolution towards a more square-wave profile, but always remains less than predicted by SCFT at a given value of $\chi_e N$.

In small-angle X-ray and small-angle neutron scattering experiments from a lamellar phase, the intensity I_n of each Bragg peak is proportional to the square $I_n \propto |A_n|^2$ of the magnitude of the corresponding Fourier component of $\phi_A(z)$. These Bragg peaks are, of course, superimposed on a diffuse background

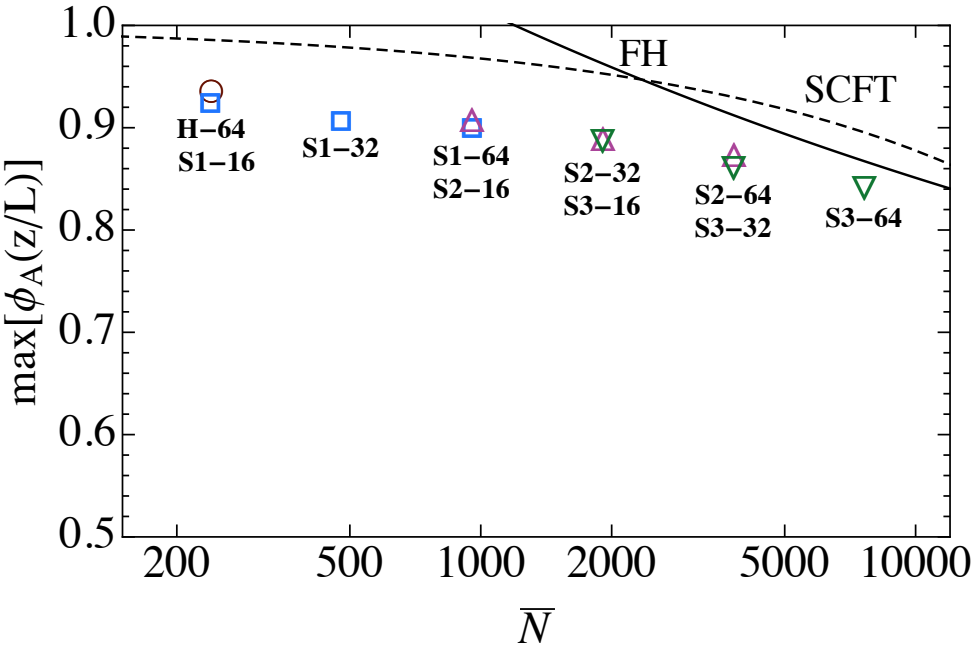

Figure 6.8: Summary of results for the maximum volume fraction $\max[\phi_A(z/L)]$ in the middle of the A domain in the ordered phase at the ODT, plotted *vs.* $\overline{N}$. Solid line shows the BLFH prediction. Dashed line shows the SCFT prediction evaluated using Eq. 6.5 for $(\chi_e N)_{\mathrm{ODT}}(\overline{N})$.

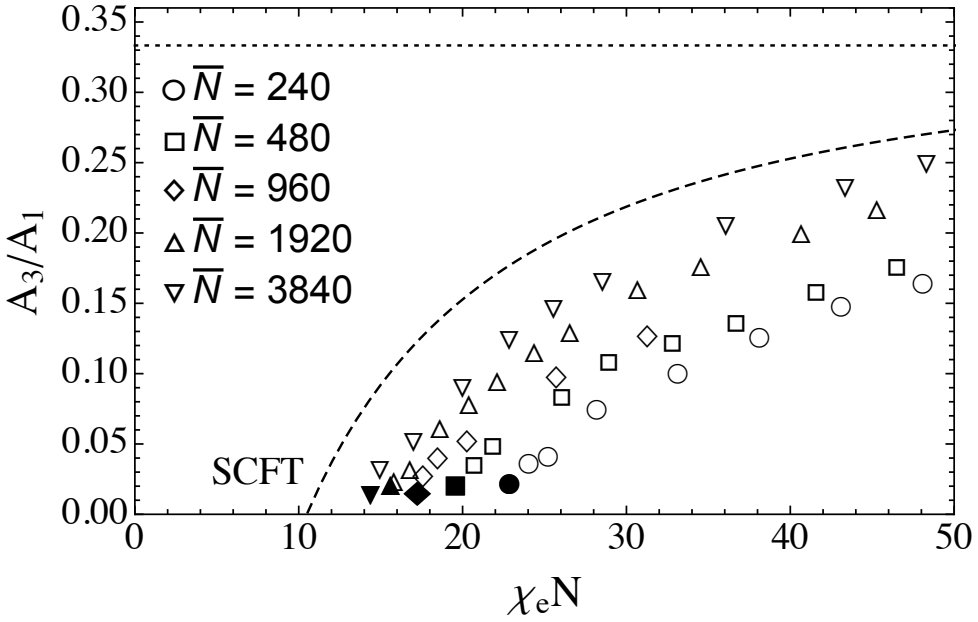

Figure 6.9: Summary of simulation results for the ratio A_3/A_1 of the third and first coefficients in the Fourier expansion of Eq. 6.7 for $\phi_A(z/L)$.

arising from composition fluctuations. Results obtained from our simulations imply that the ratio I_3/I_1 of the intensity of the first and third Bragg peaks for symmetric copolymers with $\overline{N} \lesssim 10^4$ should be approximately $I_3/I_1 \sim (0.02)^2 = 4 \times 10^{-4}$. This appears to be consistent with the observation that higher order peaks are often not observable in scattering experiments at the ODT determined by rheological measurements, and become measurable only at somewhat lower temperatures.

Differences between simulation results and SCFT predictions for the average composition profile are at least superficially larger than the differences obtained for other properties of the ordered phase. We suspect, however, that this difference is primarily the result of smearing of the profile obtained in simulation by "capillary" fluctuations of the interfaces between A and B domains, which is ignored in SCFT. To test the plausibility of this hypothesis, we consider a simple mathematical model[113,114] in which we assume that the instantaneous profile is well described as a locally displaced version of a more strongly segregated "intrinsic" profile, which we denote by $\phi_A^{(\mathrm{int})}(z)$. In this model, we approximate $\phi_A(x,y,z) \simeq \phi_A^{(\mathrm{int})}(z + h(x,y,z))$, in which $h(x,y,z)$ is a displacement perpendicular to the layers. This model predicts an average profile given by the

convolution approximation[113,114]

$$\phi_A(z) = \int dh\ \phi^{(\mathrm{int})}(z+h)P(h) \quad , \tag{6.9}$$

where $P(h)$ is the probability density for the displacement $h = h(x,y,z)$ at any point in space. If we assume a Gaussian distribution $P(h)$ with a variance $\langle h^2 \rangle \equiv \sigma^2$, then each Fourier component A_n in the Fourier series for $\phi_A(z/L)$ is given by a product

$$A_n = A_n^{(\mathrm{int})} e^{-q_n^2 \sigma^2} \quad , \tag{6.10}$$

where $q_n = 2\pi n/d$. This analysis is closely analogous to the derivation of the Debye-Waller factor for suppression of scattering from a three-dimensional crystal by phonons, which also predicts a suppression of high wavenumber Fourier components.

We conjecture that SCFT may provide a reasonable approximation to the "intrinsic" profile in the above model, but a much worse approximation for the average profile. To test the plausibility of this idea, Fig. 6.10 shows a comparison of simulation results for the data shown in Fig. 6.7 to a model that was produced by convolving the SCFT prediction shown in 6.7 by a Gaussian smearing function with an assumed standard deviation for h that is 8 % of the layer spacing d, $\langle h^2 \rangle / d^2 = (0.08)^2$. The assumed magnitude of fluctuations in h was chosen to fit this data, rather than determined independently, but appears to be plausible in light of the magnitude of fluctuations visible when we visualize the ordered phase near the ODT. The extent of deviation from perfectly sinusoidal profile can be quantified by comparing values of A_3/A_1: This smeared SCFT prediction has a value of $A_3/A_1 = 0.01$, in rough agreement with the measured of $A_3/A_1 \simeq 0.016$. This comparison merely shows that interfacial fluctuations of reasonable magnitude are sufficient to explain both the difference between the degree of segregation seen in simulations and that predicted by SCFT and the nearly sinusoidal nature of the resulting profile. A more direct analysis of interfacial fluctuations, similar to that carried out by Schmid and coworkers for polymer-polymer interfaces[115,116] would be required to more rigorously test the accuracy of SCFT predictions for the intrinsic profile.

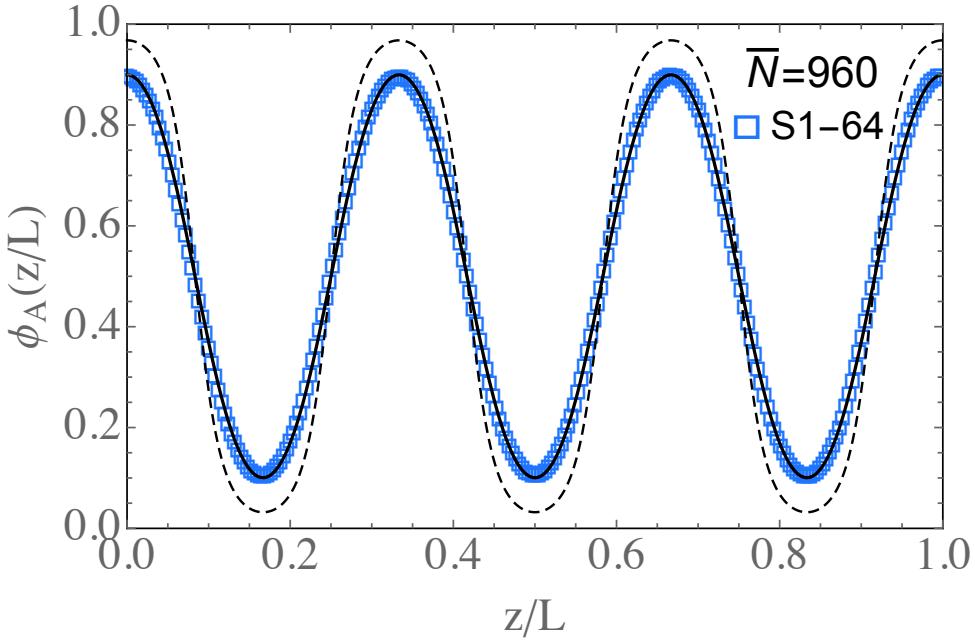

Figure 6.10: Comparison of measured composition profile $\phi_A(z/L)$ for model S1-64 (symbols) to SCFT prediction (dashed) at the ODT value of $\chi_e N$, and to a model of the form given in Eq. 6.9 (solid curve), which is computed using the dashed SCFT prediction for the intrinsic profile and assuming a Gaussian distribution of values for the normal displacement h with a standard deviation $\sqrt{\langle h^2 \rangle}/d = 0.08$.

6.6 Distribution of Local Compositions

Our results for several quantities suggest that the disordered phase near the ODT is characterized by a fluctuating structure that is similar in many respects to that of the ordered phase, except for the absence of long range order. To further quantify local structure in both phases, we analyzed the distribution of values for the per-monomer local composition in a small region around each monomer. In order to do this, we define per-monomer quantities ϕ_A and $\phi_B = 1 - \phi_A$ for every monomer in the system, which give the fraction of intermolecular neighbors of each type in a small sphere around each monomer. The per-monomer composition ϕ_A was obtained by calculating quantities S_A and S_B that measure the number of intermolecular A and B neighbors within some distance of a test monomer, and then setting $\phi_A = S_A/(S_A + S_B)$. The quantity S_i for a given monomer is defined by a sum over intermolecular neighbors of type i of values of a short-range function $f(r)$ that depends on the distance r between two particles. If $f(r)$ were taken to be a step function with a cutoff radius r_c, then ϕ_A would simply be the fraction of intermolecular neighbors of type A within a sphere radius r_c around each monomer. In practice, we smeared the results somewhat by taking $f(r)$ to be a modified Fermi function $f(r) = (1 + e^{12(r-r_c)/r_c})^{-1}$, with a cutoff value $r_c = 1.5\sigma$. We chose to include only intermolecular neighbors in our definition of ϕ_A to avoid counting the trivial enhancement of the environment around each monomer in monomers of the same type that are part of the same block of the same chain.

Fig. 6.11 shows simulation results for the probability $P_A(\phi_A)$ that a randomly chosen A monomer will have a local environment of composition ϕ_A, and the corresponding distribution $P_B(\phi_A)$ for B monomers, for various values of $\chi_e N$. Results are shown for both ordered and disordered phases, and for both the ordered and disordered phases at the transition value of $\chi_e N = 17.44$ for system S2-16 ($\overline{N}$ =960). At $\chi_e N = 0$, $P_A(\phi_A) = P_B(\phi_A)$, and both distributions are centered around $\phi_A = 1/2$. As $\chi_e N$ increases, the probability distribution for each monomer type tends to become richer in monomers of the same type. The difference between $P_A(\phi_A)$ and $P_B(\phi_A)$ builds up continuously with increasing $\chi_e N$, but becomes much more prominent in the disordered phase above the SCFT ODT value $\chi_e N = 10.5$, and even more pronounced in the ordered phase.

Note that results for the disordered and ordered phase at the ODT are extremely similar, though not identical. This comparison of local environments provides a particularly direct demonstration of the structural similarity of the ordered and disordered phases near the ODT, reinforcing the picture suggested by measurements of other properties.

For large values of $\chi_e N$, a non-negligible fraction of monomers have no neighbors of the opposite type, giving contributions with $\phi_A = 0$ for B monomers or $\phi_A = 1$ for A monomers. These monomers yield δ-function contributions to $P_B(\phi_A)$ at $\phi_B = 0$ and to $P_A(\phi_A)$ at $\phi_A = 1$ that cannot be easily depicted in plots of P_A and P_B. To show this, Fig. 6.12 displays examples of the cumulative distribution $C_B(\phi_A) = \int_0^{\phi} d\phi'_A \; P_B(\phi'_A)$, which is the probability that a B monomer will have an environment with a local volume fraction of A less than some value ϕ_A. The fraction of B monomers that have no A neighbors (i.e., for which $S_A = 0$) is given by the limiting value $\lim_{\phi_A \to 0} C_B(\phi_A)$.

6.7 Domain Spacing

Fig. 6.13 shows results for the peak wavenumber $q^\star$ in both ordered and disordered phases, normalized by $R_{g0} \equiv \sqrt{N/6}b$. In the disordered phase, $q^\star$ is determined from the maximum of the structure function $S(q)$ obtained in simulations with a cubic unit cell. In the ordered phase, $q^* = 2\pi/d$, where d is the average domain spacing obtained in simulations with a deformable tetragonal unit cell.

The value of q^* is nearly continuous across the transition, as observed in experiments. A combination of statistical scatter in the underlying data and finite size effects in results of $S(q)$ in the disordered phase at the ODT made it impossible for us to reliably measure very small discontinuities of the size reported in a recent synchrotron X-ray scattering experiment.[87] The predictions of the RPA theory, for $\chi_e N < 10.5$, and SCFT, for $\chi_e N > 10.5$, are shown by dashed curves. The nature and origins of deviations of the behavior of q^* in the disordered phase from the RPA prediction of $q_0^\star R_{g0} = 1.95$ are characterized in chapter 4.[78] The new result that is evident here is that our results for q^* in the ordered phase agree extremely well with SCFT predictions at corresponding

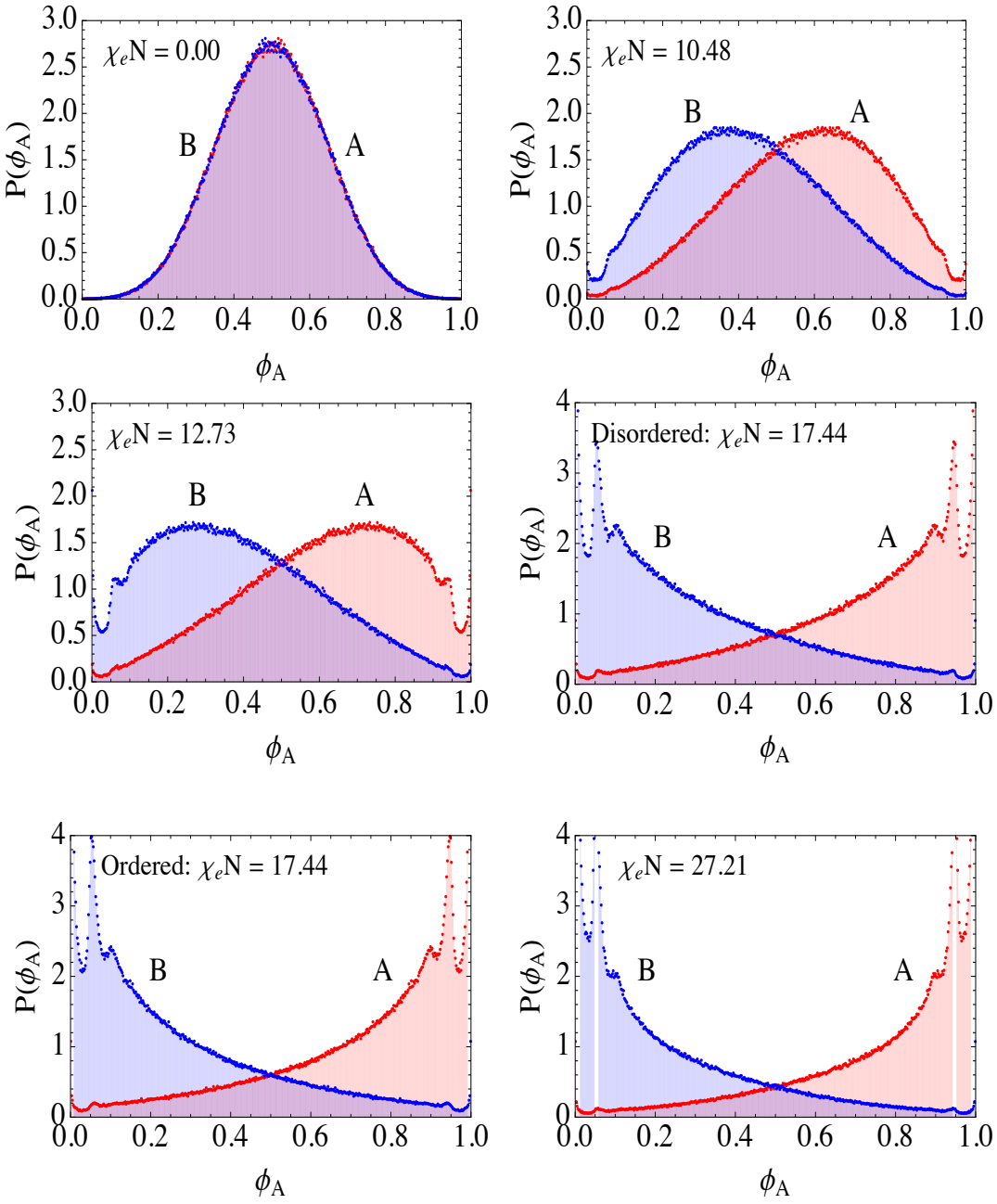

Figure 6.11: Probability distributions $P_A(\phi_A)$ and $P_B(\phi_A)$ for the composition ϕ_A of a small region around monomers of types A and B, respectively, for a series of $\chi_e N$ values from simulations of model S2-16 ($\overline{N}$ =960).

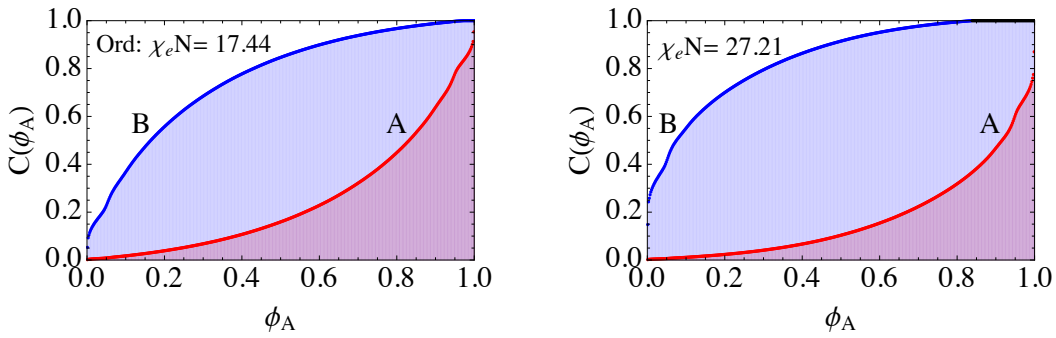

Figure 6.12: Cumulative probabilities $C_A(\phi_A)$ and $C_B(\phi_A)$ for the composition ϕ_A of a small region around monomers of types A and B, respectively, for simulations of model S2-16 ($\overline{N}$ =960).

values of $\chi_e N$. Taken together with the accuracy of SCFT predictions for g' (or the AB pair energy), this suggests that SCFT provides accurate predictions of both the structure and spacing of interfaces in the ordered phase.

Fig. 6.14 shows the value $q^\star_{\rm ODT}$ of the peak wavenumber at ODT, plotted *vs.* $\overline{N}$. Values of $q^\star_{\rm ODT}$ were obtained from measurements of domain spacing in the ordered phase at the ODT. The dashed curve shows the SCFT prediction for the domain spacing in the ordered phase calculated for each $\overline{N}$ using the value of $(\chi_e N)_{\rm ODT}(\overline{N})$ obtained from simulations, as given by Eq. 6.5. The data is adequately approximated over this range by a straight line on this semi-logarithmic plot, for which we obtain a best fit

$$(q^* R_{g0})_{\rm ODT} \simeq 1.12 + 0.07 \log(\overline{N}) \tag{6.11}$$

This empirical relationship does not approach the RPA result $q^* R_{g0} = 1.95$ in the limit $\overline{N} \to \infty$, and so should not be trusted much above the range of values studied in this work. Extension of the SCFT prediction to higher values of $\overline{N}$ would, however, show the correct limiting behavior.

6.8 Layer Compression Modulus

The one-dimensional elasticity of the ordered phase can be characterized by expressing the deviation $\delta G(d)$ of the free energy from its value at the equilibrium

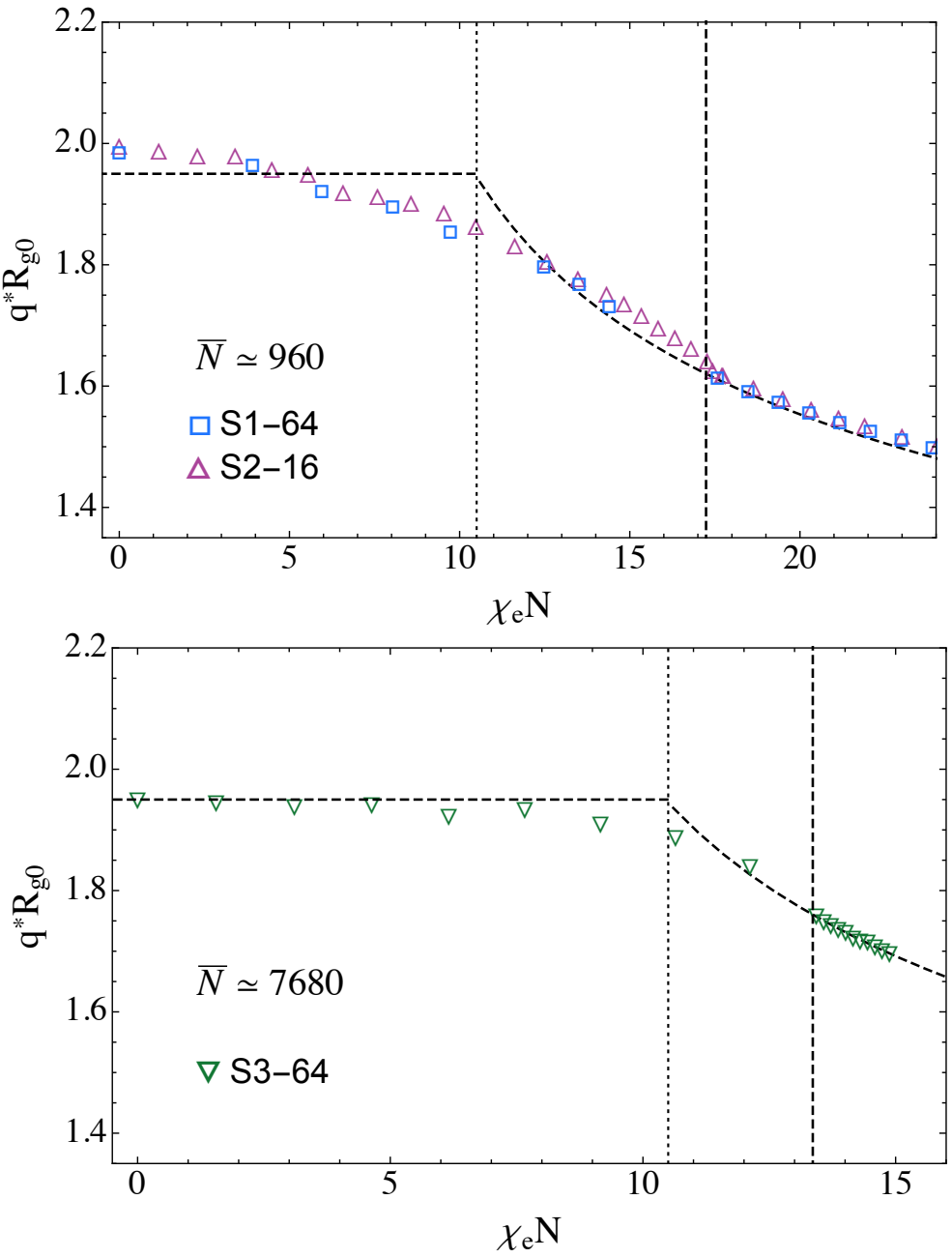

Figure 6.13: Simulation results for $q^\star R_{g0}$ *vs.* $\chi_e N$ for different $\overline{N}$ values, where $R_{g0} \equiv b\sqrt{N/6}$. The dashed curves represent RPA predictions for q^* in the disordered phase, for $\chi_e N < 10.5$, and SCFT predictions for $2\pi/d$ in the ordered phase, for $\chi_e N > 10.5$. In each plot, the dashed and dotted vertical lines indicate the measured ODT and the SCFT prediction respectively.

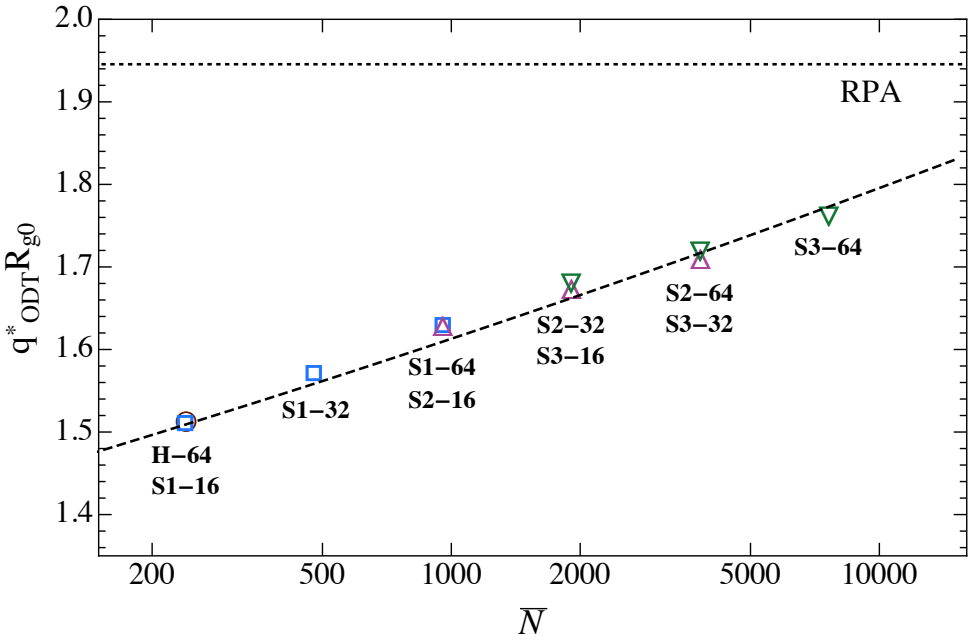

Figure 6.14: Summary of simulation results for $q^\star = 2\pi/d$ measured at the ODT, plotted *vs.* $\overline{N}$. The dashed curve is the SCFT prediction for systems with $\chi_e N$ given by Eq. 6.5 for $(\chi_e N)_{\rm ODT}(\overline{N})$.

domain spacing d^* as a harmonic function

$$\frac{\delta G}{V} = \frac{1}{2} B \epsilon^2 \tag{6.12}$$

where

$$\epsilon = (d - d^*)/d^* \tag{6.13}$$

is a dimensionless strain and B is a smectic compression modulus. The scaling relation given in Eq. 2.23 implies that the invariant modulus

$$\overline{B} \equiv BN/(ck_{\rm B}T) \tag{6.14}$$

should be a universal function of $\chi_e N$ and $\overline{N}$.

We measured the compression modulus using two methods: (1) a "passive" measurement, in which B was inferred from fluctuations in the domain spacing in a simulation with a fluctuating unit cell, or (2) an "active" measurement in which the pressure anisotropy in simulations with an imposed strain was

measured. Both types of simulation used a tetragonal unit cell with $L_x = L_y$.

In the passive method, we conducted NPT simulations of a tetragonal unit cell in which L_z can fluctuate independently of $L_x = L_y$. The value of B was then obtained from the Kubo relation $\langle \epsilon^2(d) \rangle = k_B T / VB$.

In the active method, we performed a series of constant temperature simulations (with a Nosé-Hoover thermostat) using a rigid tetragonal unit cell with a cell of length $L_z = (1 + \epsilon) L_{z0}$ that differs from the average unstrained length L_{z0} found in NPT simulations with a variable unit cell, but the same volume. We then measured the stress difference $\delta\sigma \equiv \sigma_{zz} - (\sigma_{xx} + \sigma_{yy})/2$ as a function of ϵ, and fit this to a linear function $\delta\sigma = -B\epsilon$ to estimate B. The inset of the upper panel of Fig. 6.15 shows an example of this stress difference *vs.* L_z/L_{z0} for a system with $(\chi_e N)_{\rm ord} = 45.8$. Tensile strains beyond a critical value were observed to produce a nonlinear response due to the buckling of lamellar layers and the formation of chevrons.[117,118]

Fig. 6.15 shows results for the linear modulus $\overline{B}$ *vs.* $\chi_e N$ for models S1-32 ($\overline{N} \simeq 480$) and S3-32 ($\overline{N} \simeq 3840$), corresponding to low and high values of $\overline{N}$ for which we have measured B. Results obtained by both passive and active methods are shown for system S1-32. Fig. 6.16 shows a summary of results for modulus $\overline{B}$ *vs.* $\chi_e N$ for all values of $\overline{N}$. The SCFT prediction for this quantity is shown in all these plots as a dashed line.

Several features are immediately clear from these results. Simulation results approach SCFT predictions at sufficiently large values of $\chi_e N$, deep in the ordered phase. Near the transition, however, the modulus drops significantly below SCFT predictions. The approach to SCFT predictions with increasing $\chi_e N$ is more rapid for larger $\overline{N}$. There is a slight overshoot in results for $\overline{B}$ for the relatively low value of $\overline{N} \simeq 480$, while results for the highest value of $\overline{N} = 3840$ show a more rapid monotonic approach to SCFT predictions from below.

The right side panel in Fig. 6.16 shows results of the dimensionless modulus measured at the ODT for different $\overline{N}$ values. A comparison to SCFT predictions for an ordered phase at $\chi_e N = (\chi_e N)_{\rm ODT}(\overline{N})$ shows that the measured value of $\overline{B}$ at the ODT is 20-30 % below this prediction. The dotted line is an empirical power law fit through the simulation data, which yields $\overline{B} \simeq 10.24 \overline{N}^{-0.2}$. The

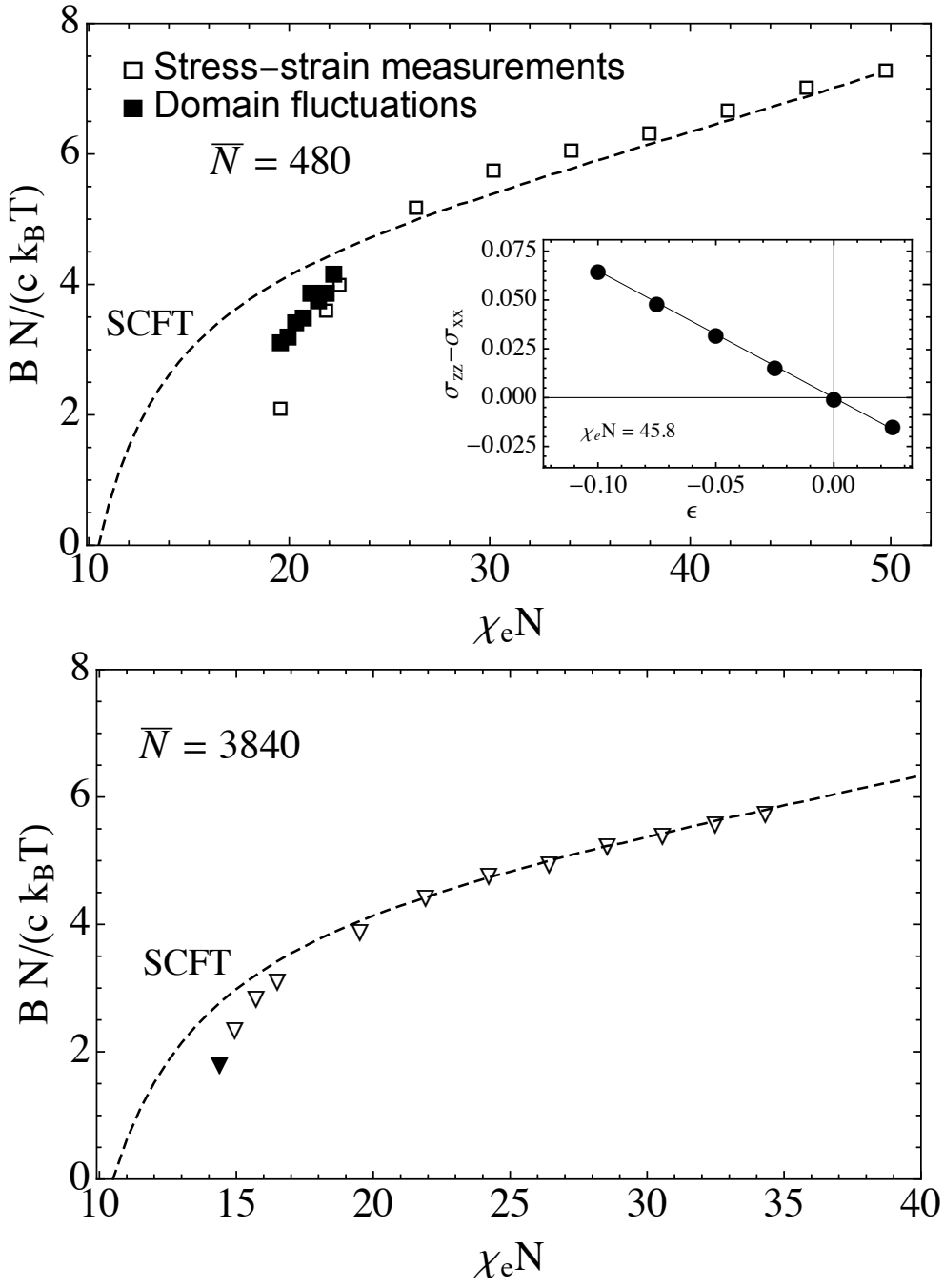

Figure 6.15: Results for the dimensionless modulus $\overline{B} \equiv BN/(ck_BT)$ *vs.* $\chi_e N$ for models S1-32 ($\overline{N}$ =480, left side panel) and S3-32 ($\overline{N} = 3840$, right side panel). In the left side panel, results obtained by active and passive measurements are shown in open and closed symbols, respectively. The inset to this panel shows an example of the measurements of stress difference $\sigma_{zz} - \sigma_{xx}$ *vs.* strain ϵ from NVT simulations of varying cell lengths.

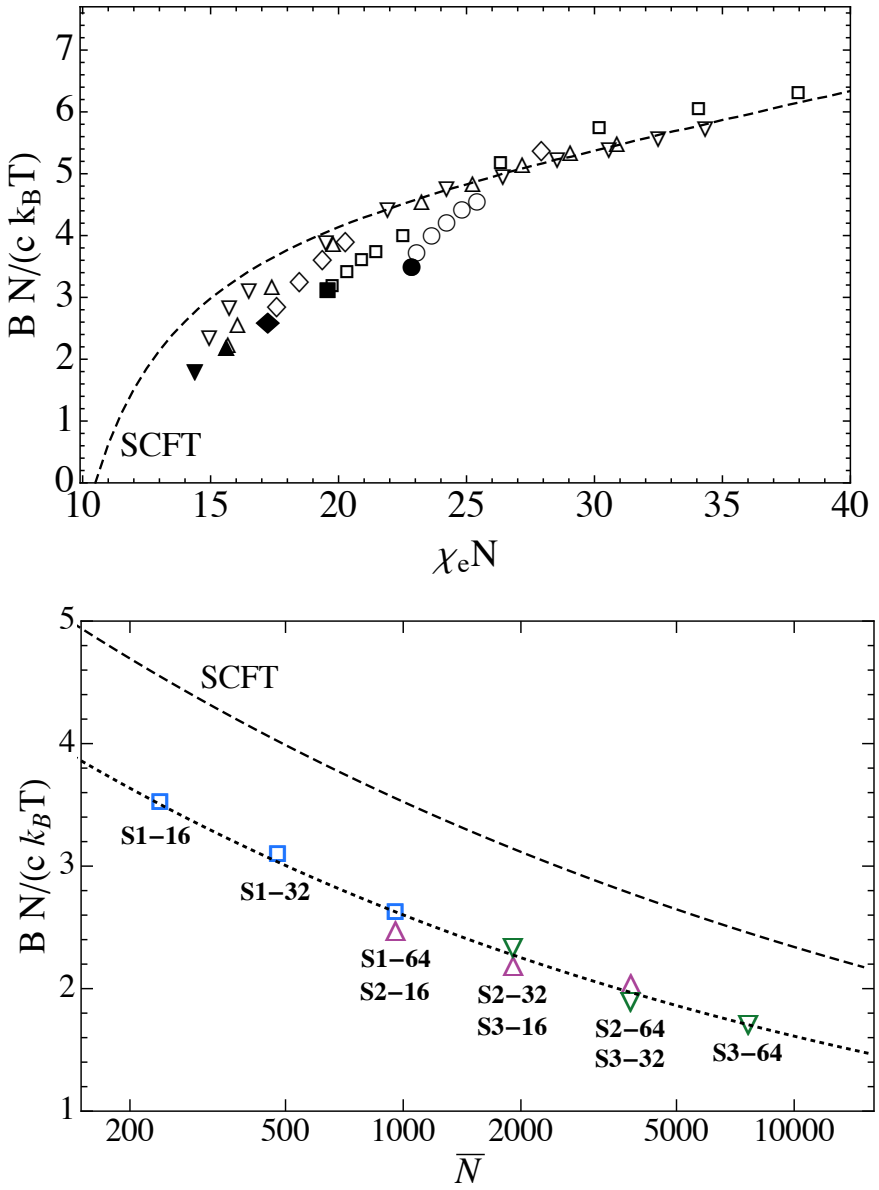

Figure 6.16: Left side panel: Dimensionless modulus $\overline{B} \equiv BN/(ck_{\rm B}T)$ *vs.* $\chi_e N$ shown for different $\overline{N}$ values. The dashed curve represents SCFT predictions. The values obtained at ODT are shown as closed symbols. Right side panel: Values of modulus at transition *vs.* $\overline{N}$. The dashed curve shows SCFT predictions for systems with $\chi_e N$ given by Eq. 6.5 for $(\chi_e N)_{\rm ODT}(\overline{N})$

magnitude of the discrepancy between simulation results and SCFT predictions for $\overline{B}$ is surprising in light of the accuracy of SCFT predictions for the values of g, g' and the layer spacing in the ordered phase at the ODT.

6.9 Incommensurability Effects

Simulations of ordered phases are susceptible to artifacts arising from incommensurability between the dimensions of the periodic simulation unit cell and the preferred dimensions of ordered phase unit cell. These can be avoided in some situations by using a deformable unit cell, as was done in some of our simulations of the ordered phase. In other cases, however, the issue remains problematic. For example, the strategy we used to design metadynamics simulations required that we design a cubic simulation cell that is commensurate with the expected value of the equilibrium layer spacing d at the ODT, despite uncertainty in our initial estimate of the value of d at the ODT.

It is thus useful to have a quantitative estimate of the magnitude of shift in the ODT that one might expect from boundary conditions that impose a given degree of strain. This can be estimated for the lamellar phase if one knows the magnitude of both the layer compression modulus B and the latent heat $\Delta g'$. Let $\Delta g = g_{\rm dis} - g_{\rm ord}$ denote the difference between g in the disordered and ordered phases, in the same simulation cell at the same simulation conditions. Consider Δg as a function of imposed strain ϵ and difference $\delta(\chi_e N) = \chi_e N - (\chi_e N)_{\rm ODT}(\epsilon = 0)$, where $(\chi_e N)_{\rm ODT}(\epsilon = 0)$ is the value of $\chi_e N$ at the ODT of a perfectly commensurate system. With the assumption that changes in simulation cell dimensions have negligible effect on g in the disordered phase, but do effect the ordered phase, we can expand

$$\Delta g(\chi_e N, \epsilon) \simeq \Delta g' \delta(\chi_e N) - \frac{1}{2}\overline{B}\epsilon^2 \quad , \tag{6.15}$$

where $\overline{B}$ is evaluated in the ordered phase at the ODT. Requiring that $\Delta g = 0$ at the ODT then yields a shift

$$\delta(\chi_e N)(\epsilon) \simeq \frac{\overline{B}}{2\Delta g'}\epsilon^2 \tag{6.16}$$

in the value of $\chi_e N$ at the ODT of a system subjected to strain ϵ.

As an example of the expected magnitude of this effect, consider a simulation performed in a periodic cubic $L \times L \times L$ unit cell of a system of symmetric diblock copolymers in which the lamellar phase has a preferred layer spacing d at the ODT. Assume that the system has enough freedom to spontaneously order in any orientation, corresponding to any reciprocal lattice vector $\mathbf{q} = (2\pi/L)(h,k,l)$, so as to produce an ordered state with a wavenumber $q = (2\pi/L)\sqrt{h^2+k^2+l^2}$ as close as possible to the preferred value of $q^* = 2\pi/d$. Fig. 6.17 shows the absolute magnitude of the minimum strain $\epsilon \simeq |q - q^*|/q^*$ for the reciprocal vector for which q is closest to q^*, as a function of the ratio L/d. This strain goes to zero at values of $L/d = \sqrt{h^2+k^2+l^2}$ for which the magnitude $|\mathbf{q}|$ for some reciprocal lattice vector becomes equal to the preferred value q^*. The maxima occur at values of L/d at which the preferred value of $\mathbf{q}$ changes from one vector for which $|\mathbf{q}| > q^*$ to another for which $|\mathbf{q}| < q^*$. The maxima tend to decrease with increasing L/d, because the increasing Fourier-space density of reciprocal lattice vectors with increasing box size L makes it increasingly easy to find a wavevector with a magnitude near any specified value. Over the range shown here, there are actually two different series of maxima. The sequence of lower, evenly spaced maxima correspond to maximum between minima that correspond to consecutive allowed integer values of $h^2+k^2+l^2$ that differ by 1. The higher irregular maxima that are visible at $L/d \simeq 2.65$, 3.87, 4.80, etc lie near values of $L/d \simeq \sqrt{7}, \sqrt{15}, \sqrt{23}$ etc. that are square roots of the relatively few integers 7, 15, 23, etc. that cannot be expressed as a sum of the squares of three integers.

For systems with $L/d \simeq 3$, such as those simulated here, the lower series of evenly spaced maxima in this curve have values of $\delta q/q \simeq 0.03$. For a system of this size with $\overline{N} \simeq 10^3$, for which $\Delta g' \simeq 0.008$ and $\overline{B} \simeq 2.8$, this would yield a maximum shift in $\chi_e N$ of $\delta(\chi_e N) \simeq 0.16$, or a fractional shift of about 1 %. This gives a sense of the maximum expected magnitude of errors from incommensurability alone in simulations of similar size in which the unit cell dimensions are not adjusted to be commensurate with the layer spacing.

In the case of our metadynamics simulations, for which we did fine-tune the cell size, the estimates of d that were used to design the simulation cell size gen-

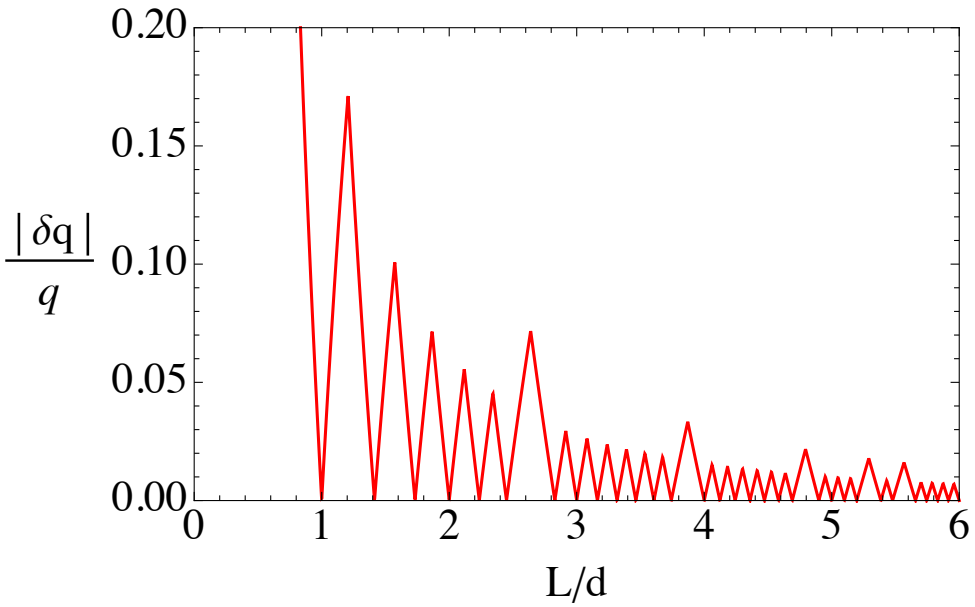

Figure 6.17: Imposed strain $\epsilon \simeq |\delta q|/q^*$ *vs.* L/d for an optimally aligned lamellar phase with a preferred layer spacing d in a cubic $L \times L \times L$ simulation cell. The strain at each value of L/d is calculated by identifying the reciprocal lattice vector for which $|\mathbf{q}|$ is closest to $q^* = 2\pi/d$.

erally agreed with the final estimates for d at the ODT to within less than 1 %. This yields maximum estimated errors in $(\chi_e N)_{\mathrm{ODT}}$ due to incommensurability of about 0.1 %, which is too small to effect any of the above results.

6.10 Conclusions

Simulations of systems of four models (H, S1, S2, and S3) have been analyzed and compared, focusing on behavior in the vicinity of the order disorder transition. Use of several different models with different levels of coarse-graining allowed us to span a wide range of $\overline{N} \simeq$200 - 8000 that covers a large part of the experimental range. By comparing results from several different models, we are able to confirm the scaling hypothesis that postulates that equivalent behavior should be obtained in corresponding states of different models, defined by equal values of the SCFT state parameter $\chi_e N$ and the overlap parameter $\overline{N}$. Results for all properties, including thermodynamic properties, such as the free energy and its derivatives, and structural properties, such as the composition profile

and layer spacing in the ordered phase, show excellent agreement with this hypothesis. The scaling hypothesis is found to apply for even surprisingly short chains: No significant deviations are found in comparisons involving chains with as few as 16 beads, or for $\overline{N}$ as small as 200. It is important to remember, however, that the scaling hypothesis has been suggested by theoretical treatments that are based on the Edwards model of polymers as continuous random walks with short-range interactions. This model cannot possibly apply to dimers or point particles, and so must eventually break down with decreasing N. For these simple models, however, universal behavior is found to apply for shorter chains than we expected.

Fredrickson-Helfand theory has a much more restricted range of validity than the scaling hypothesis. Our ODT results suggest that BLFH predictions regarding the phase transition become accurate for $\overline{N} \gtrsim 10^4$. This tentative conclusion is supported by the fact that BLFH predictions for the order parameter amplitude at the ODT seem to approach our data with increasing $\overline{N}$ and agree reasonably well with our results for the highest value $\overline{N} \simeq 8000$ that we studied. The accuracy of BLFH theory at higher values of $\overline{N}$ should thus be more directly tested by simulations with $\overline{N} > 10^4$. The reasonable agreement of BLFH theory predictions and results at $\overline{N} \simeq 8000$ implies that the range of validity of the BLFH theory is close to the more optimistic of two very different estimates provided by its authors,[34] and is about as wide as it could possibly be in light of the fact that the theory makes unphysical predictions for the order parameter amplitude for $\overline{N} \lesssim 10^3$.

Our conclusions regarding the range of validity of the BLFH theory are consistent with the results of recent field-theoretic Monte Carlo (FTMC) simulations by Stasiak and Matsen.[119] These authors conducted field theoretic simulations for systems with $\overline{N} = 10^4 - 10^6$, and found that the BLFH theory almost quantitatively described their results for ODT over this range. More direct comparisons of particle based and field-theoretic simulations would be very useful. Comparison to FTMC simulations similar to those of Stasiak and Matsen would be particularly useful because it would help clarify the consequences of the partial saddle-point approximation that underlies this type of FTMC simulation.

Within the range of values $\overline{N} \simeq 10^2 - 10^4$ studied here, the disordered and ordered phases near the ODT both appear to contain strongly segregated domains of almost pure A and B, in contrast to the assumption of weak segregation underlying the BLFH theory. In the ordered phase, the maximum local volume fraction $\max[\phi_A(z)]$ of A monomers in the middle of an A domain is 85 - 95 % throughout this range. Analysis of the effects of interfacial fluctuations upon the average composition profile suggests that this significantly underestimates the actual degree of segregation. Moreover, it has become clear that the disordered phase near the ODT is almost equally strongly segregated based on evidence of structural similarity of the two phases at the ODT, as quantified by the similarity of values for g' and the similarity of results for the distribution of local monomer-scale compositions.

These results suggest the existence of two different regimes of universal behavior at high and intermediate values of $\overline{N}$, with a crossover at $\overline{N} \sim 10^4$, and a third regime of non-universal behavior for very short chains. For $\overline{N} \gtrsim 10^4$, our results suggest that the BLFH theory applies, and we expect the degree of segregation at the ODT to slowly decrease with increasing $\overline{N}$. For the range $\overline{N} \lesssim 10^4$ studied here, all behavior remains universal, but the ordered and disordered phases are strongly segregated near the ODT, and the BLFH theory becomes progressively less accurate with decreasing $\overline{N}$. Most systems that have been studied experimentally have values of $\overline{N} \lesssim 10^4$, and thus fall in the strongly segregated regime. In addition, there must exist an oligomeric regime of even shorter chains for which the scaling hypothesis must fail. Studies of chemically realistic models with stiff angle and torsion potentials would be needed to predict where universality breaks down for real polymers.

Within the strongly-segregated universal regime, the extent of contact between A and B monomers, as characterized by the value of g', differs by about 7 % between the ordered and disordered phase at the ODT, almost independent of $\overline{N}$. If the AB contact in both phases occurs primarily along interfaces, and if the interfaces have similar intrinsic composition profiles in both phases, this implies that the interfacial area per unit volume decreases by approximately 7 % across the transition, as a result of the transition from a strongly segregated disordered bicontinuous structure to an ordered lamellar structure. The peak

wavenumber q^* is, however, nearly continuous across the ODT, as also seen in experiments.

SCFT provides a poor description of the disordered phase near the ODT, but makes surprisingly accurate predictions for several properties of the ordered phase. SCFT yields particularly accurate predictions for values of g' in the ordered phase near the ODT at modest values of $\overline{N}$, where the ordered phase is most strongly segregated. SCFT predictions for the free energy g are found to be excellent at intermediate values of $\overline{N} \sim 10^3$, but overestimate g by roughly 10^{-1} $k_{\mathrm{B}}T$ per chain for the lowest values of $\overline{N} \sim 200$ studied here. SCFT predictions for the layer spacing in the ordered phase are also surprisingly accurate, with errors of order one percent. The accuracy of SCFT predictions for free energies in the ordered lamellar phase suggests that SCFT might provide much more accurate predictions for order-order transitions than for order-disorder transitions, *if* SCFT calculations were carried out using sufficiently accurate methods of estimating χ parameters. This could be tested by comparing SCFT to experiments using values of $\chi(T)$ that are estimated using methods analogous to those used here to estimate the parameter dependence of χ in simulations.

Among the ordered phase properties we studied, the only one that is not accurately predicted by SCFT near the ODT is the layer compression modulus B. We find that B is very accurately predicted by SCFT sufficiently far above the ODT, particularly for large values of $\overline{N}$. Near the ODT, however, B exhibits a characteristic softening with decreasing $\chi_e N$ that is surprisingly not predicted by SCFT, giving measured values of B that are typically about 20 % below SCFT predictions at the ODT. A discrepancy of this magnitude is not consistent with the idea, suggested by our results for other properties, that the ordered phase is accurately described by SCFT near the ODT. It is conceivable that the softening of B near the ODT could be caused by an increased density of thermally excited layer perforations as the ODT is approached from above. We do not, however, understand how this or any other proposed explanation could cause significant deviations from SCFT predictions for B (i.e., the second derivative of g with respect to layer spacing d) without also causing significant deviations from SCFT predictions for the equilibrium layer spacing (the value of d at which g is minimum).

All of the comparisons of different simulation models to each other and to SCFT in this chapter depend critically upon how the parameter dependence of the Flory-Huggins parameter $\chi_e(\alpha)$ for each simulation model is estimated. The method we use[78,112] combines the use of perturbation theory for the linear dependence of $\chi_e(\alpha)$ on α at small values of α with a fit of the behavior of $S(q,\alpha)$ in the disordered phase to the ROL theory to estimate the nonlinear dependence at higher values of α. The strongest evidence for the accuracy of this estimate is the fact that it allows us to collapse results obtained from different simulation models for a variety of physical properties that were not used as inputs to the fitting procedure used to estimate $\chi_e(\alpha)$. Our conclusions about the accuracy of SCFT predictions are really conclusions about the accuracy of the combination of SCFT and this particular method of estimating $\chi_e(\alpha)$.

The procedure used here to estimate $\chi_e(\alpha)$ in simulations can also be used to estimate $\chi_e(T)$ in experiments, by fitting results of small-angle neutron scattering measurements of $S(q)$ to the ROL theory. In light of the observed accuracy of SCFT predictions for the ordered phase, we are hopeful that a combination of this method of estimating χ_e and SCFT could provide accurate predictions for order-order transitions, despite the inability of SCFT to describe order-disorder transitions for experimentally relevant chain lengths.

Chapter 7

Comparison to Experiments: PI-PLA Copolymers

This chapter presents a detailed quantitative comparison of experimental results, simulations results, and theoretical predictions for the structure and thermodynamics of low molecular weight symmetric ($f_{\rm PLA} \simeq 0.51$) poly(1,4-isoprene-b-DL-lactide) (PI-PLA or IL) diblock copolymers near the order-disorder transition (ODT). Small-angle neutron and X-ray scattering (SANS and SAXS) measurements obtained in the disordered phase of a PI-PLA symmetric copolymer with $N = 39$, designated as IL-1, are fit to the renormalized one-loop (ROL) theory in order to estimate the effective interaction parameter $\chi_e(T)$. Calorimetric measurements of the latent heat of the ODT for the same copolymer compare well with that obtained from corresponding coarse-grained simulations, when the comparison is based on this estimate of $\chi_e(T)$. The corresponding estimate of $(\chi_e N)_{\rm ODT}$ based on the experimental ODT temperature of this polymer is much closer to simulations master curve (Eq. 6.5) than to any theoretical prediction. A larger discrepancy between simulation and experimental results for $(\chi_e N)_{\rm ODT}$ is obtained for longer chains, with $N \geq 50$, when also calculated using $\chi_e(T, N = 39)$. Possible reasons for this discrepancy include the possibility of a significant end-group effect for these polymers. These results confirm the overwhelming importance of fluctuation effects in short diblock copolymers, and the usefulness of coarse-grained simulations as a starting point for quantitative modeling, but also indicate the need for attention to non-universal features of

specific polymers that can also become more important with decreasing chain length.

This chapter, which has been published recently in Ref.,[120] is the result of a collaboration between us and Dr. Timothy Gillard (a recent PhD graduate from Prof. Frank Bates's group and the primary author of this chapter). Specifically, all experiments were performed by Dr. Timothy Gillard, and the comparison of experimental results to simulations and theory was conducted by me. There is, however, an important difference between results presented here and those in the paper - here, we use homopolymer statistical segment lengths for block statistical segment lengths and include polydispersity effects, whereas in the paper, we used fitted estimates for block statistical segment lengths and ignored polydispersity effects. Both these points will be explained further in the main text.

The remainder of this chapter is organized as follows: We first present details of experimental measurements. We then present our analysis of experimental results from the IL-1 polymer, including the comparison of scattering measurements to the ROL theory, and a comparison of simulation and experimental results for $(\Delta H)_{\mathrm{ODT}}$ and $(\chi_e N)_{\mathrm{ODT}}$. Finally, we compare simulation results to experimental results for $(\chi_e N)_{\mathrm{ODT}}$ for several other nearly symmetric IL diblock copolymers of varying molecular weight, and state our conclusions. The next chapter is an extension of the below work, in that we compare experimental results of a few other nearly symmetric diblock copolymers that have been studied in literature to simulations results and theoretical predictions. The same analysis techniques as discussed below have been employed in the next chapter as well.

7.1 Experimental Section

Experiments described here were conducted on a poly(1,4-isoprene-b-DL-lactide) (IL) diblock copolymer designated IL-1. The synthesis, molecular characterization, and extensive thermodynamic characterization of this material have been previously described.[87] Briefly, the total number-average molecular weight $M_n = 2750\,\mathrm{g/mol}$ is divided between the poly(1,4-isoprene) (PI) (1130 g/mol)

and poly(DL-lactide) (PLA) (1620 g/mol) blocks and was determined using ^{1}H NMR experiments. The molecular weight dispersity $M_w/M_n = 1.10$ was determined by size exclusion chromatography (SEC) using tetrahydrofuran as the mobile phase (this value is slightly smaller than reported previously, attributable to the use of a different SEC instrument and a different solvent).[87] The volume fraction of PLA in IL-1 is $f_{\mathrm{PLA}} \simeq 0.51 \pm 0.01$ based on published densities[121,122] and the volumetric degree of polymerization $N = 39$, calculated using the reference temperature and repeat unit reference volume of $T_0 = T_{\mathrm{ODT}} = 96\,^{\circ}\mathrm{C}$ and $\nu_0 = 118\,\mathrm{\AA}^3$, respectively, used throughout this work. In addition to extensive characterization of IL-1, comparisons are made based on the previously reported thermodynamic properties of additional nearly symmetric IL diblock copolymers, IL-2, -3, -7, and -10, that have volume fractions of 0.54, 0.54, 0.55, and 0.50 and N values of 50, 51, 63, 58, respectively, calculated using the above reference volume and temperature.[87] All experimental values of N in this work are subject to an uncertainty of approximately ±5% resulting from uncertainties involved with molecular characterization.

7.1.1 Thermal Measurements

The glass transition temperatures, T_g, of the PI and PLA blocks of IL-1, measured by differential scanning calorimetry (DSC) experiments, are 61 and 20 °C, respectively. The symmetric IL-1 diblock forms an ordered lamellar (LAM) phase below the order-disorder transition temperature $T_{\mathrm{ODT}} = 96(1)\,^{\circ}\mathrm{C}$ as determined by DSC. IL-2, -3, -7, and -10 have reported T_{ODT} values determined by DSC of 114, 157, 112, and 147 °C, respectively.[87] Extensive thermal characterization using DSC of the ODT in IL-1 was detailed in the previous report.[87] The equilibrium value of the latent heat (enthalpy) of the ODT ($(\Delta H)_{\mathrm{ODT}}$) for IL-1 was measured in the range of 0.250.36 J/g, depending on details of the measurement (e.g. dT/dt and application of an annealing step).[87] For reliable measurements of $(\Delta H)_{\mathrm{ODT}}$, the DSC experiments required relatively fast temperature ramp rates ($dT/dt \geq 5\,^{\circ}\mathrm{C/min}$) and elaborate thermal profiles to ensure suitable signal-to-noise levels and flat baselines near the transition. To overcome these limitations and corroborate the DSC measurements of $(\Delta H)_{\mathrm{ODT}}$, a different type of calorimetric experiment, relaxation calorimetry, was performed to

measure $(\Delta H)_{\mathrm{ODT}}$ of IL-1. The details of these experiments are discussed in a separate publication.[123] Here, we simply report the main result that $(\Delta H)_{\mathrm{ODT}}$ of IL-1 was measured to be $0.26 \pm 0.02\,\mathrm{J/g}$, in general agreement with the DSC measurements. This builds confidence that the true equilibrium value of $(\Delta H)_{\mathrm{ODT}}$ is being measured by both techniques and is approximately $0.3\,\mathrm{J/g}$.

7.1.2 Small Angle Neutron Scattering (SANS)

Neutron scattering experiments were performed on the NG7 30 m SANS instrument at the National Institute of Standards and Technology Center for Neutron Research (NCNR) using a neutron wavelength of $\lambda = 6$Å, a wavelength spread $\Delta\lambda/\lambda = 0.115$, and a sample-to-detector distance of 2 m. The SANS data were corrected for background and empty cell scattering, sample transmission, sample thickness, and detector efficiency. The 2D data was converted to an absolute intensity scale, differential scattering cross section per unit volume, using measurements of the direct beam flux then radially averaged to obtain 1D plots of intensity versus the magnitude of the scattering momentum transfer vector $q = 4\pi\lambda^{-1}\sin(\theta/2)$, where θ is the scattering angle. The SANS patterns for IL-1 were collected on heating in a temperature control heating block at 105, 125, 165, and 185 °C. At each temperature, the sample was equilibrated for 5 minutes after the heating block had reached the desired set point before SANS patterns were recorded. The various calibration measurements (e.g. direct beam, background, empty cell, sample transmission etc.) were collected at 105 °C. This temperature profile was designed to minimize the amount of time the sample experienced at elevated temperatures to prevent polymer degradation. IL-1 SANS patterns were corrected for incoherent scattering by subtracting the sum of the measured q-independent incoherent scattering from PI ($M_n = 2640\,\mathrm{g/mol}$, $M_w/M_n = 1.06$) and PLA ($M_n = 9200\,\mathrm{g/mol}$, $M_w/M_n = 1.46$) homopolymers weighted by their respective volume fractions in the IL-1 diblock copolymer. Incoherent scattering from the homopolymers was measured at 105 and 185 °C and linear interpolation was used to estimate the values at intermediate temperatures.

7.1.3 Small Angle X-ray Scattering (SAXS)

SAXS experiments were conducted on the DND-CAT 5-ID-D beamline at the Advanced Photon Source (Argonne National Laboratory). Experiments utilized a sample-to-detector distance of 7495 mm and an x-ray wavelength of $\lambda = 0.729$Å. 2D SAXS patterns were collected with a Rayonix area CCD detector. All SAXS patterns were azimuthally symmetric and were integrated to obtain 1D plots of intensity (in arbitrary units) versus q. Prior to data collection, the sample was heated to 125 °C, well above the order-disorder transition temperature (see below) to eliminate any effects due to processing history, then slowly cooled (ca. 1 °C/min) to 90 °C, a protocol known to produce a well order equilibrium LAM phase. The sample was then heated to 185 °C, while stopping at several temperatures to collect scattering patterns. The sample was equilibrated at each temperature for approximately 1 minute prior to data collection while changes in temperature between measurements were fast (¿ 20 C/min). Data was similarly collected at several temperatures on cooling to 90 °C.

7.2 Results and Analysis

Most of our analysis is based on scattering measurements on the IL-1 polymer. In this section, we discuss how SAXS and SANS measurements were compared to ROL predictions in order to obtain estimates of $\chi_e(T)$ and how this estimate was used to compare experimental results for the latent heat of transition and ODT of this sample to corresponding simulation results.

7.2.1 Calibrating SAXS with SANS

To experimentally determine the peak position q^* and peak intensity $I(q^*)$ in the disordered (DIS) phase for IL-1 ($T_{\mathrm{ODT}} \approx 96$ °C, LAM at $T < T_{\mathrm{ODT}}$), we have used a combination of SANS and SAXS measurements that capitalizes on the advantages of both experimental methods. Specifically, a small number of SANS measurements were used to calibrate the intensity scale of a larger series of synchrotron SAXS measurements. This strategy overcomes instrument-smearing effects that lead to lower q resolution in SANS measurements by taking advan-

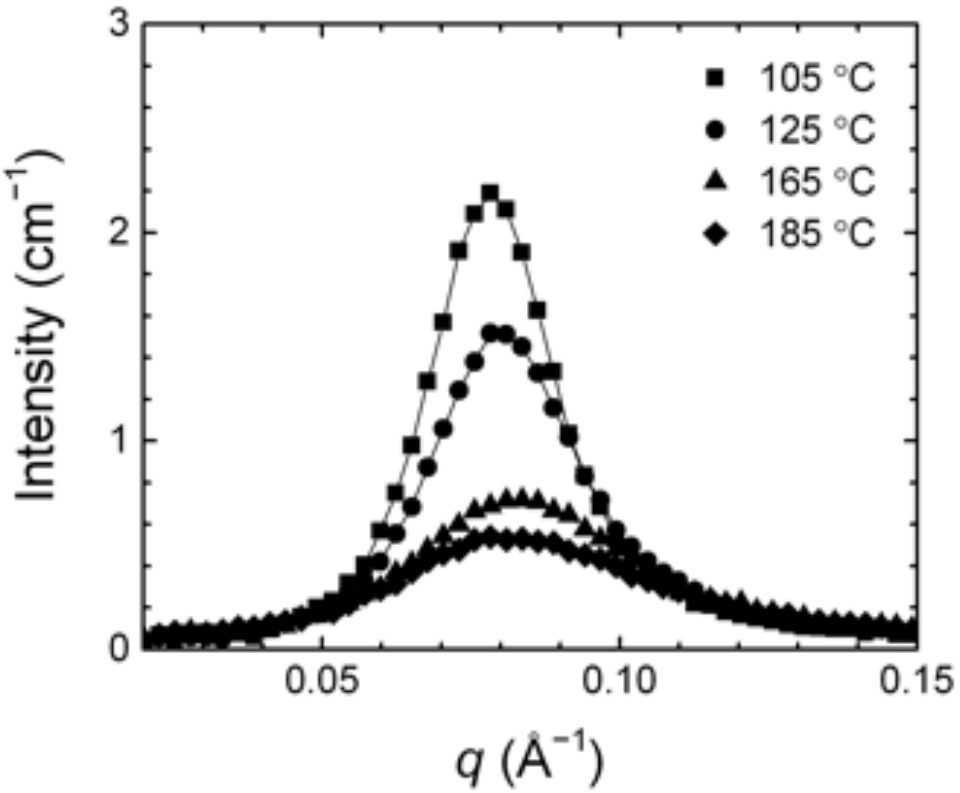

Figure 7.1: SANS intensity $I(q)$ patterns of IL-1 at four disordered phase temperatures. At each temperature, (smeared) intensity measurements $I_{\text{meas}}(q)$ are shown as circular points, and an empirical fit of measured data to a convolution function, as discussed in the main text, is marked by a solid curve.

tage of the excellent q resolution and much faster data collection of synchrotron SAXS. Using this strategy it is possible to obtain high quality scattering data with a meaningful, quantitative absolute intensity scale over a wide range of elevated temperatures quickly, avoiding the risk of degradation of the labile IL-1 material inherent in the longer experimental times required if SANS experiments alone were used.

Isothermal SANS patterns for IL-1 collected at four temperatures while heating in the DIS phase, i.e. above T_{ODT}, are shown in Fig.7.1. Isothermal SAXS patterns were collected every 510 °C from a minimum temperature of 80 °C (LAM phase) to a maximum temperature of 185 °C in the DIS phase during heating and cooling. Selected SAXS patterns are shown in Fig.7.2. For all temperatures above T_{ODT}, a single broad peak characteristic of the DIS phase is observed in the SANS and SAXS patterns, becoming less intense at higher

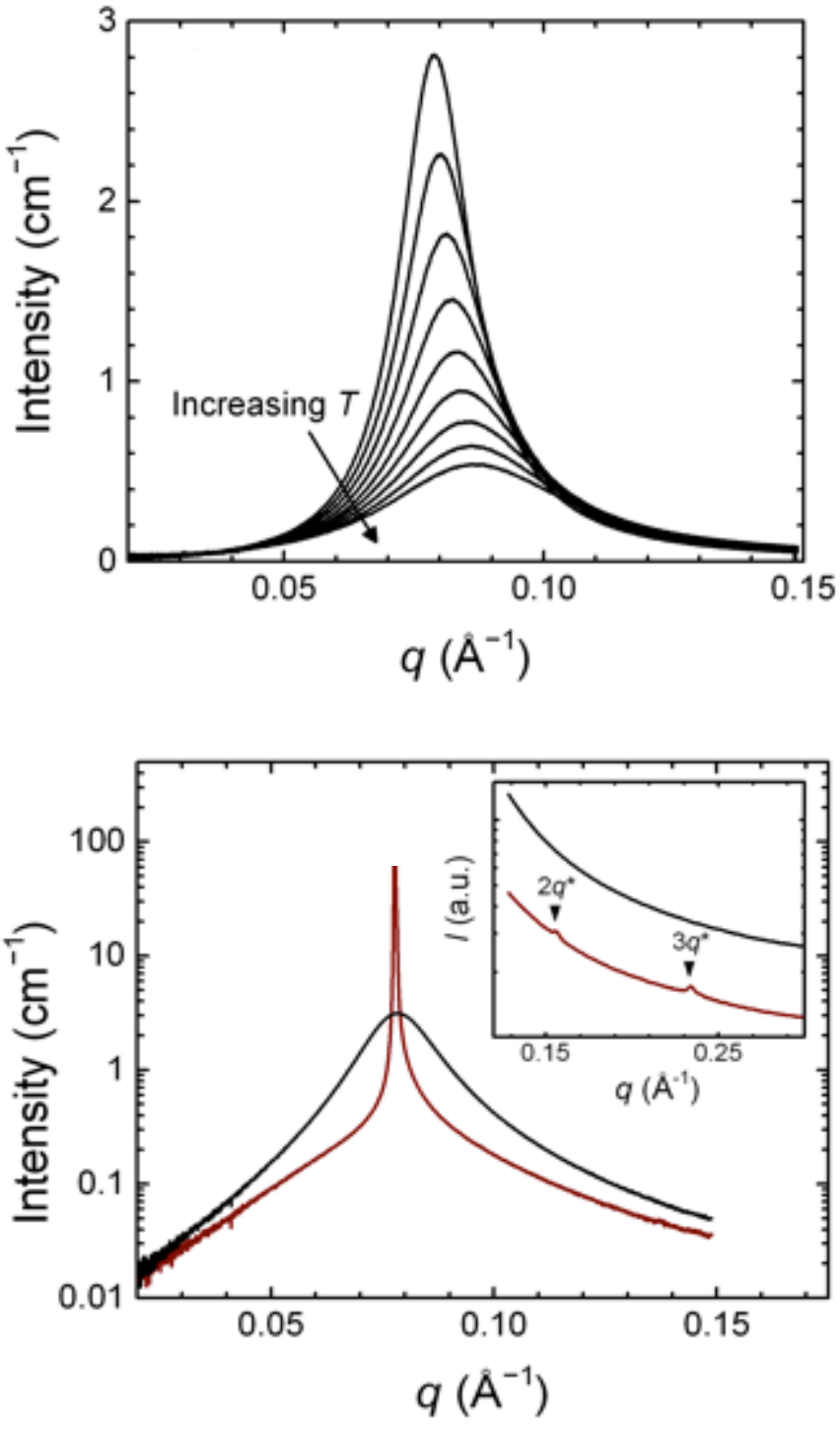

Figure 7.2: Upper panel: Selected SAXS patterns in the DIS phase collected at 105, 115, 125, 135, 145, 155, 165, 175, and 185 °C on heating. Lower panel: A comparison of SAXS patterns in the DIS phase at 100 °C (black lines) and the ordered LAM phase at 90 °C (red lines). High q data collected on the MAXS detector is shown in the inset.

temperatures, as can be seen in Fig.7.1 and upper panel of Fig.7.2. As shown in the lower panel of Fig.7.2, the SAXS patterns are dramatically different at temperatures below T_{ODT}. A narrow, intense primary peak appears (note the log scale on the intensity axis) with higher order Bragg peaks at relative positions $q/q^* = 2$ and 3, consistent with an ordered LAM phase as also seen in simulations results for $S(q)$ in ordered phase in Fig.3.6. In these experiments, the higher-order Bragg reflections (q/q^* =2, 3) were above the experimentally accessible maximum q of the SAXS detector but were captured on the so-called middle angle (MAXS) detector of the recently upgraded instrument at the DND-CAT 5-ID-D beamline, as shown in the inset of the lower panel of Fig.7.2.

The SAXS data presented here were collected on a relative intensity scale. To determine $S^1(q^*)$, the quantity required for comparison to theory and simulation, it is necessary to convert the experimental SAXS data to an absolute intensity scale. This process was accomplished using the absolute calibrated SANS data with a method outlined in Fig.7.3. The SAXS patterns were smeared with the known instrument resolution function for the configuration used during SANS data collection as shown in the upper panel of Fig.7.3. The peak intensity $I(q^*)$ was then extracted from the smeared SAXS data and the (inherently smeared) SANS data at each experimental temperature. $I^1(q^*)$ was plotted as a function of T^1. The data set extracted from the smeared SAXS data was scaled by a single calibration factor adjusted to allow the SAXS data to overlay the absolute intensity SANS data on the $I^1(q^*)$ *vs.* T^1 plot, as shown in the lower panel of Fig.7.3. This procedure allows us to convert the SAXS data to the absolute intensity scale of the SANS measurements (i.e. the differential scattering cross section per unit volume based on the scattering length density contrast in neutron scattering measurements). To convert the unsmeared SAXS patterns to the intensity scale appropriate to the SANS experiment, the extracted calibration factor is then applied to the full SAXS data set. The temperature dependence of q^* and $I^1(q^*)$ were extracted from the resulting calibrated, unsmeared SAXS data. The results are plotted in Fig.7.4.

As shown in the upper panel of Fig.7.4, q^* changes continuously through the T_{ODT}, with no measurable discontinuity in q^* at the transition. The temperature dependence of q^* obtained here from isothermal SAXS measurements is

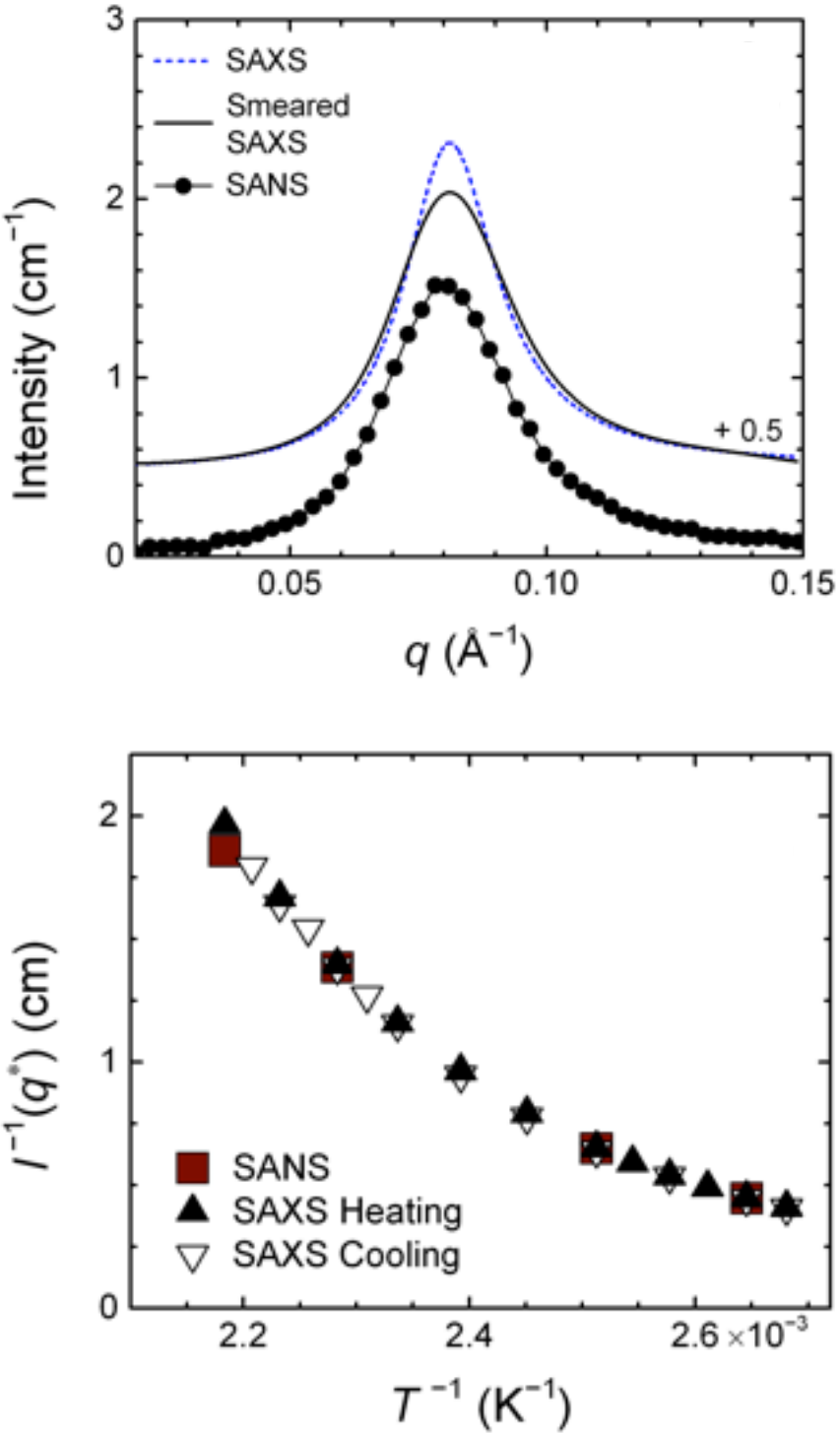

Figure 7.3: Routine used to convert SAXS patterns to the SANS absolute intensity scale. Upper panel: The SANS pattern, SAXS pattern, and SAXS pattern smeared with the SANS instrument resolution function, all collected at 125 °C. Lower panel: $I^1(q^*)$ as a function of T^1 extracted from SANS (squares) and smeared SAXS measurements (triangles). The SAXS calibration factor of 5.13 is extracted by scaling the smeared SAXS data to overlay the SANS data.

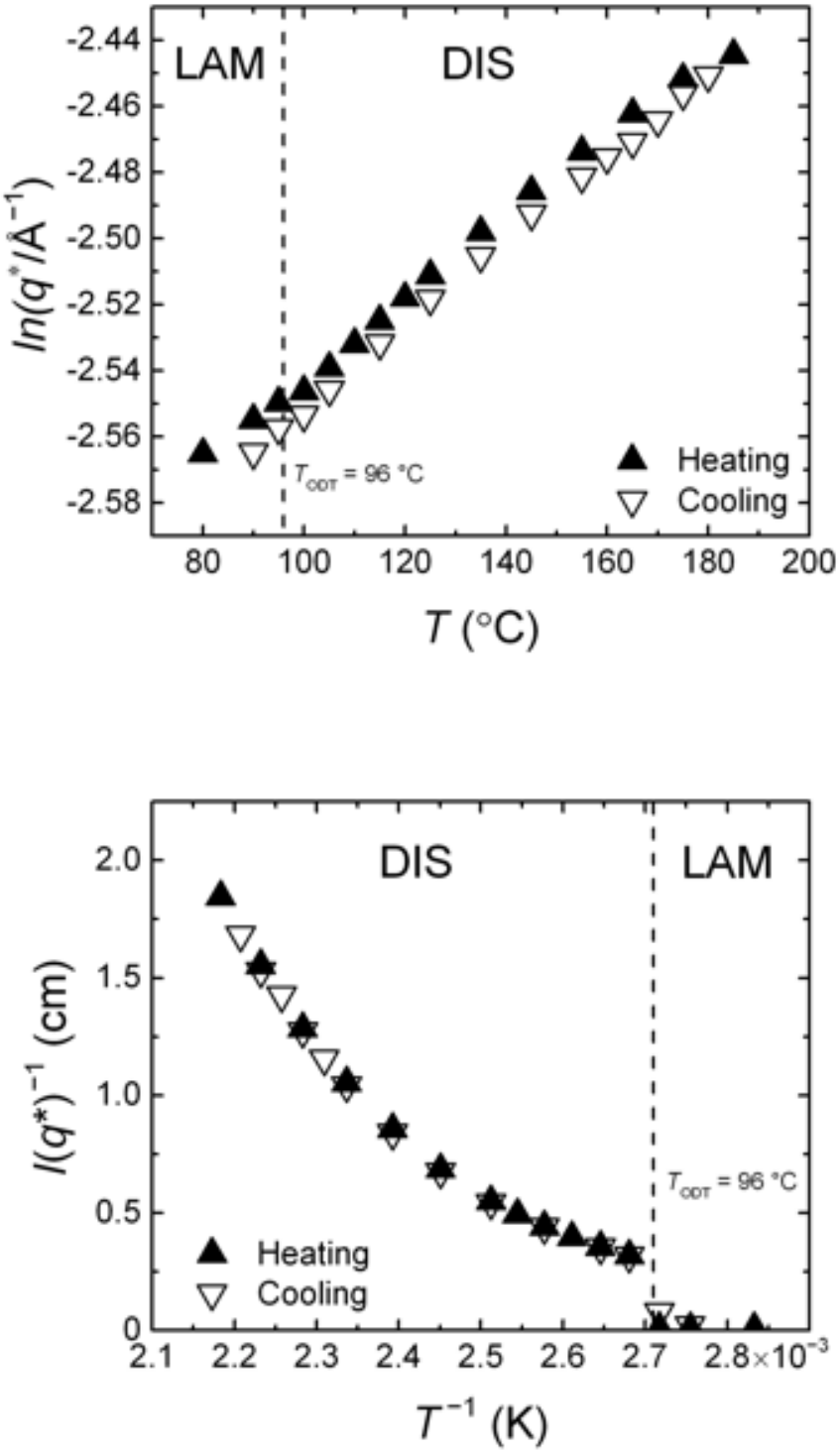

Figure 7.4: Upper panel: Temperature dependence of q^* extracted from SAXS measurements. Lower panel: Temperature dependence of $I^1(q^*)$ extracted from SAXS measurements.

consistent with that extracted previously from SAXS measurements collected for IL-1 during a dynamic heating ramp (dT/dt =10 °C/min).[87] The inverse peak intensity $I^1(q^*)$ shown in the lower panel of Fig.7.4 does exhibit a large discontinuous change at T_{ODT}. $I(q^*)$ for the primary Bragg peak in the LAM phase is orders of magnitude larger than that of the diffuse peak associated with the DIS phase, as seen in the lower panel of Fig.7.2. Departure from linearity in $I^1(q^*)$ on T^1 in the lower panel of Fig.7.4 is inconsistent with the prediction of the random phase approximation (RPA), indicative that fluctuation effects are important throughout the experimentally accessible range of temperatures for this polymer. To convert the calibrated values of $I^1(q^*)$ of Fig.7.2 to the relevant quantities related to the structure factor for comparison to the ROL theory, the neutron scattering contrast factor must be taken into account. Specifically, according to the notation used throughout this work and in Ref.:[78] $S(q^*) = I(q*)/[\nu_0\,(\Delta\mathrm{SLD})]^2$, where $(\Delta\mathrm{SLD}) \equiv |l_A/\nu_A - l_B/\nu_B|$ is the difference in coherent neutron scattering length densities of the PI and PLA blocks (2.4×10^7 and 1.6×10^6 Å^2, respectively at 140 °C). We note that $S(q)$ has the units of number concentration of monomers and is related to the dimensionless structure factor common in the experimental literature, $S_{\mathrm{Exp}}(q)$, through normalization by the monomer reference volume $S_{\mathrm{Exp}}(q) = \nu_0 S(q)$.

7.2.2 Comparison of Scattering Results to ROL Theory

Here, we discuss the analysis required to estimate $\chi_e(T)$ by fitting ROL predictions to the scattering results discussed above. Before attempting such a fit, we must compute or estimate values for N and the monomer statistical lengths, which (along with χ_e) are required as inputs to the theory. In what follows, we define volumetric degrees of polymerization, statistical segment lengths and an interaction parameter $\chi_e(T)$ using a fixed segment volume of $\nu_0 = 118$ Å^3. Volumetric degrees of polymerization for both blocks are calculated from the block molecular weights and densities of the pure materials. These are given by $N_{\mathrm{PI}}(T) = M_{\mathrm{PI}}/\left(\nu_0 N_{\mathrm{Avo}} \rho_{\mathrm{PI}}(T)\right)$ for PI and $N_{\mathrm{PLA}}(T) = M_{\mathrm{PLA}}/\left(\nu_0 N_{\mathrm{Avo}} \rho_{\mathrm{PLA}}(T)\right)$ for PLA, where M_{PI} and M_{PLA} are the number average molecular weights of the two blocks, $\rho_{\mathrm{PI}}(T)$ and $\rho_{\mathrm{PLA}}(T)$ are temperature-dependent densities of the two species, and N_{Avo} is Avogadros number. Because the densities

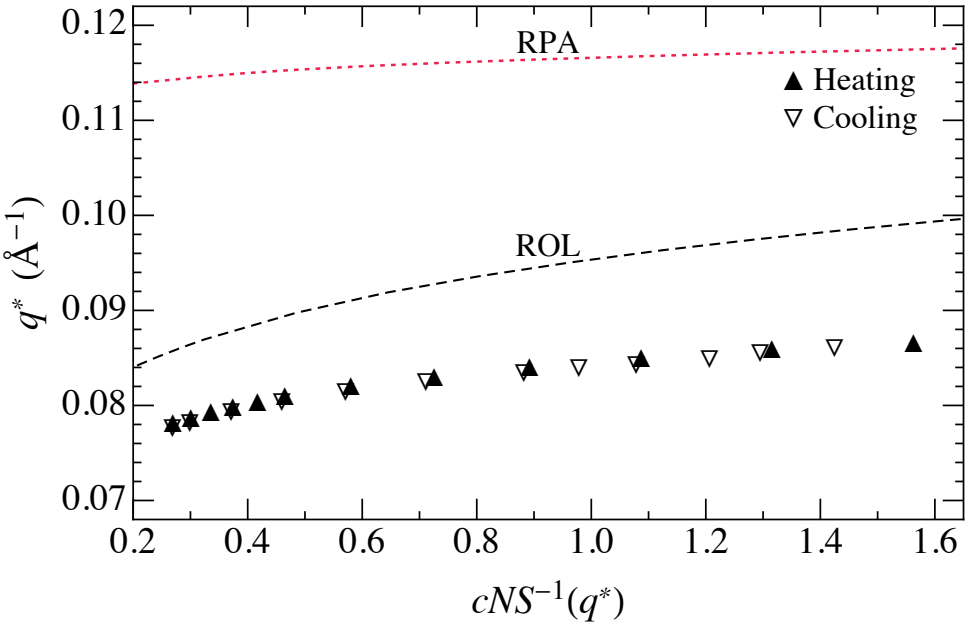

Figure 7.5: Comparison of the temperature dependence of q^* of IL-1 (triangles) to RPA (red dashed line) and ROL (black dashed line) theory predictions.

of both pure materials vary with temperature, our use of a fixed monomer reference volume yields definitions for N_{PI} and N_{PLA} that also vary slightly with temperature. Values for the monomer statistical segment lengths b_{PI} and b_{PLA} of the PI and PLA blocks are assumed to be equal to those obtained in literature from measurements on homopolymer melts of PI and PLA. Converting literature results to our chosen segment volume ($\nu_0 = 118\,\text{Å}^3$) yields statistical segment lengths $b_{\mathrm{PI}} = \exp\left[(1/2)(0.0004T + 3.445)\right]$ Å and $b_{\mathrm{PLA}} = \exp\left[(1/2)(0.00141T + 4.484)\right]$ Å.[124–126] This yields values of $b_{\mathrm{PI}} = 6.0$Å, $b_{\mathrm{PLA}} = 7.2$Å, and $\overline{N} \equiv N(T)(f_{\mathrm{PI}}b_{\mathrm{PI}}^2(T) + f_{\mathrm{PLA}}b_{\mathrm{PLA}}^2(T))^3/\nu_0^2 = 267$ at a reference temperature of 96 °C. Below, we show a comparison of SAXS results for q^* of IL-1 to theoretical predictions. We focus on a comparison to predictions of the ROL theory because the ROL theory, as illustrated in chapter 4, provides accurate predictions for structure factor behavior in simulations, thus allowing the ROL theory to be used as a surrogate for simulations results.

Fig. 7.5 shows the comparison. There, we plot q^* *vs.* the normalized inverse peak structure factor $cNS^{-1}(q^*)/2$, where c is the number concentration of monomers and equal to ν_0^{-1}. The advantage of plotting the data in

this manner is that it allows a comparison of results for q^* to ROL predictions in a way that does not require us to first estimate how $\chi_e(T)$ depends on temperature. Note that in simulations too (see Fig.4.9), we employed the same trick by plotting q^* as a function of the apparent interaction parameter $\chi_a^\star N \equiv 10.495 - (cNS^{-1}(q^*)/2)$, where $\chi_a^\star$ is, by definition, equal to the value of χ_e that would be inferred by fitting the measured inverse peak structure factor to the RPA prediction, $cNS^{-1}(q^*) \equiv 2\,(10.495 - \chi_e N)$. In the figure, SAXS results are shown in triangles. The simplest theoretical prediction is provided by the RPA, according to which $q^* R_{g0}$ is a constant (1.9495 for perfectly symmetric copolymers) at all temperatures in disordered phase of diblock copolymers. The RPA prediction, which is shown as a red dashed line labeled RPA, is approximately 20% larger than the experimental results. ROL theory predictions, evaluated at $\overline{N} = 267$, are marked as a black dashed line labeled ROL. Use of the ROL theory reduces the discrepancy, but yields predicted values of q^* that are still approximately 10% larger than experimental values. As shown in the next chapter, discrepancies of similar magnitudes are observed in all the other experimental systems we have analyzed in this work. In light of the excellent agreement obtained between ROL theory predictions and results of q^* from simulations, as discussed in chapter 4, the level of discrepancy seen here is disturbing.

A key difference between systems in simulations and IL-1 is that, simulations systems can be designed to have perfectly symmetric blocks with precisely the same statistical segment lengths and chain lengths whereas experimental polymers are prone to slight asymmetries such as different statistical segment lengths for the two blocks, as well as slightly different values for block chain lengths. These slight asymmetries were, therefore, taken into account in the evaluation of ROL theory predictions by using input parameters for block chain lengths and statistical segment lengths that are slightly different for the two blocks. The other important difference between our simulations systems and real experimental samples is the polydisperity in molecular weight (or chain length) of experimental samples. As discussed in appendix A and section 8.1.4, polydispersity affects the behavior of $S(q)$ significantly and shifts both peak wavenumber and peak structure factor considerably. Here, we simply use results derived in

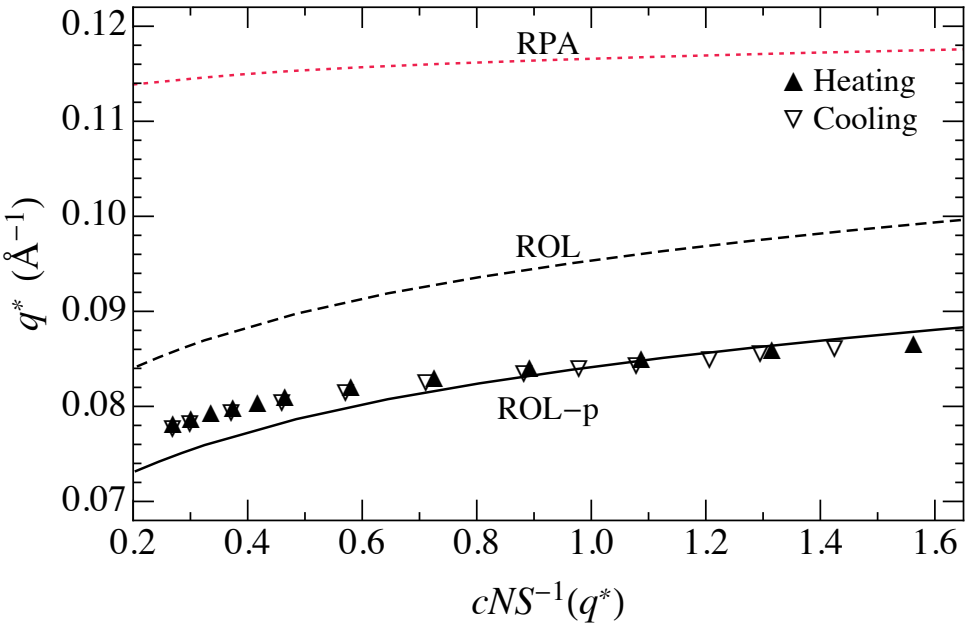

Figure 7.6: Comparison of the temperature dependence of q^* of IL-1 (triangles) to monodisperse RPA (red dashed line) and ROL (black dashed line), as well as polydispersity-corrected ROL theory predictions (black solid curve labeled ROL-p). RPA polydispersity shift was calculated based on measured PDI of 1.10.

section 8.1.4 for polydispersity corrections to ROL theory predictions. The polydispersity corrected ROL theory predictions are shown in a black solid curve, labeled ROL-p. It is evident that inclusion of polydispersity effects improves the agreement between SAXS results of IL-1 (PDI = 1.10) and ROL theory predictions drastically.

In our recent publication of this work,[120] we did not consider polydispersity effects in evaluation of theoretical predictions, and instead used a fitting procedure in which corrections to the literature values of statistical segment lengths of PI and PLA blocks were obtained to resolve the disagreement between the monodisperse ROL theory predictions and experimental results. We chose to allow for such corrections because it is known that the statistical segment length of a polymer depends somewhat upon its chemical environment, and can thus be somewhat different in an environment that contains a mixture of two blocks than in a homopolymer. We, however, found the magnitude (20%) of the required correction to be surprisingly large based on what is known about the sensitivity of statistical segment lengths to changes in chemical environment. For this reason and to keep the analysis of experimental scattering results consistent with our analysis of simulations results, we chose to ignore the larger "corrected" statistical segment lengths here onward. Note that a 20% increase in statistical segment lengths implies approximately a three-fold increase in the value of $\overline{N}$, which in turn affects the $\chi_e(T)$ estimate that is obtained from a fit of $S^{-1}(q^*)$ *vs.* T data to ROL theory predictions.

By assuming a function of the form $\chi_e(T) = A/T + B$, we fitted the measured temperature dependence of the peak structure factor $S(q*)$ for IL-1 to monodisperse ROL theory predictions at $\overline{N} = 267$. Fig.7.7 illustrates the excellent quality of the fit; resulting fitted estimate is $\chi_e(T) = 531.4T^1 - 0.75$. On including RPA predicted polydispersity shift, as discussed in section 8.1.4, we get $\chi_e^{\mathrm{ROL-p}}(T) = 531.4T^1 - 0.77$. This estimate is different from $\chi_e(T) = 381T^1 - 0.48$ reported previously,[120] which is largely attributable to the use of a different value for $\overline{N} = 631$ based on corrected or fitted statistical segment lengths.

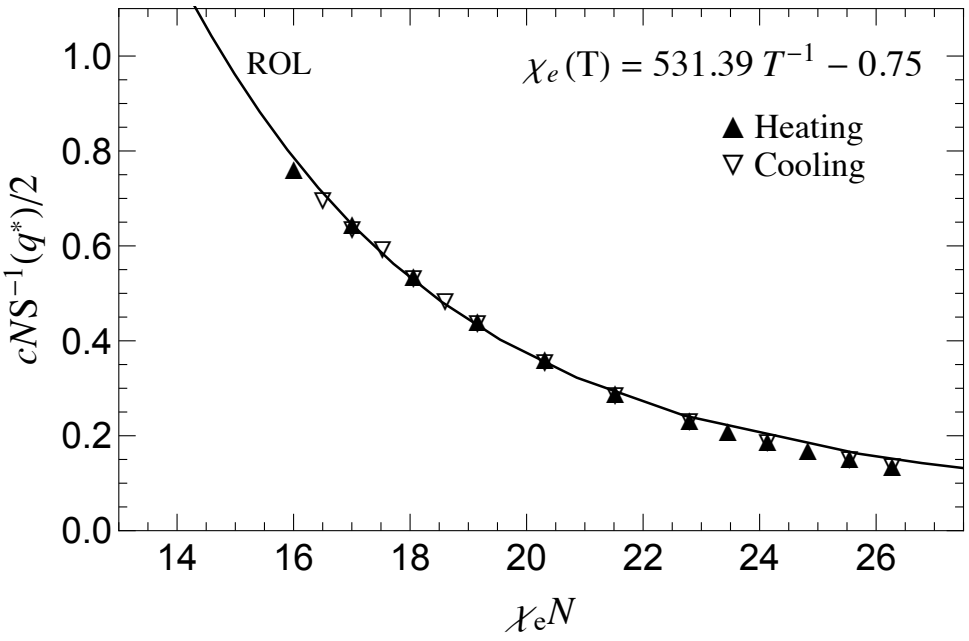

Figure 7.7: Extraction of $\chi_e(T)$ by fitting the temperature dependence of $S^1(q^*)$ to the ROL theory with $\overline{N} = 267$ (solid line). The dashed line is the RPA prediction.

7.2.3 Comparison of Latent Heat of Transition

Analysis of simulations results in section 6.4 yields a universal scaling law for latent heat $(\Delta g')_{\rm ODT} \equiv g'_{\rm dis} - g'_{\rm ord}$ in terms of the invariant degree of polymerization $\overline{N}$. In order to compare experimental and simulations results of latent heat, we use Eq. 6.4 of chapter 6, according to which the free energy derivative g' and excess enthalpy H of a diblock copolymer are related through $g' = \frac{\langle H \rangle}{NM}\left[k_{\rm B}\frac{d\chi_e(T)}{d(1/T)}\right]^{-1} = \frac{\langle H \rangle}{NM}\frac{1}{k_{\rm B}A}$. In the last expression, we have taken $\partial\left(\chi_e(T)/\,\partial(1/T)\right. = A$ based on the approximation $\chi_e(T) = A/T + B$. This implies $(\Delta g')_{\rm ODT} = \frac{(\Delta H)_{\rm ODT}}{NM}\frac{1}{k_{\rm B}A}$, where $(\Delta H)_{\rm ODT}$ is the latent enthalpy of transition that is measured in calirometry experiments. This equation allows us to compare results for the latent heat from experiments and simulations.

According to the simulation results, $(\Delta g')_{\rm ODT} \simeq 0.006 \pm 0.0005$ at $\overline{N} = 267$, where the uncertainty is an estimate of the scatter of results obtained from different simulation models. On substituting above estimate for $A = 531.4K$ in equation $(\Delta g')_{\rm ODT} = \frac{(\Delta H)_{\rm ODT}}{NM}\frac{1}{k_{\rm B}A}$, we get $(\Delta H)_{\rm ODT} = 0.38$J/g based on the

molecular weight 2750 g/mol of IL-1. This prediction is slightly greater than the range of the measured values $(\Delta H)_{\mathrm{ODT}} = 0.250.36\mathrm{J/g}$ determined by DSC, and the more precise value of $(\Delta H)_{\mathrm{ODT}} = 0.3\mathrm{J/g}$ determined independently by relaxation calorimetry.[123] This level of agreement is nevertheless encouraging in light of the fact that the analysis required to compare simulation and experimental results for latent heat depends sensitively on how we estimate χ_e.

7.2.4 Comparison of Order-Disorder Transition

Next, we compare ODT measurements of IL-1 ($\overline{N} = 267$) to simulation results for the ODT. As reported in chapter 6, results of several simulation models yield a master curve for $(\chi_e N)_{\mathrm{ODT}}$ *vs.* $\overline{N}$ (Eq. 6.5) when χ_e is estimated for each model by a procedure similar to that used above. Using the estimate of $\chi_e(T)$ obtained above, we obtain $(\chi_e N)_{\mathrm{ODT}}$ of IL-1. In Fig.7.8, we show this experimental result on the same plot as the simulation results, along with SCFT and BLFH predictions for the ODT. The estimated value of $(\chi_e N)_{\mathrm{ODT}}$ is much closer to the simulation results than to either BLFH or (particularly) SCFT predictions.

7.2.5 Dependence of ODT on Molecular Weight

To this point, our analysis has exclusively considered experimental data for the IL-1 polymer. However, values of T_{ODT} of 5 nearly symmetric IL diblock copolymers of varying molecular weight were also reported in Ref.,[87] of which IL-1 was the lowest in molecular weight. These additional data points allow an extension of our analysis to the chain length dependence of $(\chi_e N)_{\mathrm{ODT}}$ based on our estimate of $\chi_e(T)$, as well as providing a test of the robustness of various methods used to extract $\chi_e(T)$. It is important to note that the only polymer for which disordered phase scattering data was collected and analyzed in the fashion described above was IL-1. T_{ODT}s for all polymers were determined by DSC.

Fig.7.9 shows experimental results for $(\chi_e N)_{\mathrm{ODT}}$ for this series of IL polymers plotted *vs.* $\overline{N}$ calculated using several different methods of estimating $\chi_e(T)$. The most stringent comparison of experiment and simulations, shown by black

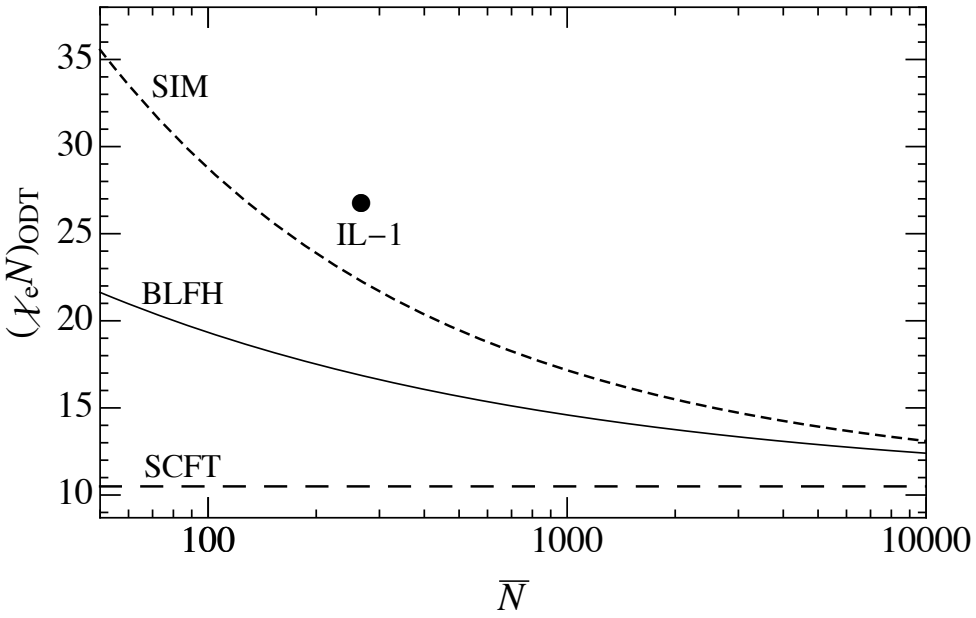

Figure 7.8: Comparison of experimental value of $(\chi_e N)_{\mathrm{ODT}}$ of IL-1 to the simulations master curve given by Eq.6.5 (dashed line) and theoretical predictions (SCFT long dashed line; BLFH - solid line).

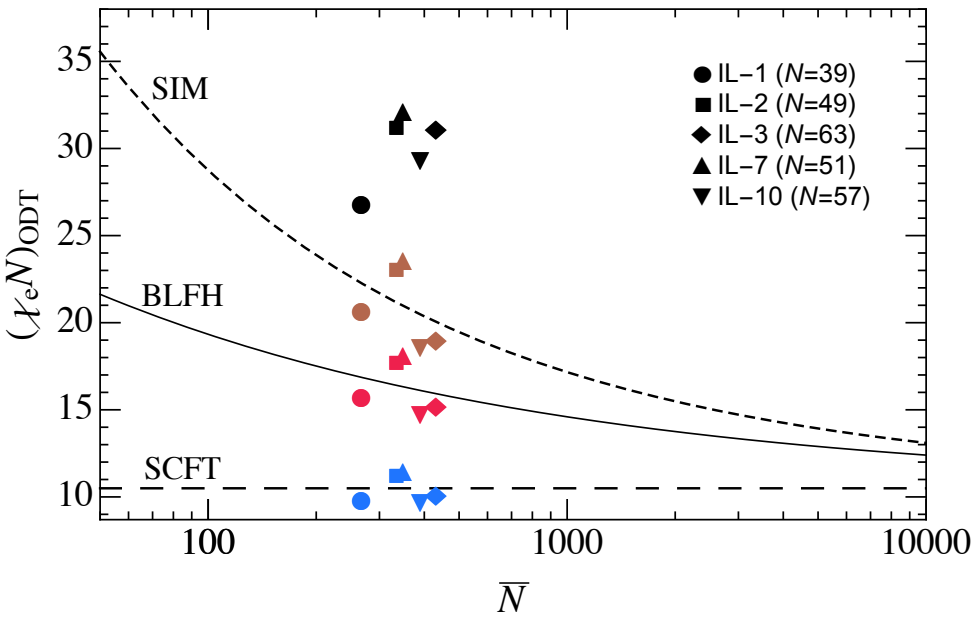

Figure 7.9: Comparison of experimental values of $(\chi_e N)_{\mathrm{ODT}}$ calculated using the four different $\chi_e(T)$ functions shown in Fig.7.10 (ROL black symbols; SIM-ODT brown symbols; BLFH-ODT - red symbols; SCFT-ODT blue symbols).

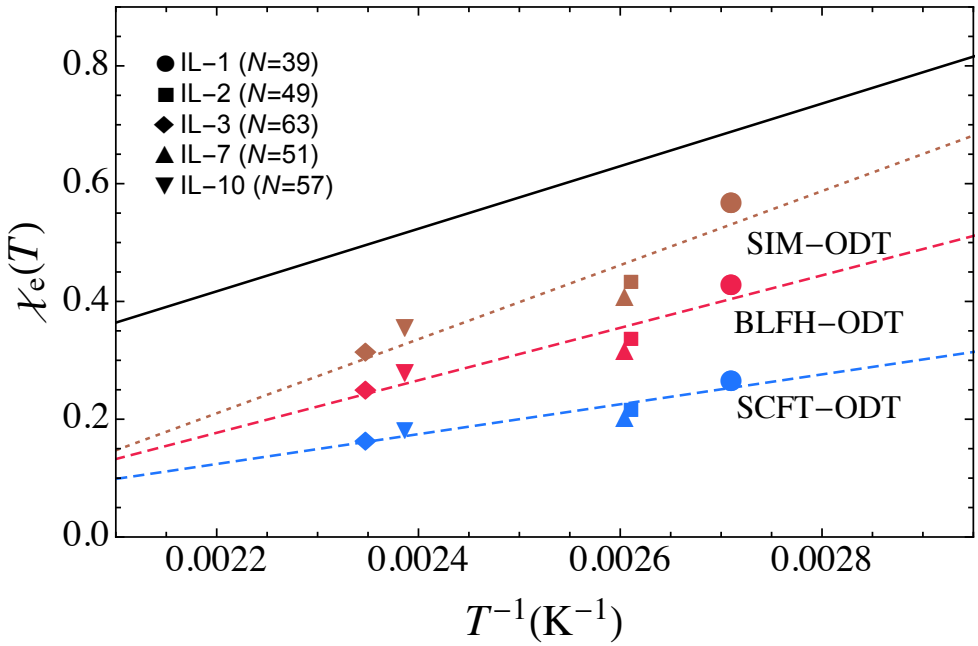

Figure 7.10: Comparison of $\chi_e(T)$ functions obtained from four different fitting procedures: 1. ROL (solid black line) Fit of peak scattering intensity data to ROL theory predictions and corrected for polydispersity effects. 2. SIM-ODT (dotted brown line, brown symbols) Fit of measured $T_{\rm ODT}$s of different chain lengths to the universal scaling law from simulations results. 3. BLFH-ODT (dashed red line, red symbols) Fit of measured $T_{\rm ODT}$s of different chain lengths to BLFH prediction for $(\chi_e N)_{\rm ODT}$. 4. SCFT-ODT (dashed blue line, blue symbols) Fit of measured $T_{\rm ODT}$s of different chain lengths to SCFT prediction for $(\chi_e N)_{\rm ODT}$. The four functions are $\chi_e^{\rm ROL}(T) = 531.4\,T^{-1} - 0.75$, $\chi_e^{\rm SIM}(T) = 628.8\,T^{-1} - 1.17$, $\chi_e^{\rm BLFH}(T) = 445.7\,T^{-1} - 0.80$, and $\chi_e^{\rm SCFT}(T) = 253.6\,T^{-1} - 0.43$.

symbols, uses the estimate of $\chi_e(T)$ obtained by analyzing scattering from IL-1 to plot values of $(\chi_e N)_{\rm ODT}$ as a function of $\overline{N}$ for all 5 samples. The results are devastating compared to those obtained by analyzing experiments on IL-1 alone (Fig.7.8): The values of $(\chi_e N)_{\rm ODT}$ for the other 4 samples are all greater, and further from the simulation results, than those obtained for IL-1. The values for $(\chi_e N)_{\rm ODT}$ for the longer 4 polymers do not show a clear trend with molecular weight. The only clear trend is that the result from sample IL-1 (the sample which we used to extract $\chi_e(T)$, and the shortest polymer) lies noticeably closer to the simulation results than the others.

For comparison, we also show results for $(\chi_e N)_{{\rm ODT}u}$ obtained using three

methods of fitting the measured ODTs to simulation results, BLFH, and SCF theoretical predictions in Fig.7.9. The brown symbols show the results obtained when $\chi_e(T)$ was estimated by fitting the measured ODTs to Eq.6.5 (i.e., to the curve SIM-ODT in Fig.7.9). The red and blue symbols show the previously reported results of a fit to the BLFH and SCF theoretical prediction, respectively. All three fits assumed a function of the form $\chi_e(T) = A/T + B$. Fig.7.10 shows the estimates of $\chi_e(T)$ obtained by all four methods. The difference between the estimates obtained by fitting ODTs to SCFT and from the other three methods is neither disturbing nor surprising: It is known that SCFT cannot quantitatively describe ODTs for such short polymers. The discrepancy between the estimate obtained from fitting the ROL theory to scattering from IL-1 and that obtained from fitting ODTs from several chain lengths to Eq.6.5 is more significant, however, because it indicates a substantial difference between the behavior of this sequence of polymers and that of the simulation models studied in chapters 4 and 6. It is also clear from the values of the coefficients in expressions of the form $\chi_e(T) = A/T + B$, that the difference between estimates of $\chi_e(T)$ obtained by these two methods is primarily the result of a difference in the coefficient B, which represents an entropic contribution, rather than a difference in the A coefficient, which controls the heat of mixing.

7.3 Discussion and Conclusions

We have analyzed experimental measurements from low molecular weight poly(1,4-isoprene-b-DL-lactide) diblock copolymers with respect to theoretical predictions and coarse-grained simulations. The comparison takes advantage of an unusually comprehensive set of measurements of a single polymer, IL-1, that includes both SANS and SAXS scattering experiments and measurements of the latent heat of the ODT, as well as more limited data for the T_{ODT} of other symmetric IL diblock copolymers. Our comparison of experiments and simulations also relies on the availability of an unusually comprehensive analysis of simulations data to which we compare. As shown in chapter 4, results from several simulation models for the structure factor $S(q)$ in the disordered phase can all be fit by the ROL theory over a range of chain lengths using a single es-

timate of how the effective interaction parameter χ_e for each simulation model depends on the simulation AB repulsion parameter α. Simulation results in chapter 6 have shown that, by using the resulting estimates of χ_e to analyze other properties, it is possible to obtain consistent results for $(\chi_e N)_{\mathrm{ODT}}$ and for the scaled latent heat $(\Delta g')_{\mathrm{ODT}}$ from different simulation models.[111] To allow as direct as possible a comparison of experiments to simulations, our experimental results for the T_{ODT} and latent heat $(\Delta H)_{\mathrm{ODT}}$ for IL-1 were converted to values for $(\chi_e N)_{\mathrm{ODT}}$ and $(\Delta g')_{\mathrm{ODT}}$ by the same procedure, using an estimate of $\chi_e(T)$ obtained by fitting experimental results for $S(q)$ in the disordered phase to the ROL theory.

To compare scattering results to the ROL theory, we focused first on the temperature dependence of peak wavenumber q^*. Previous analysis of simulation results for q^* had shown good agreement with predictions of the ROL theory, using values of statistical segment lengths obtained from independent simulations of homopolymer melts.[78] Experimental results for q^* for IL-1 did not, however, agree with ROL predictions obtained using statistical segment lengths of PLA and PI homopolymers. In a recent publication, we presented a fitting procedure in which statistical segment length values of the PI and PlA blocks that are assumed to be equal to literature values of PI and PLA homopolymers, were "corrected" so as to bring the ROL theory predictions into agreement with experimental results. We, however, chose to ignore that route here because we found that incorporating polydispersity effects in the ROL predictions largely resolves the discrepancies between ROL theory and experimental results, thus obviating the need for a fitting procedure of estimating "corrections" to the homopolymer values of statistical segment lengths of the two blocks. Moreover, we could not justify the surprisingly large magnitude (20%) of the predicted "corrections" based on what is known about the sensitivity of statistical segment lengths to changes in chemical environment.[127] Specifically, the required correction is larger than the differences between values of statistical segment lengths measured in a homopolymer melt and in theta solvent for most (though not all) common polymers, as summarized in Table 7.1, page 268 of Ref.[127]

By assuming a function of the form $\chi_e(T) = A/T + B$, we were able fit the measured temperature dependence of the peak intensity $S(q^*)$ for IL-1 to

predictions of the ROL theory, and subsequently correct the resulting $\chi_e(T)$ estimate for polydispersity effects. This sort of a fit of data from a single polymer is, by itself, not a particularly stringent test of the theory, and simply provides a way of calibrating $\chi_e(T)$ in a manner consistent with the earlier analysis of simulation results. One particularly strong sign of the success of our comparison of experiment and simulation results was the rough agreement between experimental results for IL-1 and corresponding simulation results for the normalized latent heat of transition. The success of this comparison is particularly gratifying in light of the fact that accurate experimental and simulation results for the latent heat both became available only recently, so that this is the first attempt to compare them.

For the location of the ODT, we obtained $(\chi_e N)_{\mathrm{ODT}} = 26.8$ for IL-1 ($\overline{N} = 267$), using the estimate of $\chi_e(T)$ obtained from fitting scattering in the disordered phase to the ROL. For comparison, SCFT predicts of $(\chi_e N)_{\mathrm{ODT}} = 10.495$, the BLFH theory predicts $(\chi_e N)_{\mathrm{ODT}} = 10.495 + 41\overline{N}^{(-1/3)} = 17.2$ at the value of $\overline{N} = 267$. For the same value of $\overline{N}$, the empirical correlation obtained from simulations, Eq.6.5, yields 23.0. The fact that the experimental value is more than twice the SCFT prediction reinforces the overwhelming importance of fluctuations. The fact that it is also significantly greater than the BLFH prediction confirms the inadequacy of this theory for quantitative predictions for such short polymers. The predicted value of 23.0 obtained from simulations is in reasonable agreement with the experimental result. The combination of the ROL theory for $S(q)$ and simulation results for other quantities thus provides a reasonable description of data for polymer IL-1, which appears to be a substantial improvement over either the RPA/SCFT theory or the BLFH theory. This agreement between simulation and experiment broke down completely, however, when we compared simulation results both to scattering experiments on IL-1 and to measurements of the T_{ODT} of a series of nearly symmetric IL diblock copolymers of varying (greater) molecular weight.

At this point, we can only speculate about possible causes of this disagreement. The consistency of the results obtained from simulations of different coarse-grained models in chapters 4 and 6 leads us to believe that these simulation results represent a close approximation to the behavior of the ideal-

ized "standard model" of dense polymer liquids as Gaussian random walks with short-range interactions. The identification of statistically significant differences between experimental and simulation results imply that there are physical differences between real IL copolymers and the simple bead-spring models used in these simulations that cannot be adequately described by the standard model. Physical effects that could lead to such differences include: (1) breakdown of the random walk description of chain statistics for sufficiently short chains, (2) breakdown of the assumption that repulsive interactions can be adequately described by a wavenumber independent interaction parameter, due to the non-zero range of effective interactions, (3) end-group contributions to the free energy of mixing, due to the fact that chemical structure and environment of a chain end group is always somewhat different from that of any monomer.

In addition to the fundamental physical differences outlined above between the standard model and real IL polymers, there exist a variety of possible sources of experimental error that, while present, are difficult to quantify and may contribute to the lack of perfect agreement between experiments, simulations, and theory in our analysis. A partial list of such factors include: (1) the use of literature values for polymer densities that originate from high molecular weight materials (i.e. uncorrected for any molecular weight dependence of density), (2) dispersity in composition (only for dispersity in molecular weight has been accounted), (3) systematic errors possibly introduced during various utilized fitting and interpolation routines. For the IL systems here, it is perhaps most relevant that the PLA-terminal end-segment of the block polymer contains a hydroxyl group. This hydroxyl group can interact with the PLA backbone carbonyl groups through a hydrogen bonding interaction. Frielinghaus et al. have studied the effect of a hydroxyl end group on the thermodynamics of a poly(styrene)-b-poly(ethylene oxide) (PS-PEO) diblock copolymer by synthesizing otherwise similar polymers in which the PEO block is terminated by either a polar hydroxyl or nonpolar methoxy group.[128,129] They found that the presence of a hydroxyl end group increased the ODT temperature in PS-PEO copolymers with M_n of approximately 20 kg/mol, relative to analogous systems with a methoxy end group, by approximately $45K$. For IL-1 ($M_n = 2750\,\mathrm{g/mol}$), there are only, on average, 22 PLA repeat units per chain, making the terminal

PLA unit a non-negligible fraction of the total number of PLA repeat units. The expected effect of this end-group is to lead to an estimate of $\chi_e(T)$ somewhat larger than the hypothetical "bulk" parameter that would be obtained in the absence of this end-group. Because the relative effect of the end-group upon scattering and thermodynamics is expected to become stronger with decreasing chain length, this could plausibly lead to an overestimate of $\chi_e(T)$ when the value extracted from the shortest IL polymer, IL-1, is applied to longer chains, for which the terminal PLA unit is a smaller fraction of the total PLA block. It appears to us that the documented effect of a hydroxyl end-group on PS-PEO polymers is more than enough to explain the discrepancies that we observe when comparing data from chains of different length.

The fact that the best agreement between experimental and simulation results for $(\chi_e N)_{\mathrm{ODT}}$ is obtained when we compared scattering and ODT measurements from a single polymer could be explained if we assume that the ODT in a system with some specified invariant degree of polymerization occurs at some critical value of the invariant peak intensity $S(q^*)/cN$. To explain the near-consistency of $S(q)$ and ODT data obtained from a single polymer, we would need to assume that this critical value is not strongly effected by non-idealities (such as end-group effects) that can modify how the magnitude of fluctuations at wavenumbers near q^* depends on temperature and molecular weight in a particular chemical system. We note that this seemingly ad hoc conjecture is consistent with both the phenomenology of crystallization in simple liquids[130] and with BLFH theory, both of which predict a universal value at the crystallization transition for an appropriate measure of the scattering amplitude $S(q^*)$ at the critical wavenumber q^*.

The results presented here provide encouraging evidence of the ability of coarse-grained simulations to correctly describe the dominant effect of strong composition fluctuations in measurements on short diblock copolymers near the ODT, in a manner that improves upon the BLFH theory. These results include the first comparison of simulation and experimental results for the latent heat. Our results also, however, make clear the need to compare result of chains of differing length in order to adequately test the relationships among experiments, simulations and theory, and the need for attention to possible chemically

specific non-idealities, such as end-group effects, when comparing very generic simulations to experimental data on very short chains.

Chapter 8

Comparison of Experiments to Simulations and Theory

This chapter presents a comparison of results from several experimental studies of symmetric diblock copolymer melts to the theoretical predictions and simulation results discussed in previous chapters. Deviations from the universal behavior found in our simulations could be caused by a variety of chemistry- or model-specific effects that are not allowed for in the the standard model of dense polymer liquids, such as end-group contributions to the free energy of mixing. It is clear from the remarkable consistency of simulations results of chapters 4 and 6 that such non-idealities are small for the simple bead-spring models studied in our simulations. Such deviations need not, however, be equally small for real polymers. Quantitative comparison is need to determine the extent to which the behavior of real polymers is similar to that found in simplified bead-spring simulation models.

The analysis procedure used here is similar in most respects to that presented in the previous chapter on PI-PLA copolymers.[120] The main difference is that here, we analyze experimental results from several systems of different chemistry that, taken together, span a large range of values of $\overline{N}$. For each system of interest, scattering intensity results obtained in the disordered phase of one or more chain lengths of a diblock copolymer are fitted to the renormalized one-loop (ROL) theory to estimate the effective interaction parameter $\chi_e(T)$. This estimate of $\chi_e(T)$ is then used to compute values of ODT $(\chi_e N)_{\mathrm{ODT}}$, based on

experimental ODT temperatures, which are compared to the simulation master curve for $(\chi_e N)_{\mathrm{ODT}}$ *vs.* $\overline{N}$ as well as to corresponding SCF and BLFH theory predictions.

The systems that we analyze here were chosen by searching the literature for experimental studies of nearly symmetric diblock copolymer melts that report both absolute calibrated results for the scattering intensity $I(q)$ from small-angle neutron or X-ray scattering experiments in the disordered phase over a range of temperatures and report measurements of the order disorder temperature T_{ODT}. Despite the large number of experimental studies on diblock copolymer melts, only a few published studies meet this requirement. From among those that do, we chose four studies for detailed analysis, as summarized in Table 8.1. The first of these is the study of poly(ethylene-propylene-*b*-ethyl-ethylene) (PEP-PEE) diblock copolymers by Bates, Rosedale, and Fredrickson.[25,26] This is the system that was originally used to test the Brazovskii-Leibler-Fredrickson-Helfand (BLFH) theory. The second is a study of di- and tri-block copolymers polystyrene (PS) and polyisoprene (PI) blocks by Lin and Balsara.[89] The third is a study of symmetric diblock copolymers and blends of polyethylene (PE) and polyethylenepropylene (PEP) by Maurer, Bates, Lodge and coworkers.[1] This system is of interest, both here and in the original study, in part because it exhibits an unusually low χ parameter, and thus allows acess to unusually large values of $\overline{N}$. The last study selected is a study of poly(styrene-*b*-ethylene-oxide) (PS-PEO or SEO) diblock copolymers by Teran and Balsara[131] for which the authors graciously provided access to raw data from absolute calibrated X-ray scattering experiments.

The remainder of this chapter is organized as follows: Section 8.1 presents our methodology for analysis and comparison of experimental results to theoretical predictions and simulations. Sections 8.2 - 8.6 present analysis for each of the four selected chemical systems individually. Finally, we state our conclusions in section 8.7.

DBC	Reference paper	System(s)	Experimental results	$\overline{N}$
PEP-PEE	Bates *et al., J. Chem. Phys.*, 1992	PEP-PEE-5H	SANS $I(q)$ $T_{\mathrm{ODT}} = 125°\mathrm{C}$	3724
		PEP-PEE-2H	$T_{\mathrm{ODT}} = 96°\mathrm{C}$	3463
		PEP-PEE-3H	$T_{\mathrm{ODT}} = 291°\mathrm{C}$	5394
PS-PI	Lin *et al.*, *Macromolecules*, 1994	SI7	SANS $I(q)$ $T_{\mathrm{ODT}} = 84°\mathrm{C}$	606
		SI6	SANS $I(q)$ $T_{\mathrm{ODT}} = 78°\mathrm{C}$	547
PE-PEP	Maurer *et al., J. Chem. Phys.*, 1998	PE-PEP-6H	SANS $I(q)$ $T_{\mathrm{ODT}} = 139°\mathrm{C}$	28,239
		PE-PEP-1D	$T_{\mathrm{ODT}} = 119°\mathrm{C}$	21,194
		PE-PEP-3D	$T_{\mathrm{ODT}} = 159°\mathrm{C}$	30,486
PS-PEO	Teran and Balsara, *J. Phys. Chem. B*, 2004	SEO7	SAXS $I(q)$ $T_{\mathrm{ODT}} = 107.5°\mathrm{C}$	845
		SEO5	SAXS $I(q)$	637

Table 8.1: List of experimental studies on symmetric diblock copolymers selected for analysis for comparison to simulations and theory

8.1 Methodology

8.1.1 Estimation of Molecular Parameters

The first step in comparing experimental results to theoretical predictions and simulations is to compute values for the volumetric degree of polymerization, statistical segment lengths b_A and b_B of the two blocks, and $\overline{N} \equiv Nb^6\nu^{-2}$ that are required as input parameters in coarse-grained theories. In this work, we define values of N and statistical segment lengths for each diblock copolymer (DBC) based on a monomer reference volume ν_{ref} that is the same for both blocks, and independent of temperature. For each system, we have chosen ν_{ref} to be equal to the geometric mean $\nu_0 = \sqrt{\nu_A \nu_B}$ of the temperature-dependent chemical monomer volumes $\nu_A(T)$ and $\nu_B(T)$ at a reference temperature T_{ref} that is chosen to be the order-disorder transition of one of the samples.

The overall volumetric degree of polymerization N is calculated using

$$N(T) \equiv \frac{M_A}{\rho_A(T) N_{\mathrm{Av}} \nu_{\mathrm{ref}}} + \frac{M_B}{\rho_A(T) N_{\mathrm{Av}} \nu_{\mathrm{ref}}} \quad , \tag{8.1}$$

where M_A and M_B are reported number-average molecular weights of the two blocks, $\rho_A(T)$ and $\rho_B(T)$ are temperature dependent densities of the two pure components, and N_{Av} is Avogadros number.

A temperature dependent statistical segment length $b(T)$ for each type of monomer is computed from literature results for chain conformations in homopolymer melts, and is expressed as a product

$$b(T) = b_0 \exp\left[c(T - T_0)\right] \tag{8.2}$$

in which b_0 is a value at a reference temperature T_0 and c is temperature expansion coefficient $c = \partial \ln \mathrm{b(T)} / \partial \mathrm{T}$. The reference value b_0 for our choice of reference volume is obtained from literature values for the ratio for mean-square end-to-end chain dimensions $\langle R_0^2 \rangle / M$ to molecular mass at temperature T_0 as a ratio

$$b_0 = \left(\frac{R_0^2 / M}{\rho(T_0) N_{\mathrm{Av}} \nu_{\mathrm{ref}}} \right)^{1/2} \quad . \tag{8.3}$$

The expansion coefficient c is obtained from literature values for temperature co-

efficient of mean-square end-to-end chain dimensions using $c = 0.5\partial \ln\langle \mathrm{R}_0^2\rangle/\partial \mathrm{T}$.

Values of $\overline{N}$ are evaluated using $\overline{N}(T) = N(T)b^6(T)/\nu_{\mathrm{ref}}^2$, where $b(T) = \left(f_A b_A^2(T) + f_B b_B^2(T)\right)^{1/2}$ is calculated using above defined homopolymer statistical segment lengths. Note that values of $\overline{N}$, unlike values of N and b, are invariant with respect to changes in our arbitrary choice of a value for the monomer reference volume ν_{ref} for each system, which is why this quantity is sometimes referred to as an"invariant" degree of polymerization. Table 8.1 lists values of $\overline{N}$ at the reference temperature T_{ref} for each system considered here. As shown, these values span a wide range $(400 - 30,000)$, implying that this choice of systems provides a meaningful test of simulation results and theoretical predictions for the variation of physical poperties with changes in $\overline{N}$.

8.1.2 Overview of Analysis

In all studies considered here, results for the absolute scattering intensity $I(q)$ is reported for two or more temperatures in the disordered phase of one or more nearly symmetric diblock copolymer chain lengths. $I(q)$ measurements were obtained using either small-angle neutron (SANS) or small-angle X-ray scattering (SAXS). In several cases, results for the peak intensity $I(q^*)$ and peak wavenumber q^* are reported for a larger number of temperatures, while full $I(q)$ is given for only a few select temperatures. In addition, for each system, ODT temperatures are reported for one or more chain lengths.

The first step in the analysis of experimental results is to extract values for the peak scattering intensity $I(q^\star)$ and peak wavenumber q^* as functions of temperature T from $I(q)$ profiles reported at several temperatures in the disordered phase. In cases where the intensity $I(q)$ profiles were measured using small-angle neutron scattering (SANS), experimental results for $I(q)$ must first be corrected for instrumental smearing effects before extracting results for peak intensity $I(q^\star)$ and wavenumber q^* of the desmeared data. This desmearing procedure was not necessary for the data analyzed in chapter 7 because of availability of absolute-calibrated, desmeared, small-angle X-ray scattering (SAXS) data. Results for absolute peak intensity $I(q^*)$ obtained from desmeared SANS or SAXS data are converted to normalized inverse peak structure factor $cNS^{-1}(q^*)$ values to facilitate comparison to theory and simulation results, where $c \equiv 1/\nu_{\mathrm{ref}}$.

Experimental results for the peak wavenumber q^* and peak intensity $S(q^*)$ are then compared to theoretical predictions. Both quantities are compared here to a variant of the ROL theory in which we have introduced a simple correction for the effects of polydispersity. Here, as in our analysis of PI-PLA copolymers, we use comparisons to the ROL theory as a surrogate for direct comparisons to simulation results on mondisperse systems, because of the accuracy of the agreement between ROL predictions and our simulation results. Results for q^* are compared to this polydispersity-corrected ROL theory by plotting experimental results and predictions for q^* as a function of inverse normalized peak intensity $cNS^{-1}(q^*)$, as done for PI-PLA copolymers in chapter 8. This is similar to the method used to compare simulation results for q^* to theoretical predictions in chapter 4, where we plotted q^* as a function of the apparent interaction parameter $\chi_a^\star N \equiv 10.495 - (cNS^{-1}(q^*)/2$, where $\chi_a^\star$, by definition, is equal to the value of χ that would be inferred by fitting the measured inverse peak structure factor to the RPA prediction, $cNS^{-1}(q^*) \equiv 2\,(10.495 - \chi N)$. Results for temperature dependence of $cNS^{-1}(q^*)$ are then fitted to monodisperse ROL theory predictions in order to obtain an estimate for the effective interaction parameter $\chi_e(T)$, which we denote as $\chi_e^{\mathrm{ROL}}(T)$. A temperature dependence of the form $\chi_e(T) \equiv A/T + B$ is assumed in this fit. This step is analogous to that used in section 3.2.4 in which estimates for $\chi_e(\alpha)$ were obtained for our simulation models by simultaneously fitting results for $cNS^{-1}(q^*)$ *vs.* α of different chain lengths of each model to ROL theory predictions.

The resulting estimates $\chi_e(T)$ estimates are then used to compare experimental results of $(\chi_e N)_{\mathrm{ODT}}$ to the simulation master curve for $(\chi_e N)_{\mathrm{ODT}}$ *vs.* $\overline{N}$ given by Eq. 6.5. When values of T_{ODT} are available for two or more samples of differing chain length, which may include some samples that were not used in our estimate of $\chi_e(T)$, the same estimate of $\chi_e(T)$ is used to analyze all systems of the same chemistry.

8.1.3 Extraction of Peak Scattering Data

Desmearing SANS Intensity: As mentioned earlier, measured SANS data must be desmeared using the instrument resolution function before extracting results for peak wavenumber and peak scattering intensity. Our procedure for

doing this is based on the analysis of instrument resolution given in Ref.,[132] which considers contributions to instrument resolution function arising from the wavelength spread, finite collimation and detector resolution, but concludes that smearing effects from wavelength spread generally dominate over other effects for q not close to 0. Because $\Delta\lambda/\lambda$ generally dominates over other smearing contributions, we account only for these effects in our re-analysis below, which is based on information of only peak scattering intensity and wavenumber. Accordingly, the measured intensity $I_{\mathrm{M}}(q)$ is fitted to a convolution

$$I_{\mathrm{M}}(q) = \int dq_0 R(q, q_0) I_{\mathrm{D}}(q_0) \tag{8.4}$$

of the (unknown) desmeared intensity $I_{\mathrm{D}}(q)$ profile and an instrument resolution function R given by a Gaussian function

$$R(q, q_0) = \frac{1}{(2\pi)^{1/2}\sigma} \exp\left[-\frac{1}{2}\frac{(q-q_0)^2}{\sigma^2}\right] \quad , \tag{8.5}$$

with standard deviation $\sigma(q_0) = q_0 \frac{\Delta\lambda}{\lambda} \frac{1}{2\sqrt{2\ln 2}}$ that linearly increases with q, where $2\sqrt{2\ln 2}\sigma$ is the full width at half maximum (Eq. 6 of Ref.[132]). We model the desmeared intensity profile as

$$I_{\mathrm{D}}^{-1}(q) \simeq a_0 \left[F_0\left(qR_g, f, p\right) - 2\chi N\right] \quad . \tag{8.6}$$

Here, $F_0(qR_g, f, p)$ is the generalization of Leibler's intramolecular correlation function F_0 to arbitrary composition f and packing fraction $p = R_{g,A}^2/R_g^2$ and a_0, R_g, χ, and N are adjustable parameters. Eq. 8.6 with fitted coefficients is then used to extract values of the desmeared peak scattering intensity $I(q^\star)$ and peak wavenumber $q^\star$ at a given temperature. In the cases of PS-PI SANS data and PS-PEO SAXS data, we found the model

$$I_{\mathrm{D}}^{-1}(q) \simeq a_0 \left[F_0\left(qR_g, f, p\right) + a + bq^2 + cq^4\right] \tag{8.7}$$

to better fit the measured data. Here, a_0, R_g, a, b, and c are adjustable parameters.

In cases where the full intensity profile $I_{\mathrm{M}}(q)$ is reported at only a select few

temperatures, but results for peak intensity $I_{\mathrm{M}}(q^{\star})$ are provided for a larger set of temperatures, values of the ratio of smeared and desmeared peak scattering intensities are first evaluated for temperatures in the former, smaller set and subsequently used to estimate values of the ratio for temperatures in the latter, larger set by fitting.

With synchrotron SAXS data, since the instrument resolution is not an issue, the reported scattering intensity profiles are directly fitted to Eq. 8.6 to obtain results for the temperature dependence of peak scattering intensity and wavenumber.

Peak Structure Factor: To convert values of absolute peak scattering intensity $I(q^*)$ to the relevant quantities $cNS^{-1}(q^*)$ related to the structure factor, the neutron or X-ray scattering contrast factor must be taken into account. Specifically, according to the notation used throughout this work and in Ref.:[78]

$$S(q^*) = I(q^*) / \left[\nu_{\mathrm{ref}} \left(\frac{l_A}{\nu_A} - \frac{l_B}{\nu_B} \right) \right]^2 \quad , \tag{8.8}$$

where ν_{ref} is the fixed reference volume (N and b are defined with respect to ν_{ref}) and $\left(\frac{l_A}{\nu_A} - \frac{l_B}{\nu_B} \right)$ is the difference in coherent neutron or X-ray scattering length densities of the two blocks. As defined in chapter 3, $S(q)$ has units of monomer number concentration. The dimensionless structure factor that is often reported in experimental literature is given by the product $\nu_{\mathrm{ref}} S(q)$.

8.1.4 Correcting for Polydispersity

One phenomena that is unavoidable in experiment, but that is absent in our simulations, is the effect of molecular weight (or chain length) polydispersity. Previous theoretical studies have shown that inclusion of polydispersity effects within the RPA shifts the predicted peak wavenumber q^* to lower wavenumbers and increases the predicted peak intensity $S(q^*)$,[23,133,134] as shown in in Figs. 8.1 and 8.2.

The RPA theory for a polydisperse symmetric copolymer melt (discussed in greater deail in appendix A) yields a normalized inverse structure of the form

$$cNS^{-1}_{RPA}(q) = F(q,k) - 2\chi_e(T)N \tag{8.9}$$

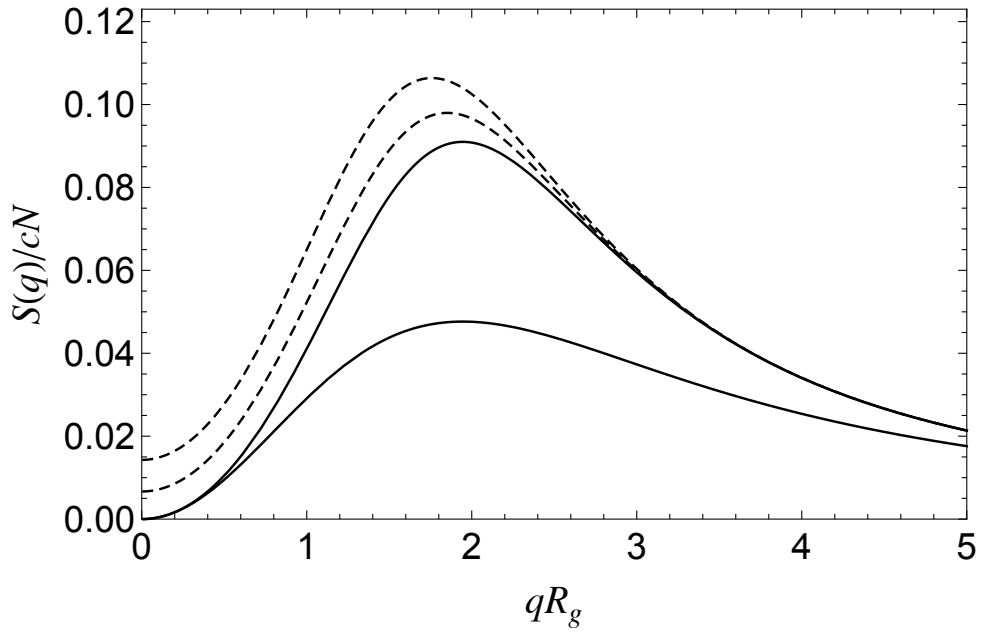

Figure 8.1: Effects of polydispersity on the RPA prediction for structure factor $S(q)/cN$: $N_w/N_n = 1$, $\chi N = 0$ and 5.0, lower and upper solid curves, respectively; $\chi_N = 5.0$, $N_w/N_n = 1.05$ and 1.1, lower and upper dashed curves, respectively.

in which $F(q,k)$ is a function that depends upon the polydispersity index $PDI = M_w/M_n \equiv 1 + k^{-1}$ as well as the wavenumber q, and in which the simple linear dependence on χ_e of the original theory is unchanged. As one consequence of the form of this result, the inclusion of polydispersity in the RPA yields a shift in q^* by an amount Δq_p^* that is independent of $\chi_e(T)$, and that increases approximately linearly with increasing PDI (see Fig. 8.2). Regarding peak intensity, the effect of polydispersity is to decrease the predicted inverse peak intensity by a constant in a manner equivalent to increasing $\chi_e N$ by a T-independent (but PDI-dependent) constant $\Delta(\chi_e N)$ that also increases approximately linearly with increasing PDI.

According to Eq. 2.20, the ROL theory prediction for peak structure factor is given by a sum of the form

$$cNS^{-1}(q) = cNS_{RPA}^{-1}(q) + \overline{N}^{-1/2} H(q, \chi_a^* N) \tag{8.10}$$

of the RPA prediction and a one-loop correction term. The ROL theory has

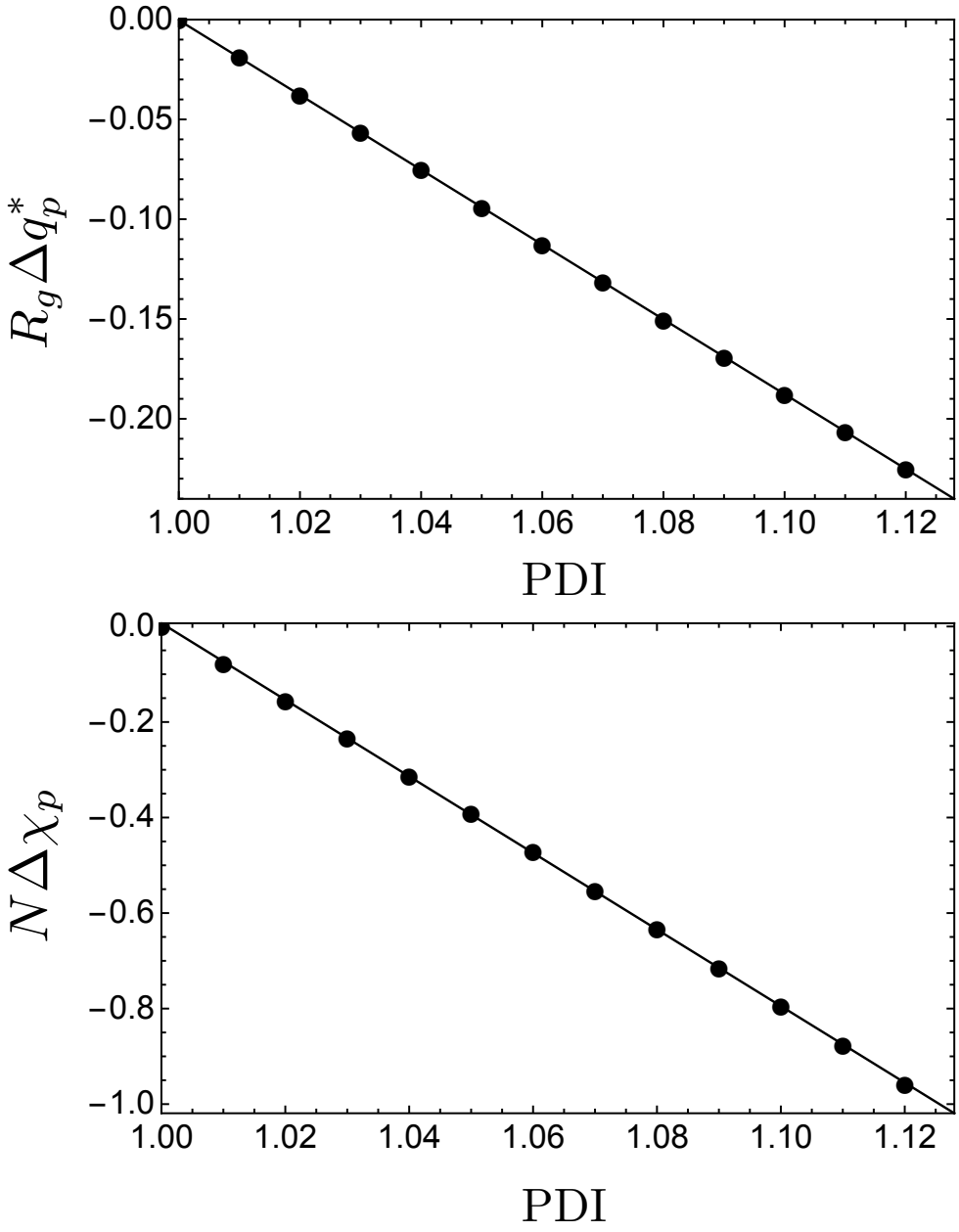

Figure 8.2: Top: RPA prediction for shift in peak wavenumber $R_g \Delta q_p^* \equiv q^* R_g - q_p^* R_g$ *vs.* PDI. Bottom: RPA prediction for $N \Delta \chi_p \equiv (\chi N) - (\chi N)_p$ *vs.* PDI.

never been generalized to take into account the effects of polydispersity upon the one-loop correction. In order to approximately incorporate polydispersity effects in the ROL prediction for $cNS^{-1}(q)$, we assume that the most important corrections arising from polydispersity are incorporated by using the RPA theory for the polydisperse melt as the first term on the RHS of Eq. 8.10, and use the ROL theory for a monodisperse melt for the one-loop correction. Because the main effect of polydispersity upon the RPA prediction is to shift q^* to a lower value by a T-independent amount that increases with increase in the PDI, we have taken into account the effects of polydispersity in the ROL theory by simply decreasing the ROL prediction for q^* by the shift Δq_p^* predicted by the RPA. Similarly, when fitting the normalized desmeared peak structure factor $cNS^{-1}(q^*)$, we first obtain $\chi_e^{\mathrm{ROL}}(T)$ by fitting to the monodisperse ROL theory predictions, and then shift the resulting fitted estimate by the shift $\Delta\chi_p$ predicted by the RPA (see bottom panel of Fig.8.2). This implies that the final polydispersity-corrected ROL based estimate, which we denote as $\chi_e^{\mathrm{ROL-p}}(T) = A/T + B$, will have the same temperature coefficient A, but a slight reduced value of B compared to $\chi_e^{\mathrm{ROL}}(T)$ of monodisperse ROL theory predictions.

Studies have shown that values of the PDI M_w/M_n determined using size exclusion chromatography (SEC) are often overestimates of the true PDI values, primarily as a result of band broadening effects in SEC.[135–137] The authors of Ref.[137] obtained PDI values of polystyrene polymers of varying molecular weights using both SEC and temperature gradient interaction chromatography (TGIC). They found an increasing level of agreement between PDI estimates from TGIC and the asymptotic value of $1 + 1/N_n$ given by the Poisson distribution with increasing molecular weight, indicating the close proximity of TGIC values to the actual true values. More importantly, values obtained from SEC were larger than corresponding TGIC estimates, and the percentage discrepancy increased with increasing molecular weight. We therefore believe that PDI values obtained using SEC, as is the case for all diblock copolymers analyzed here, represent an upper bound to the true values. Polydispersity corrections to theoretical predictions calculated based on these values, as done here, may thus over-correction for the effects of polydispersity.

8.2 PEP-PEE

In a seminal study[25,26] on fluctuation effects in the disordered phase, Bates, Rosedale, and Fredrickson compared absolute scattering intensity results of a nearly symmetric poly(ethylene-propylene-*b*-ethyl-ethylene) diblock copolymer of moderately high molecular weight, labeled PEP-PEE-5H, to predictions of the BLFH fluctuations theory and concluded that a reasonable level of agreement between BLFH theory and experimental scattering results. In a later related paper,[27] these authors analyzed scattering and rheology results for several nearly symmetric PEP-PEE, PEP- PE, PEE-PE diblocks, including the 1990 sample, PEP-PEE-5H, to study the variation of fluctuation effects with $\overline{N}$. For our re-analysis below, we extracted experimental scattering results from the former paper, and values of required parameters (N, b_A, b_B) and results for ODT temperatures of PEP-PEE copolymers of different chain lengths from the latter paper.

The chemical and isotopic compositions of PEP-PEE-5H, which contains a fully hydrogenous PEP block and a partially deuterated PEE block, were obtained from ^{1}H NMR and density gradient column experiments as 55% by volume PEP and 75% deuterium content for PEE, respectively. Light scattering and size exclusion chromatography (SEC) were employed to determine the weight-average molecular weight, $M_w = 57.5$kg/mol, and polydispersity index (PDI), $M_w/M_n = 1.05$, respectively.[25] Note that the reported M_n value refers to the hydrogenous equivalent rather than the true molecular mass. The theoretical value for PDI, based on Poisson distribution, is 1.001 for PEP-PEE-5H.

The authors obtained SANS intensity data of PEP-PEE-5H for different temperatures in both disordered and ordered phases. For purposes of this work, we are interested in only the disordered phase data. Complete $I_{\rm M}(q)$ profiles are reported for three temperatures (126.3, 151.6, and 181.6 °C) in the disordered phase (Fig. 8 in Ref.[25]) and results for inverse peak intensity $I_{\rm M}^{-1}(q^*)$ and peak wavenumber q^* are reported for several temperatures between 126.3 and 181.6 °C (Fig. 9 in Ref.[25]). Their SANS data was obtained using a neutron wavelength of $\lambda = 8$Å and a relative wavelength spread $\Delta\lambda/\lambda = 0.25$. This value was used to calculate smearing effects from wavelength distribution, which were then added to lesser smearing contributions from collimation and detector resolution

to estimate desmeared $I_{\mathrm{D}}(q)$ profiles from measured intensity data.

ODT temperature of PEP-PEE-5H was obtained as 125 °C based on a sharp discontinuity in measurements of the dynamic elastic modulus. In Ref.,[27] the authors report ODT temperatures of two other nearly symmetric PEP-PEE systems, PEP-PEE-2H ($M_w = 53.6$kg/mol and $f_{\mathrm{PEP}} = 0.56$) and PEP-PEE-3H ($M_w = 85.3$kg/mol and $f_{\mathrm{PEP}} = 0.53$), as 96 and 291 °C, also from measurements of elastic modulus.[27] PEP-PEE-2H and PEP-PEE-3H contain full hydrogenous PEE blocks. In all cases, ODT temperatures determined rheologically were found to agree within experimental error (±1 °C) with those obtained by SANS from appearance of a Bragg peak. No scattering information is reported for the other 2 systems.

In both 1990 and 1995 papers, the authors defined segments on the basis of equal repeat unit molecular weights, namely 56 g/mol, corresponding to a hydrogenous PEE unit. Accordingly, they obtained overall degrees of polymerization as $N_w = 57500/56 = 1026$ and $N_n = 57500/1.05/56 = 978$.[27] Because of a negligible difference in pure component densities of PEP and PEE, a definition for segments based on a common molecular weight is equivalent to a common statistical segment volume, $\nu_A = \nu_B = \nu_0$. Based on densities and thermal expansivities of polyolefins (PEP, PEE, PE) reported in literature,[121,138] the authors estimated $\nu_0 = 108 \exp\left[6.85 \times 10^{-4}(T - 25\,^{\circ}\mathrm{C})\right]$ Å^3. Ref.[27] provides temperature dependent functions for statistical segment lengths of PEP and PEE homopolymers as $b_{\mathrm{PEP}} = 7.2 \exp\left[-0.58 \times 10^{-3}(T - 25\,^{\circ}\mathrm{C})\right]$ Å and $b_{\mathrm{PEE}} = 5.0 \exp\left[0.2 \times 10^{-3}(T - 25\,^{\circ}\mathrm{C})\right]$ Å. The difference in neutron scattering lengths of PEP and PEE repeat units is reported as $|l_A - l_B| = 6.26 \times 10^{-4}$ Å.[25]

The authors obtained an estimate for $\chi_e(T)$ of PEP-PEE by fitting available T_{ODT}s of different chain lengths to the BLFH prediction for $(\chi_e N)_{\mathrm{ODT}}$, which is given by $(\chi_e N)_{\mathrm{ODT}} = 10.7 + 43.16\,\overline{N}^{-1/3}$ for $f = 0.55$.[25] Estimates obtained are $\chi_e(T) = 4.69\,T^{-1} + 0.000444$ (1990[25]) and $\chi_e(T) = 4.46\,T^{-1} + 0.0021$ (1995[27]). For the former estimate, an effective statistical segment length $b \equiv \sqrt{6R_g^2/N}$ obtained from fitting q^* results of PEP-PEE-5H to the RPA prediction for $q^* R_g$ was used to calculate $\overline{N}$ values. Given that the RPA prediction for $q^* R_g$ is an over estimation, the resulting $\overline{N}$ values ($8600 \lesssim \overline{N} \lesssim 15800$) are significantly larger than ones ($3400 \lesssim \overline{N} \lesssim 5500$) used in Ref.[27] based on homopolymer

values. Both estimates were derived with respect to the common segment volume ν_0 defined above.

Ref.[25] employed the resulting $\chi_e(T)$ estimate to obtain BLFH theory predictions for fluctuation effects on the behavior of structure factor $S(q)$. BLFH theory predictions for $S(q)$ are identical to the RPA prediction, $cNS^{-1}(q) = (F(qR_g, f) - 2\chi N)$, except that the Flory-Huggins interaction parameter χ is substituted with a renormalized interaction parameter χ_{fluc} that depends on temperature, composition, and chain length (more specifically, $\overline{N} = Nb^6\nu^{-2}$). It is obtained numerically by solving the algebraic equation

$$\chi_{\text{fluc}} = \chi + \frac{C(f)}{2\overline{N}^{1/2}N}\left[N^{-1}F(x^*, f) - 2\chi\right]^{-1/2} \quad , \tag{8.11}$$

where, $C(f)$ is a composition-dependent constant ($C(0.55) = 277$),[34] $\overline{N}$ is the invariant degree of polymerization, and χ is a Flory-Huggins interaction parameter determined independently from systems in the absence of fluctuation effects (e.g. fit of scattering intensity far from ODT to the RPA prediction). This equation yields predictions for $S^{-1}(q^*)$ *vs.* χN, which can be converted to obtain $S^{-1}(q^*)$ *vs.* T^{-1} based on the input χ parameter. In this case,[25] it was $\chi_e(T) = 4.69\,T^{-1} + 0.000444$. The authors found reasonable agreement between experimental results and BLFH predictions for all temperatures of PEP-PEE-5 SANS data, which correspond to $10.6 < \chi N < 12.5$. Below, we re-analyze this set of scattering results using $\overline{N}$ values obtained from homopolymer statistical segment lengths, and additionally include ROL theory predictions for comparing experimental results.

Re-analysis: For our re-analysis of PEP-PEE results, we define segments based on a fixed common segment volume $\nu_{\text{ref}} = 116\text{Å}^3$, which is the value of the above defined ν_0 at the ODT temperature of PEP-PEE-5H, 125 °C, which is fixed as the reference temperature. Eq. 8.1 is used to obtain volumetric degrees of polymerization based on these reference conditions. Accordingly, we obtained N_n =976, 893, and 1460 for PEP-PEE-5H, PEP-PEE-2H, and PEP-PEE-3H, respectively; these values are only slightly different from those given by the authors. Values for PEP and PEE statistical segment lengths are obtained as 6.79 and 5.10Å, respectively, at the reference temperature using the authors'

functions for b_{PEP} and b_{PEE} given above. These values yield $\overline{N}$ =3724, 3463, and 5394 for the 3 copolymers.

Fig. 8.3 shows measured SANS data at 126.3, 151.6, and 181.6 °C obtained by digitizing Fig. 8 in Ref.[25] For each temperature, we fitted the measured data to a convolution of $I_{\mathrm{D}}(q)$ model of Eq.8.6 and a Gaussian function with $\Delta\lambda/\lambda = 0.25$. Values of the ratio $I_{\mathrm{D}}(q^*)/I_{\mathrm{M}}(q^*)$ of peak desmeared and smeared peak intensities were subsequently extracted from the fitted $I_{\mathrm{D}}(q)$ and $I_{\mathrm{M}}(q)$ functions. As illustrated in the inset of Fig. 8.4, these ratios were used to construct a quadratic fit to obtain values of the ratio for temperatures between 126.3 and 181.6 °C for which only (smeared) peak intensities, but not the complete $I_{\mathrm{M}}(q)$ profiles, are reported; results for (smeared) peak intensity *vs.* T^{-1} were obtained by digitizing Fig. 9 in Ref.[25] Fig. 8.4 plots the resulting desmeared peak intensities as a function of temperature.

Fig. 8.5 shows results for peak wavenumber q^* *vs.* normalized inverse peak structure factor $cNS^{-1}(q^*)/2$ of PEP-PEE-5H (circular data points) along with corresponding theoretical predictions. The simplest theoretical prediction is provided by the RPA, according to which q^*R_{g0} is a constant (1.9495 for perfectly symmetric copolymers) for the entire disordered phase temperature range. The monodisperse RPA prediction is shown by a red dashed line. ROL theory predictions evaluated at $\overline{N} = 3724$ are shown as a black dashed line labeled ROL. The black solid curve labeled ROL-p represents polydispersity-corrected ROL theory predictions obtained by shifting monodisperse ROL theory predictions by Δq_p^*, which, as discussed in section 8.1.4, is the RPA prediction for shift in q^* from polydispersity effects. The reported PDI of 1.05 was used to calculate Δq_p^*.

Next, we obtained an estimate for $\chi_e(T)$ by fitting results for normalized inverse peak structure factor $cNS^1(q^*)/2$ *vs.* T^{-1} to monodisperse ROL theory predictions for $cNS^1(q^*)/2$ *vs.* $\chi_e N$. Fig. 8.6 shows the fit. Here, the abscissa $\chi_e N$ is evaluated using the resulting fitted estimate, $\chi_e^{\mathrm{ROL}}(T) = 7.05\,T^{-1} - 0.0031$, and experimental results and corresponding monodisperse ROL predictions are marked by discrete data points and solid curves, respectively. The RPA prediction is shown as a dashed line. Subsequently, we fitted the same data to monodisperse BLFH theory predictions, which were obtained by solving

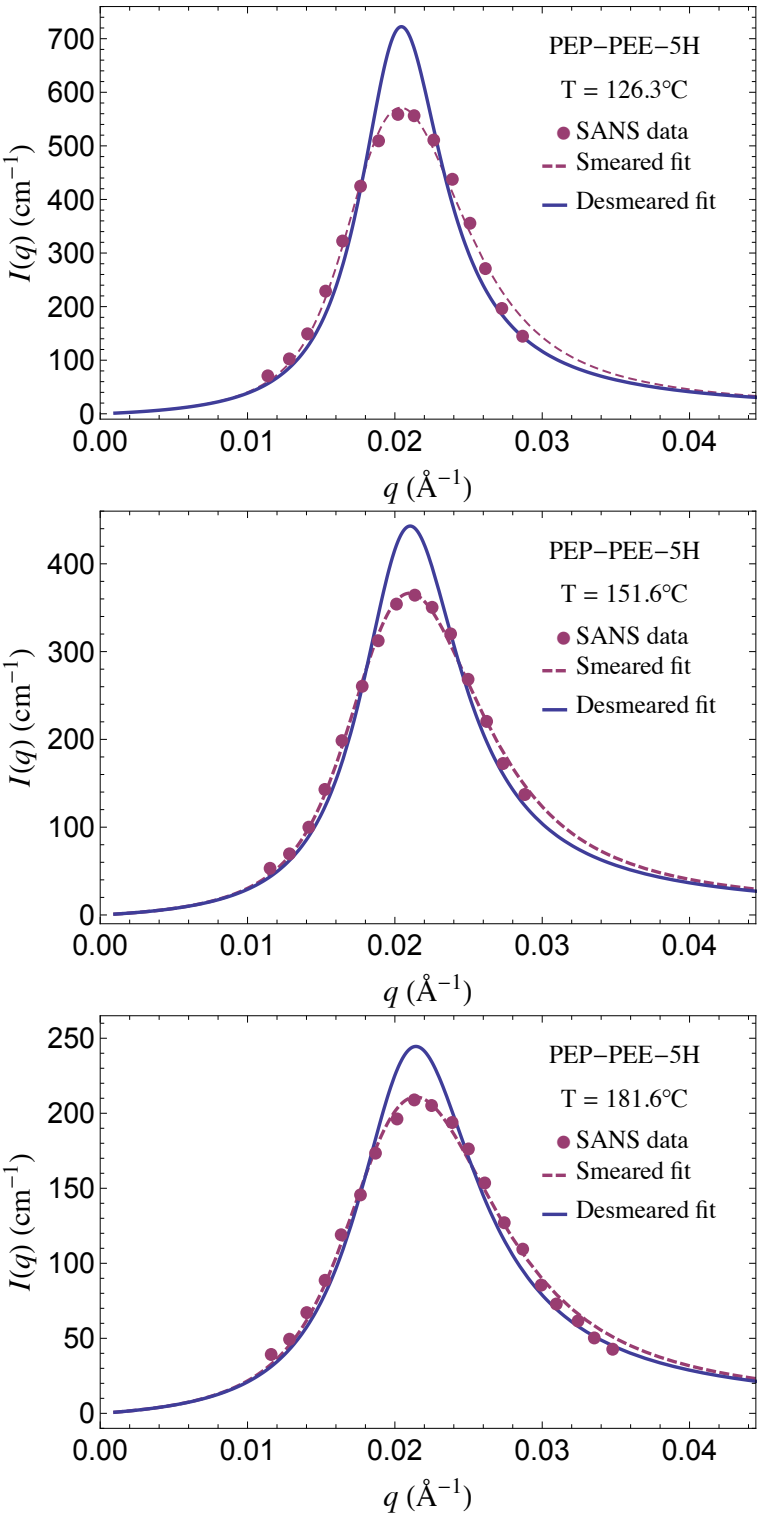

Figure 8.3: SANS intensity $I(q)$ profiles of PEP-PEE-5H at three disordered phase temperatures. For each temperature, the smeared and desmeared intensity $I(q)$ functions obtained from fitting the measured SANS data (circles) to the convolution discussed in the main text are marked by red dashed and blue solid curves, respectively.

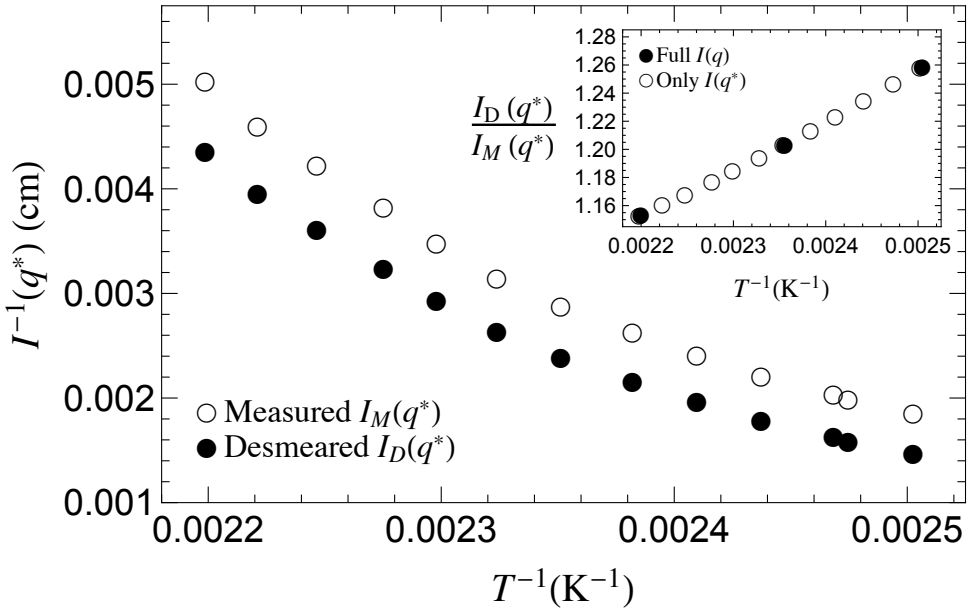

Figure 8.4: Temperature dependence of inverse peak intensity $I^{-1}(q^*)$ extracted from fitted $I_{\mathrm{D}}(q)$ (filled) and $I_{\mathrm{M}}(q)$ (empty) functions of PEP-PEE-5H. Inset: Quadratic fit used to obtain values of the ratio $I_{\mathrm{D}}(q^*)/I_{\mathrm{M}}(q^*)$ of desmeared and smeared peak intensities for temperatures between 126.3 and 181.6 °C for which complete $I_{\mathrm{M}}(q)$ profiles are not reported.

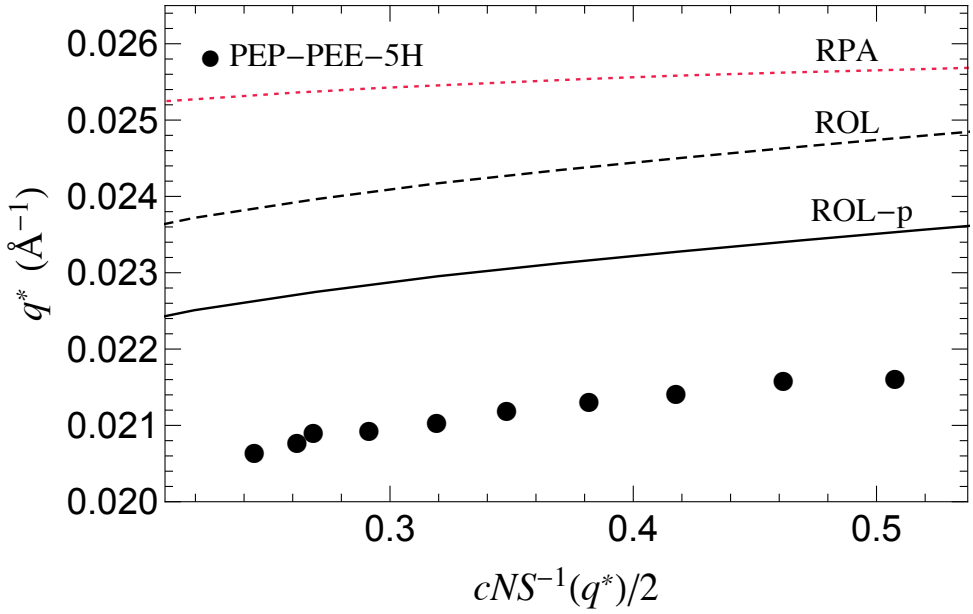

Figure 8.5: Comparison of experimental results of q^* of PEP-PEE-5H (circles) to monodisperse RPA (red dotted line) and ROL (black dashed line) theory predictions, as well as polydispersity-corrected ROL theory predictions (black solid curve labeled ROL-p). RPA polydispersity shift was calculated based on measured PDI of 1.05. Theoretically predicted minimum for PDI is 1.001 for this system.

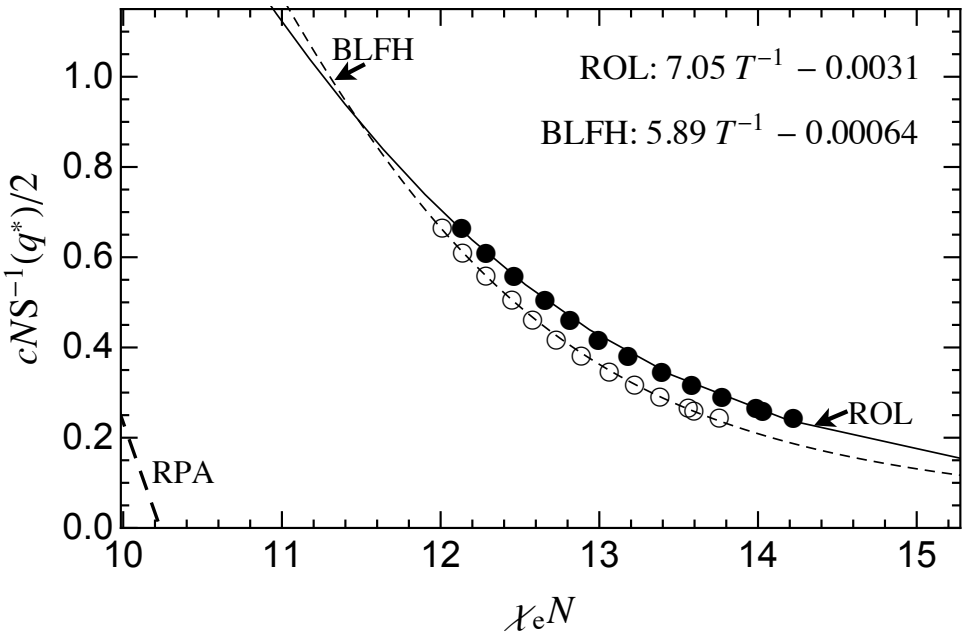

Figure 8.6: Extraction of $\chi_e(T)$ estimates of PEP-PEE by fitting results of $cNS^1(q^*)/2$ *vs.* T^{-1} of PEP-PEE-5H to monodisperse ROL (solid line, filled circles) and monodisperse BLFH (dashed line, open circles) theory predictions. The dashed line is the monodisperse RPA prediction. Resulting $\chi_e(T)$ estimates are given in the legend.

Fitting procedure	A (K)	B	T range
ROL	7.05	-0.0031	T range: $126.3 - 181.6$°C
BLFH	5.89	-0.00065	T range: $126.3 - 181.6$°C
SIM-ODT	7.05	-0.0029	$T_{\rm ODT}$s: 96, 125, and 291 °C
BLFH-ODT	6.44	-0.0023	$T_{\rm ODT}$s: 96, 125, and 291 °C
SCFT-ODT	4.87	-0.0012	$T_{\rm ODT}$s: 96, 125, and 291 °C
Bates-BLFH-ODT[27]	4.46	0.0021	$T_{\rm ODT}$s: 96, 125, and 291 °C

Table 8.2: Estimates of $\chi_e(T) = A\,T^{-1} + B$ of PEP-PEE obtained using different fitting procedures.

Eq. 8.11 numerically. This yields $\chi_e^{\rm BLFH}(T) = 5.89\,T^{-1} - 0.00065$. Both estimates are shifted by the same T-independent constant $\Delta\chi_p$, where $N\Delta\chi_p$ is the RPA prediction for shift in $(\chi_e N)$ from polydispersity effects (see Fig. 8.2). This results in $\chi_e^{\rm ROL-p}(T) = 7.05\,T^{-1} - 0.0035$ and $\chi_e^{\rm BLFH-p}(T) = 5.89\,T^{-1} - 0.0011$ (p for polydispersity-corrected estimates).

We also obtained $\chi_e(T)$ estimates by fitting $T_{\rm ODT}$s of the 3 PEP-PEE copolymers to (1) simulations scaling law given by Eq.6.5, (2) BLFH $(\chi_e N)_{\rm ODT}$ prediction for $f = 0.55$; this same fit was performed by Bates *et al.* in the original paper, and (3) SCFT prediction for $(\chi_e N)_{\rm ODT}$. The lower panel of Fig.8.7 shows all three $\chi_e(T)$ estimates along with the monodisperse ROL based estimate, $\chi_e^{\rm ROL}(T)$. For each ODT-based $\chi_e(T)$ estimate, symbols denote predicted values of $\chi_{e\rm ODT}$ by the underlying scaling law (SIM-ODT or BLFH-ODT or SCFT-ODT) *vs.* measured $T_{\rm ODT}^{-1}$ of the 3 PEP-PEE samples. Discrepancies between predicted values and the fitted $\chi_e(T)$ estimate are clearly small for all 3 systems. See Table 8.2 for values of A and B of resulting $\chi_e(T)$ estimates.

8.3 PS-PI

Balsara's group synthesized a series of di- and tri-block copolymers containing polystyrene (PS) and polyisoprene (PI) to study the effects of molecular weight (1.2×10^4 to 4.1×10^4 g/mol), composition, and architecture on scattering behavior of block copolymers.[89] SI7 and SI6 are the only diblock copolymers from the study with nearly symmetric compositions, which is $f_{\rm PS} = 0.46$ for both. The microstructural composition of the polyisoprene block was obtained by ^{1}H

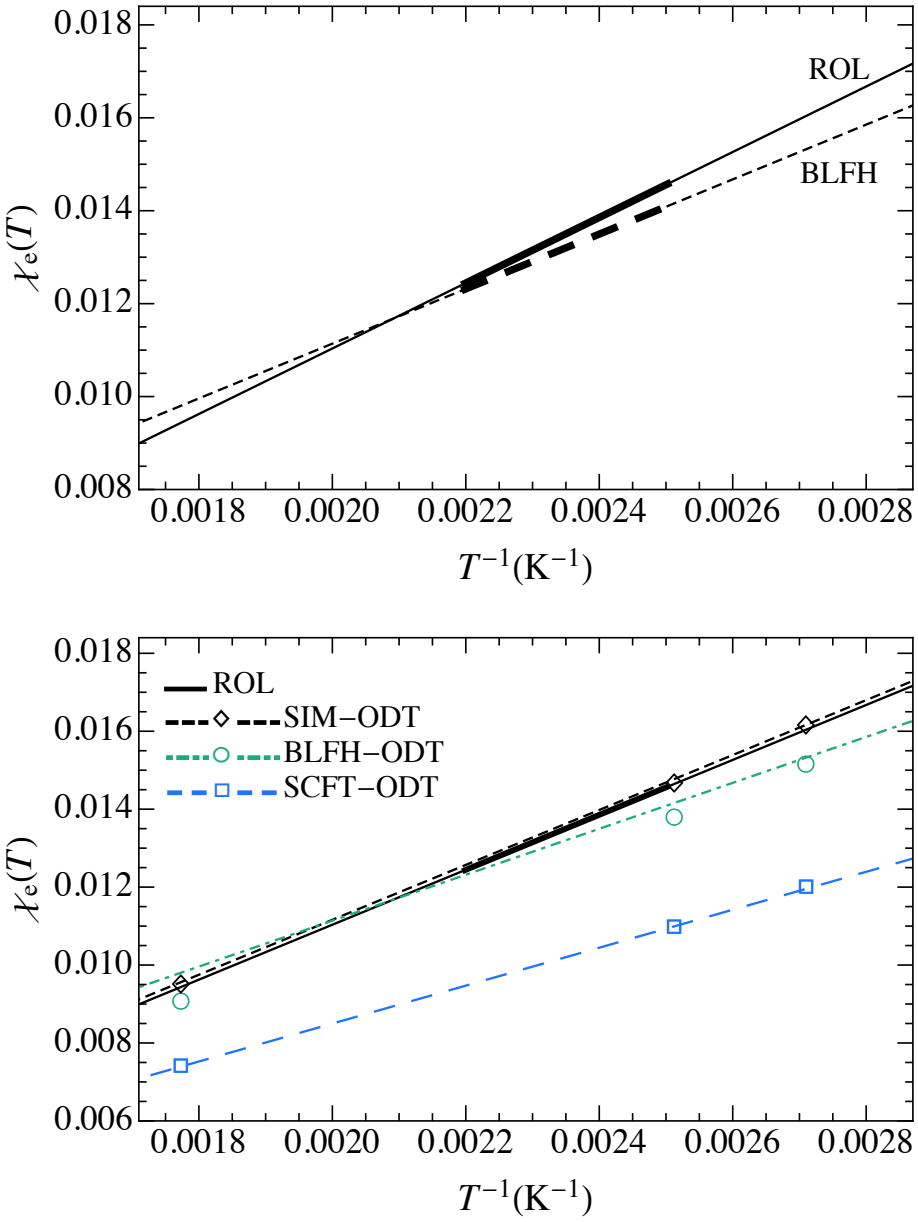

Figure 8.7: Upper: Comparison of $\chi_e(T)$ estimates of PEP-PEE obtained from fitting peak intensity data of PEP-PEE-5H to monodisperse ROL (solid line) and monodisperse BLFH (dashed line) theory predictions. The temperature range of peak intensity data used to obtain $\chi_e^{\mathrm{ROL}}(T)$ and $\chi_e^{\mathrm{BLFH}}(T)$ is indicated by thicker line segments. Lower: Comparison of $\chi_e^{\mathrm{ROL}}(T)$ to $\chi_e(T)$ estimates obtained from fitting T_{ODT}s of PEP-PEE-5H ($N = 976$ and $T^{-1} = 0.0025\mathrm{K}^{-1}$), PEP-PEE-2H ($N = 893$ and $T^{-1} = 0.0027\mathrm{K}^{-1}$) and PEP-PEE-3H ($N = 1447$ and $T^{-1} = 0.0018\mathrm{K}^{-1}$) to different predictions: SIM-ODT Universal scaling law of Eq.6.5 from simulations, BLFH-ODT - BLFH theory prediction for $(\chi_e N)_{\mathrm{ODT}}$ for $f = 0.55$, SCFT-ODT - SCFT prediction for $(\chi_e N)_{\mathrm{ODT}}$ for $f = 0.55$. All estimates are defined with respect to ν_{ref} defined in the main text.

NMR as 93% 1,4 and 7% 3,4, which is the same as what Rounds[139] and Owens[22] studied. Reported weight-average molecular weights of PS and PI blocks are $M_{w,\mathrm{PS}} = M_{w,\mathrm{PI}} = 7.2\,\mathrm{kg/mol}$ and $M_{w,\mathrm{PS}} = M_{w,\mathrm{PI}} = 6.5\,\mathrm{kg/mol}$ in SI7 and SI6, respectively; clearly, SI7 and SI6 are low molecular weight polymers. Polydispersity, as obtained using gel permeation chromatography (GPC), is reported as $M_w/M_n = 1.05$ for both systems. Theoretical values based on Poisson distribution are 1.006 and 1.007 for SI7 and SI6, respectively. These values become asymptotically accurate for high molecular weights. Based on results presented in Ref.,[137] we believe that the reported GPC values, although slightly larger, are closer to the true values than the Poisson values.

The authors obtained absolute SANS intensity $I(q)$ profiles for three temperatures (99, 123, and 147 °C) for SI7 (Fig. 9 in Ref.[89]) and for four temperatures (83, 103, 121, and 147 °C) for SI6 (Fig. 6 in Ref.[89]). The SANS instrument used has the following configuration: $\lambda = 9$Å and$\Delta\lambda/\lambda = 0.25$. On accounting for instrumental smearing effects from wavelength spread and other factors, the authors concluded that χ estimates that were obtained from fits of scattering intensity data to RPA prediction (see below) show only a 1% difference between use of measured, smeared data and extracted, desmeared data. Nevertheless, we implemented the desmearing procedure discussed in section 8.1.3 for our re-analysis of their scattering data. ODT temperatures, as determined by identifying sharp drops in the material birefringence as it transitions from an ordered to a disordered phase, are reported as 84 and 78 °C for SI7 and SI6, respectively.

For their analysis, the authors defined chemical repeat units as the corresponding block segment, *i. e.,* C_8 unit for polystyrene and C_8 unit for polyisoprene. Specific segmental volumes are given by $\nu_{\mathrm{PS}} = 176.4 \exp\left[-0.00055(T - 123\,^\circ\mathrm{C})\right]$ Å^3 and $\nu_{\mathrm{PI}} = 132.3 \exp\left[-0.00065(T - 123\,^\circ\mathrm{C})\right]$ Å^3 from molar masses of styrene (104.15 g/mol) and isoprene (68.12 g/mol) and literature values for densities and thermal expansion coefficients of PS and PI homopolymers.[121] Their convention yields $N_S = 7200/104.15 = 69$ and $N_I = 7200/68.12 = 106$ and $N_S = 7200/104.15 = 62$ and $N_I = 7200/68.12 = 95$ for SI7 and SI6, respectively. Neutron scattering lengths of PS and PI repeat units, as reported by the authors, are $l_{\mathrm{PS}} = 2.32 \times 10^{-4}$ Å and $l_{\mathrm{PI}} = 3.3 \times 10^{-5}$ Å; we obtained the

same values from our calculations using neutron scattering lengths of carbon (0.0000665 Å), hydrogen (-0.0000374Å), and oxygen (0.000058Å) atoms.

The authors fitted measured SANS data from their di- and triblock copolymers to polydispersity-corrected RPA prediction (see appendix A) and therefrom obtained individual $\chi_e(T)$ estimates for each system. The resulting $\chi_e(T)$ estimates show a strong dependence on chain length N and a slight curvature with T^{-1}, clearly demonstrating that the RPA prediction does not account for fluctuation effects and that fluctuation effects vary with chain length, or as is now well understood, with the invariant chain length, $\overline{N}$. In order to include fluctuation effects, the authors revised their RPA based $\chi_e(T)$ estimates using Eq. eq:chifluc.[34] The resulting fluctuations corrected $\chi_e(T)$ estimates for different chain lengths of PS-PI were observed to be largely consistent with $\chi_e(T) = 26.6\,T^{-1} + 0.0118$ ($\pm 10\%$), with the exception of a low molecular weight ($M_w = 12.6\,\mathrm{kg/mol}$), asymmetric diblock copolymer ($f_{\mathrm{PS}} = 0.22$). This estimate was based on a reference segment volume of $150.3\,\mathrm{\AA}^3$.

Previous Work: PS-PI is a heavily studied model system. As a result, many previous studies have obtained $\chi_e(T)$ estimates for PS-PI with an isoprene microstructure similar to that of the polymers studied by Lin *et al.*. A few notable previous analyses are discussed here. Rounds[139] measured turbidity temperature as a function of the blend composition of a ternary blend, PS-PI/PS/PI ($<$ 5kg/mol), and extrapolated the resulting data to obtain critical temperature of the pure diblock copolymer, which was then compared to a thermodynamic theory for microphase separation[140] to obtain $\chi_e(T) = 71.4\,T^{-1} - 0.086$ based on a reference segment volume of $144\,\mathrm{\AA}^3$ (according to Khandpur *et al.*[86]) Khandpur *et al.* used this $\chi_e(T)$ estimate by Rounds to map out the phase diagram of PS-PI diblock copolymers based on measurements of ODT temperatures of ten PS-PI diblock copolymers, spanning a wide composition range $f_{\mathrm{PI}} \simeq 0.24 - 0.82$. Specifically, ODT temperature of a nearly symmetric diblock copolymer, labeled IS-54 ($f_{\mathrm{PI}} = 0.54$), is reported as $124\,^{\circ}\mathrm{C}$. Owens *et al.*[22] obtained $\chi_e(T) = 25\,T^{-1} + 0.009$ by fitting results for scattering intensity in the disordered phase of a relatively low molecular weight (11kg/mol) asymmetric diblock copolymer to the RPA prediction. This estimate was defined with respect to an average segmental volume of PS and PI monomers, similar to our

Reference	Method	A (K)	B	ν_{ref} $\left(\text{Å}^3\right)$
Lin&Balsara[89]	Fit of SI7 and SI6 peak intensities to RPA	26.6	0.012	150.3
Rounds[139]	Critical temperatures of blends	71.4	−0.086	144
Owens&Russell[22]	Fit of diblocks peak intensities to RPA	25	0.009	157

Table 8.3: Estimates of $\chi_e(T) = A\,T^{-1} + B$ of PS-PI obtained in previous experimental studies. See the main text for details on fitting procedures.

re-analysis below. Table 8.3 lists $\chi_e(T)$ estimates from all these studies.

Re-analysis: For our re-analysis of SI copolymers, we define segments based on a fixed segmental volume $\nu_{\text{ref}} = 157\text{Å}^3$ equal to the value of geometric mean of PS and PI molar volumes $\nu_0 = \sqrt{\nu_{\text{PS}}\nu_{\text{PI}}}$ at a reference temperature T_{ref} of 81 °C (average of ODT temperatures of SI7 and SI6). Eq. 8.1 was used to estimate volumetric degrees of polymerization on the basis of ν_{ref}; Based on known block molecular weights and homopolymer densities, resulting values are $N_{\text{SI7}} = 163$ and $N_{\text{SI6}} = 147$ at the reference temperature. We obtained temperature dependent functions for homopolymer statistical segment lengths from reported literature values of end-to-end chain dimensions R_0^2/M[121] and thermal expansion coefficient $d\ln\langle \text{R}_0^2\rangle/\text{dT}$.[124,141] Resulting functions, defined with respect to ν_{ref}, are $b_{\text{PS}} = \exp\left[(1/2)(0.00044T + 3.52)\right]$ Å and $b_{\text{PI}} = \exp\left[(1/2)(0.0004T + 3.77)\right]$ Å. As a result, $b_{\text{PS}} = 6.28$Å and $b_{\text{PI}} = 7.06$Å at the chosen reference temperature, and as a result, $\overline{N}_{\text{SI7}} = 606$ and $\overline{N}_{\text{SI6}} = 547$. Also, we obtained $N = 208$ and $\overline{N} = 773$ for IS-54 of Ref.[86] based on reported molecular weight $M_n = 17\,\text{kg/mol}$.

Figs. 8.8 and 8.9 show SANS data of SI7 and SI6 that we obtained by digitization of Figs. 6 and 9 in Ref.,[89] respectively. Also shown are our fitted estimates for smeared $I_{\text{M}}(q)$ and desmeared $I_{\text{D}}(q)$ intensity functions at different temperatures. Fig. 8.10 shows a comparison of results of q^* *vs.* $cNS^{-1}(q^*)/2$ of SI7 and SI6 to polydispersity-corrected ROL predictions. For the sake of comparison, we also show monodisperse RPA and ROL theoretical predictions.

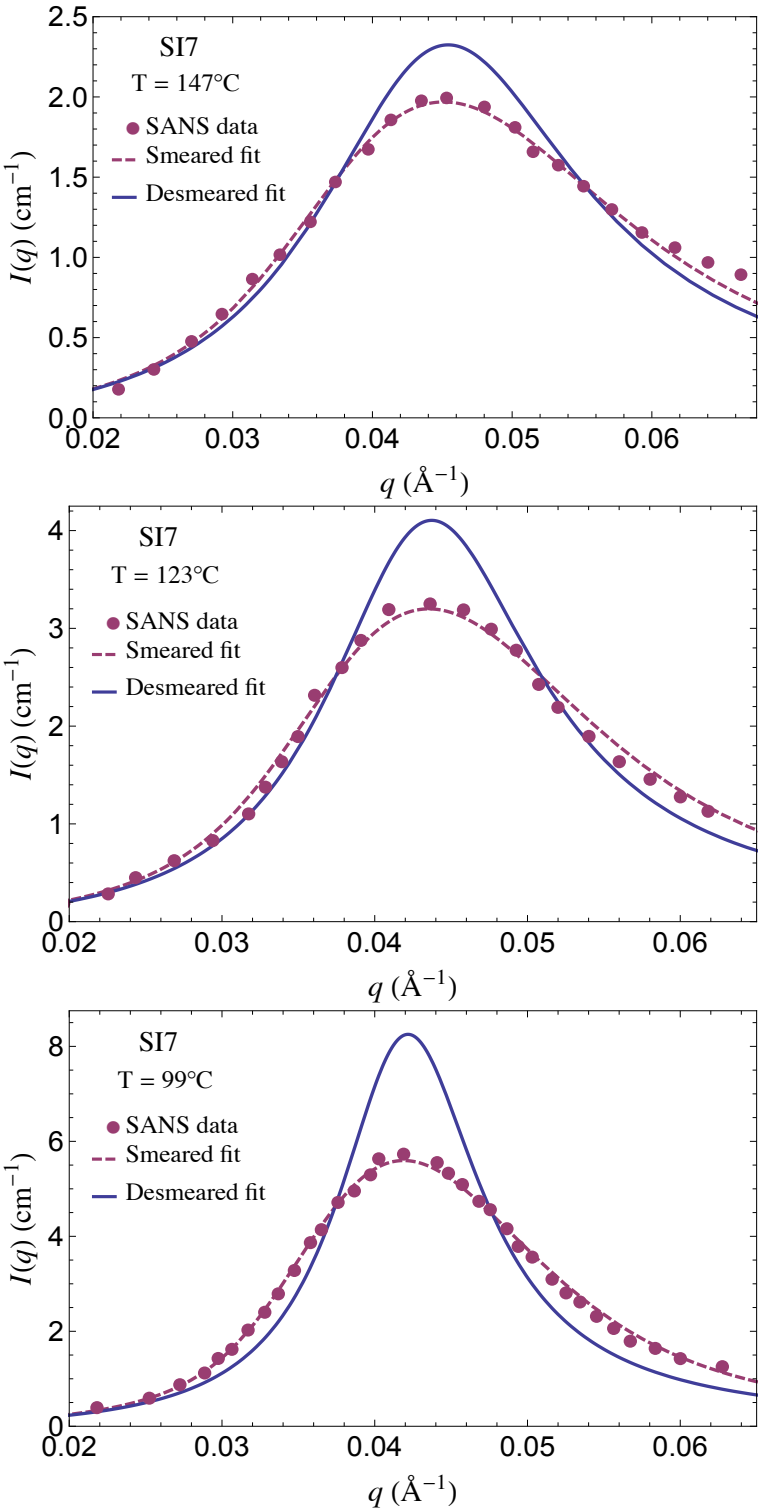

Figure 8.8: SANS intensity $I(q)$ profiles of SI7 at three disordered phase temperatures. For each temperature, the smeared and desmeared intensity $I(q)$ functions obtained from fitting the measured SANS data (circles) to the convolution discussed in the main text are marked by red dashed and blue solid curves, respectively.

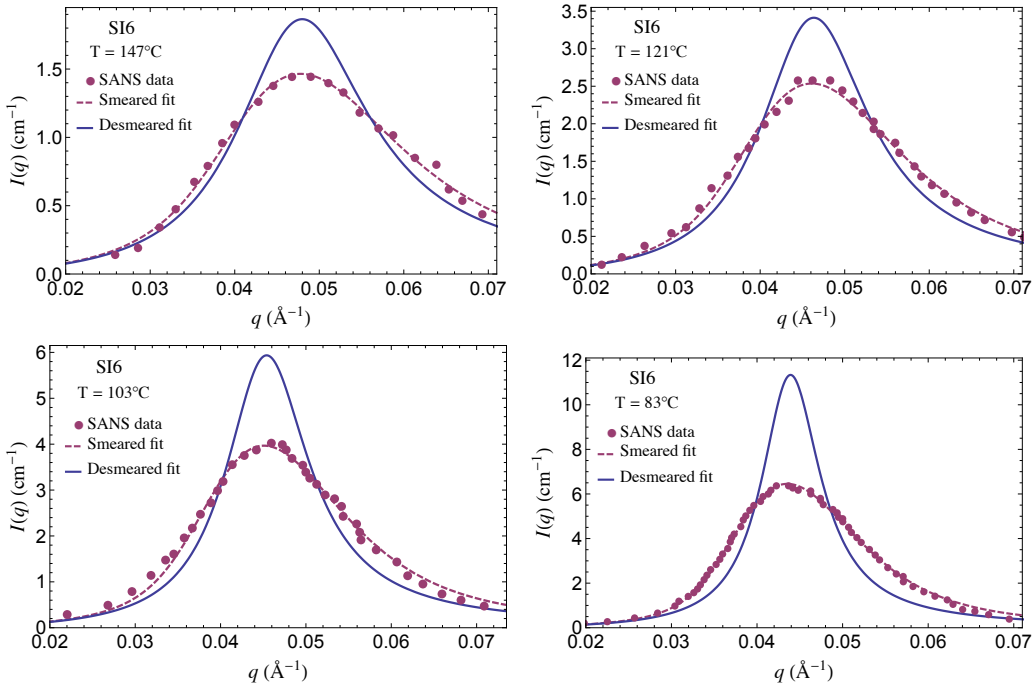

Figure 8.9: SANS intensity $I(q)$ profiles of SI6 at four disordered phase temperatures. For each temperature, the smeared and desmeared intensity $I(q)$ functions obtained from fitting the measured SANS data (circles) to the convolution discussed in the main text are marked by red dashed and blue solid curves, respectively.

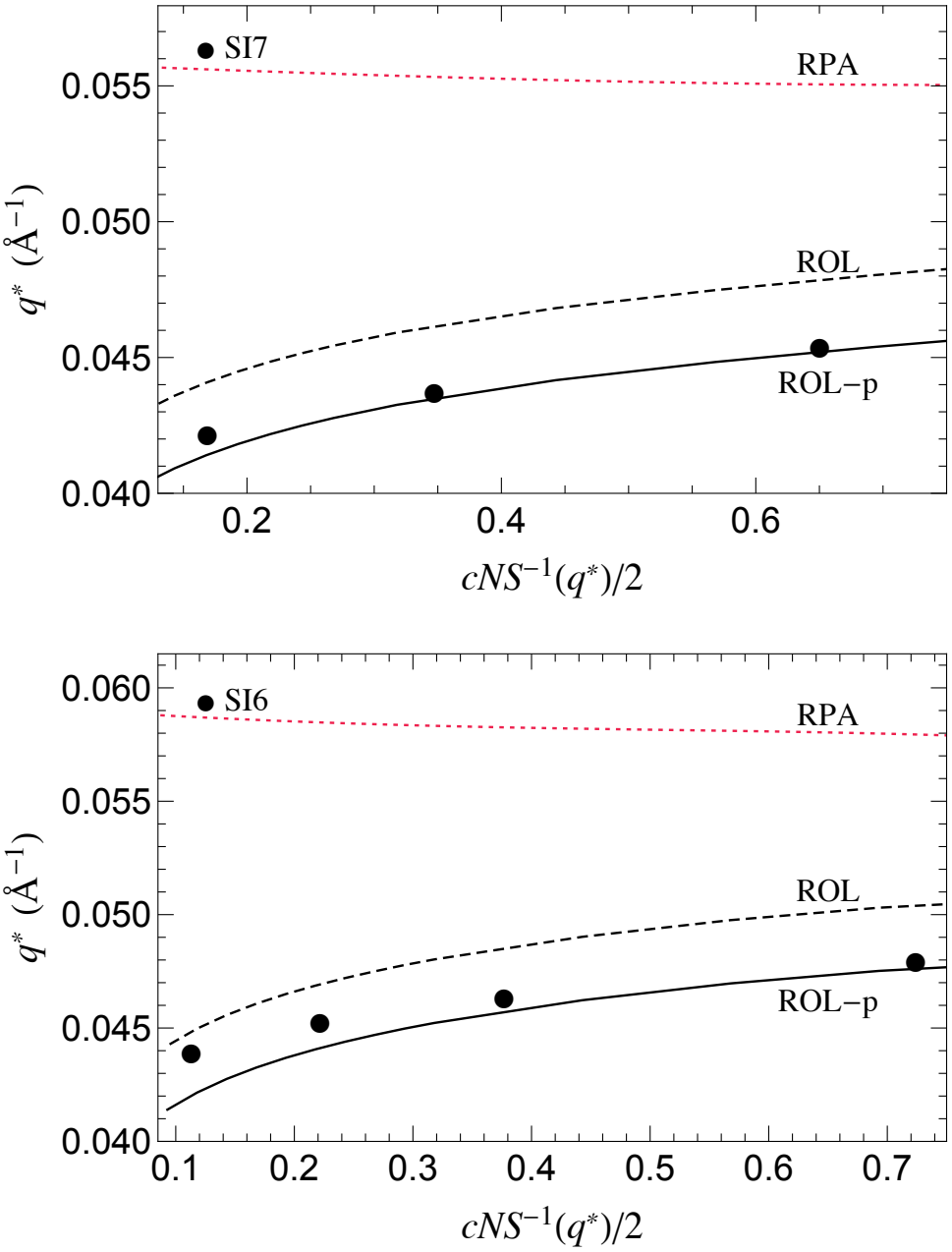

Figure 8.10: Comparison of experimental results of q^* of SI7 (upper) and SI6 (lower) to monodisperse RPA (red dotted line) and monodisperse ROL (black dashed line) theory predictions, as well as polydispersity-corrected ROL predictions (black solid curve labeled ROL-p). RPA polydispersity shift was calculated based on measured PDI of 1.05. Theoretically predicted minimum for PDI is 1.006 for this system.

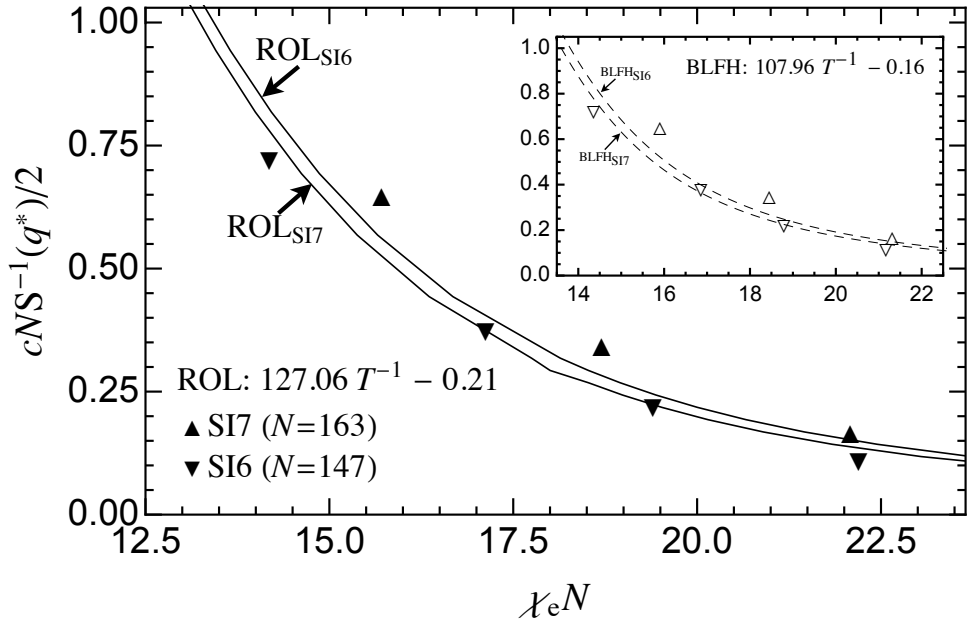

Figure 8.11: Extraction of $\chi_e(T)$ of PS-PI by fitting results of $cNS^1(q^*)/2$ *vs.* T^{-1} of SI7 and SI6 to monodisperse ROL (solid line, filled triangles) theory predictions. Inset: $\chi_e(T)$ from fit to monodisperse BLFH theory (dashed line, open triangles) predictions. Resulting $\chi_e(T)$ estimates are given in corresponding legends.

Next, we obtained $\chi_e(T)$ by simultaneously fitting results for normalized inverse peak structure factor $cNS^1(q^*)$ of both SI7 and SI6 to corresponding monodisperse ROL theory predictions. The fit, as shown in Fig. 8.11, yields $\chi_e^{\rm ROL}(T) = 127.05\,T^{-1} - 0.206$. On including the RPA prediction for polydispersity shift $\Delta\chi_p$, or in this case, the average of shifts for SI7 and SI6, we get $\chi_e^{\rm ROL-p}(T) = 127.05\,T^{-1} - 0.209$. Inset of Fig. 8.11 shows the same fit using monodisperse BLFH theory predictions, which results in $\chi_e^{\rm BLFH}(T) = 107.96\,T^{-1} - 0.160$, and polydispersity-corrected estimate of $\chi_e^{\rm BLFH-p}(T) = 107.96\,T^{-1} - 0.162$.

In order to test the consistency of $\chi_e(T)$ estimates obtained from scattering and ODT temperatures, we also obtained $\chi_e(T)$ estimates by fitting $T_{\rm ODT}$s of SI7, SI6, and IS-54[86] copolymers to (1) simulations scaling law given by Eq.6.5, (2) BLFH $(\chi_e N)_{\rm ODT}$ prediction for $f = 0.46$, and (3) SCFT prediction for $(\chi_e N)_{\rm ODT}$ for $f = 0.46$. The upper panel of Fig.8.12 shows all three $\chi_e(T)$

Fitting procedure	A (K)	B	T range
ROL	127.05	-0.21	T range: $83 - 147\,^{\circ}\mathrm{C}$
BLFH	107.96	-0.16	T range: $83 - 147\,^{\circ}\mathrm{C}$
SIM-ODT	124.0	-0.23	T_{ODT}s: 78, 84, and $124\,^{\circ}\mathrm{C}$
BLFH-ODT	98.0	-0.17	T_{ODT}s: 78, 84, and $124\,^{\circ}\mathrm{C}$
SCFT-ODT	60.42	-0.10	T_{ODT}s: 78, 84, and $124\,^{\circ}\mathrm{C}$

Table 8.4: Estimates of $\chi_e(T) = A\,T^{-1} + B$ of PS-PI obtained using different fitting procedures.

estimates along with the monodisperse ROL based estimate, $\chi_e^{\mathrm{ROL}}(T)$. For each ODT-based $\chi_e(T)$ estimate, symbols denote predicted values of $\chi_{e\mathrm{ODT}}$ by the underlying scaling law (SIM-ODT or BLFH-ODT or SCFT-ODT) *vs.* measured T_{ODT}^{-1} of the 3 PS-PI samples. Discrepancies between predicted values and the fitted $\chi_e(T)$ estimate are less than the symbol size for IS-54, but are visible for SI7 and SI6 for all 3 fits. See Table 8.4 for A and B values of resulting $\chi_e(T) = A\,T^{-1} + B$ estimates.

The lower panel of Fig. 8.12 compares $\chi_e^{\mathrm{ROL}}(T)$ and $\chi_e^{\mathrm{BLFH}}(T)$ to estimates reported in literature and given in Table 8.3. All reported $\chi_e(T)$ estimates were normalized to $\nu_{\mathrm{ref}} = 157\,\mathrm{\AA}^3$ using $\chi_e = \chi_e^*\nu_{\mathrm{ref}}/\nu^*$.

8.4 PE-PEP

Maurer, Bates, Lodge and coworkers[1,142] examined the influence of architecture on interaction parameter $\chi_e(T)$ by comparing estimates determined from blends and diblock copolymers of polyethylene (PE) and polyethylenepropylene (PEP). Results for structure behavior and critical temperatures of PE/PEP blends and a PE-PEP diblock copolymers were fitted to mean-field (SCFT/RPA) and fluctuations (BLFH) theory predictions to obtain different $\chi_e(T)$ estimates. Their key conclusion was a lack of agreement between $\chi_e(T)$ estimates obtained from blends and diblock copolymers; the authors attributed this disparity to the failure of block copolymer theories (RPA and BLFH) to account for chain stretching in diblock copolymers in the vicinity of ODT. Here, we re-analyze results of diblock copolymers presented in the study. Among the 4 diblock copolymers (all symmetric) that were studied, SANS intensity results are reported for only 1

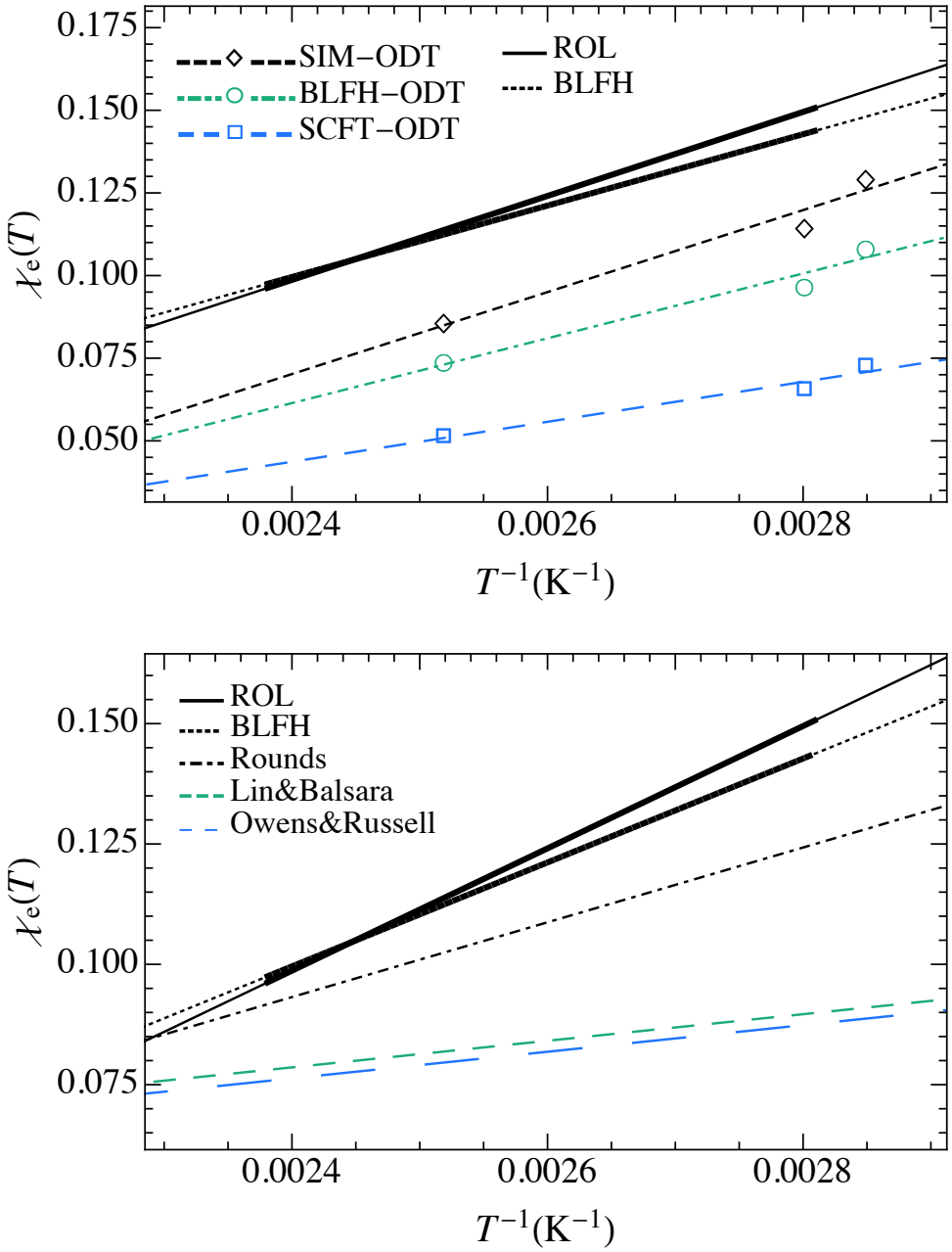

Figure 8.12: Upper: Comparison of $\chi_e^{\mathrm{ROL}}(T)$ and $\chi_e^{\mathrm{BLFH}}(T)$ of PS-PI to $\chi_e(T)$ estimates obtained by fitting T_{ODT}s of SI7 ($N = 163$ and $T^{-1} = 0.0028\mathrm{K}^{-1}$), SI6 ($N = 147$ and $T^{-1} = 0.00285\mathrm{K}^{-1}$), and IS-54 ($N = 208$ and $T^{-1} = 0.0025\mathrm{K}^{-1}$) to different predictions for ODT: SIM-ODT Universal scaling law of Eq.6.5 from simulations, BLFH-ODT - BLFH theory prediction for $(\chi_e N)_{\mathrm{ODT}}$ for $f = 0.46$, SCFT-ODT - SCFT prediction for $(\chi_e N)_{\mathrm{ODT}}$ for $f = 0.46$. IS-54 is obtained from Ref.[86] The temperature range of peak intensity data used to obtain $\chi_e^{\mathrm{ROL}}(T)$ and $\chi_e^{\mathrm{BLFH}}(T)$ is indicated by thicker line segments. Lower: Comparison of $\chi_e(T)$ estimates of PS-PI obtained in different studies. All estimates are defined with respect to $\nu_{\mathrm{ref}} = 157\text{Å}^3$.

diblock copolymer, namely PE-PEP-6H.[1,27,142]

PE-PEP-6H contains equal volumes of PE and PEP and a partially deuterated PE block. The isotopic composition was confirmed by a Rutherford backscattering measurement as D:H= 0.6. This precise value is used to calculate the neutron scattering contrast between PE and PEP repeat units required in analysis of absolute intensity SANS data (see below). Light scattering and SEC measurements yielded weight-average molecular weight and polydispersity index of PE-PEP-6H as M_w = 128kg/mol and M_w/M_n = 1.09.[27] The reported M_n value refers to the hydrogenous equivalent rather than the true molecular mass. The Poisson distribution value for PDI of PE-PEP-6H is 1.0005. Since PE-PEP-6H is clearly a high molecular weight polymer (chemical repeat unit degree of polymerization is 1887), the true value of PDI is expected to be near this theoretical minimum, implying that the SEC value is way off in this case.

Fig. 3.3 in Ref.[142] shows absolute SANS intensity $I(q)$ patterns for 10 temperatures (between and including 140.7 and 159.9 °C) in the disordered phase; Fig. 3.5 in Ref.[142] shows results for inverse peak intensity $I^{-1}(q^*)$ (cm) and peak wavenumber $q^*\left(\text{Å}^{-1}\right)$ *vs.* temperature for 18 temperatures between 140.7 and 159.9 °C including the 10 temperatures for which $I(q)$ profiles are reported. Ref.[142] (and Ref.[1]) analyzes this set of peak intensity results for obtaining $\chi_e(T)$ estimates based on scattering behavior of diblock copolymers. Since a complete description of the SANS instrument configuration is provided in Maurer's thesis,[142] we include contributions from collimation effects and detector resolution apart from wavelength spread in evaluating the instrument resolution function for desmearing. Eqs. 3.14-3.17 in Ref.[142] are used for this purpose. Note that standard deviations σ of the collimation and detector resolution terms are constant and do not vary with wavenumber q unlike the standard deviation associated with the wavelength spread. As a consequence, the peak position q^* is also affected by the desmearing procedure.

ODT temperatures were obtained for PE-PEP-6H, PE-PEP-1D (M_w = 93.4kg/mol and $f_{\text{PE}} = 0.5$), and PE-PEP-3D (M_w = 136kg/mol and $f_{\text{PE}} = 0.49$) as 139, 119, and 159 °C from dynamic mechanical spectrascopy experiments. No scattering information was obtained for the latter two systems. Also, both these systems contain partially deuterated PE and PEP blocks, but exact isotope com-

positions were not determined.

As mentioned in the introductory paragraph of this section, Ref.[1,142] primarily focuses on comparison of $\chi_e(T)$ estimates obtained from blends and diblock copolymers data. To this end, low-q SANS data obtained for several temperatures in the single-phase regime of PE/PEP blends with varying composition ($0.1 \leq \phi \leq 0.9$) were extrapolated to obtain $I^{-1}(q=0)$ *vs.* T^{-1} plots for different compositions. These results were then fitted to RPA prediction for blends to extract $\chi_e(T) = \alpha T^{-1} + \beta$ estimates for each composition. Resulting values of α and β from the fits were found to be composition independent within limits of uncertainties in intensity measurements, and consistent with a least squares fit: $\chi_e^{\mathrm{BL-RPA}}(T) = 7.9\,T^{-1} - 0.0146$ (BL for blends). In addition, the authors obtained 4 $\chi_e(T)$ estimates by fitting results from symmetric diblock copolymers. Specifically, they fitted (1) temperature dependence of peak scattering intensity $I(q^*)$ of PE-PEP-6H to RPA prediction for $S^{-1}(q^*)$, (2) temperature dependence of peak scattering intensity $I(q^*)$ of PE-PEP-6H to BLFH prediction for $S^{-1}(q^*)$, (3) T_{ODT}s of PE-PEP-6H, PE-PEP-1D, and PE-PEP-3D to SCFT prediction for ODT, $(\chi_e N)_{\mathrm{ODT}} = 10.5$, and (4) T_{ODT}s of PE-PEP-6H, PE-PEP-1D, and PE-PEP-3D to BLFH prediction for ODT, $(\chi_e N)_{\mathrm{ODT}} = 10.5 + 41.0\,\overline{N}^{-1/3}$. The resulting estimates are given by: $\chi_e^{\mathrm{DB-RPA}}(T) = 14.4\,T^{-1} - 0.029$ (DB for diblocks), $\chi_e^{\mathrm{BLFH}}(T) = 16.7\,T^{-1} - 0.034$, $\chi_e^{\mathrm{SCFT-ODT}}(T) = 9.1\,T^{-1} - 0.017$, and $\chi_e^{\mathrm{BLFH-ODT}}(T) = 10.3\,T^{-1} - 0.019$. All estimates were obtained relative to a polyolefin segment volume, $\nu_0 = 108 \exp\left[7.5 \times 10^{-4}(T - 23\,^{\circ}\mathrm{C})\right]$ Å^3. Note that the same ν_0 (slightly different coefficient - 6.85×10^{-4}) was used for analysis of PEP-PEE diblock copolymers in section 8.2. Fig. 8.13 plots Maurer's 5 $\chi_e(T)$ estimates. For each ODT-based $\chi_e(T)$ estimate, symbols denote predicted values of $\chi_{e\mathrm{ODT}}$ by the underlying scaling law (BLFH-ODT or SCFT-ODT) *vs.* measured T_{ODT}^{-1} of the 3 PE-PEP samples. Table 8.5 lists coefficients A and B of all the above $\chi_e(T)$ estimates.

Maurer *et al.* concluded that among their 4 $\chi_e(T)$ estimates obtained from diblock copolymers data (see above), $\chi_e^{\mathrm{SCFT-ODT}}(T)$ obtained from fitting T_{ODT}s of PE-PEP copolymers to SCFT prediction for ODT agrees best with $\chi_e^{\mathrm{BL-RPA}}(T)$ obtained from fitting blends scattering data to RPA, which is assumed to be the true interaction parameter $\chi_e(T)$ of PE and PEP segments.

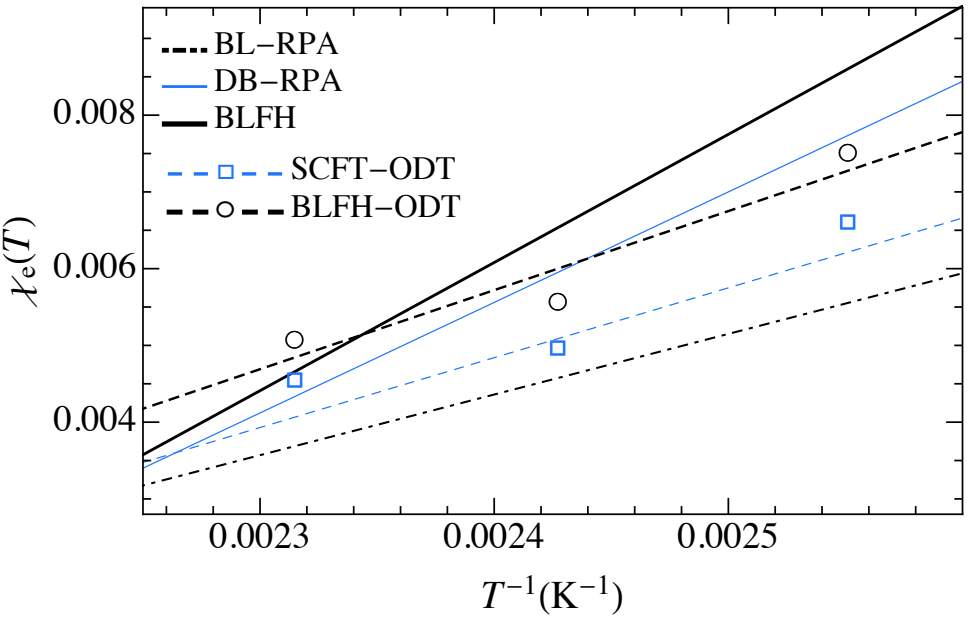

Figure 8.13: Comparison of $\chi_e(T)$ estimates of PE-PEP obtained by Maurer *et al.*[1] using different fitting procedures: 1. BL-RPA Fit of $I(q = 0)$ data of PE/PEP blends to RPA prediction 2. DB-RPA Fit of $I(q^*)$ *vs.* T^{-1} of PE-PEP-6H to RPA prediction (only the highest 10 temperatures were used) 3. BLFH Fit of $I(q^*)$ *vs.* T^{-1} of PE-PEP-6H to BLFH predictions 4. SCFT-ODT Fit of T_{ODT}s of PE-PEP-6H ($N = 2120$ and $T^{-1} = 0.00243\mathrm{K}^{-1}$), PE-PEP-1D ($N = 1591$ and $T^{-1} = 0.00255\mathrm{K}^{-1}$), and PE-PEP-3D ($N = 2316$ and $T^{-1} = 0.00231\mathrm{K}^{-1}$) to SCFT prediction for $(\chi_e N)_{\mathrm{ODT}}$ for $f = 0.5$ 5. BLFH-ODT Fit of T_{ODT}s of PE-PEP-6H, PE-PEP-1D, and PE-PEP-3D to BLFH prediction for $(\chi_e N)_{\mathrm{ODT}}$ for $f = 0.5$. All estimates are defined with respect to common segment volume ν_0 given in the main text.

Fitting procedure	A (K)	B	T range
BL-RPA	7.9	−0.0146	T range: $134 - 165\,^{\circ}\mathrm{C}$
DB-RPA	14.4	−0.029	T range: $147 - 159.9\,^{\circ}\mathrm{C}$
BLFH	16.7	−0.034	T range: $147 - 159.9\,^{\circ}\mathrm{C}$
SCFT-ODT	9.1	−0.017	T_{ODT}s: 119, 139, and $159\,^{\circ}\mathrm{C}$
BLFH-ODT	10.3	−0.019	T_{ODT}s: 119, 139, and $159\,^{\circ}\mathrm{C}$

Table 8.5: Estimates of $\chi_e(T) = A\,T^{-1} + B$ of PE-PEP obtained by Maurer *et al.* using different fitting procedures.[1]

As noted by the authors, use of RPA for fitting scattering intensity data is justified in the case of the PE/PEP blend in this study, because the relatively high molecular weights of PE and PEP polymers used means that the mean-field treatment breaks down only within a small temperature window around the critical temperature. The data for $I(q)$ obtained for the blend in this study was nearly perfectly described by the RPA, suggesting that the critical region did not fall within the range of temperatures and wavenumbers that was studied.[1] The RPA treatment of scattering in the disordered phase is, however, definitely not an adequate description for these diblock copolymers, as is evident from the curvature observed in results of $I^{-1}(q^*)$ *vs.* T^{-1} of PE-PEP-6H for $T \to T_{\mathrm{ODT}}$. For $\overline{N}$ values as large as these (see below: $20000 \lesssim \overline{N} \lesssim 30000$), we expect the BLFH theory predictions for both scattering intensity and ODT to be accurate; Ref.[41] shows that BLFH and ROL theory predictions for scattering intensity are practically indistinguishable for $\overline{N} \gtrsim 10000$ and the simulations results for the ODT shown in chapter 6,[111] suggest that BLFH prediction for ODT also become accurate for $\overline{N} \gtrsim 10^4$.

Re-analysis: For our re-analysis, we define segments based on a fixed segment volume $\nu_{\mathrm{ref}} = 117\,\text{Å}^3$, which is the value of the above polyolefin segment volume ν_0 at the ODT temperature of PE-PEP-6H, 139 °C, which we fix as the reference temperature. Note that we used the same segment volume ν_0 for our analysis of PEP-PEE copolymers in section 8.2, except at a different reference temperature. With $\nu_{\mathrm{ref}} = 117\,\text{Å}^3$, Eq. 8.1 yields values for volumetric degrees of polymerization at the reference temperature as N_n =2120, 1591, and 2316 for PE-PEP-6H, PE-PEP-1D, and PE-PEP-3D, respectively. The authors[27] report temperature dependent functions for statistical segment lengths of PE and PEP homopolymers as $b_{\mathrm{PE}} = 8.8 \exp\left[-0.58 \times 10^{-3}(T - 25\,^\circ\mathrm{C})\right]$ Å and $b_{\mathrm{PEP}} = 7.2 \exp\left[-0.58 \times 10^{-3}(T - 25\,^\circ\mathrm{C})\right]$ Å with respect to segment volume ν_0. From values of statistical segment lengths at the reference temperature, namely $b_{\mathrm{PE}} = 8.24$Å and $b_{\mathrm{PEE}} = 6.74$Å, we get $\overline{N}$ =28,239, 21,194, and 30,486 for the 3 copolymers. Neutron scattering lengths of the partially deuterated PE (D:H = 0.6) and fully hydrogenated PEP repeat units were calculated from known neutron scattering lengths of carbon (0.0000665 Å), hydrogen (-0.0000374 Å), and deuterium (0.0000667 Å) atoms to result in $|l_A - l_B| = 6.325 \times 10^{-4}$ Å.

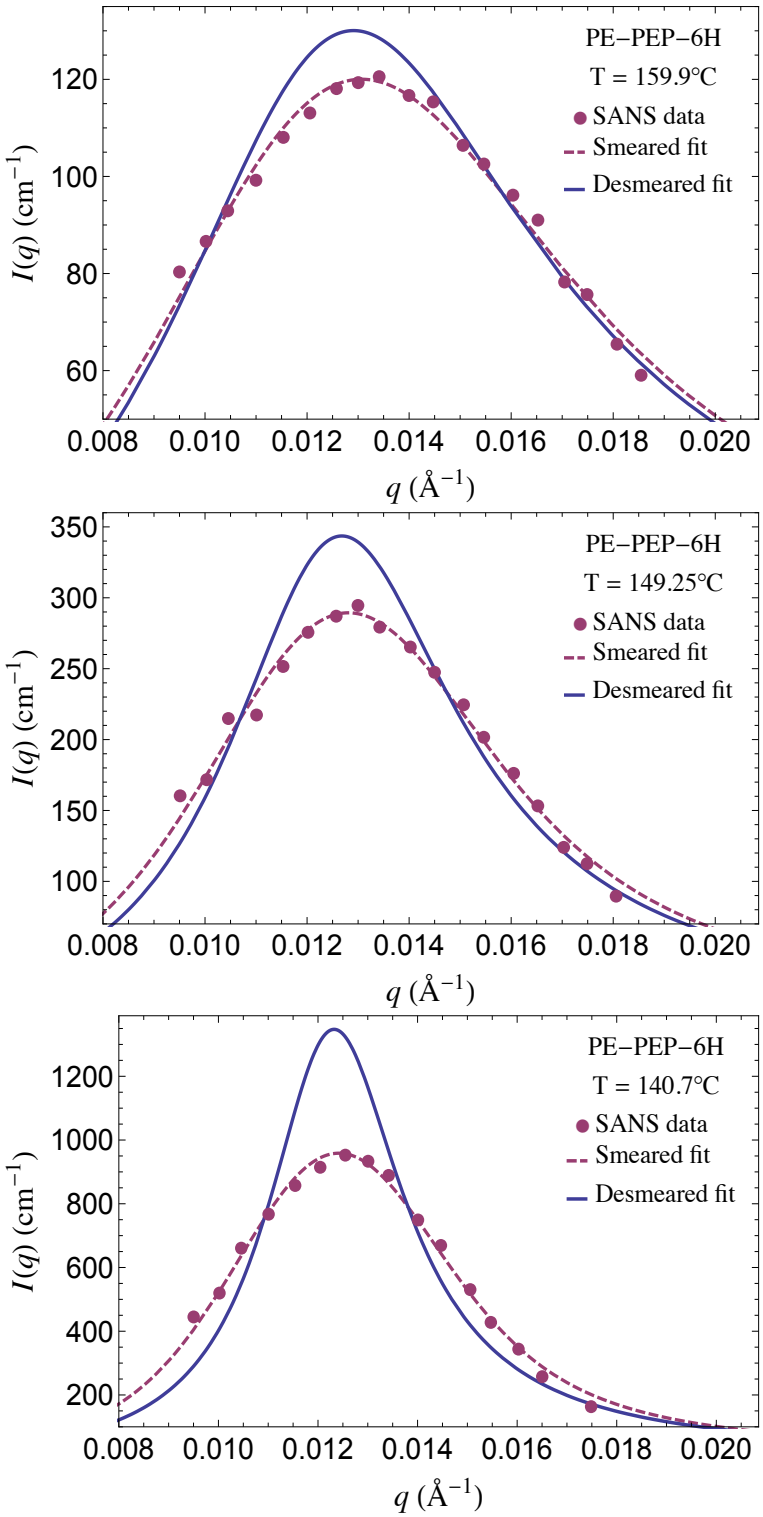

Figure 8.14: SANS intensity $I(q)$ profiles of PE-PEP-6H at three disordered phase temperatures. For each temperature, the smeared and desmeared intensity $I(q)$ functions obtained from fitting the measured SANS data (circles) to the convolution discussed in the main text are marked by red dashed and blue solid curves, respectively.

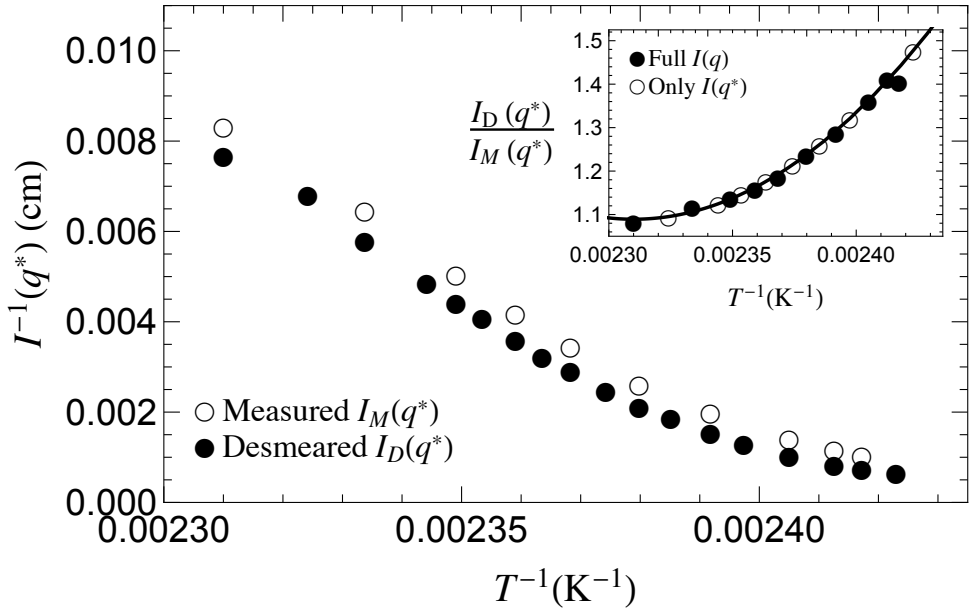

Figure 8.15: Temperature dependence of inverse peak intensity $I^{-1}(q^*)$ extracted from fitted $I_{\mathrm{D}}(q)$ (filled) and $I_{\mathrm{M}}(q)$ (empty) functions of PE-PEP-6H. Inset: Quadratic fit used to obtain values of the ratio $I_{\mathrm{D}}(q^*)/I_{\mathrm{M}}(q^*)$ of desmeared and smeared peak intensities for temperatures between 140.7 and 159.9 °C for which complete $I_{\mathrm{M}}(q)$ profiles are not reported.

Fig. 8.14 shows measured SANS data at 3 temperatures (140.7, 149.25, and 159.9 °C) from reported data at 10 temperatures in Fig. 3.3 of Ref.[142] The same procedure as employed for PEP-PEE-5H data is applied here too to obtain desmeared peak intensity $I_{\mathrm{D}}(q^*)$ data for temperatures between 140.7 and 159.9 °C for which only (smeared) peak intensities, but not the complete $I_{\mathrm{M}}(q)$ profiles, are reported; we obtained results for (smeared) peak intensity *vs.* T^{-1} from Fig. 3.5 in Ref.[142] Fig. 8.15 shows the resulting data.

Fig. 8.16 shows a comparison of results of q^* *vs.* $cNS^{-1}(q^*)/2$ of PE-PEP-6H to polydispersity-corrected ROL theory predictions as well as monodisperse RPA and ROL theory predictions. Note that results for q^* are shown only for the 10 temperatures for which we had complete $I(q)$ profile data.

The next step is to estimate the interaction parameter $\chi_e(T)$ by fitting results of $cNS^1(q^*)$ to monodisperse ROL theory predictions. Fig. 8.17 shows experimental results for $cNS^1(q^*)/2$ *vs.* $\chi_e N$ plotted using the resulting fitted estimate: $\chi_e^{\mathrm{ROL}}(T) = 15.89\,T^{-1} - 0.0330$. A fit to monodisperse BLFH theory predictions

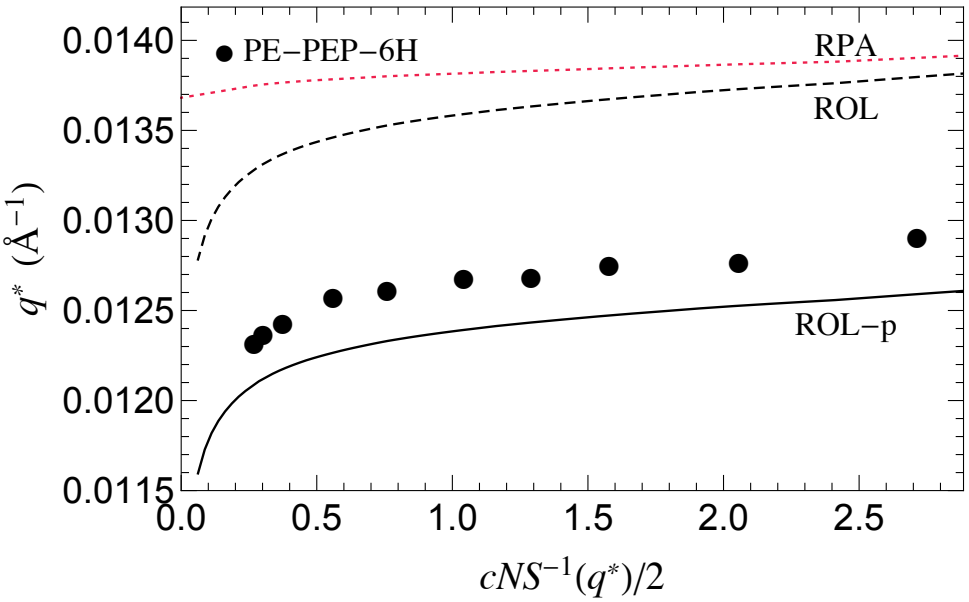

Figure 8.16: Comparison of experimental results of q^* of PE-PEP-6H (circles) to monodisperse RPA (red dashed line) and ROL (black dashed line) theory predictions, as well as polydispersity-corrected ROL predictions (black solid curve labeled ROL-p). RPA polydispersity shift was calculated based on measured PDI of 1.09. Theoretically predicted minimum for PDI is 1.0005 for this system.

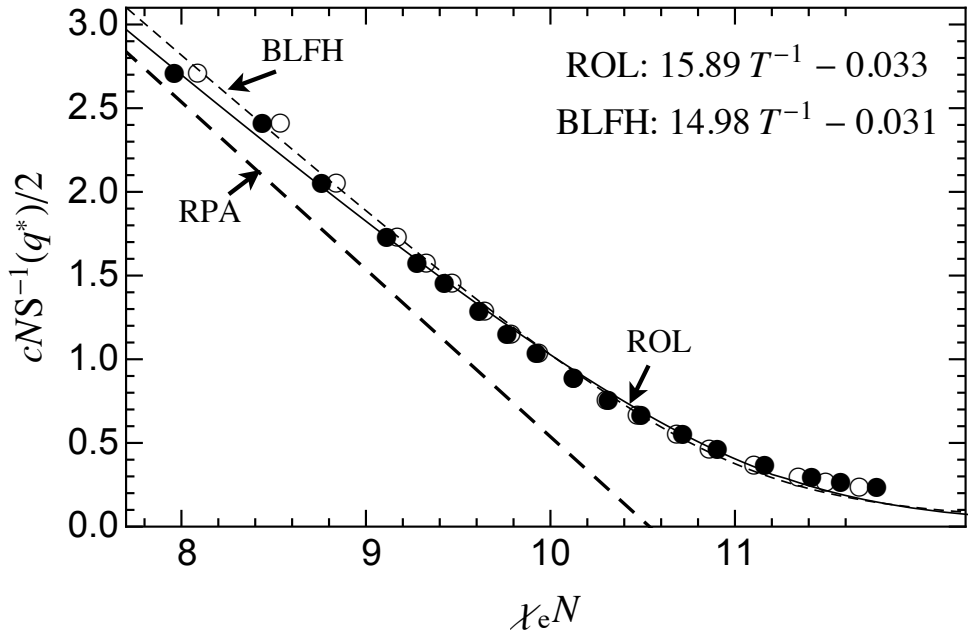

Figure 8.17: Extraction of $\chi_e(T)$ of PE-PEP by fitting results of $cNS^1(q^*)/2$ *vs.* T^{-1} of PE-PEP-5H to monodisperse ROL (solid line, filled circles) and monodisperse BLFH (dashed line, open circles) theory predictions. The dashed line is the monodisperse RPA prediction. Resulting $\chi_e(T)$ estimates are given in the legend.

at $\overline{N} = 28,239$ yields $\chi_e^{\rm BLFH}(T) = 14.98\,T^{-1} - 0.0308$. Inclusion of polydispersity shift $\Delta\chi_p$ predicted by RPA yields $\chi_e^{\rm ROL-p}(T) = 15.89\,T^{-1} - 0.0333$ and $\chi_e^{\rm BLFH-p}(T) = 14.98\,T^{-1} - 0.0311$. In order to conduct a complete comparison to Maurer's $\chi_e(T)$ estimates, we also obtained $\chi_e^{\rm RPA}(T)$ by fitting data of $cNS^{-1}(q^*)$ *vs.* T^{-1} from the highest 10 temperatures (same as Maurer's DB-RPA fit) to the monodisperse RPA prediction for $\chi_e N$ dependence of peak intensity. The resulting estimate is $\chi_e^{\rm RPA}(T) = 13.06\,T^{-1} - 0.026$.

In addition, $\chi_e(T)$ estimates were obtained by fitting reported ODT temperatures of PE-PEP-6H, PE-PEP-1D, and PE-PEP-3D copolymers to (1) simulations scaling law of Eq.6.5, (2) BLFH prediction for $(\chi_e N)_{\rm ODT}$ for $f = 0.5$, and (3) SCFT prediction for $(\chi_e N)_{\rm ODT}$ for $f = 0.5$. Fig. 8.18 shows resulting $\chi_e(T)$ estimates along with $\chi_e^{\rm ROL}(T)$ and $\chi_e^{\rm BLFH}(T)$ obtained by fitting SANS results of PE-PEP-6H to monodisperse ROL and BLFH theory predictions, respectively. For each ODT-based $\chi_e(T)$ estimate, symbols denote predicted values of $\chi_{e\rm ODT}$

Fitting procedure	A (K)	B	T range
RPA	13.06	-0.026	T range: $147 - 159.9\,^{\circ}$C
BLFH	14.98	-0.031	T range: $140.7 - 159.9\,^{\circ}$C
ROL	15.89	-0.033	T range: $140.7 - 159.9\,^{\circ}$C
SCFT-ODT	9.46	-0.018	T_{ODT}s: 119, 139, and 159 °C
BLFH-ODT	11.16	-0.021	T_{ODT}s: 119, 139, and 159 °C
SIM-ODT	11.75	-0.022	T_{ODT}s: 119, 139, and 159 °C

Table 8.6: Estimates of $\chi_e(T) = A\,T^{-1} + B$ of PE-PEP obtained using different fitting procedures.

by the underlying scaling law (SIM-ODT or BLFH-ODT or SCFT-ODT) *vs.* measured T_{ODT}^{-1} of the 3 PE-PEP copolymers. Discrepancies between predicted values and the fitted $\chi_e(T)$ estimate are visible for all 3 systems. Table 8.6 provides precise values of coefficients of resulting $\chi_e(T) = A\,T^{-1} + B$ estimates.

Figs. 8.19 and 8.20 compare corresponding $\chi_e(T)$ estimates obtained by us and by Maurer *et al.*

8.5 PS-PEO

Teran and Balsara obtained scattering measurements for poly(styrene-*b*-ethylene-oxide) (PS-PEO or SEO) diblock copolymers of different chain lengths. Similar to their study on PS-PI diblock copolymers (section 8.3), this study too demonstrated that $\chi_e(T)$ estimates obtained from fitting scattering intensity results of PS-PEO diblock copolymers to the RPA prediction exhibit a strong dependence on chain length. Among the five nearly symmetric diblock copolymers that were studied, we focus on only two systems here, namely SEO(6.4-7.3) and SEO(4.9-5.5), because scattering intensity from other copolymers was too weak to be fit reliably; this is due to a combination of very small chain lengths of the other copolymers and the relatively low scattering contrast between PS and PEO repeat units. Here, we shorten the labels of SEO(6.4-7.3) and SEO(4.9-5.5) to SEO7 and SEO5 respectively. SEO7 and SEO5 contain 48% by volume PS. Numbers in the parentheses denote number-average molecular weights of PS and PEO blocks, respectively, and so, M_n of the two blocks are 6.4 and 7.3 kg/mol and 4.9 and 5.5 kg/mol of SEO7 and SEO5, respectively. In both cases,

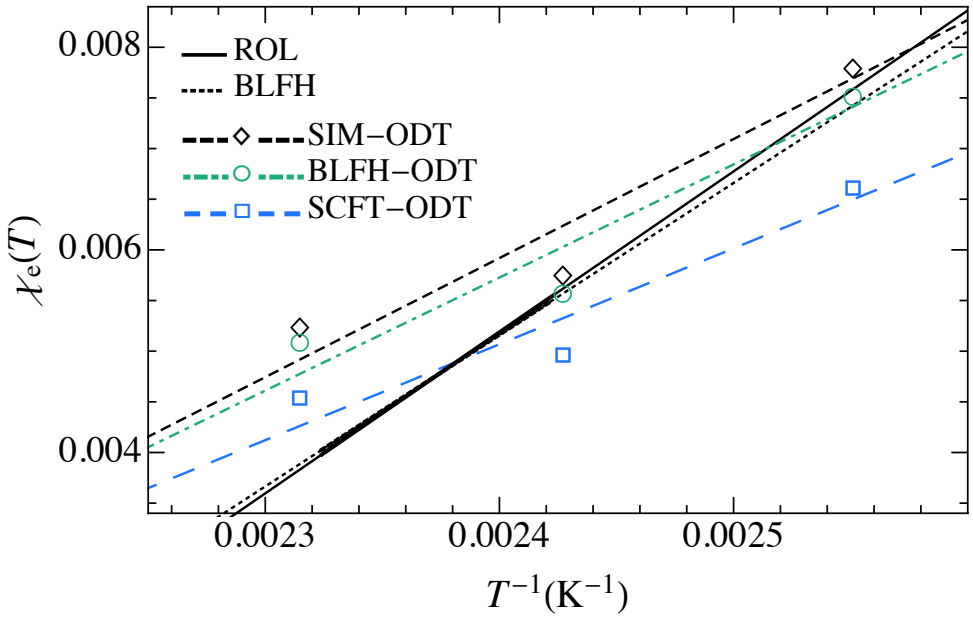

Figure 8.18: Comparison of $\chi_e(T)$ estimates of PE-PEP determined using five different fitting procedures: 1. ROL Fit of peak scattering intensity data of PE-PEP-6H to monodisperse ROL theory predictions. 2. BLFH Fit of peak scattering intensity data of PE-PEP-6H to monodisperse BLFH theory predictions. 3. SIM-ODT Fit of T_{ODT}s of PE-PEP-6H ($N = 2120$ and $T^{-1} = 0.00243\mathrm{K}^{-1}$), PE-PEP-1D ($N = 1591$ and $T^{-1} = 0.00255\mathrm{K}^{-1}$), and PE-PEP-3D ($N = 2316$ and $T^{-1} = 0.00231\mathrm{K}^{-1}$) to the universal scaling law from simulations results. 4. BLFH-ODT Fit of T_{ODT}s of PE-PEP-6H, PE-PEP-1D, and PE-PEP-3D to the BLFH theory prediction for $(\chi_e N)_{\mathrm{ODT}}$ for $f = 0.5$. 5. SCFT-ODT Fit of T_{ODT}s of PE-PEP-6H, PE-PEP-1D, and PE-PEP-3D to the SCFT prediction for $(\chi_e N)_{\mathrm{ODT}}$ for $f = 0.5$. The temperature range of peak intensity data used to obtain $\chi_e^{\mathrm{ROL}}(T)$ and $\chi_e^{\mathrm{BLFH}}(T)$ is indicated by thicker line segments. All estimates are defined with respect to 117 $\mathrm{\AA}^3$.

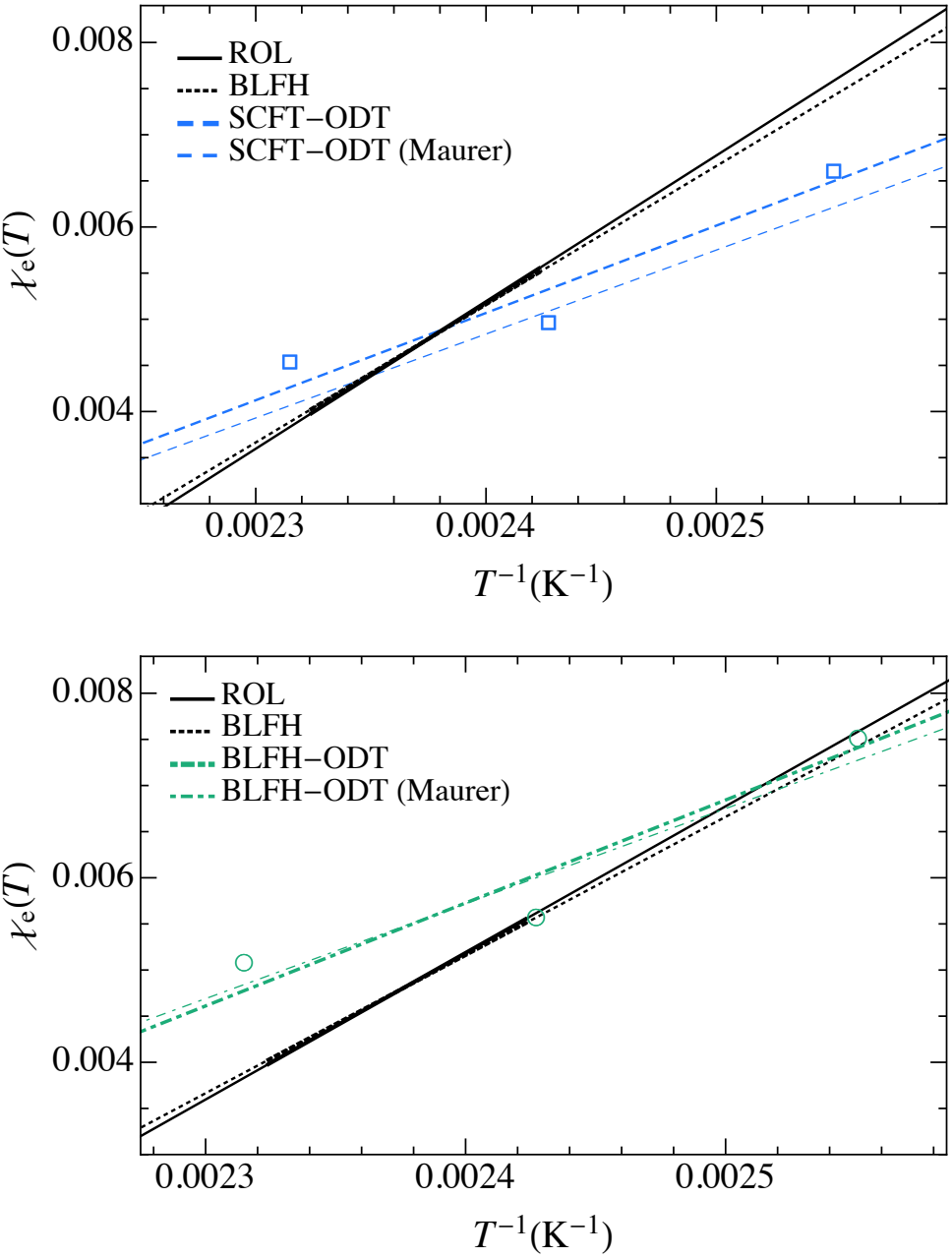

Figure 8.19: Comparison of $\chi_e(T)$ estimates of PE-PEP obtained by us and by Maurer *et al.* from fits to SCFT (upper) and BLFH (lower) predictions for ODT. Lines labeled ROL and BLFH represent our $\chi_e(T)$ estimates obtained from fitting SANS peak intensity data of PE-PEP-6H to monodisperse ROL and BLFH theory predictions, respectively.

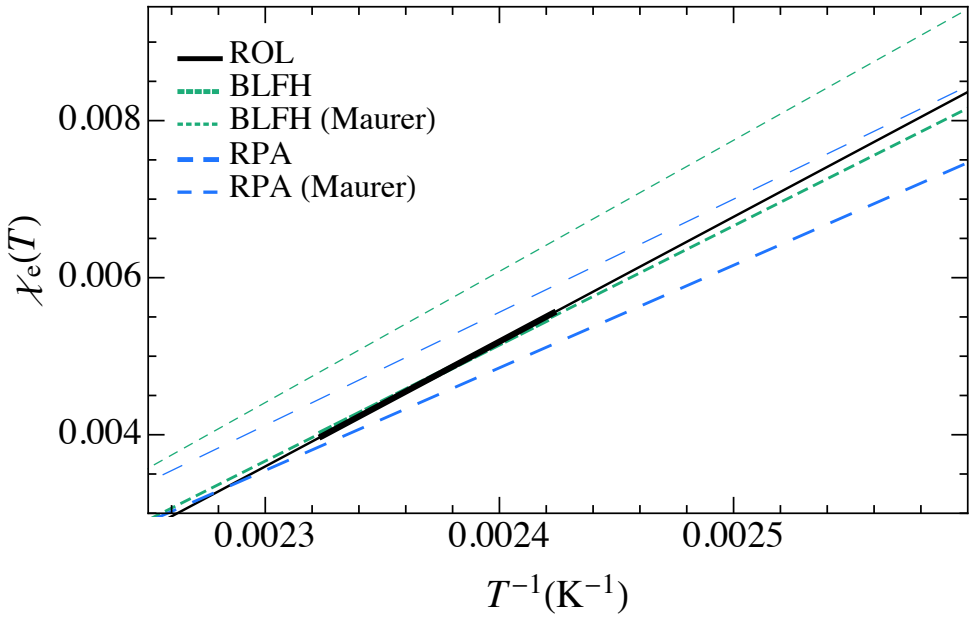

Figure 8.20: Comparison of PE-PEP $\chi_e(T)$ estimates obtained by us and Maurer *et al.* from fitting SANS peak intensity data of PE-PEP-6H to RPA and BLFH theory predictions. $\chi_e^{\mathrm{ROL}}(T)$ is obtained from fitting SANS peak intensity data of PE-PEP-6H to monodisperse ROL theory predictions.

the reported polydispersity index is $M_w/M_n = 1.04$, presumably from SEC measurements. Theoretical values based on Poisson distribution are 1.004 and 1.006 for SEO7 and SEO5, respectively. Here too, as in the case of SI7 and SI6, we expect the reported polydispersity indices to be closer to the true values than the theoretical values because the chemical degree of polymerization of SEO7 and SEO5 are relatively moderate and not large.

The authors reported absolute SAXS intensity $I(q)$ profiles for all five PS-PEO copolymers, each for several temperatures in the disordered phase. This is one among very few studies that report SAXS intensity data in absolute units (cm^{-1}); the authors determined the scaling calibration using measurements from a calibrated glassy carbon standard. An important advantage of SAXS measurements over SANS is that they are not prone to instrumental smearing effects from poor q resolution, and therefore, results for peak intensity can be directly extracted from the measured data. It must be mentioned that in this one case, we obtained data for SAXS intensity profiles directly from the authors of Ref.[131] ODT was observed for only SEO7; it was identified as 107.5 °C from appearance of a Bragg peak.

For their analysis, the authors defined segments based on a fixed reference segment volume, $\nu_{\mathrm{ref}} = 100\,\mathrm{\AA}^3$, equal to the geometric mean of molar volumes of PS and PEO at 140 °C. Molar volumes $\nu = M/\rho$ were obtained from molar masses of styrene (104.15 g/mol) and ethylene oxide (44.05 g/mol) and temperature dependent functions for PS and PEO homopolymer densities reported in literature.[143] The exact functions used by the authors are $\rho_{\mathrm{PS}} = 1.139 - 7.31 \times 10^{-4} T\,\mathrm{g/cm^3}$ and $\rho_{\mathrm{PEO}} = 1.0865 - 6.19 \times 10^{-4} T + 1.36 \times 10^{-7} T^2\,\mathrm{g/cm^3}$, where T is in °C. With these input parameters, Eq. 8.1 yields $N_{SEO7} = 212$ and $N_{SEO5} = 161$ at 140 °C; the same values are reported in the paper. They obtained chain size R_g from fitting scattering intensity $I(q)$ profiles to the RPA prediction, and hence did not require estimates for statistical segment lengths of PS and PEO homopolymers. In a private communication, the authors reported using X-ray scattering lengths of PS and PEO repeat units as $l_{\mathrm{PS}} = 1.58 \times 10^{-3}$ Å and $l_{\mathrm{PEO}} = 6.76 \times 10^{-4}$ Å, respectively.

From fits of SAXS profiles to polydisperse RPA prediction (see appendix A), the authors obtained $\chi_e(T)$ estimates for four different chain lengths (we

were able to fit data of only SEO7 and SEO5 though), that exhibit a systematic dependence on chain length N. As mentioned in section 8.3, $\chi_e(T)$ estimates obtained from fitting SANS data of PS-PI diblock copolymers of different chain lengths to the RPA prediction also exhibit N-dependence. It is a clear indication of the importance of fluctuation effects for molecular weights employed in the study.

Previous Work: Frielinghaus *et al.* published two papers on PS/PEO that are relevant here: 1. In Ref.,[128] they fitted SANS peak intensity results obtained from a PS/PEO blend and a PS-PEO diblock copolymer to BLFH theory predictions; based on their results for $\chi_e(T) = A\,T^{-1} + B$, the temperature coefficient A of diblock systems is 34% smaller and B values are similar in magnitude, but of opposite sign. In addition, the authors compared their pair of $\chi_e(T)$ estimates to similar pairs obtained from studies of other systems, such as Maurer's study for PE and PEP,[1] and found differences between estimates from blends and diblocks for all systems, but to varying degrees that do not show any systematic behavior. 2. In Ref.,[129] effect of different end groups was examined by obtaining χ estimates from PS/PEO blends and diblock copolymers with the PEO polymer/block terminated with either a methoxy or a hydroxy end group. First, the intuitive picture that corrections of end groups are of order $(N\nu)^{-1}$ was confirmed by their results of A *vs.* $(N\nu)^{-1}$ and B *vs.* $(N\nu)^{-1}$, where A and B are interaction parameter coefficients obtained from fitting measurements of critical SANS intensity ($S^{-1}(q = 0)$ and $S^{-1}(q = q^*)$ for blends and diblocks, respectively) of chain length N to BLFH theory predictions. Effective $\chi_e(T)$ parameters of blends and diblocks were subsequently obtained by extrapolating these results to infinite chain length, or equivalently to $(N\nu)^{-1} = 0$. The resulting $\chi_e(T)$ estimates of both blends and diblocks reveal a significant difference between a hydroxy and methoxy end group for PEO polymer/block. The authors showed that the bulk of the measured differences stems from the hydrogen-bond energy of a hydroxy end group using calculations from density functional theory. The end group effect is larger in blends than in diblocks as demonstrated by the shift in phase boundary by 90K in blends (2.0 kg/mol) and 45K in diblock copolymers (18.0 kg/mol); $\chi_e(T)$ estimate obtained from PS-PEO-OH diblock copolymers is about 10-15% greater than that from PS-PEO-

me diblock copolymers, and the same difference in blends is about 35%. Note that blends and diblocks employed in Ref.[128] have a methoxy end group, and $\chi_e(T)$ estimates obtained from these systems agree with corresponding methoxy end group estimates of Ref.[129] to within error limits.

Re-analysis: For our re-analysis of SEO copolymers, we define segments based on a fixed common segment volume $\nu_{\rm ref} = 108\,\text{Å}^3$, equal to the geometric mean of molar volumes of PS and PEO segments at a reference temperature of 107.5 °C, which is the ODT temperature of SEO7. Segment volumes were calculated from molar volumes and densities given above. Based on these parameters, Eq. 8.1 yields $N_{\rm SEO7} = 243$ and $N_{\rm SEO5} = 185$. Using the procedure described in section 8.1.1, temperature dependent functions for statistical segment lengths of PS and PEO homopolymers are obtained as $b_{\rm PS} = \exp\left[(1/2)(0.00044T + 3.00)\right]$ Å[121,141] and $b_{\rm PEO} = \exp\left[(1/2)(0.00023T + 3.69)\right]$ Å[144] with respect to $\nu_{\rm ref} = 108\,\text{Å}^3$. Accordingly, we get $b_{\rm PS} = 4.88$Å, $b_{\rm PEO} = 6.60$Å at the chosen reference temperature, and accordingly, $\overline{N}_{\rm SEO7} = 845$ and $\overline{N}_{\rm SEO5} = 637$.

Fig. 8.21 shows SAXS intensity profiles of SEO7 and SEO5 for several disordered phase temperatures. Peak scattering intensity and wavenumber were extracted from the fits to measured data. Fig. 8.22 shows a comparison of results of q^* *vs.* $cNS^{-1}(q^*)/2$ to polydispersity-corrected ROL predictions of SEO7 and SEO5.

We obtained an interaction parameter $\chi_e(T)$ estimate by simultaneously fitting results of normalized inverse peak structure factor $cNS^1(q^*)$ of SEO7 and SEO5 to corresponding monodisperse ROL theory predictions. As shown in Fig. 8.23, the fit yields $\chi_e^{\rm ROL}(T) = 41.22\,T^{-1} - 0.027$. On including RPA predicted polydispersity shift (average of shifts for SEO7 and SEO5), we get $\chi_e^{\rm ROL-p}(T) = 41.22\,T^{-1} - 0.028$. As shown in the inset of Fig. 8.23, an estimate for $\chi_e(T)$ was also obtained by fitting results of SEO7 and SEO5 to corresponding monodisperse BLFH theory predictions. The result is $\chi_e^{\rm BLFH}(T) = 35.68\,T^{-1} - 0.012$, and accordingly, the polydispersity-corrected estimate is $\chi_e^{\rm BLFH-p}(T) = 35.68\,T^{-1} - 0.013$.

In Fig. 8.24, we compare $\chi_e^{\rm ROL}(T)$ and $\chi_e^{\rm BLFH}(T)$ to those obtained by Frielinghaus *et al.*[128] discussed earlier. Table 8.7 lists A and B values of the 4 $\chi_e(T)$

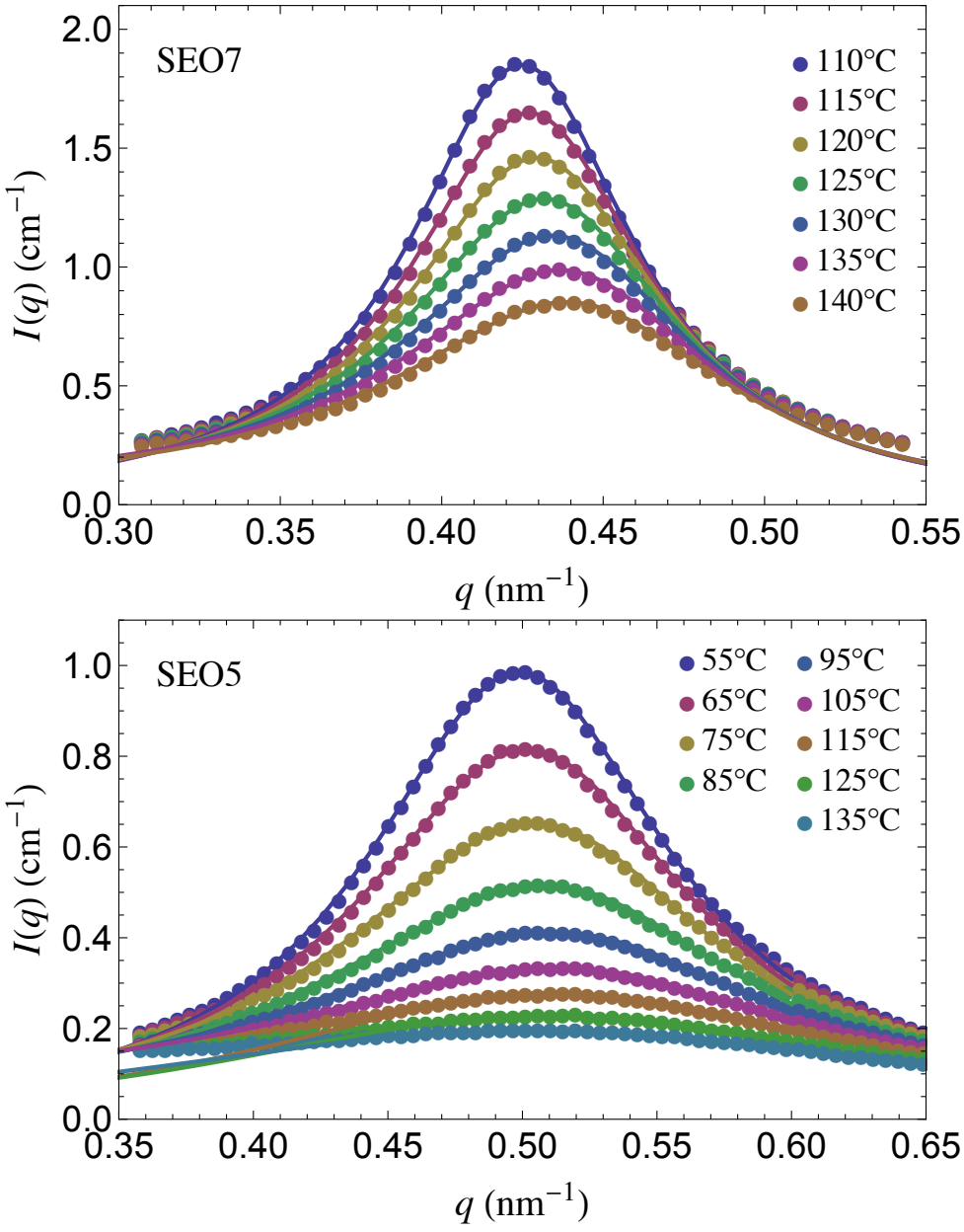

Figure 8.21: SAXS intensity $I(q)$ profiles of SEO7 (upper) and SEO5 (lower) for a series of disordered phase temperatures. For each temperature, the solid line through the data represents a fit to Eq.8.7.

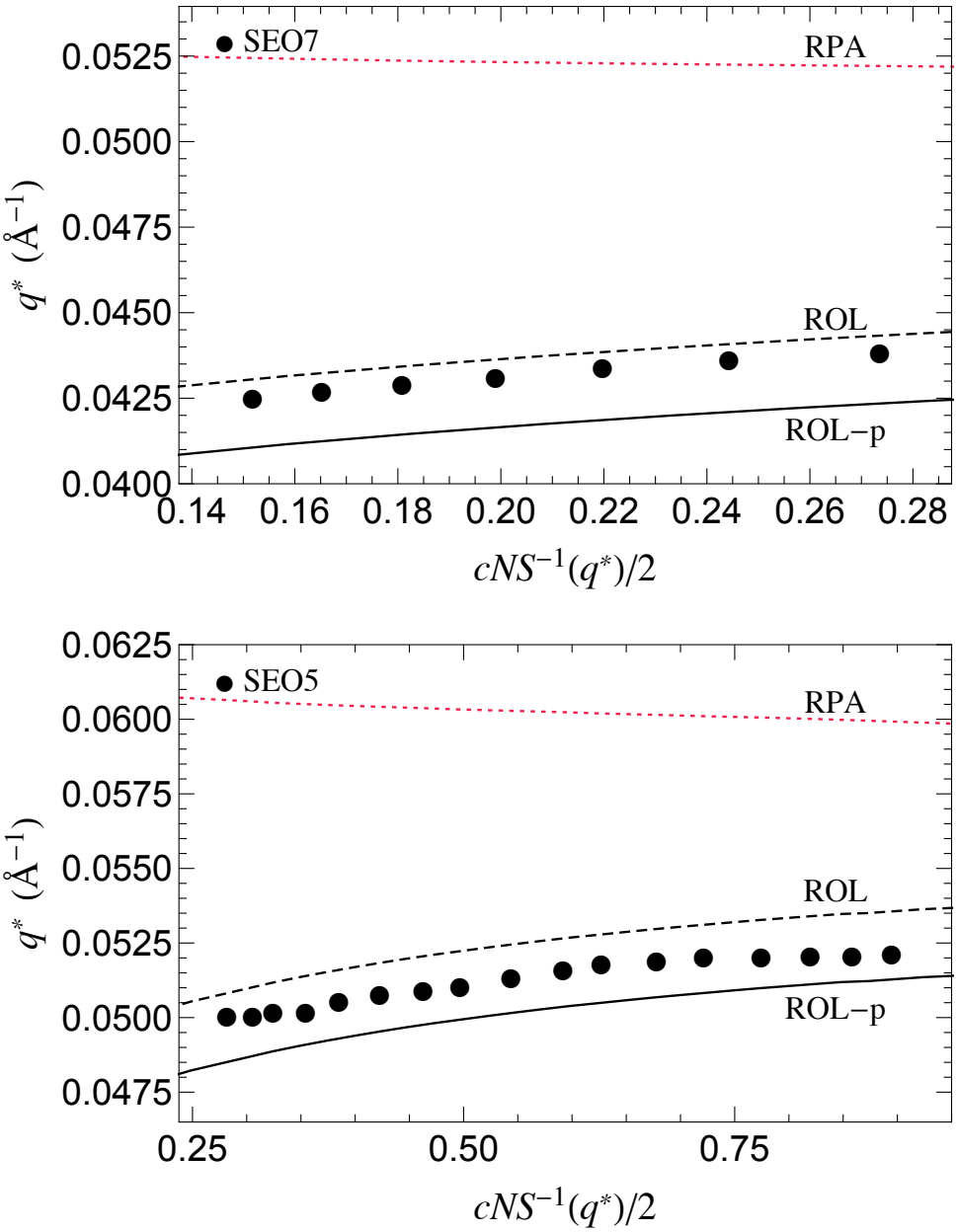

Figure 8.22: Comparison of experimental results of q^* of SEO7 (upper) and SEO5 (lower) to monodisperse RPA (red dotted line) and ROL (black dashed line) theory predictions, as well as polydispersity-corrected ROL predictions (black solid curve labeled ROL-p). RPA polydispersity shift was calculated based on measured PDI of 1.04 for both SEO7 and SEO5. Theoretically predicted minimums for PDI are 1.004 and 1.006 for SEO7 and SEO5, respectively.

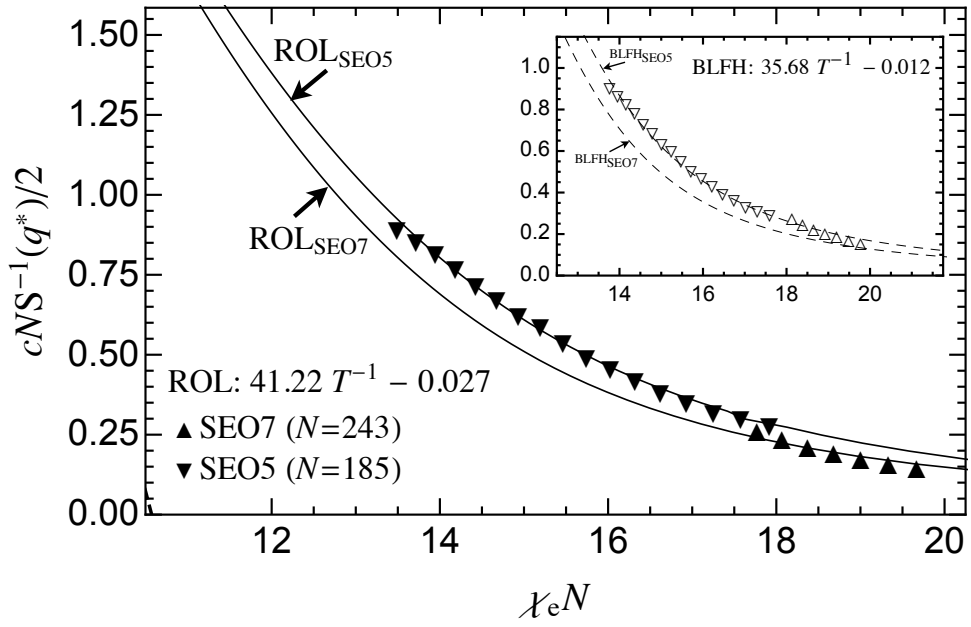

Figure 8.23: Extraction of $\chi_e(T)$ of PS-PEO by simultaneously fitting results of $cNS^1(q^*)$ *vs.* T of SEO7 and SEO5 to monodisperse ROL theory predictions. Inset: $\chi_e(T)$ from fit to monodisperse BLFH theory predictions.

estimates shown in the figure.

8.6 Order-Disorder Transition *vs.* $\overline{N}$

Fig. 8.25 shows experimental values of $(\chi_e N)_{\rm ODT}$ plotted *vs.* $\overline{N}$ for DBC systems analyzed here with known $T_{\rm ODT}$. The upper panel of Fig. 8.25 uses $\chi_e^{\rm ROL}(T)$ estimates obtained from fits to monodisperse ROL theory predictions. The lower panel uses polydispersity-corrected $\chi_e^{\rm ROL-p}(T)$ estimates. See Table 8.8 for pre-

Fitting procedure	A (K)	B	T range
ROL	41.22	−0.027	T range: 60 − 140 °C
BLFH	35.68	−0.013	T range: 60 − 140 °C
Frielinghaus-DB	18.55	0.0073	T range: 60 − 278 °C
Frielinghaus-BL	24.80	−0.0066	T range: 80 − 170 °C

Table 8.7: Estimates of $\chi_e(T) = A\,T^{-1} + B$ of PS-PEO obtained using different fitting procedures.

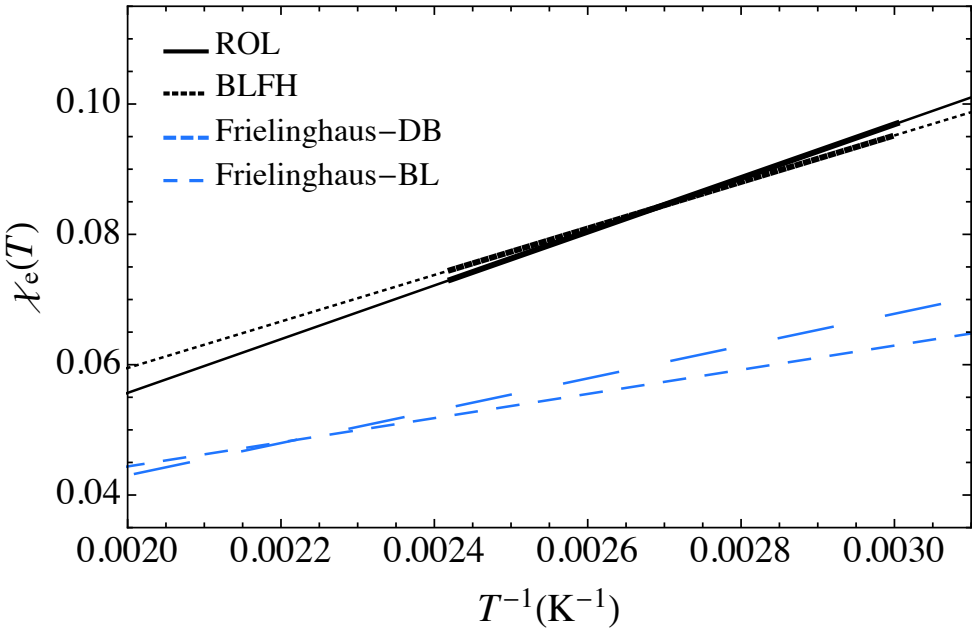

Figure 8.24: Comparison of $\chi_e(T)$ estimates of PS-PEO obtained by different fitting procedures: 1. ROL Fit of peak scattering intensity data of SEO7 and SEO5 to monodisperse ROL theory predictions. 2. BLFH Fit of peak scattering intensity data of SEO7 and SEO5 to monodisperse BLFH theory predictions. 3. Frielinghaus-DB Fit of SANS peak intensity results of a PS-PEO diblock copolymer to Fredrickson-Helfand theory predictions. 4. Frielinghaus-BL - Fit of SANS peak intensity results of a PS/PEO homopolymer blend to fluctuations theory predictions. The temperature range of peak intensity data used to obtain $\chi_e^{\mathrm{ROL}}(T)$ and $\chi_e^{\mathrm{BLFH}}(T)$ is indicated by thicker line segments. All estimates are defined with respect to $\nu_{\mathrm{ref}} = 108\mathrm{\AA}^3$.

cise values of the two estimates for all diblock copolymer pairs analyzed here. On the same plot, we show the simulations master curve (dashed curve labeled SIM) and SCF (horizontal long-dashed line) and BLFH (solid curve) theoretical predictions. It must be mentioned here that $\chi_e^{\mathrm{ROL}}(T)$ estimates were obtained using ROL theory predictions that account for asymmetries in composition and conformation, but the simulations master curve, which is our baseline for comparing $(\chi_e N)_{\mathrm{ODT}}$ values of different chemical samples, does not include these effects. Different symbols denote different diblock copolymer pairs: PI-PLA - Diamonds (IL-1 system is discussed in detail in chapter 7), PS-PI - Triangles, PS-PEO - Star, PEP-PEE - Squares, and PE-PEP - Circles. Also, for each diblock copolymer pair, we mark ODT values of those chain lengths whose scattering data was unavailable for fitting to obtain $\chi_e^{\mathrm{ROL}}(T)$ with the appropriate matching symbol, but specially, in non-black colors (eg: blue triangle for IS-54). Values given in parentheses of the legends are $\overline{N}$ values of systems. Note that IS-54 is a nearly symmetric PS-PI system studied by Bates and coworkers in Ref.,[86] different from the reference study of SI7 and SI6 whose peak scattering data is fitted to obtain $\chi_e^{\mathrm{ROL}}(T)$ of PS-PI.

Table 8.8 summarizes $\chi_e^{\mathrm{ROL}}(T)$ and $\chi_e^{\mathrm{BLFH}}(T)$ estimates for the 4 chemical pairs analyzed here. Also provided are polydispersity corrected ROL -based $\chi_e^{\mathrm{ROL-p}}(T)$ estimates. Remember that the effect of polydispersity is to shift $\chi_e(T)$ by a T-independent constant, which is approximated using monodisperse and polydisperse RPA expressions, and is therefore the same for $\chi_e(T)$ estimates from both ROL and BLFH theories. It is clear that the effect of polydispersity on $\chi_e(T)$ is negligible for all systems here.

8.7 Conclusions

We have analyzed scattering results from disordered phase of several experimental systems in a manner that allows for a direct comparison to simulation results and theoretical predictions. Two types of comparison are considered here. First, we test for each system whether the ROL theory can predict the temperature dependent peak wavenumber q^* on the basis of literature data for homopolymer statistical segment lengths. Second, we test whether we obtain values of $\chi_e N$

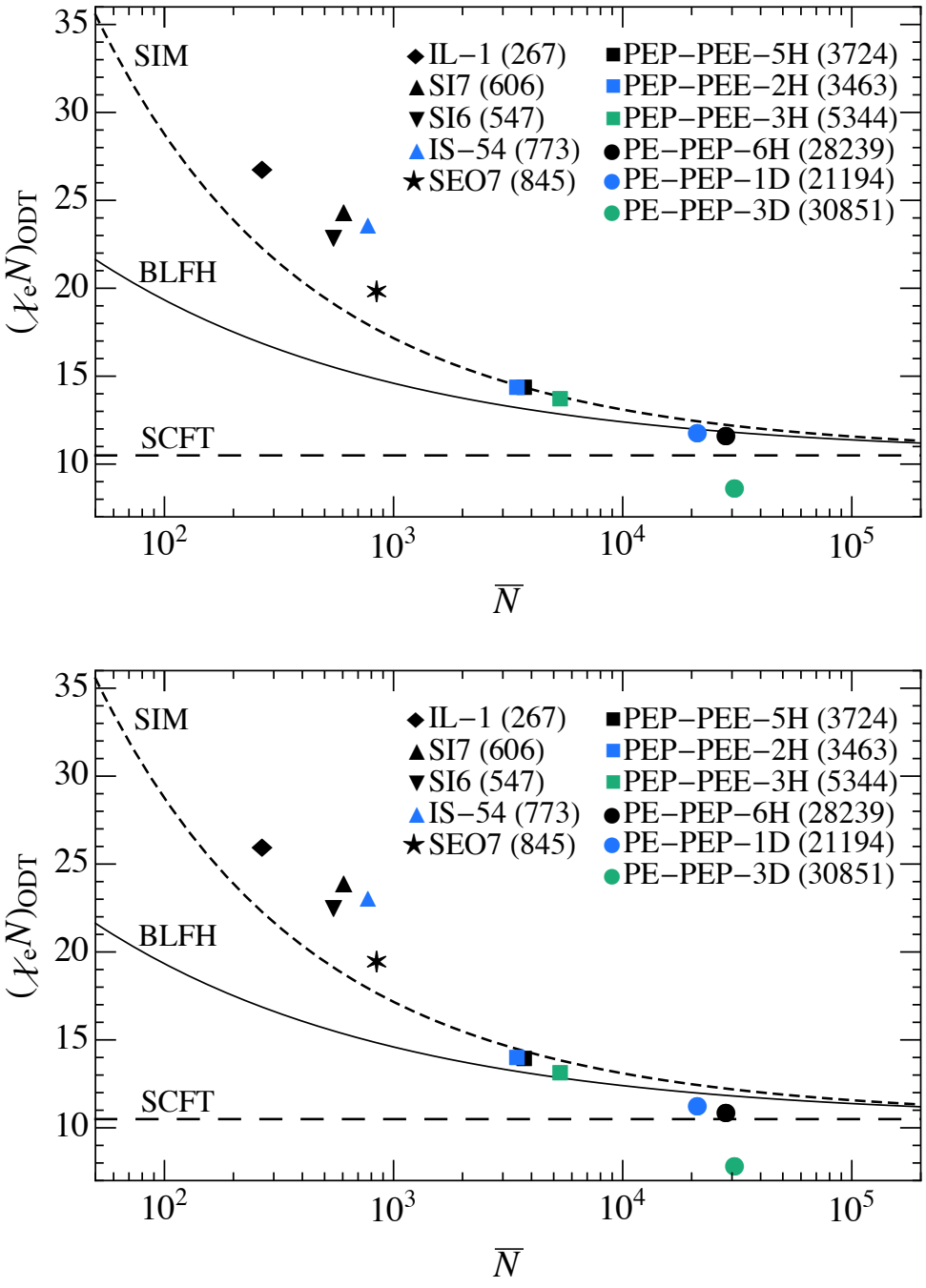

Figure 8.25: Comparison of experimental values of $(\chi_e N)_{\mathrm{ODT}}$ *vs.* $\overline{N}$ of several, nearly symmetric diblock copolymer melts to simulations master curve and SCF and FH theoretical predictions for $f = 0.5$. Experimental values of $(\chi_e N)_{\mathrm{ODT}}$ are plotted using corresponding $\chi_e^{\mathrm{ROL}}(T)$ (upper) and $\chi_e^{\mathrm{ROL-P}}(T)$ (lower) estimates. Black symbols indicate systems whose scattering data was fitted to obtain $\chi_e^{\mathrm{ROL}}(T)$.

DBC	$\overline{N}$	$R^2_{g,A}/R^2_g$	Fitting procedure	A (K)	B	$(\Delta\chi_e)_{\max}$
PEP-PEE	3724	0.68	ROL	7.05	-0.0031 (-0.0035)	3.2%
			BLFH	5.89	-0.00065	
PS-PI	606 & 547	0.41	ROL	127.05	-0.206 (-0.209)	4.5%
			BLFH	107.96	-0.159	
PE-PEP	$28,239$	0.60	ROL	15.89	-0.0330 (-0.0333)	1.6%
			BLFH	14.98	-0.0308	
PS-PEO	845 & 637	0.68	ROL	41.22	-0.027 (-0.028)	2.2%
			BLFH	35.68	-0.012	

Table 8.8: Estimates of $\chi_e(T)$ estimates of the different chemical systems analyzed here, obtained from fits of peak intensity data to monodisperse ROL and monodisperse BLFH theory predictions. Values in the parentheses are shifted values of B of polydispesity corrected ROL-based $\chi_e^{\mathrm{ROL-p}}(T)$ estimates. Polydispersity corrections were evaluated using reported SEC values for PDI.

at the order-disorder transition similar to those obtained in simulation using a value of $\chi_e(T)$ that is estimated by fitting the ROL theory to experimental results for the peak scattering intensity $I(q^*)$ in the disordered phase. In both types of analysis, we use the ROL theory as a surrogate for simulation results for characteristics of scattering in the disordered phase, because the ROL theory was previously found to accurately predict simulation results for rigorously symmetric, rigorously monodisperse simulation models. The variant of the ROL theory used here does, however, incorporate asymmetry in statistical segment lengths, which we take into account by using literature values for statistical segment lengths of both blocks in the theory, and the effects of polydispersity, which we take into account by assuming that the shifts in q^* and $cNS^{-1}(q^*)$ due to polydispersity are approximately the same as those obtained from the polydisperse RPA theory. The simulation results which we use as the basis of comparison for experimental values of $(\chi_e N)_{\mathrm{ODT}}$ are, however, simulations of rigorously symmetric, monodisperse bead-spring polymers.

When assessing the level of agreement between experimental results and simulation or theory, it is important to be cognizant of known experimental uncertainties. One of the most important sources of uncertainty in analysis of experimental results for either scattering intensities or ODTs is the uncertainty in the experimental characterization of the molecular weight M_n. Bates *et al.* estimated this uncertainty to be $\pm 5\%$ for anionically polymerized PEP-PEE copolymers. Uncertainty in the degree of polydispersity can also have a significant effect on predictions for the peak position q^*, and a smaller effect on our estimates of χ_e. Our discussion is based on the assumption that the true PDI lies somewhere between a lower bound given by the theoretical prediction for ideal anionic polymerization and an upper bound given by the value measured in a conventional SEC experiment. Because the predicted values of the PDI are close to unity for this systems considered here, this is essentially the same as saying that the PDI is bounded above by the reported value.

In comparisons of measurements of the peak wavenumber q^* to predictions of the ROL theory, the results obtained from three of the four chemical systems considered here lay between the upper bound obtained from the monodisperse and polydispersity-corrected variants of the ROL theory, using homopolymer

literature data for the temperature-dependent statistical segment length. In these cases, the ROL theory also seemed to adequately predict the temperature dependence of q^* near the ODT. The only exception to this general agreement is the PE-PEE system originally studied by Bates, Rosedale and coworkers, for which the measured value of q^* is less than that predicted by the polydispersity corrected ROL theory by nearly 10 %, as shown in Fig. 8.5. A similar, but somewhat smaller discrepancy of the same sign was seen previously in our study of the PI-PLA system. The fact that this discrepancy is only seen in some chemical systems suggests that it could be caused by a real difference between statistical segment lengths in a mixture and those found in homopoymer melts due to differences in local environment. One way to test this hypothesis would be to examine the q-dependence of $S(q)$ for homopolymer blends at wavenumber much greater than the inverse radius of gyration in systems that exhibit this discrepancy, to see if the discrepancy in the value of q^* in the diblock copolymer is accompanied by a corresponding change in the apparent statistical segment length in the blend. We note in passing that an analysis of the effective statistical segment has been measured in PE / PEP homopolymer blends by Maurer *et al.*,[1] who obtained an effective segment length very similar to the value expected on the basis of homopolymer data, consistent with our conclusion that the value of q^* in that system is consistent (to within experimental uncertainties) with the value predicted by the ROL theory or simulations.

The first step in our analysis of data for order disorder transitions is to obtain an estimate of $\chi_e(T)$ for each system by analyzing the peak-scattering in the disordered phase. We relied primarily on comparisons to the ROL theory for this purpose. One reason for this was to mimic as closely as possible the analysis that we applied to our simulations, in which the dependence of χ_e upon a simulation parameter was determined by comparison to the ROL theory. The use of the ROL theory, rather than the older BLFH theory, was essential to our analysis of simulation data because the two theories give very different predictions for deviations from the RPA deep in the disordered phase, far from the ODT, and because our simulation data included a wide range of values of χ_e and N that included a great deal of data measured far from the ODT. All of the experimental data for SANS or SAXS data analyzed here was, however, taken

in a comparatively narrow range of thermodynamic conditions near the ODT, in which $cNS^{-1}(q) < 1.0$, where the high scattering intensity facilitates accurate measurement. In this parameter regime, the predictions of the ROL and BLFH theories for the peak intensity are quite similar, particularly for systems with large $\overline{N}$, as shown in Figs. 8.6 and 8.17, and rather similar results for $\chi_e(T)$ are thus obtained by fitting to either theory. Predictions of the BLFH theory for the value of $\chi_e N$ at the ODT do, however, differ from those obtained from simulations, with differences that become more important with decreasing $\overline{N}$.

Our analysis of values of $(\chi_e N)_{\rm ODT}$ for symmetric diblock copolymers, shown in Fig. 8.25, provides the most comprehensive available test of the accuracy of theoretical predictions and simulation results for the location of the ODT. This is the first analysis in which experimental ODT results of different diblock copolymers with widely varying values of $\overline{N}$ have been plotted vs. $\overline{N}$, using estimates of $\chi_e(T)$ that were obtained by applying the same fitting procedure to all of the experimental systems and to the simulation results to which we compare. At a qualitative level, the results clearly support the prediction, originally due to Fredrickson and Helfand, that values of $(\chi_e N)$ at the ODT tend to systematically decrease with increasing $\overline{N}$, and approach the prediction of $\chi_e N = 10.5$ in the limit $\overline{N} \to \infty$. The validity of this prediction, though already widely accepted, had not previously been tested in a comparable manner. This analysis also demonstrates the existence of very large deviations from the SCFT prediction for systems with modest values of $\overline{N} = 10^2 - 10^3$, for which the magnitude of these deviations is roughly comparable to those obtained in simulations, and significantly larger than predicted by the BLFH theory.

At a quantitative level, however, the level of agreement between experimental data for $(\chi_e N)_{\rm ODT}$ and the master curve obtained from simulations is clearly worse than the near perfect agreement obtained among the different simulation models. One source of the difference may be the fact that polymer systems all have A and B blocks with nearly equal volumes but unequal statistical segment lengths, and thus unequal radii of gyration, while the simulation models were rigorously symmetric. We do not know to what extent these conformational asymmetries effect this comparison, and have not attempted to correct for this effect. The interpretation of experiments on PE-PEP polymers is also compli-

cated slightly by the fact that χ_e is small enough so that the effects of isotope labeling may be relevant, and the fact that these used several PE-PEP copolymers with somewhat different levels of deuteration. In light of these and other known uncertainties and sources of systematic error, we regard the agreement between experimental results for $(\chi_e N)_{\mathrm{ODT}}$ and simulation results as adequate for PE-PEP (circles) and SEO (star), and excellent for the PEP-PEE polymers. Among the systems studied in this chapter, the largest deviations from the master curver are obtained the SI polymers, which exhibit an upward deviation comparable to that obtained in chapter 7 for the lower molecular weight IL-1 polymer. Compared to the IL polymers, however, the SI polymers appear to exhibit more consistent behavior among polymers of differing molecular weights, which makes it less plausible in this case that the discrepancy is caused by an end-group effect.

Chapter 9

Conclusions

This chapter summarizes key conclusions of the different topics studied in this thesis.

Simulation Models

Four different off-lattice bead spring simulation models, namely H, S1, S2, and S3, were designed and calibrated to allow us to simulate systems with $\overline{N}$ values spanning over a wide range from $200 - 8000$. Model parameters of statistical segment length, pressure for NPT simulations, and the prefactor in the linear approximation for the interaction parameter χ are estimated by extrapolating results from simulations of finite chain length homopolymer simulations to infinite chain length. This procedure for defining microscopic parameters, which we supplemented by some data fitting to obtain an improved nonlinear estimate for $\chi_e(\alpha)$, is an essential part of our methodology for comparing results from a several different simulation models.

Correlations in the Disordered Phase

Results for several properties in the disordered phase from simulations of two different simulation models were compared to each other and to ROL theory predictions. Comparison of results from pairs of systems of different models at matched values of $\overline{N}$ allowed us to test the corresponding states hypothesis for properties of the disordered phase.

The ROL theory was shown to yield accurate predictions for all quantities for sufficiently long chains, and remarkably accurate predictions for some of them. All simulations results appear to be consistent with the hypothesis that the ROL

correctly predicts the dominant $\mathcal{O}(\overline{N}^{-1/2})$ corrections to the RPA in the limit $\overline{N} \to \infty$, but the rate of convergence is different for different quantities.

The ROL theory gives particularly accurate predictions for the structure factor $S(q)$ of symmetric copolymers in the limit $\alpha = 0$. Because this quantity only depends on conformational properties of individual chains, this confirms the accuracy of ROL theory predictions for single chain correlations in dense one-component liquids. The ROL theory also provides very accurate predictions for the peak wavenumber $q^\star$ for all but the shortest chains. Because our comparison of results and predictions for $q^\star$ involved using the measured "apparent" peak intensity $\chi_a^* N$ as a correlating variable, this test of the theory did not involve any fitting parameters.

The ROL theory also accurately predicts simulation results for $S(q)$ over a wide range of values of N and α if and only if the effective interaction parameter χ_e is assumed to be a nonlinear function of AB repulsion parameter α. The need for a nonlinear approximation for $\chi_e(\alpha)$ is demonstrated by the failure of results for $cNS^{-1}(q^\star)$ from different models to collapse when plotted *vs.* $\chi_e^1(\alpha)N$, where $\chi_e^1(\alpha)$ is linear approximation for $\chi_e(\alpha)$ based on perturbation theory. We estimated the dependence of $\chi_e(\alpha)$ upon α for each model from a simultaneous fit of simulation results for peak intensity $S(q^\star)$ *vs.* α of different chain lengths to the ROL theory.

The physical origin of the decrease in peak wavenumber $q^\star$ with increasing AB repulsions was clarified by separating intra- and intermolecular contributions to $cNS^{-1}(q)$, based on an appropriate form of the Ornstein-Zernike equation. The observed decrease was shown to be a result of the wavenumber dependence of the apparent interaction parameter $\chi_a(q)$, as predicted by the ROL theory, rather than a result of changes in single-chain statistics or overall coil size.

Predictions for a variety of single-chain properties, including radii of gyration of chains and blocks and $F(q_0^*)$, appear to be consistent with convergence towards ROL predictions as $\overline{N} \to \infty$, but with slower convergence than seen for other quantities.

Order-Disorder Transition and Lamellar Phase

Simulations of systems of four models (H, S1, S2, and S3) were analyzed and compared, focusing on behavior in the vicinity of the order disorder transition.

By comparing results from several different models, we were able to confirm the hypothesis that postulates that equivalent behavior should be obtained in corresponding states of different models, defined by equal values of $\chi_e N$ and $\overline{N}$. Universal behavior was found over a much wider range of $\overline{N}$ and $\chi_e N$ values than the range of validity of any existing quantitative theory.

Results for all properties suggest that ordered and disordered phases are strongly segregated near the ODT for the range $\overline{N} \lesssim 10^4$ studied here, and that the Fredrickso-Helfand theory of the transition becomes progressively less accurate with decreasing $\overline{N}$ in this regime. Most systems studied experimentally have values of $\overline{N} \lesssim 10^4$, and thus fall in the strongly segregated regime. Within the strongly-segregated universal regime, the extent of contact between A and B monomers, as characterized by the value of g', differs by about 7 % between the ordered and disordered phase at the ODT, almost independent of $\overline{N}$. The value of the peak wavenumber q^* is found to be nearly continuous across the ODT, as also seen in experiments. SCFT yields surprisingly accurate predictions for several properties of the ordered phase in this parameter regime.

All of the comparisons of different simulation models to each other and to theoretical predictions depend critically upon definitions for the Flory-Huggins parameter $\chi_e(\alpha)$ for each simulation model. We used estimates obtained from fits of disordered phase peak intensity data of different chain lengths of a model to the ROL theory. Our conclusions about the validity of universal scaling hypothesis and the accuracy of SCFT predictions are contingent upon the use of this particular method of estimating $\chi_e(\alpha)$.

Comparison of Experiments to Simulations and Theory

Our analysis of experimental scattering data of different chemical systems yields $\chi_e(T)$ estimates obtained by the same fitting procedure as used for our simulation models, *i. e.,* from fitting peak scattering intensity data in the disordered phase of different chain lengths of a chemical system to corresponding ROL theory predictions. The resulting $\chi_e(T)$ estimates are used to construct a plot of $(\chi_e N)_{\mathrm{ODT}}$ *vs.* $\overline{N}$ from experimentally measured ODT temperatures of different molecular weights for different chemical systems. The results clearly support the prediction, originally due to Fredrickson and Helfand, that values of $(\chi_e N)$ at the ODT tend to systematically decrease with increasing $\overline{N}$, and

approach the prediction of $\chi_e N = 10.5$ in the limit $\overline{N} \to \infty$. Our analysis also demonstrates the existence of very large deviations from the SCFT prediction for systems with modest values of $\overline{N} = 10^2 - 10^3$, for which the magnitude of these deviations is roughly comparable to those obtained in simulations, and significantly larger than predicted by the BLFH theory.

Bibliography

[1] W. M. Maurer, F. S. Bates, T. P. Lodge, K. Almdal, K. Mortensen, and G. H. Fredrickson. Can a single function for χ account for block copolymer and homopolymer blend phase behavior? *J. Chem. Phys.*, 108:2989–3000, 1998.

[2] F. S. Bates and G. H. Fredrickson. Block copolymers-designer soft materials. *Physics Today*, 52(2):32–38, 1999.

[3] M. W. Matsen. The standard Gaussian model for block copolymer melts. *J. Phys.: Condens. Matter*, 14:R21–R47, 2002.

[4] L. Leibler. Theory of microphase separation in block copolymers. *Macromolecules*, 13:1602–1617, 1980.

[5] G. H. Fredrickson and E. Helfand. Fluctuation effects in the theory of microphase separation in block copolymers. *J. Chem. Phys.*, 87(1):697, 1987.

[6] S. Brazovskiĭ. Phase transition of an isotropic system to a nonuniform state. *Sov. Phys., JETP*, 41:85, 1975.

[7] R. Holyst and A. Vilgis. Critical temperature and concentration versus molecular weight in polymer blends: Conformations, fluctuations, and the Ginzburg criterion. *J. Chem. Phys.*, 99(6):4835–4844, 1993.

[8] A. Kudlay and S. Stepanow. Short range fluctuations in the Hartree theory of diblock copolymer melts. *J. Chem. Phys.*, 118(9):4272–4276, 2003.

[9] Z.-G. Wang. Concentration fluctuation in binary polymer blends: χ parameter, spinodal and ginzburg criterion. *J. Chem. Phys.*, 117(1):481–500, 2002.

[10] J. P. Wittmer, H. Meyer, J. Baschnagel, A. Johner, S. Obukhov, L. Mattioni, M. Müller, and A. N. Semenov. Long range bond-bond correlations in dense polymer solutions. *Phys. Rev. Lett.*, 93:147801, 2004.

[11] J. P. Wittmer, P. Beckrich, H. Meyer, A. Cavallo, A. Johner, and J. Baschnager. Intramolecular long-range correlations in polymer melts: The segmental size distribution and its moments. *Phys. Rev. E*, 76:011803, 2007.

[12] P. Beckrich, A. Johner, A. N. Semenov, S. P. Obukhov, H. Benoît, and J. P. Wittmer. Intramolecular form factor in dense polymer systems: Systematic deviations from the Debye formula. *Macromolecules*, 40:3805–3814, 2007.

[13] D. C. Morse. Diagrammatic analysis of correlations in polymer fluids: Cluster diagrams via Edwards field theory. *Annals of Physics*, 321(10):2318–2389, 2006.

[14] P. Grzywacz, J. Qin, and D. C. Morse. Renormalization of the one-loop theory of fluctuations in polymer blends and diblock copolymer melts. *Phys. Rev. E*, 76:061802, 2007.

[15] J. Qin and D. C. Morse. Renormalized one-loop theory of correlations in polymer blends. *J. Chem. Phys.*, 130:224902, 2009.

[16] D. C. Morse and J. Qin. Relationships among coarse-grained field theories of fluctuations in polymer liquids. *J. Chem. Phys.*, 134(8):084902, 2011.

[17] J. Qin, P. Grzywacz, and D. C. Morse. Renormalized one-loop theory of correlations in disordered diblock copolymers. *J. Chem. Phys.*, 135:084902, 2011.

[18] M. W. Matsen and M. Schick. Stable and unstable phases of a diblock copolymer melt. *Phys. Rev. Lett.*, 72:2660, 1994.

[19] M. W. Matsen and M. Schick. Stable and unstable phases of a linear multiblock copolymer melt. *Macromolecules*, 27:7157, 1994.

[20] M. W. Matsen and F. S. Bates. Unifying weak- and strong-segregation block copolymer theories. *Macromolecules*, 29(4):1091–1098, 1996.

[21] G.H. Fredrickson, V. Ganesan, and F. Drolet. Field-theoretic computer simulation methods for polymers and complex fluids. *Macromolecules*, 35:16–39, 2002.

[22] J. H. Owens, I. S. Gancarz, J. T. Koberstein, and T. P. Russel. Investigation of the microphase separation transition in low molecular weight diblock copolymers. *Macromolecules*, 22:3380–3387, 1989.

[23] F. S. Bates and M. A. Hartney. Block copolymers near the microphase separation transition. 3. Small-angle neutron scattering study of the homogeneous melt state. *Macromolecules*, 18:2478–2486, 1984.

[24] K. Mori, A. Hasegawa, and T. Hashimoto. Order-disorder transition of polystyrene-*block*-polyisoprene. I. Thermal concentration fluctuations in single-phase melts and solutions and determination of χ as a function of molecular weight and composition. *J. Chem. Phys.*, 104:7765–7777, 1996.

[25] F. S. Bates, J. H. Rosedale, and G. H. Fredrickson. Fluctuation effects in symmetric diblock copolymer near the order-disorder transition. *J. Chem. Phys.*, 92:6255–6270, 1990.

[26] F. S. Bates, J. H. Rosedale, G. H. Fredrickson, and C. J. Glinka. Fluctuation-induced first-order transition of an isotropic system to a periodic state. *Phys. Rev. Lett.*, 61:2229–2232, 1988.

[27] J. H. Rosedale, F. S. Bates, K. Almdal, K. Mortensen, and G. D. Wignall. Order and disorder in symmetric diblock copolymer melts. *Macromolecules*, 28:1429–1443, 1995.

[28] K. Almdal, K. Mortensen, A. J. Ryan, and F. S. Bates. Order, disorder, and composition fluctuation effects in low molar mass hydrocarbon-

poly(dimethylsiloxane) diblock copolymers. *Macromolecules*, 28:1429–1443, 1995.

[29] N. Sakamoto and T. Hashimoto. Order-disorder transition of low molecular weight polystyrene-*block*-polyisoprene. 1. SAXS analysis of two characteristic temperatures. *Macromolecules*, 28:6825–6834, 1995.

[30] T. Hashimoto, T. Ogawa, and C. D. Han. Determination of sharpness of order-disorder transition of block copolymers by scattering methods. *J. Phys. Soc. Jpn.*, 63(6):2206–2214, 1994.

[31] V. T. Bartels, V. Abetz, K. Mortensen, and M. Stamm. Microphase separation of symmetric poly(styrene-b-paramethylstyrene) diblock copolymer. *Europhys. Lett.*, 27(5):371–376, 1994.

[32] T. Wolff, C. Burger, and W. Ruland. Synchrotron SAXS study of microphase separation transition in diblock copolymers. *Macromolecules*, 26:1707–1711, 1993.

[33] F. S. Bates. Measurement of the correlation hole in homogeneous block copolymer melts. *Macromolecules*, 18:525–528, 1985.

[34] G. H. Fredrickson and E. Helfand. Fluctuation effects in the theory of microphase separation in block copolymers. *J. Chem. Phys.*, 87(1):697–705, 1987.

[35] J. L. Barrat and G. H. Fredrickson. Collective and single-chain correlations near the block copolymer order-disorder-transition. *J. Chem. Phys.*, 95(2):1281–1289, 1991.

[36] M. Olvera de la Cruz. Transitions to periodic structures in block copolymer melts. *Phys. Rev. Lett.*, 67(1):85–88, 1991.

[37] A. M. Mayes and M. Olvera de la Cruz. Concentration fluctuation effects on disorder-order-transitions in block copolymer melts. *J. Chem. Phys.*, 95:4670, 1991.

[38] D. J. Amit. *Field theory, the renormalization group, and critical phenomena*. World Scientific, 1984.

[39] K. S. Schweizer and J. G. Curro. RISM theory of polymer liquids: Analytical results for continuum models of melts and alloys. *Chemical Physics*, 149(00):105–127, 1990.

[40] K. S. Schweizer and J. G. Curro. Integral equation theories of the structure, thermodynamics, and phase transitions of polymer fluids. *Advances in Chemical Physics*, 98:1–142, 1997.

[41] J. Qin. *Studies of block copolymer melts by field theory and molecular simulation*. PhD thesis, University of Minnesota, 2009.

[42] J. Qin, P. Grzywacz, and D. C. Morse. Renormalized one-loop theory of correlations in disordered diblock copolymers. *J. Chem. Phys.*, 135:84902, 2011.

[43] I. Y. Erukhimovich. Fluctuations and the formation of domain structure in heteropolymers. *Polymer Science U.S.S.R.*, 24:2223–2232, 1982.

[44] J. Glaser, J. Qin, P. Medapuram, M. Müller, and D.C. Morse. Test of a scaling hypothesis for the structure factor of disordered diblock copolymer melts. *Soft Matter*, 8:11310–11317, 2012.

[45] J. K. Chung. *Correlations in polymer blends: Simulations, perturbation theory, and coarse-grained theory*. Ph. d. thesis, University of Minnesota, 2009.

[46] P. G. de Gennes. De-mixtion in polymer liquids. *J. Phys. Lett.*, 38:44, 1977.

[47] A. Chakrabarti, P. Toral, and J. D. Gunton. Microphase separation in block copolymers. *Phys. Rev. Lett.*, 63(24):2661–2664, 1989.

[48] H. Fried and K. Binder. The microphase separation transition in symmetric diblock copolymer melts: A Monte Carlo study. *J. Chem. Phys.*, 94(12):8349–8366, 1991.

[49] H. Fried and K. Binder. Non-Gaussian conformational behaviour in diblock copolymer melts : Is the RPA valid? *Europhys. Lett.*, 16(3):237–242, 1991.

[50] K. Binder and H. Fried. Asymmetric block copolymer melts near the microphase separation transition: A Monte Carlo simulation. *Macromolecules*, 26:6878–6883, 1993.

[51] Y. Yang, J. Lu, D. Yan, and J. Ding. Monte Carlo simulation of phase separations of block copolymers and of corresponding blends. *Macromol. Theory Simul.*, 3:731–741, 1994.

[52] R. G. Larson. Simulation of lamellar phase transitions in block copolymers and surfactants. *Mol. Sim.*, 13:321–345, 1994.

[53] R. G. Larson. Simulation of lamellar phase transitions in block copolymers. *Macromolecules*, 27(15):4198–4203, 1994.

[54] U. Micka and K. Binder. Unusual finite size effects in the Monte Carlo simulation of microphase formation of block copolymer melts. *Macromol. Theory Simul.*, 4:419–447, 1995.

[55] L. A. Molina and J. J. Freire. Monte Carlo study of symmetric diblock copolymers in selective solvents. *Macromolecules*, 28:2705–2713, 1995.

[56] M. B. Ko and W. L. Mattice. Monte-Carlo simulation of concentrated diblock copolymers in a selective solvent: Anisotropy of the diffusion. *Macromolecules*, 28:6871–6877, 1995.

[57] G. S. Grest, M. D. Lacasse, K. Kremer, and A. M. Gupta. Efficient continuum model for simulating polymer blends and copolymers. *J. Chem. Phys.*, 105(23):10583–10594, 1996.

[58] R. G. Larson. Monte Carlo simulations of the phase behavior of surfactant solutions. *J. Phys. II France*, 6:1441–1463, 1996.

[59] T. Dotera and A. Hatano. The diagonal bond method: A new lattice polymer model for simulation study of block copolymers. *J. Chem. Phys.*, 105(18):8413–8427, 1996.

[60] T. Pakula, K. Karatasos, S. H. Anastasiadis, and G. Fytas. Computer simulation of static and dynamic behavior of diblock copolymer melts. *Macromolecules*, 30:8463–8472, 1997.

[61] A. Hoffmann, J. U. Sommer, and A. Blumen. Statics and dynamics of dense copolymer melts: A Monte Carlo simulation study. *J. Chem. Phys.*, 106(16):6709–6721, 1997.

[62] A. Hoffmann, J. U. Sommer, and A. Blumen. Computer simulations of asymmetric block copolymers. *J. Chem. Phys.*, 107(18):7559–7570, 1997.

[63] R. D. Groot and T. J. Madden. Dynamic simulation of diblock copolymer microphase separation. *J. Chem. Phys.*, 108(20):8713–8724, 1998.

[64] M. Murat, G. S. Grest, and K. Kremer. Statics and dynamics of symmetric diblock copolymers: A molecular dynamics study. *Macromolecules*, 32(3):595–609, 1999.

[65] A. J. Schultz, C. K. Hall, and J. Genzer. Computer simulation of copolymer phase behavior. *J. Chem. Phys.*, 117(22):10329–10338, 2002.

[66] Q. Wang, P. F. Nealey, and J. J. de Pablo. Lamellar structures of symmetric diblock copolymers: Comparisons between lattice Monte Carlo simulations and self-consistent mean-field calculations. *Macromolecules*, 35:9563–9573, 2002.

[67] O. N. Vassiliev and M. W. Matsen. Fluctuation effects in block copolymer melts. *J. Chem. Phys.*, 118(16):7700–7713, 2003.

[68] F. J. Martınez-Veracoechea and F. A. Escobedo. Lattice Monte Carlo simulations of the gyroid phase in monodisperse and bidisperse block copolymer system. *Macromolecules*, 38:8522–8531, 2005.

[69] M. W. Matsen, G. H. Griffiths, R. A. Wickham, and O. N. Vassiliev. Monte Carlo phase diagram for diblock copolymer melts. *J. Chem. Phys.*, 124:024904, 2006.

[70] F. J. Martínez-Veracoechea and F. A. Escobedo. Simulation of the gyroid phase in off-lattice models of pure diblock copolymer melts. *J. Chem. Phys.*, 125:104907, 2006.

[71] F. J. Martínez-Veracoechea and F. A. Escobedo. Bicontinuous phases in diblock copolymer/homopolymer blends: Simulation and self-consistent field theory. *Macromolecules*, 42:1775–1784, 2009.

[72] F. A. Detcheverry, D. Q. Pike, P. F. Nealey, M. Müller, and J.J. de Pablo. Monte Carlo simulation of coarse grain polymeric systems. *Phys. Rev. Lett.*, 197801:2009, 102.

[73] D.Q. Pike, F.A. Detcheverry, M. Müller, and J.J. de Pablo. Theoretically informed Monte Carlo simulation of polymeric systems. *J. Chem. Phys.*, 084903:2009, 131.

[74] F. A. Detcheverry, D. Q. Pike, P. F. Nealey, M. Müller, and J. J. de Pablo. Simulation of theoretically informed coarse grain models of polymeric systems. *Faraday Discussion*, 111:2010, 144.

[75] T. M. Beardsley and M. W. Matsen. Monte Carlo phase diagram for diblock copolymer melts. *Eur. Phys. J. E*, 32:255–264, 2010.

[76] J. Zong and Q. Wang. Fluctuation/correlation effects in symmetric diblock copolymers: On the order-disorder transition. *J. Chem. Phys.*, 139:124907, 2013.

[77] J. Qin and D. C. Morse. Fluctuations in symmetric diblock copolymers: Testing theories old and new. *Phys. Rev. Lett.*, 108:238301, 2012.

[78] J. Glaser, J. Qin, P. Medapuram, and D.C. Morse. Collective and single-chain correlations in disordered melts of symmetric diblock copolymers: Quantitative comparison of simulations and theory. *Macromolecules*, 47:851–869, 2014.

[79] M. Müller. Comparison of selfconsistent field theory and Monte Carlo simulations. *Soft Matter, Volume 1: Polymer Melts and Mixtures*, 1:179–282, 2006.

[80] M. Mueller and K. Binder. Computer simulation of asymmetric polymer mixtures. *Macromolecules*, 28:1825–1834, 1995.

[81] D. C. Morse and J. K. Chung. On the chain length dependence of local correlations in polymer melts and a perturbation theory of symmetric polymer blends. *J. Chem. Phys.*, 130:224901, 2009.

[82] A. Gauger, A. Weyersberg, and T. Pakula. Phase transition in diblock copolymers: Theory and Monte Carlo simulations. *Phys. Rev. E*, 48(1):377–390, 1993.

[83] M. Müller. Effects of structural disparities in polymer blends: A Monte-Carlo investigation. *Macromolecules*, 28:6556–6564, 1995.

[84] R. D. Groot and P. B. Warren. Dissipative particle dynamics: Bridging the gap between atomistic and mesoscopic simulation. *J. Chem. Phys.*, 107(11):4423–4435, 1997.

[85] F. S. Bates, M. F. Schulz, A. K. Khandpur, S. Förster, J. H. Rosedale, K. Almdal, and K. Mortensen. Fluctuations, conformational asymmetry and block copolymer phase behavior. *Faraday Discuss.*, 98:7–18, 1994.

[86] A. K. Khandpur, S. Foerster, F. S. Bates, I. W. Hamley, A. J. Ryan, W. Bras, K. Almdal, and K. Mortensen. Polyisoprene-polystyrene diblock copolymer phase diagram near the order-disorder transition. *Macromolecules*, 28:8796–8806, 1995.

[87] S. Lee, T. M. Gillard, and F. S. Bates. Fluctuations, order and disorder in short diblock copolymers. *AIChE Journal*, 59:3502–3513, 2013.

[88] N. P. Balsara, S. V. Jonnalagadda, C. C. Lin, C. C. Han, and R. Krishnamoorti. Thermodynamic interactions and correlations in mixtures of two homopolymers and a block copolymer by small angle neutron scattering. *J. Chem. Phys.*, 99:10011, 1993.

[89] C. C. Lin, S. V. Jonnalagadda, P. K. Kesani, H. J. Dai, and N. P. Balsara. Effect of molecular structure on the thermodynamics of block copolymer melts. *Macromolecules*, 27:7769, 1994.

[90] C. C. Lin, H. S. Jeon, N. P. Balsara, and B. Hammouda. Spinodal decomposition in multicomponent polymer blends. *J. Chem. Phys.*, 103:1957, 1995.

[91] C. C. Lin, S. V. Jonnalagadda, N. P. Balsara, C. C. Han, and R. Krishnamoorti. Thermodynamic interactions in multicomponent polymer blends. *Macromolecules*, 29:661, 1996.

[92] H. S. Jeon, J. H. Lee, and N. P. Balsara. Predictions of the thermodynamic properties of multicomponent polyolefin blends from measurements on two-component systems. *Macromolecules*, 31:3328, 1998.

[93] H. S. Jeon, J. H. Lee, N. P. Balsara, and M. C. Newstein. An experimental study of the thermodynamic properties of multicomponent polyolefin blends with ordered and disordered phases. *Macromolecules*, 31:3340, 1998.

[94] G. Floudas, B. Vazaiou, F. Schipper, R. Ulrich, U. Wiesner, H. Iatrou, and N. Hadjichristidis. Poly(ethylene oxide-b-isoprene) diblock copolymer phase diagram. *Macromolecules*, 34:2947–2957, 2001.

[95] M. Müller and F. Schmid. Incorporating fluctuations and dynamics in self-consistent field theories for polymer blends. *Advances in Polymer Science*, 185:1–58, 2005.

[96] G. J. Martyna, D. J. Tobias, and M. L. Klein. Constant pressure molecular dynamics algorithms. *J. Chem. Phys.*, 101:4177–4189, 1994.

[97] J. Anderson, C. Lorenz, and A. Travesset. General purpose molecular dynamics simulations fully implemented on graphics processing units. *J. Comp. Phys.*, 227(10):5342–5359, 2008.

[98] D. C. Morse. Simpatico, 2013. "`http://github.com/dmorse/simpatico`".

[99] K. Almdal, J. H. Rosedale, F. S. Bates, G. D. Wignall, and G. H. Fredrickson. Gaussian to stretched-coil transition in block copolymer melts. *Phys. Rev. Lett.*, 65:1112–1115, 1990.

[100] I. Ya. Erukhimovich and A. V. Dobrynin. Conformation of molten diblock copolymer macromolecules near the point of microphase separation transition. *Macromolecules*, 25(17):4411, 1992.

[101] T. A. Vilgis and R. Borsali. Screening of interactions in homopolymer blends and in diblock copolymer systems. *Macromolecules*, 23(12):3172–3178, 1990.

[102] A. Laio and M. Parrinello. Escaping free-energy minima. *Proceedings of the National Academy of Sciences of the United States of America*, 99(20):12562–12566, 2002.

[103] A. Barducci, G. Bussi, and M. Parrinello. Well-tempered metadynamics: A smoothly converging and tunable free-energy method. *Phys. Rev. Lett.*, 100(2):020603, 2008.

[104] D. Branduardi, G. Bussi, and M. Parrinello. Metadynamics with adaptive gaussians. *J. Chem. Th. and Comp.*, 8(7):2247–2254, 2012.

[105] P. Raiteri, A. Laio, F. L. Gervasio, C. Micheletti, and M. Parrinello. Efficient reconstruction of complex free energy landscapes by multiple walkers metadynamics. *J. Phys. Chem. B*, 110(8):3533–3539, 2006.

[106] R. W. Hockney and J. W. Eastwood. *Computer Simulation using Particles*. IOP Publishing Ltd., 1988.

[107] M. Bonomi, A. Barducci, and M. Parrinello. Reconstructing the equilibrium boltzmann distribution from well-tempered metadynamics. *J. Comp. Chem.*, 30(11):1615–1621, 2009.

[108] `http://github.com/jglaser/metadynamics-plugin`.

[109] R. H. Bisseling. *Parallel Scientific Computation*. Oxford University Press, 2004.

[110] `http://github.com/jglaser/dfftlib`.

[111] P. Medapuram, J. Glaser, and D. C. Morse. Universal phenomenology of symmetric diblock copolymers near the orderdisorder transition. *Macromolecules*, 48:819–839, 2015.

[112] J. Glaser, P. Medapuram, T. M. Beardsley, M. W. Matsen, and D.C. Morse. Universality of block copolymer melts. *Phys. Rev. Lett.*, 113:068302, 2014.

[113] K. R. Shull, A. M. Mayes, and T. P. Russell. Segment distributions in lamellar diblock copolymers. *Macromolecules*, 26:3929–3936, 1993.

[114] A. N. Semenov. Scattering of statistical structure of polymer/polymer interfaces. *Macromolecules*, 27(10):2732–2735, 1994.

[115] F. Schmid and M. Müller. Quantitative comparison of self-consistent field theories for polymers near interfaces with Monte Carlo simulations. *Macromolecules*, 28:8639, 1995.

[116] A. Werner, F. Schmid, M. Müller, and K. Binder. Intrinsic profiles and capillary waves at homopolymer interfaces: A Monte Carlo study. *Phys. Rev. E*, 59:728, 1999.

[117] K. Amundson and E. Helfand. Quasi-static mechanical properties of lamellar block copolymer microstructure. *Macromolecules*, 26:1324, 1993.

[118] Z.-G. Wang. Response and instabilities of the lamellar phase of diblock copolymers under uniaxial stress. *J. Chem. Phys.*, 100:2298, 1994.

[119] P. Stasiak and M.W. Matsen. Monte Carlo field-theoretic simulations for melts of symmetric diblock copolymer. *Macromolecules*, 46:8037–8045, 2013.

[120] T. M. Gillard, P. Medapuram, D. Morse, and F. S. Bates. Fluctuations, phase transitions, and latent heat in short diblock copolymers: Comparison of experiment, simulation, and theory. *Macromolecules*, 48:4733–4741, 2015.

[121] J. Fetters, D. J. Lohse, D. Richter, T. A. Witten, and A. Zirkel. Connection between polymer molecular weight, density, chain dimensions, and melt viscoelastic properties. *Macromolecules*, 27:4639–4647, 1994.

[122] D. R. Witzke, R. Narayan, and J. J. Kolstad. Reversible kinetics and thermodynamics of the homopolymerization of l-lactide with 2-ethylhexanoic acid tin(II) salt. *Macromolecules*, 30:7075–7085, 1997.

[123] T. M. Gillard, D. Phelan, C. Leighton, and F. S. Bates. Determination of the lamellae-to-disorder heat of transition in a short diblock copolymer by relaxation calorimetry. *Macromolecules*, 48:2801–2811, 2015.

[124] R. Krishnamoorti, W. W. Graessley, A. Zirkel, D. Richter, N. Hadjichristidis, L. J. Fetters, and D. J. Lohse. Melt-state polymer chain dimensions as a function of temperature. *J. Poly. Sci.: Part B: Poly. Phys.*, 40:1768–1776, 2002.

[125] T. A. Shefelbine, M. E. Vigild, M. W. Matsen, D. A. Hajduk, M. A. Hillmyer, E. L. Cussler, and F. S. Bates. Core-shell gyroid morphology in a poly(isoprene-block-styrene-block-dimethylsiloxane) triblock copolymer. *J. Amer. Chem. Soc.*, 121:8457–8465, 1999.

[126] K. S. Anderson and M. A. Hillmyer. Melt chain dimensions of polylactide. *Macromolecules*, 37:1857–1862, 2004.

[127] W. W. Graessley. *Polymeric Liquids and Networks: Structure and Properties*. Taylor and Francis, New York, 2004.

[128] H. Frielinghaus, K. Mortensen, and K. Almdal. Difference of interaction parameter of a PS/PEO homopolymer blend and diblock copolymer in comparison to other systems. *Macromolecular Symposia*, 149:63–67, 2000.

[129] H. Frielinghaus, W. B. Pedersen, P. S. Larsen, K. Almdal, and K. Mortensen. End effects in poly(styrene)/poly(ethylene oxide) copolymers. *Macromolecules*, 34:1096–1104, 2001.

[130] J. P. Hansen and L. Verlet. Phase transitions of the Lennard-Jones system. *Physical Review*, 184:151–161, 1969.

[131] A. A. Teran and N. P. Balsara. Thermodynamics of block copolymers with and without salt. *The Journal of Physical Chemistry B*, 118:4–17, 2014.

[132] J. S. Pedersen, D. Posselt, and K. Moretensen. Analytical treatment of the resolution function for small-angle scattering. *J. App. Crys.*, 23:321–333, 1990.

[133] L. Leibler and H. Benoit. Theory of correlations in partially labelled homopolymer melts. *Polymer*, 22:195–201, 1981.

[134] K. Mori, H. Tanaka, H. Hasegawa, and T. Hashimoto. Small-angle X-ray scattering from block copolymers in disordered state: 2. Effect of molecular weight distribution. *Polymer*, 30:1389–1398, 1989.

[135] G. R. Meira. Data reduction in size exlcusion chromatography of polymers. In H. G. Barth and J. W. Mays, editors, *Modern Methods of Polymer Characterization*. John Wiley and Sons, New York, 1991.

[136] A. F. Johnson, M. A. Mohsin, and Z. G. Meszena. Predicted and observed molecular weight distributions and dispersity indices in living polymerization processes: Some comments. *J. Macromol. Sci. - Rev. in Macromol. Chem. and Phys.*, C39:527–560, 1999.

[137] W. Lee, H. Lee, J. Cha, T. Chang, K. J. Hanley, and T. P. Lodge. Molecular weight distribution of polystyrene made by anionic polymerization. *Macromolecules*, 33:5111–5115, 2000.

[138] F. S. Bates, M. F. Schulz, J. H. Rosedale, and K. Almdal. Correlation of binary polyolefin phase behavior with statistical segment length asymmetry. *Macromolecules*, 25:5547–5550, 1992.

[139] N. A. Rounds. *PhD Dissertation*. PhD thesis, University of Akron, 1970.

[140] D. J. Meier. Theory of block copolymers. I. Domain formation in A-B block copolymers. *J. Poly. Sci. Part C: Poly. Symp.*, 26:81–98, 1969.

[141] T. A. Orofino and A. Ciferri. Temperature dependence of the unperturbed dimensions of polystyrene. *J. Phys. Chem.*, 68:31363141, 1964.

[142] W. W. Maurer. *Thermodynamics of homopolymer/homopolymer/diblock copolymer blends*. PhD thesis, University of Minnesota, Sept. 1998.

[143] J. E. Mark. *Physical Properties of Polymers Handbook*. Springer, Philadelphia, PA, 2007.

[144] J. E. Mark and P. J. Flory. The configuration of the polyoxyethylene chain. *J. Amer. Chem. Soc.*, 87:1415–1423, 1965.

Appendices

Appendix A

Effect of Polydispersity on RPA $S(q)$ Prediction

Leibler and Benoit[133] were the first to study polydispersity effects on the behavior of $S(q)$ and show that polydispersity shifts both peak wavenumber and peak structure factor significantly. They incorporated polydispersity effects in the RPA prediction for $S(q)$ (see Eq. in section 2.1.1) by obtaining a modified expression for the single-chain form factor $F(q) \equiv cN\Sigma_{ij}\Omega_{ij}(q)/\det|\Omega_{ij}(q)|$, which, as mentioned in chapter 2, is a function of the intramolecular correlation function $\Omega_{ij}(q)$ $(i,j = A \text{ or } B)$. In the absence of polydispersity, the random walk model assumed in Leibler's RPA yields the following expressions for intra-block correlation function $\Omega_{ii,0}(q)$ for $i = A$ or B, and inter-block correlation function $\Omega_{ij,0}(q)$ for $i \neq j$:

$$\begin{aligned} \Omega_{ii,0}(q) &= cNf_i^2 g\left(q^2R_{g,i}^2\right) \\ \Omega_{ij,0}(q) &= cNf_if_j h\left(q^2R_{g,i}^2\right) h\left(q^2R_{g,j}^2\right), \end{aligned} \tag{A.1}$$

where $R_{g,i}^2 = f_iNb_i^2/6$ is the radius of gyration of the i-th block, $g(x) \equiv 2(e^x1 + x)/x^2$ is the Debye function, and $h(x) \equiv (1e^x)/x$. In order to include polydispersity effects, Leibler and Benoit[133] substituted $Ng\left(q^2R_{g,i}^2\right)$ and

$Nh\left(q^2R_{g,i}^2\right)h\left(q^2R_{g,j}^2\right)$ in the above expressions with corresponding averages

$$\overline{Ng\left(q^2R_{g,i}^2\right)} \equiv \int_0^\infty \int_0^\infty P(N_A)P(N_B)g\left((N_A+N_B)\frac{q^2b^2}{6}f_i\right)dN_AdN_B$$

$$\overline{Nh\left(q^2R_{g,i}^2\right)h\left(q^2R_{g,j}^2\right)} \equiv \int_0^\infty \int_0^\infty P(N_A)P(N_B)h\left((N_A+N_B)\tfrac{q^2b^2}{6}f_i\right)h\left((N_A+N_B)\tfrac{q^2b^2}{6}f_j\right)dN_AdN_B,$$

where $i, j = A$ or B derived assuming each block in a copolymer has a chain length (or molecular weight) distribution independent of the other (which they are in the usual two-step synthesis methods) and each given by the Schultz-Zimm distribution $P(N) = \frac{k^{k+1}}{\Gamma(k+1)}\frac{N^{k-1}}{N_n^k}\exp\left(-k\frac{N}{N_n}\right)$. Here, $P(N)$ is the probability that a block contains N segments, parameter k is related to polydispersity index N_w/N_n through $N_w/N_n = (k+1)/k$, and $\Gamma(x)$ denotes the gamma function (when k is an integer $\Gamma(k+1) = k!$). Leibler and Benoit additionally assumed identical Schultz-Zimm distributions for the two blocks, *i. e.,* $k_A = k_B$, and also, limited themselves to symmetric diblock copolymers with an average fraction of $f_A = N_{An}/(N_{An} + N_{Bn}) = 0.5$. Later, Bates and Hartney[23] extended Leibler-Benoit calculations to asymmetric block copolymers with $f_A \neq 0.5$. This generalization is important because most of the block copolymers, including those analyzed in chapter 8, are asymmetric.

Mori *et al.*[134] further generalized Bates-Hartney expressions to cases where both blocks can have different polydispersity indexes. Specifically, they considered two cases: Case 1 in which both A and B blocks have Schultz-Zimm distributions, thus resulting in compositional polydispersity and case 2 in which the composition fraction f is fixed and only the total chain length N has a Schultz-Zimm distribution. Case 2, which is a special case of the general case 1, is the same as what Bates and Hartney originally studied. Mori *et al.*, however, obtained somewhat different formulas than Bates and Hartney and, furthermore, attributed the discrepancy to an oversight in the calculations by Bates and Hartney. Accordingly, for analysis of experimental scattering results of diblock copolymer systems in chapters 7 and 8, for which information on chain length distributions of individual blocks is unavailable, we use the case 2 expressions provided by Mori *et al.* rather than those by Bates and Hartney. According

to Mori *et al.*, the polydispersity included expression for the single-chain form factor is given by

$$F_0\left(q,k\right)=cN_n\frac{f_A^2N_ng\left(q^2R_{g,A}^2,k\right)+2f_A(1-f_A)N_nh\left(q^2R_{g,A}^2,k\right)h\left(q^2R_{g,B}^2,k\right)+(1-f_A)^2N_ng\left(q^2R_{g,B}^2,k\right)}{f_A^2(1-f_A)^2N_n^2\left(g\left(q^2R_{g,A}^2,k\right)g\left(q^2R_{g,B}^2,k\right)-h\left(q^2R_{g,A}^2,k\right)^2h\left(q^2R_{g,B}^2,k\right)^2\right)}, \tag{A.2}$$

where k is the parameter related to polydispersity index N_w/N_n and $N_ng\left(q^2R_{g,i}^2,k\right)$ and $\overline{N_nh\left(q^2R_{g,i}^2,k\right)h\left(q^2R_{g,j}^2,k\right)}$ are analytical expressions for the averages $\overline{Ng\left(q^2R_{g,i}^2\right)}$ and $\overline{Nh\left(q^2R_{g,i}^2\right)h\left(q^2R_{g,j}^2\right)}$ defined in Eq. A. Their exact expressions are given by

$$g\left(x_i,k\right)=\frac{2}{x^2}\left(x_i+\left(\frac{k}{k+x_i}\right)^k-1\right)$$

$$h\left(x_i,k\right)=\frac{1}{x_i}\left(1-\left(\frac{k}{k+x_i}\right)^k\right)$$

,

where $x_i\equiv q^2R_{g,i}^2$. Fig. A.1 shows the RPA prediction $cNS_0^{-1}(q)=F_0(q)-2\chi_eN$ using both monodisperse ($F_0(q)$) and polydisperse ($F_0(q,k)$) expressions for the single-chain form factor F_0. It is clear from the lower and upper dashed curves in this plot that a higher polydispersity index results in greater shifts in peak wavenumber and structure factor. The fact that polydispersity causes a *left-ward* shift in the peak wavenumber is promising given the *sign* of observed discrepancies between experimental results of q^* and theoretical predictions in chapter 8.

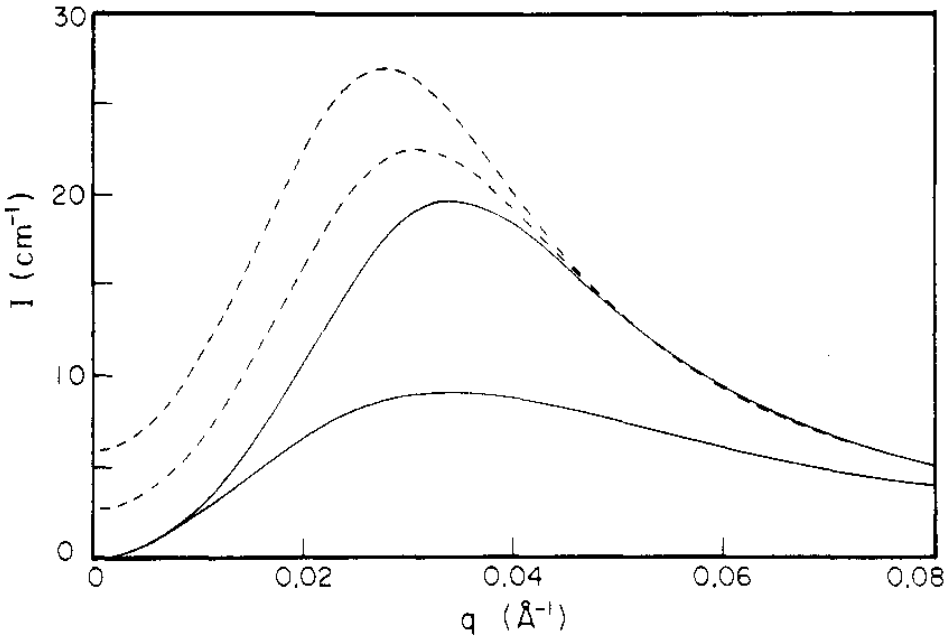

Figure A.1: Figure 11 in Ref.[23] shows effects of polydispersity on the RPA prediction for structure factor $S(q)$: $N_w/N_n = 1$, $\chi N = 0$ and 5.68, lower and upper solid curves, respectively; $\chi_N = 5.68$, $N_w/N_n = 1.05$ and 1.1, lower and upper dashed curves, respectively.

Appendix B

Details of Comparison of Experimental Scattering Results to Theoretical Predictions

This appendix provides details relevant to comparison of experimental scattering results to theoretical predictions in chapter 8.

The numerical code we use for evaluating ROL theory predictions outputs peak wavenumber and peak structure factor as functions of the apparent interaction parameter $\chi_a^\star N$ instead of the interaction parameter $\chi_e N$ (see Eq.2.20). The code assumes $\tilde{N} = \tilde{\nu} = 1$ for input parameters. This implies a scaling transformation $N \to \lambda N = 1$, $\nu \to \nu/\lambda$ and $b \to \lambda^{-1/2} b$, where $\lambda = 1/N$. Since additionally $\tilde{\nu} = 1$, the unit of length in this framework becomes $(\nu/\lambda)^{1/3}$. Hence, in these units, block statistical segment lengths are given in the form of input parameters $\tilde{b}_i = b_i N^{1/6}/\nu^{1/3}$. Values of b_i, N, and ν at the system's reference temperature are used to evaluate $\tilde{b}_i$. This implies that the T-dependence of input parameters b_i, N, and ν is neglected in evaluation of ROL theory predictions.

In order to include the T-dependence of these parameters, we would have to know the T-dependence of $\chi_a^\star$ or equivalently of χ_e apriori. We could have implemented an iterative procedure in which an assumed, initial T-dependence of χ_e is eventually revised until convergence is reached. We, however, opted for an easier, although less accurate method in which all parameters are taken at a

fixed reference temperature.

For evaluation of BLFH theory predictions for $cNS^{-1}(q^*)$ *vs.* $\chi_e N$, we used composition dependent constant $C(f) = C(1-f)$ of Eq.8.11. Specifically, we used $C(0.55) = 277$ for PEP-PEE-5H ($f = 0.56$), SI7 ($f = 0.46$), and SI6 ($f = 0.46$) and $C(0.5) = 256.778$ for PE-PEP-6H ($f = 0.49$), SEO7 ($f = 0.48$), and SEO5 ($f = 0.48$). Similarly, for fitting $T_{\rm ODT}$s to the BLFH theory prediction for ODT, we used $(\chi_e N)_{\rm ODT} = 10.698 + 43.16\overline{N}^{-1/3}$ for PEP-PEE and PS-PI samples and $(\chi_e N)_{\rm ODT} = 10.495 + 41.022\overline{N}^{-1/3}$ for PE-PEE samples.